Crustal Strain and Seismic Hazard of the NE Tibetan Plateau

Qi Ou

Thesis submitted to the University of Oxford

for the degree of Doctor of Philosophy

in

Earth Sciences

Department of Earth Sciences

and

University of Oxford

Michaelmas, 2020

Supervised by Prof. Richard Walker and Prof. Barry Parsons

Declaration

The contents of this thesis are all my own work, except where otherwise stated. The views and opinions expressed herein are mine and not necessarily those of any other person or body unless so attributed.

Abstract

Crustal Strain and Seismic Hazard of the NE Tibetan Plateau

Qi Ou
St Cross College, Oxford

Michaelmas Term, 2020

This thesis focuses on the seismic hazard of the NE Tibetan Plateau, an area that hosted one of the largest and most deadly earthquakes in China's recorded history. In order to estimate rates of earthquake occurrence from strain rates, it is necessary to use the Gutenberg-Richter relationship and assume a maximum magnitude. The largest recorded earthquake in the NE Tibetan Plateau is the 1920 Haiyuan Earthquake. It has often been quoted as of M 8.7, on a magnitude scale of uncertain meaning, a result of unknown origin and an outlier in empirical magnitude and rupture parameter relationships. Therefore, I first use historical seismograms, modern Pleiades imagery and field-acquired drone data to re-estimate the magnitude of the 1920 Haiyuan Earthquake, which is corrected to M_W 7.9±0.2. Literature review suggests the possibility that many magnitudes of historical Chinese earthquakes based on the intensity and magnitude scaling relationships could be systematically overestimated. An existing conversion method is highlighted for quick magnitude re-estimations for historical earthquakes, though careful systematic revisits to historical earthquake magnitudes are recommended. Second, 10 ascending and 13 descending frames of Sentinel-1 interferometric synthetic aperture radar (InSAR) data acquired between 2014 to 2019 and covering the NE Tibetan Plateau are analysed to determine crustal velocities in the satellite line of sight. These frame-based line-of-sight velocities are combined with constraints from Global Navigation Satellite System (GNSS) velocities to derive a high-resolution 3-dimensional velocity field for the region in a well-defined frame of reference. The crustal velocities can be used to constrain geodetic slip rates across the Haiyuan, Gulang and East Kunlun Faults, creep time series over the Laohushan Section of the Haiyuan fault, as well as enabling the determination of crustal strain rates that can be used to determine the rates of earthquake occurrence for the region.

Extended Abstract

Crustal Strain and Seismic Hazard of the NE Tibetan Plateau

Qi Ou

St Cross College, Oxford

Michaelmas, 2020

This thesis is designed to improve the seismic hazard assessment of the NE Tibetan Plateau, one of the most tectonically active regions in China. Existing seismic hazard assessments in China are largely based on seismic catalogues. Nevertheless, instrumental catalogues, which only start in the beginning of the 20th century, are too short to capture the recurrence intervals of large earthquakes. Although China has a historical earthquake catalogue going back to B.C. 230, this catalogue is especially incomplete in the NE Tibetan Plateau due to its relative remoteness. An alternative approach is to estimate earthquake rates from interseismic strain rate using the Gutenberg-Richter relationship. The launch of the Sentinel-1 satellites enables high-resolution measurement of crustal strain from InSAR time series. To apply the Gutenberg-Richter relationship, a maximum magnitude of earthquakes in a region is required, which for the NE Tibetan Plateau can be assumed to be that of 1920 Haiyuan Earthquake. However, this event has been reported with a broad range of magnitudes from M_W7.8 to M8.7, which, if not better constrained, would result in large uncertainties in the earthquake rates obtained.

In Chapter 2, I first reestimate the moment magnitude of the 1920 Haiyuan Earthquake using both seismological and geomorphological methods. By analysing and modelling historical seismograms and measuring horizontal offsets from high resolution satellite and drone imagery, I obtain independent results that converge to $M_W 7.9 \pm 0.2$. I also summarise the distinction and relations between Gutenberg's surface wave magnitude (M), Gutenberg and Richter's broad-band body wave magnitude (m_B), the 1-Hz body-wave magnitude (m_b), the modern surface wave magnitude (M_S) and the moment magnitude (M_W), the definitions of which tend to blur in historical catalogues and non-seismological studies. After reviewing literature through the history of the evolution of earthquake magnitudes, I raise a caution that the intensity-based magnitudes of historical earthquakes in China could be systematically overestimated.

Chapters 3 to 5 are dedicated to measuring the crustal strain of the NE Tibetan Plateau. Chapter 3 performs time series analysis on 5 years of InSAR data to generate frame-sized velocity maps that cover the NE Tibetan Plateau. Over 10000 interferograms are generated semiautomatically using the LiCSAR processing chain. Effectiveness of the Generic Atmospheric Correction Online Service (GACOS) models for correcting atmospheric delay is evaluated. New Small Baselines Subset (NSBAS) method is used to identify interferograms with unwrapping mistakes and extract velocities from the time series data. This work results in 10 frames of ascending and 13 frames of descending line-of-sight velocity maps with $\sim$1 mm/yr uncertainty.

Chapter 4 presents a method of mosaicing the 23 frames of individually referenced velocity maps into regional velocity maps in a reference frame provided by Global Navigation Satellite System (GNSS) data. Through a joint inversion of offsets between InSAR frame overlaps and offsets between InSAR and GNSS line-of-sight velocities, frames along each track are stitched together with resultant average frame overlap pixel offsets of -0.05 ± 0.87 mm/yr. A two-step velocity decomposition is performed to first extract east and subvertical velocities from the ascending and descending velocities and then separate the vertical component from the subvertical velocity with interpolated north velocity from GNSS. Preliminary interpretations of the east and vertical velocity maps are provided.

Chapter 5 produces horizontal strain rate maps from the derivatives of the east and north velocity maps from InSAR and GNSS, respectively. The resultant strain rate map is better at highlighting strain on the tectonic features than that derived from GNSS data alone. The major strike-slip Haiyuan and East Kunlun Faults are highlighted as areas of the fastest strain accumulation. Especially, the fault branches at the east end of the East Kunlun Fault exhibit high strain rate due to the slower eastward movement of the Bailongjiang microblock than its surrounding crust. Combining the total strain rate in the mapped area and the reestimated magnitude of the 1920 Haiyuan Earthquake, I provide estimates of earthquake rates using the Gutenberg-Richter relationship and compare them with three catalogues covering different time periods and magnitude ranges.

Chapter 6 concludes the thesis by summarising the research outcomes, outlining further scientific results that can be derived from the InSAR velocity maps, as well as questions that are still open for future seismic hazard assessment.

Acknowledgements

When I started this project, it didn't occur to me that it will be the centenary year of the Haiyuan earthquake when I finish. A kid growing up on the east coast of China, I was never aware of this disastrous event. The 2008 Wenchuan Earthquake was the first earthquake in my memory, in my first year of studying abroad. When I visited the Hexi Corridor before starting university, I was marvelling at the Great Wall of the Han Dynasty and the paintings in the Mogao Caves, not knowing a subject called Geology. Fate is an interesting thing. It has brought me from Physics to Geology. Being a geologist has then brought me back to the Hexi Corridor three more times, and now I will never forget there was a devastating earthquake that happened in the Ningxia and Gansu Provinces in 1920 that took many lives.

I would like to thank my supervisors Richard Walker and Barry Parsons for their guidance, patience and support through the past four years, and for giving me the opportunity to work on these fascinating problems. I would like to thank James Jackson for sending an email to Peizhen Zhang about a 'smart' student wishing to help out in the aftermath of the 2013 Lushan Earthquake and thank Weitao Wang, Zhuqi Zhang and Caicai Liu for taking me to their field trip in Qaidam that summer. It was because of these experiences I was excited by Richard's proposal on seismic hazard assessment for Northern China and attracted to Barry's vision of using InSAR for this purpose. I am glad I became their students and I am glad I spent the past four years working on this project.

Too many people have helped me through this project. Galina Kulikova is thanked for her incredible patience and instructions throughout the seismological journey, be it at Potsdam, at Oxford or over emails. Austin taught me photogrammetry and became my best buddy in our seismogram and seismograph hunts. Many colleagues worldwide scanned seismograms for me for free and generously shared with me their knowledge and expertise. Jingxing Yu spent a lot of time checking my fault mapping and offset measurements and handled all the logistics for my two field trips for which I cannot thank more. The field support from Siyu Wang, Weitao Wang, and Cheng Wang are warmly appreciated. Wenjun Zheng provided me with a scan of a very informative map of the Haiyuan Fault Zone which helped my interpretation of the geomorphology. Various useful discussions with Peizhen Zhang, Wenjun Zheng, Chuanyou Li, Zhikun Ren and Zhuqi Zhang are also remembered and appreciated.

My InSAR result is a fruit of years of hard work from many people who are in or have been through COMET. I am grateful to Milan Lazecký for his continual support through my processing of the InSAR data. I also thank Chen Yu for providing me with the GACOS atmospheric corrections. In particular, I am indebted to Simon Daout who taught me everything about InSAR, from the principles of time series analysis to the interpretation of results at all stages, and tailor-made various tools for my particular use cases. The frame stitching method which Lin Shen generously shared with me was a great inspiration. Jonathan Weiss helped me run VELMAP tests for my strain rate study. Chris Rollins shared with me his latest thoughts and methods for earthquake rate estimation. Simon, Jonathan and Chris are all thanked for proofreading and improving my writing in the InSAR chapters of the thesis. Last but not least, I would like to thank Tim Wright and Jess Hawthorne for examining my thesis. The discussion during and after the viva were very helpful and gave me many ideas for future work.

I also thank everyone in the 50.03 office for creating a cosy working environment. Various scripts and tutorials passed down from David Mackenzie, Timothy Middledon, Yu Zhou and Eleanor Ainscoe were bibles in my first year. Camaraderie offered by Nick Dodds and JD constantly reminded me that I am not alone, and their telling of my drinking stories always made me feel easy when ordering juice in pubs. Wendy Tsai and Roberta Wilkinson's arrival made all the difference to the gender balance in the office as if my voice also became louder. Ben Johnson and Neil Marshall's interest in historical seismogram made me think maybe I also have something to pass on. The 'office' actually expanded after the COVID lock-down, to Richard's plot, to the University Park and to Zoom and Slack; Tamarah King, Ian Piece and everybody's effort in cultivating and maintaining a lively and stimulating Slack group certainly gave me a source of strength in the final months of writing this thesis.

Many people have come and gone in the past four years. I thank all the friends I made at St Cross, at Department, at Stonemason, at Iffley Road, at Castle Mill, at conferences and everybody who have accompanied me and helped me through the various stages of my DPhil life. Especially, I thank Weimu Xu for always being a caring mentor and Yuhang He for providing technical, emotional and nutritional support during the lock-down and writing-up period. Last but not least, I would like to thank my parents, for their believing in me, for enduring 13 years of not having me around and for their endless love.

None of the seismological studies would have been possible without the seismograms from the following institutions: the USGS,University of Potsdam, University of Hamburg, Northwestern University, John Carroll University Meteorological and Seismological Observatory (*JCUMSO*, 2019), Australia National University, Swedish National Seismic Network (*SNSN*, 1904), Observatorio San Calixto (Bolivia), Istituto Nazionale di Geofisica e Vulcanologia (Italy, (*INGV*, 2019)), the Japan Meteorological Agency, Servicio Sismológico Nacional (http://www.susu.adep.or.jp/), Instituto de Geofísica (Mexico, *SSN* (2019)), Royal Netherlands Meteorological Institute, GNS Science (New Zealand), Institut Cartogràfic i Geològic de Catalunya (*ICGC*, 2019), Observatori de l'Ebre, El Observatorio Fabra (*RACAB*, 2019), and Instituto Geográfico Nacional (Spain). The contact information of these institutions can be found in the supplementary data set S1. Our scanned and digitised seismograms can be found in the IRIS Seismo Archives (https://ds.iris.edu/seismo-archives/quakes/1920haiyuan/)

I have been supported through scholarships and awards from China Scholarship Council-Pacific Alliance Group Oxford Scholarship, Great Britain-China Educational Trust and Burdett Coutts Fund, which are warmly appreciated.

Contents

List of Figures

List of Tables

Chapter 1

Introduction

1.1 Earthquake Hazard of China

China is a country often shaken by earthquakes. Its over 2000-year long earthquake record includes over a thousand damaging earthquakes, some of them the most tragic in human history (*CEA-PBED*, 1995). The 1556 Huaxian Earthquake, for example, caused over 830,000 deaths, the largest earthquake death toll recorded worldwide (*Hou et al.*, 1998). Since 1900, China has totalled over 640,000 earthquake casualties, more than any other country in the world (*CEA-PBED*, 1995) (Fig 1.1). Out of the ten most deadly earthquakes in the past century, three of them occurred in China (Fig 1.1). The 1920 Haiyuan Earthquake, the largest of the three, caused 200,000 casualties (*Zhang et al.*, 1987). The 1976 M_W7.5 Tangshan Earthquake took over 240,000 lives, injured ∼800,000, and resulted in direct economic loss of USD 2 billion (*Zhang et al.*, 2003). The most recent 2008 M_W7.9 Wenchuan Earthquake killed ∼87,000, injured over 374,000, destroyed over 5 million houses and damaged 21 million more; the total economic loss reached USD 86 billion. Therefore, earthquake damage mitigation is of paramount importance for China.

Earthquake hazard is not evenly distributed across China, nor is its population. As shown in Fig 1.2a,b, most of the population reside in the topographically flat

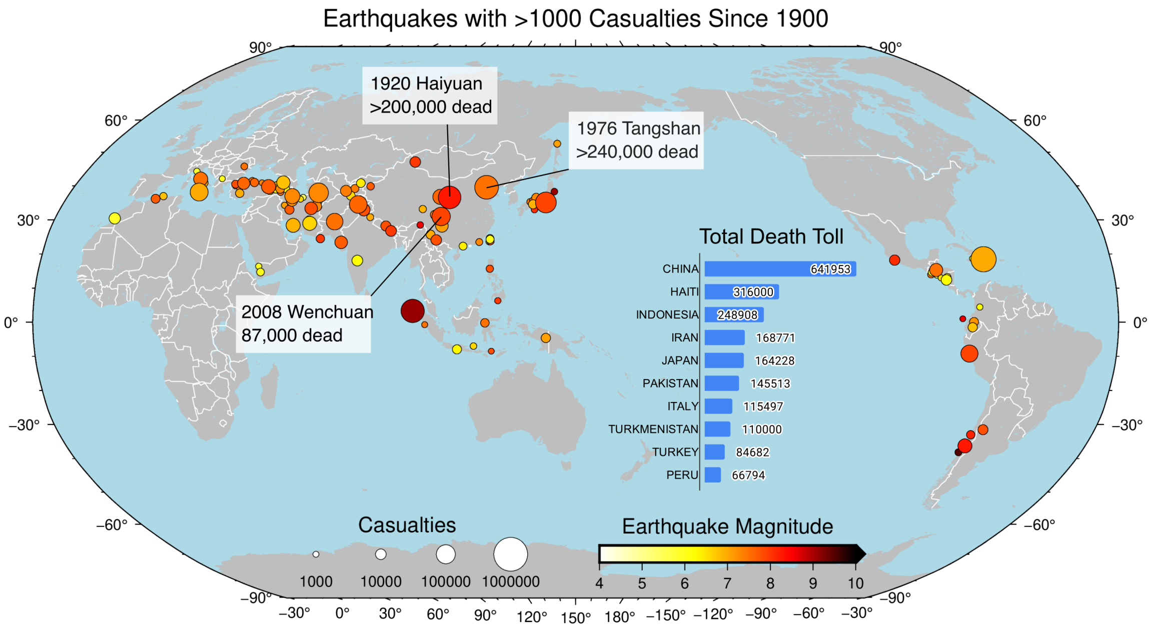

Figure 1.1: Earthquakes with over 1000 casualties since 1900, from data compiled by *National Geophysical Data Center / World Data Service (NGDC/WDS)* (2020). The three most deadly earthquakes in China in the past century, the 1920 Haiyuan Earthquake, 1976 Tangshan Earthquake and the 2008 Wenchuan Earthquake, are labeled in text. The bar chart shows the ten countries with the highest cumulative earthquake casualties in since 1900 calculated from the same data source.

North China Plain and more generally the eastern part of China, whereas most of the earthquakes in continental China recorded between 1906 and 2016 by the International Seismological Center Global Earthquakes Model (*ISC*, 2019)(white circles in Fig 1.2b) happened in and around the Tibetan Plateau. This makes the margins of the eastern Tibetan Plateau, where these two distributions overlap, the locations where devastating earthquakes are most likely to happen. This trend is reflected in the earthquake records through history (Fig 1.2c), where the majority of the devastating earthquakes with over 1000 casualties were recorded along the eastern margin of Tibetan Plateau, hence the name "the north-south seismic belt" (*Zhang*, 2013).

The heavy loss of the 2008 Wenchuan Earthquake at the boundary between the Tibetan Plateau and the Sichuan Basin served as a dire reminder of the importance of earthquake disaster mitigation. Since then, significant progress has been made

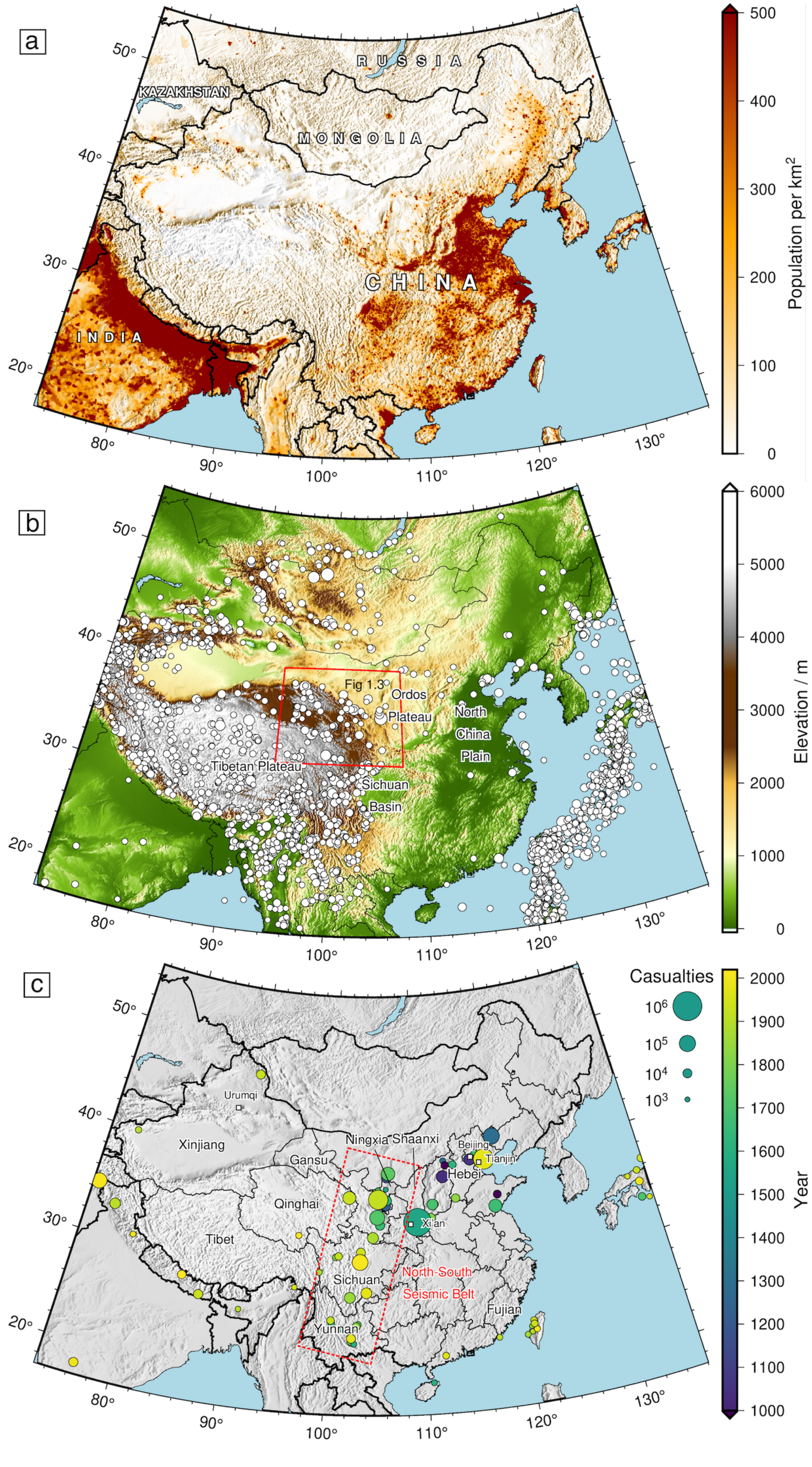
a
RUSSIA
KAZAKHSTAN
MONGOLIA
CHINA
INDIA
50°
40°
30°
20°
80°
90°
100°
110°
120°
130°
Population per km^2
500
400
300
200
100
0
b
Fig 1.3
Ordos
Plateau
North
China
Plain
Tibetan Plateau
Sichuan
Basin
Elevation / m
6000
5000
4000
3000
2000
1000
0
c
Urumqi
Xinjiang
Gansu
Ningxia
Shaanxi
Beijing
Tianjin
Hebei
Qinghai
Xi'an
Tibet
Sichuan
North-South
Seismic Belt
Fujian
Yunnan
Casualties
10^6
10^5
10^4
10^3
Year
2000
1900
1800
1700
1600
1500
1400
1300
1200
1100
1000

to improve China's earthquake resilience. A fifth-generation seismic ground-motion zonation map of China was implemented to update building codes (*Gao*, 2015). An earthquake scenario has been created based on a historical earthquake for Weinan, Shaanxi Province, near the 1556 Huaxian Earthquake (*Rodgers et al.*, 2020). Novel technologies such as virtual reality have been employed to create earthquake drill simulation systems and improve earthquake education (*Zhou and Jia*, 2011; *Gong et al.*, 2015). Three pilot earthquake early warning systems have been deployed by the China Earthquakes Administration to cover the Sichuan-Yunnan Region, in the southeast margin of the Tibetan Plateau, the Beijing-Tianjin-Heibei Region, near the 1976 Tangshan Earthquake and where the population density is the highest, and the Fujian coastal area in collaboration with the National Taiwan University (*Peng et al.*, 2020). As such, with the recent memory of the 2008 Wenchuan earthquake, more earthquake resistant infrastructures in the rebuilt areas, and the experiences gained with the early warning system that come with subsequent earthquakes (e.g., 2017 M_W 6.5 Jiuzhaigou earthquake) that continue to shake the region (*Fu et al.*, 2019; *Peng et al.*, 2020; *Li et al.*, 2020b), the area around the southeast margin of the Tibetan Plateau is on its way to becoming one of the most earthquake resilient areas of China.

On the other hand, the northeastern margin of the Tibetan Plateau, where the 1920 Haiyuan Earthquake took over 200,000 lives, has not experienced the same

Figure 1.2 *(preceding page)*: (a) 30 arc-second resolution population density map based on 2015 census data and adjusted to match the 2015 revision of the United Nations World Population Prospects country totals from *CIESIN* (2018) shaded by topography from ETOPO1 (*Amante and Eakins*, 2008). (b) ISC-GEM catalogue from 1906 to 2016 (*ISC*, 2019) on top of topography. (c) Historical record of earthquakes with over 1000 casualties (*National Geophysical Data Center / World Data Service (NGDC/WDS)*, 2020) with today's provincial administrative boundaries of China. Provincial administration boundaries of China are from EU Open Data Portal (*EUODP*, 2020). The red solid box in (b) shows the extent of Fig 1.3 and the red dashed box in (c) outlines the north-south seismic belt.

level of resilience improvement, partly due to its slower economic development and relatively lower population density. This region is comprised of parts of the Qinghai, Gansu and Ningxia Provinces (Fig 1.3a), three out of the five Chinese provinces of the lowest gross domestic products (GDP) between 2015 and 2019 (*NBSC*, 2019). This region is traditionally known as the Hexi Corridor, a narrow stretch of lower-lying habitable plain between the hostile terrains of the Gobi Desert and the Qilianshan Mountains (Fig 1.3b). Due to this unique geographical location, the Hexi Corridor formed the first leg of the ancient Silk Road (inset of Fig 1.3b), a trans-continental trade route linking the prosperous North China Plain and the countries in Central Asia and Europe. With the launch of the Belt Road Initiative in 2013, China is rejuvenating the concept of the historical Silk Road by investing hundreds of billions into infrastructure building in countries along the ancient Silk Road to improve cross-border co-operation (*OECD*, 2018). In 2014, a new high speed railway opened along the Hexi Corridor, with trains running at speeds of 200-250 km/h between the cities of Tianshui, Lanzhou, Xining, Zhangye and Jiuquan, each of which has a population over a million (*Lawrence et al.*, 2019), and connecting them to Urumuqi of Xinjiang Province in the northwest and Xi'an of Shaanxi Province in the southeast (Fig 1.2) where it joins a much more extensive railway network across the eastern part of China. With the greater connectivity comes more communication and economic activities. At the same time, the number of people and properties susceptible to earthquake damage will also increase. If the potential seismic risk is not mitigated, future earthquakes could pose greater threat to the economic and societal development of this region. Therefore, this thesis focuses on the seismic hazard of the NE Tibetan Plateau.

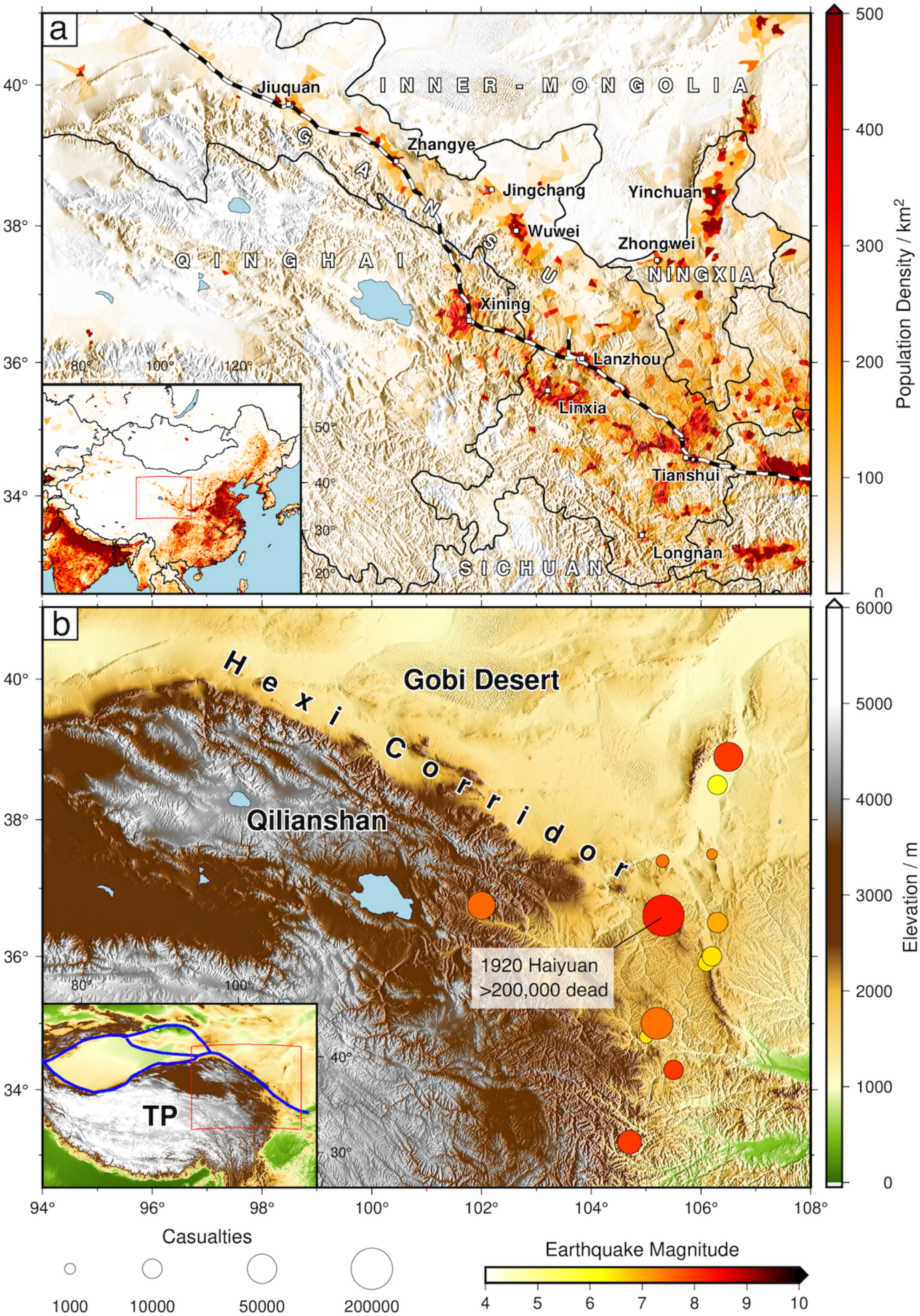

Figure 1.3: (a) Population density of the NE Tibetan Plateau with the high speed railways connecting the major cities of Tianshui, Lanzhou, Xining, Zhangye and Jiuquan. Population data from *CIESIN* (2018). High speed railway and station data from *Li* (2016); *OpenStreetMap contributors* (2020). (b) Topography of the NE Tibetan Plateau and location of the Hexi Corridor. Blue lines in the inset of panel (b) indicate the approximate routes of the ancient Silk Roads in China digitised from the map of The Silk and Spice Routes in (*UNESCO*, 2002). TP=Tibetan Plateau.

1.2 Characteristics of Continental Tectonics

Being in part of the Indo-Asia collision zone, the most prominent feature in the Alpine-Himalayan belt (Fig 1.4), the seismicity of the NE Tibetan Plateau obeys characteristics of continental tectonics. Unlike the plate margins where deformation and earthquakes are localised on narrow zones of plate boundary faults, deformation in the continental collision zones spread over 100s to 1000s kilometers with earthquakes distributed over complex networks of faults (*Thatcher*, 2009). The debate on whether continental deformation is better described by relative motion between rigid blocks (*Avouac and Tapponnier*, 1993b; *Tapponnier et al.*, 2001b) or a viscous continuum that flows under external forces (*England and Mckenzie*, 1982; *England and Houseman*, 1985; *Copley*, 2012) has been ongoing for decades. The former assumes most of the strength of continental lithosphere lies in the brittle upper crust whereas the latter assumes a stronger ductile layer beneath that which drives the relative motion in the upper crust (*Thatcher*, 2009). Both idealised models only fit surface observations to some extent, with the block model focused on the slip rates on the major faults (*Tapponnier et al.*, 2001a) and the continuum model focused on the long-wavelength deformation pattern (*England and Molnar*, 2005). The heterogeneous strength of the continental lithosphere, due to its complex tectonic and petrological history as well as the temperature and pressure conditions it is under (*Vauchez et al.*, 1998; *Ziegler et al.*, 1998; *Mo et al.*, 2006; *Gatinsky and Prokhorova*, 2014), means the real system most likely lies somewhere in between these two end members. Nevertheless, which deformation style is dominating in a particular setting does have an implication on the hazard distribution in the region. The block model predicts focused deformation, hence earthquake hazard, along the major faults, whereas the continuum model predicts slower slip rates on the faults and higher strain rate in the block interior, hence more distributed seismic hazard. With the improved spatial distribution of and better constraint on the measurements of surface motion and crustal strain, from geological slip rates on faults (*He et al.*, 2013; *Yuan et al.*, 2011, 2013; *Li et al.*, 2009) to ground-based geodetic velocity fields (*Gan et al.*, 2007; *Zheng et al.*, 2013a; *Wang and Shen*, 2020), and more recently, to the high resolution velocity and strain mapping from satellite radar (*Cavalié et al.*, 2008; *Elliott et al.*, 2016; *Weiss et al.*, 2020), we are getting closer to revealing the surface kinematics of continental deformation, which will in turn help constrain models related to the underlying rheology and dynamic processes that control the surface deformation (*Thatcher*, 2009; *England and Houseman*, 1985; *Clark et al.*, 2005; *England and Molnar*, 2015; *Copley*, 2017; *Chen et al.*, 2017a).

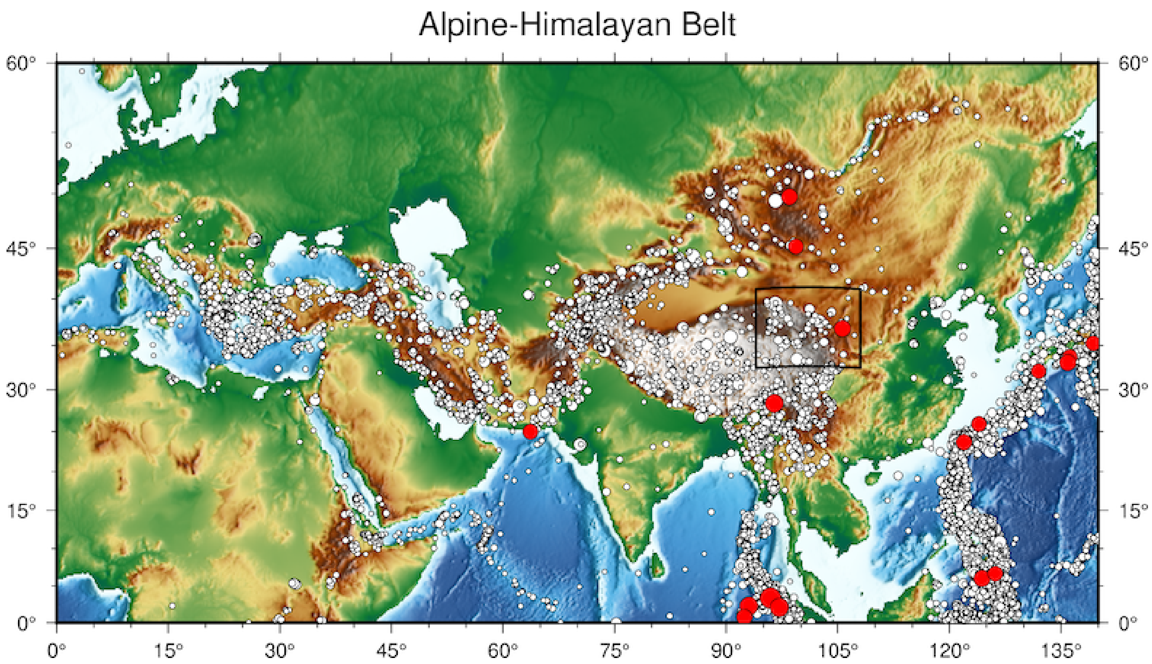

Figure 1.4: Seismicity of the Alpine-Himalayan Belt from the International Seismological Centre Global Earthquake Model (ISC-GEM) catalogue from 1906 to 2016 (*ISC*, 2019). Earthquakes with $M_W > 8$ are highlighted in red. Box shows the NE Tibetan Plateau.

1.3 Tectonics of the NE Tibetan Plateau

The NE Tibetan Plateau is at the front of the northward expansion of the Tibetan Plateau under the continued underthrusting of the Indian Plate (*Avouac and Tap-*

ponnier, 1993a; *Yuan et al.*, 2013). It abuts the rigid Tarim Basin in the northwest, the stable Gobi Alashan Block in the northeast, the undeforming Ordos Plateau on the east and the cratonic Sichuan Basin in the southeast (Fig 1.5). The motions on the Altyn Tagh, West Qinling Faults and the thrust faults on the north and south sides of the Qaidam Basin started between 50 and 30 Ma (*Horton et al.*, 2004), not long after the India-Eurasia collision (*Dupont-Nivet et al.*, 2010). The NWW-SEE trending Haiyuan and Kunlun Faults and the NNW-SEE trending Riyueshan and Elashan Faults initiated at around mid-Miocene age, marking a shift in deformation style and a phase of expansion towards the northeast (*Duvall et al.*, 2013; *Yuan et al.*, 2013) (Fig 1.6).

Numerous studies have been conducted to obtain geological and geodetic slip rates on the Altyn Tagh Fault (*Mériaux et al.*, 2005, 2012; *Zhang et al.*, 2007; *Gold et al.*, 2009, 2011; *Elliott et al.*, 2010; *He et al.*, 2013; *Zheng et al.*, 2013a), the Haiyuan Fault (*Zhang et al.*, 1988a; *Gaudemer et al.*, 1995; *Lasserre et al.*, 1999, 2002; *Li et al.*, 2009; *Zheng et al.*, 2013a; *Yao et al.*, 2019; *Shao et al.*, 2020) and the Kunlun fault (*Kirby et al.*, 2007; *Harkins et al.*, 2010; *Li et al.*, 2016b, 2020a). Early geological slip rates were wide-ranging on both the Altyn Tagh Fault (*Mériaux et al.*, 2005, 2012; *Zhang et al.*, 2007; *Gold et al.*, 2009, 2011) and the Haiyuan Fault (*Zhang et al.*, 1988a; *Gaudemer et al.*, 1995; *Lasserre et al.*, 1999, 2002; *Li et al.*, 2009), with late Pleistocene (10-13 ka) to early Holocene (7-10 ka) slip rates up to three times different obtained at closely spaced sites (Fig 1.5), spurring discussions of pulsed strain release on these faults (e.g. *Gold et al.*, 2017). Nevertheless, many of the fast slip rates (e.g., ~20 mm/yr on the Altyn Tagh Fault (*Mériaux et al.*, 2005) and >10 mm/yr on the Haiyuan Fault (*Gaudemer et al.*, 1995; *Lasserre et al.*, 1999, 2002), see Fig 1.5) assumed complete refreshment of terrace riser before the abandonment of the lower terrace, which is arguably more suitable for perennial fluvial systems than the semi-arid environment in the NE Tibetan Plateau; hence, these slip rates

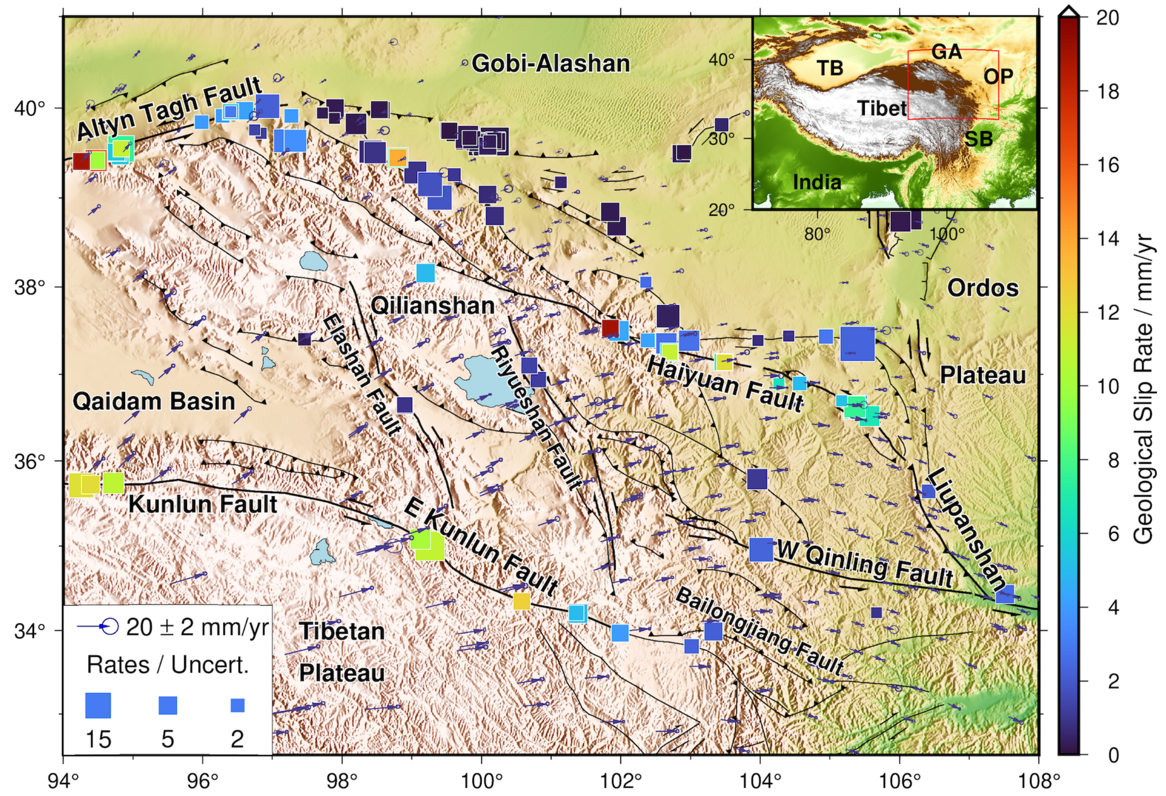

Figure 1.5: Fault map of the NE Tibetan Plateau with horizontal geological slip rates primarily compiled by Jingxing Yu combined with those reported by *Zheng et al.* (2016), *Li et al.* (2020a), *Yao et al.* (2019), *Shao et al.* (2020) and references therein. Each square represents a slip rate result with the best estimate value represented by colour. The size of the squares are scaled by the ratio between the best estimate and the uncertainties of each slip rate measurements such that the larger squares represent slip rates that are more tightly constrained. When a slip rate is reported as a range, the centre point of the range is taken as the best estimate and half of the range is taken as the slip rate uncertainties. The exceptionally high slip rates of ∼20 mm/yr on the Altyn Tagh Fault and >10 mm/yr on the Haiyuan Fault are likely overestimated (see discussions in *Zhang et al.*, 2007; *Yao et al.*, 2019; *Shao et al.*, 2020). Arrows show horizontal Global Navigation Satellite System (GNSS) velocities reported by *Wang and Shen* (2020). Inset shows its location relative to the stable blocks surrounding the Tibetan Plateau. TB=Tarim Basin, GA=Gobi-Alashan, OP=Ordos Plateau, SB=Sichuan Basin.

have been recently regarded as strict upper bounds (*Zhang et al.*, 2007; *Zheng et al.*, 2013a; *Yao et al.*, 2019; *Shao et al.*, 2020). With the improved dating techniques and higher-resolution topographic data, most sites that generated exceptionally high slip rates have been reinterpreted (*Zhang et al.*, 2007; *Cowgill et al.*, 2009; *Zheng et al.*, 2013a; *Yao et al.*, 2019; *Shao et al.*, 2020) and the revised millennial geological slip rates can now be reconciled with the modern decadal geodetic slip rates (*Cavalié*

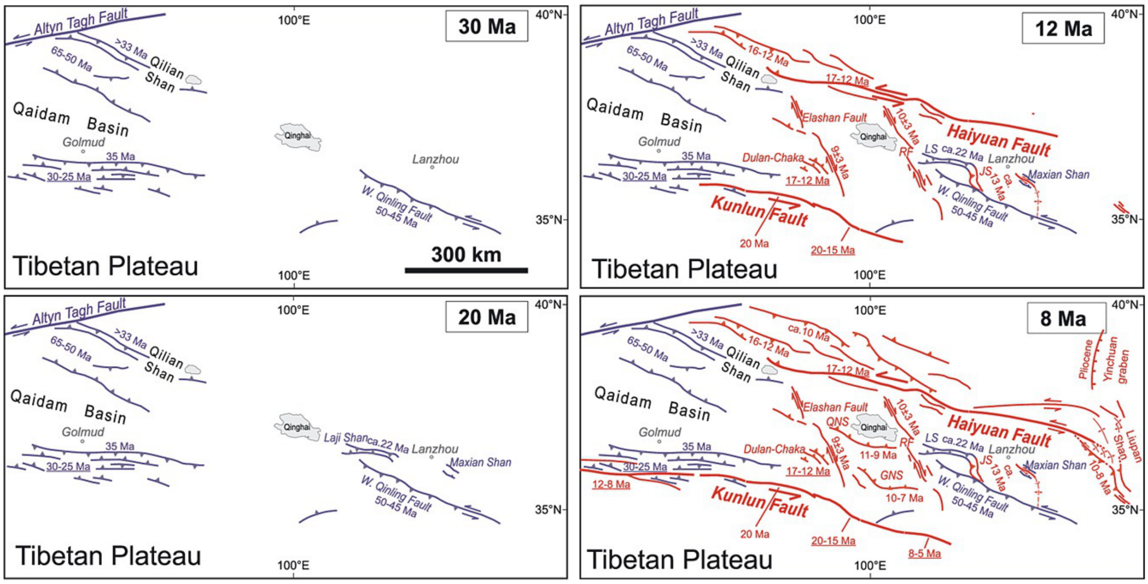

Figure 1.6: Evolution of the NE Tibetan Plateau based on fault initiation ages reproduced from *Yuan et al.* (2013).

et al., 2008; *Elliott et al.*, 2008; *Jolivet et al.*, 2012; *Daout et al.*, 2016b; *Shen et al.*, 2019). *Zheng et al.* (2016) summarised the latest slip rate results with a simplified kinematic model as in Fig 1.7 with deformation dominated by the left-lateral motions along the three major boundary strike-slip faults (∼10 mm/yr, ∼10 mm/yr and ∼5 mm/yr on the strike-slip portions of the Altyn Tagh, Kunlun and Haiyuan Faults, respectively); the slower-moving thrusts in the Qilianshan and Liupanshan and the right-lateral strike-slip Elashan and Riyueshan Faults act to partition and adjust for the different slip vectors at the ends of these strike-slip faults (*Zheng et al.*, 2013a, 2016). As only few slip rate results have been obtained on the secondary faults within the NE Tibetan Plateau, e.g., the slip rates on the Riyueshan and Elashan Faults by *Yuan et al.* (2011), such kinematic models are likely to be subjected to future revision as more data become available.

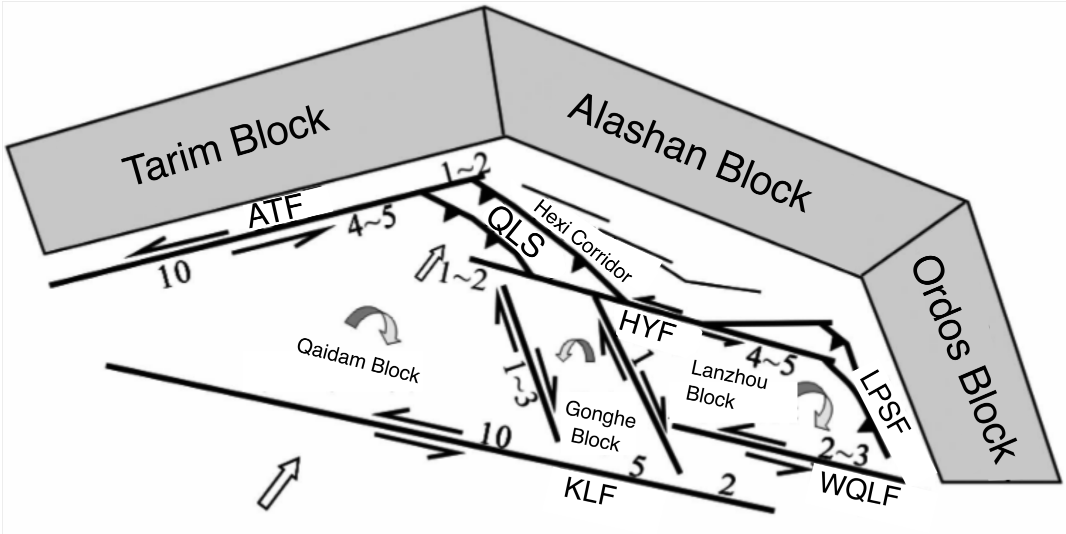

Figure 1.7: Kinematic model of the NE Tibetan Plateau reproduced and translated from (*Zheng et al.*, 2016). ATF=Altyn Tagh Fault, QLS=Qilianshan, HYF=Haiyuan Fault; WQLF=West Qiling Fault; KLF=Kunlun Fault. Numbers are the preferred geological slip rates at the corresponding sections of the faults (*Zheng et al.*, 2016).

1.4 Methods of seismic hazard assessment

Traditional approaches to seismic hazard assessment have been largely reliant on earthquake catalogues (*Zhang*, 1993; *Zhang et al.*, 1999; *Gao*, 2003; *Li et al.*, 2016a; *Feng et al.*, 2020), be they the deterministic approaches adopted in the 1950s where earthquakes of similar magnitudes were assumed to happen again in the future (*Zhang et al.*, 1999; *Gao*, 2003), or the probabilistic approaches where different statistical analysis are performed on predetermined seismic zones based on past seismicity and earthquake sources (*Zhang*, 1993; *Zhang et al.*, 1999; *Rong et al.*, 2020). Nevertheless, it is widely acknowledged that our knowledge about past earthquakes is far from complete (*England and Jackson*, 2011; *Zhang et al.*, 1999). Instrumental catalogues are available for just over a century, much shorter than the recurrence period of large earthquakes (*England and Jackson*, 2011). Although China has one of the longest historical seismic catalogues in the world, this record is both spatially and temporally incomplete (*Lee et al.*, 1976; *Zhang et al.*, 1999). Moreover, large uncertainties exist in the translation from textual descriptions of earthquake damages to magnitudes (e.g., *Middleton et al.* (2015)) and from historical place names to latitude and longitude locations (e.g., *Ma et al.* (2020)). Comparing the spatial distributions of ISC-GEM catalogue (*ISC*, 2019) over the past 110 years and the historical catalogue (*CEA-PBED*, 1995) over the 2000 years before that, we see vastly different patterns (Fig 1.8). Most of the M_W >7 earthquakes in the past century occurred on or near the major boundaries faults, but all the significant historical earthquakes recorded seem to have happened on the slower moving faults (compare Fig 1.8 and Fig 1.5). As the spatial distribution of historical catalogue is largely influenced by the population density of the time, seismic hazard derived from these catalogues are very likely biased by where people lived and earthquakes were recorded in the past. As such, if uncaptured by the historical catalogue, the seismogenic potential of the secondary faults in the interior of the NE Tibetan Plateau, such as where Xining (capital city of the Qinghai Province) is located, would remain largely unknown.

An alternative approach to seismic hazard assessment is to estimate rates of earthquakes based on interseismic tectonic strain (*Molnar*, 1979). If there is to be an earthquake, there has to be an accumulation of elastic strain. Therefore, if we measure a surface strain that is not related to aseismic processes like folding or fault creep, there is likely to be an earthquake hazard even if there is no obvious fault. With the proliferation of the geodetic measurements in the 21st Century, this method has become increasingly feasible and gained popularity for its ability to inform seismic hazard independent of earthquake catalogues (*Bird et al.*, 2010; *Bird and Kreemer*, 2015; *Avouac*, 2015) or together with earthquake catalogues (*Rollins and Avouac*, 2019; *Rong et al.*, 2020). To convert the measured strain rate into expected rates of earthquakes over a range of magnitudes, this method typically employs the Gutenberg-Richter relationship, a log-linear relationship between earthquake frequency and magnitude (*Gutenberg and Richter*, 1954) up to a maximum

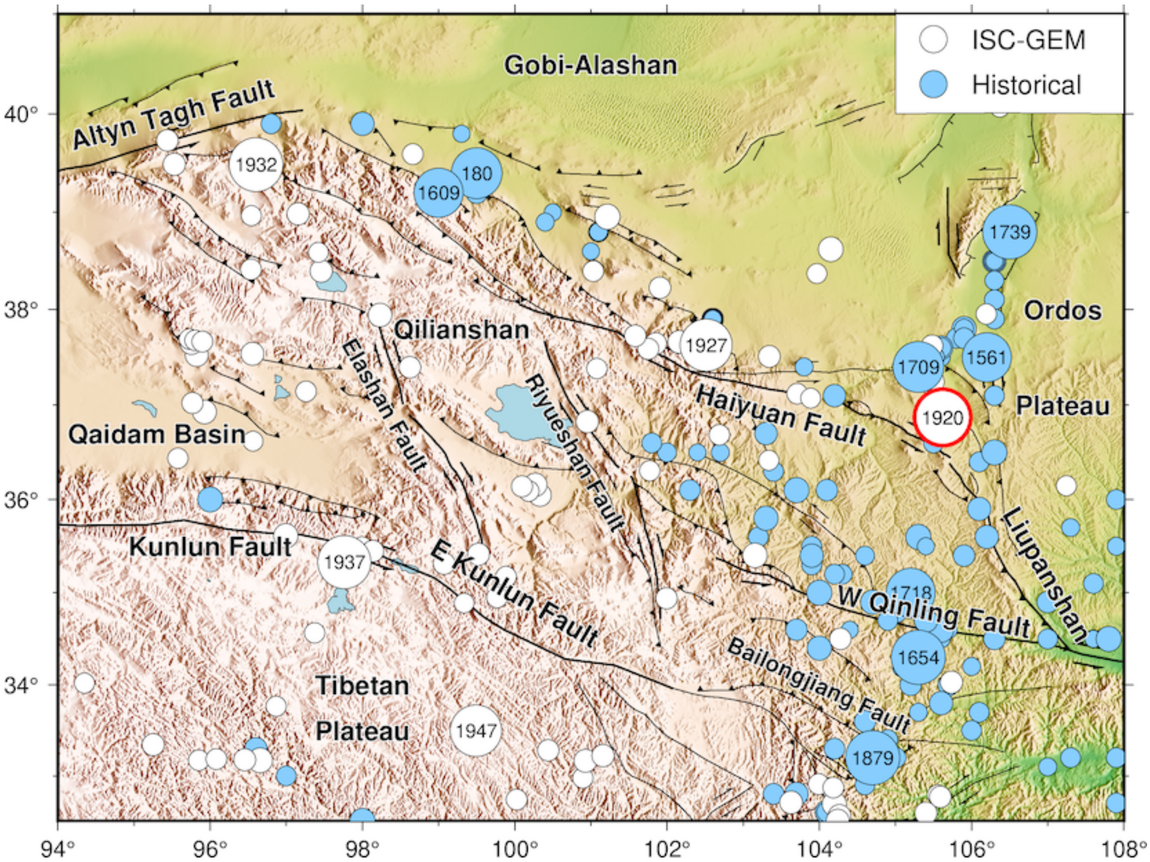

Figure 1.8: Seismicity of the NE Tibetan Plateau. Blue circles are events based the historical records of earthquake damage between BC230 to AD1911 (*CEA-PBED*, 1995). White circles are from the instrumental ISC-GEM catalogue, with the 1920 Haiyuan earthquake highlighted in red (*ISC*, 2019). Earthquakes above magnitudes 7 are enlarged with the year of the event labeled.

possible magnitude in the region (*Molnar*, 1979)(Fig 1.9). *Bird and Kreemer* (2015) demonstrated success of this approach with retrospective testing of seismic forecasts derived from the Global Strain Rate Model (GSRM v.2.1) which was based on Global Navigation Satellite System (GNSS) velocity data (*Kreemer et al.*, 2014) (Fig 1.10a). Soon after, strain rate maps with more GNSS data from longer time series have been produced for smaller focus regions of China (*Zheng et al.*, 2017; *Wang and Shen*, 2020)(e.g., Fig 1.10b) and the NE Tibetan Plateau (*Li et al.*, 2017c, 2018; *Su et al.*, 2019; *Pan et al.*, 2020). Nevertheless, the limited spatial density of the GNSS stations means such strain rate maps are at best smoothed representations of the strain distribution of the region (Fig 1.5a-c), and the highlighted features are clearly biased by the availability and spatial distribution of the GNSS stations (compare the locations of GNSS vectors in Fig 1.5 and areas of high and low strain rates in Fig 1.10c, especially on the west end of the East Kunlun Fault and the interior of the Qilianshan).

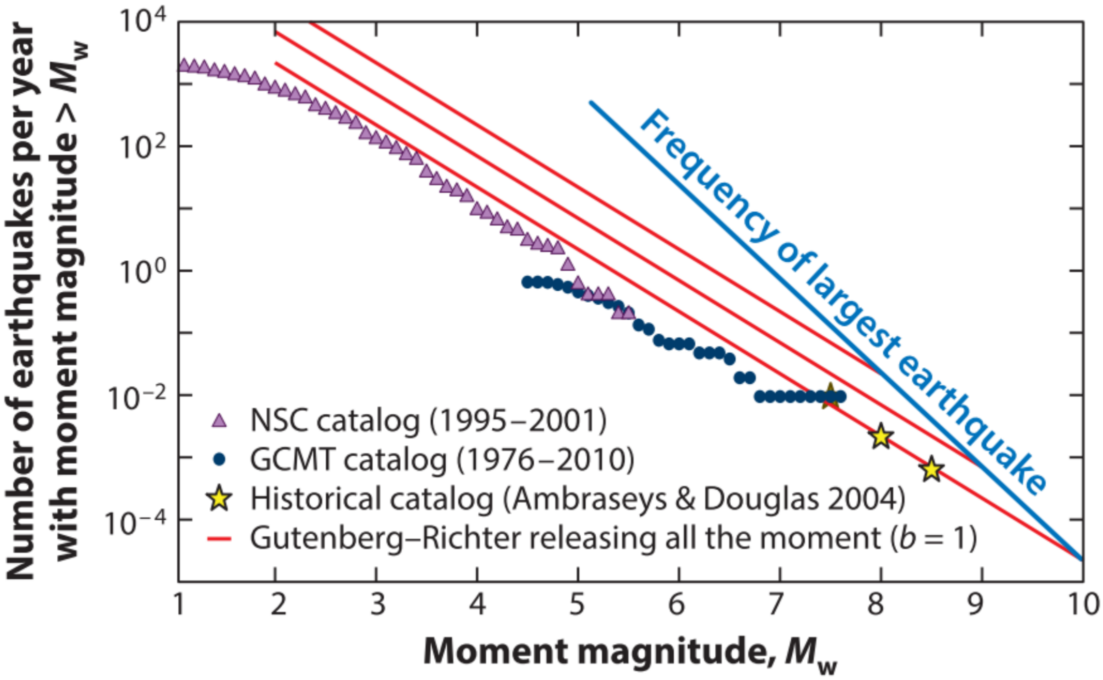

Figure 1.9: Example of Gutenberg-Richter plot of the seismicity in Nepal, reproduced from *Avouac* (2015). NSC=National Seismic Centre local catalog. GCMT=Global Centroid Tensor Catalog.

As we enter a new era of space-based tectonic geodesy with the advent and maturation of the InSAR technique, high-resolution strain rate mapping based on satellite radar imagery has become possible (*Cavalié et al.*, 2008; *Elliott et al.*, 2016). The interseismic strain rate map over the Haiyuan Fault Zone, produced by *Song et al.* (2019) with a joint inversion of GNSS and 6 tracks of descending ENVISAT data, already demonstrated InSAR's ability to help highlight the high strain areas on the Haiyuan Fault with much higher resolution than purely GNSS-based strain rate maps (Fig 1.10d). With the launch of the Sentinel-1A and -1B satellites in 2014 and 2016, radar imagery in both ascending and descending flight directions have been routinely acquired (*Elliott et al.*, 2016), which means, with the help of the GNSS point data, high resolution velocity maps in both vertical and east directions can be obtained for regional strain rate mapping (*Hussain et al.*, 2018; *Weiss et al.*, 2020). Such high-resolution velocity mapping will not only help with identifying previously unmapped active faults (*Wicks et al.*, 2013) which can be potential earthquake sources, but will also improve slip rate measurements on faults that do not have an optimal distribution of GNSS stations (e.g., the middle section of the Kunlun Fault) or easy road access (e.g., in the interior of the Qilianshan) or do not have optimal morphology for geological sampling (e.g., the loess-covered West Qinling Fault). More importantly, such high-resolution strain rate maps are expected to provide a clear view of the strain distribution which can help with the understanding of fault kinematics in the region. The total strain rate can also be converted to a tectonics-based earthquake rate estimates for the region.

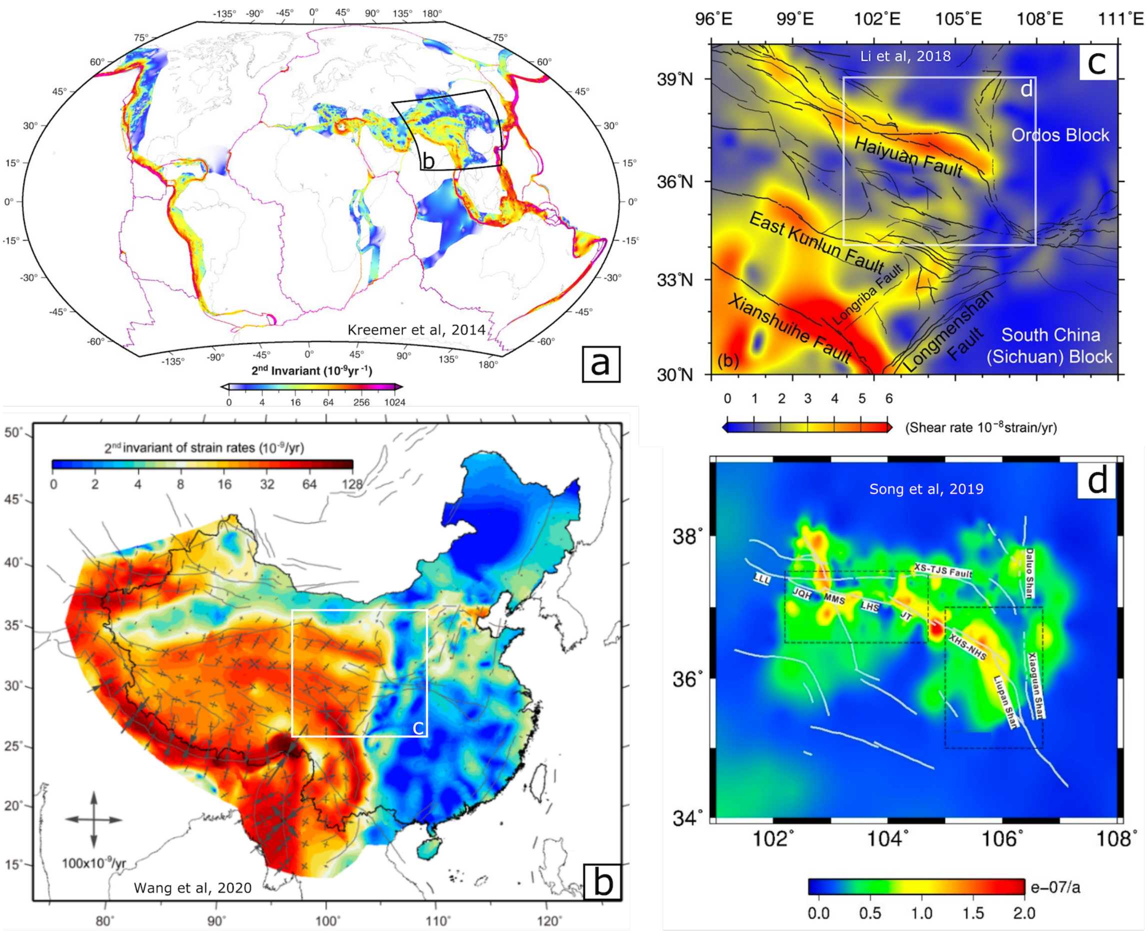

Figure 1.10: State-of-the-art of strain rate maps of (a) the world, (b) China, (c) the NE Tibetan Plateau and (d) the Haiyuan Fault Zone, reproduced from *Kreemer et al.* (2014), *Wang and Shen* (2020), *Li et al.* (2018) and *Song et al.* (2019), respectively. Panels (a-c) are derived from Global Positioning System velocity data. Panel (d) is derived from a joint inversion of GNSS and 6 descending tracks of ENVISAT InSAR data. Panels (a,b,d) are second invariant of horizontal strain rate whereas panel (c) depicts shear strain rate.

1.5 Overview of this thesis

This thesis aims to improve the understanding of seismic hazard of the NE Tibetan Plateau by mapping the present-day crustal strain rate from 5 years of Sentinel-1A and -1B satellite data and estimating the rates of earthquakes using the Gutenberg-Richter relationship. The maximum earthquake magnitude for this region is assumed to be that of the 1920 Haiyuan Earthquake as it is the largest earthquake in the historical and instrumental catalogues combined (Fig 1.8) and the number of casualties from this event is the highest ever recorded in this region (Fig 1.3b). As a wide range of magnitudes between $M_W 7.8$ (*Liu-zeng et al.*, 2015) and M8.7 (*Zhang et al.*, 1987) has been reported for the 1920 Haiyuan Earthquake, I first reestimate its magnitude in Chapter 2 using both historical seismograms and Pleiades optical satellite imagery. Then, in Chapter 3, I analyse 23 frames of Sentinel-1 data from 2014 to 2019 covering ascending and descending areas as outlined in Fig 1.11. In Chapter 4, I develop methods for stitching the maps of InSAR line-of-sight (LOS) velocities for each frame and decomposing the LOS velocities into regional east and vertical velocity maps. Finally, I derive strain rate maps and preliminary earthquake rate estimates in Chapter 5, and summarise and outline future work in Chapter 6.

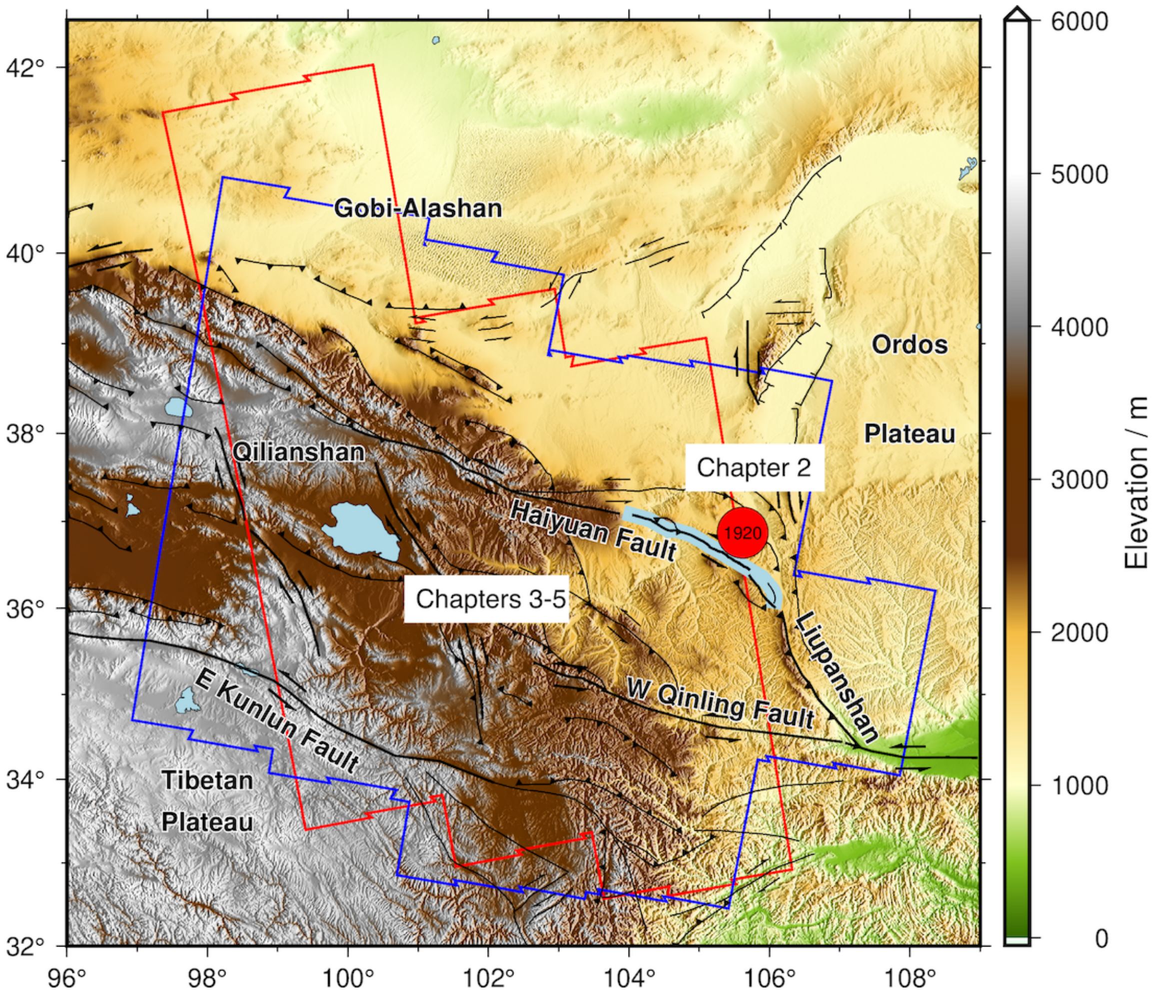

Figure 1.11: Summary of the contents of this thesis where Chapter 2 will reevaluate the magnitude of the 1920 Haiyuan Earthquake and Chapter 3 to 5 focus on generating regional high-resolution velocity and strain rate maps for seismic hazard assessment of the NE Tibetan Plateau.

1.6 Publication arising from this thesis

Chapter 2 has been published as:

> Ou, Q., Kulikova, G., Yu, J., Elliott, A., Parsons, B., Walker, R. (2020). Magnitude of the 1920 Haiyuan earthquake reestimated using seismological and geomorphological methods. Journal of Geophysical Research: Solid Earth, 125, e2019JB019244. https://doi.org/10.1029/2019JB019244

All supplementary data sets mentioned in Chapter 2 are available at `https://doi.org/10.1029/2019JB019244`. The scanned and digitized seismograms can be found in the IRIS Seismo Archives `https://ds.iris.edu/seismo-archives/quakes/1920haiyuan/`.

Chapters 3 and 4 are being prepared as a paper on the method of frame stitching. Chapter 5 is being prepared as a paper on the seismic hazard of the NE Tibetan Plateau.

Chapter 2

Magnitude of the 1920 Haiyuan Earthquake Reestimated Using Seismological and Geomorphological methods

2.1 Introduction

The 1920 Haiyuan earthquake is one of the most destructive earthquakes of the past century (*Chen and Molnar*, 1977; *Zhang et al.*, 1988b) and is commonly reported as the largest known event in the tectonically active northeastern Tibetan Plateau (Fig 2.1). Accurate knowledge of its magnitude and strain release is of great importance to our understanding of the seismic risks in this area. However, a confusing number of magnitude values on different scales have been reported for this earthquake (Table A.1). The most often quoted of these are M 8.7 (*Cavalié et al.*, 2008; *Deng et al.*, 1986; *Lasserre et al.*, 1999, 2002; *Zhang et al.*, 1987, 1988b), M 8 (*Cavalié et al.*, 2008; *Lasserre et al.*, 2007; *Li et al.*, 2016d), although the definition of the M

used is unclear, and M_S 8.5 (*Ren et al.*, 2016, 2018). However, M_W 8.3 is currently listed on the International Seismological Centre - Global Earthquake Model (ISC-GEM) catalogue (*ISC*, 2019) and M_W 7.8 was estimated by *Liu-zeng et al.* (2015) based on length of rupture and maximum slip.

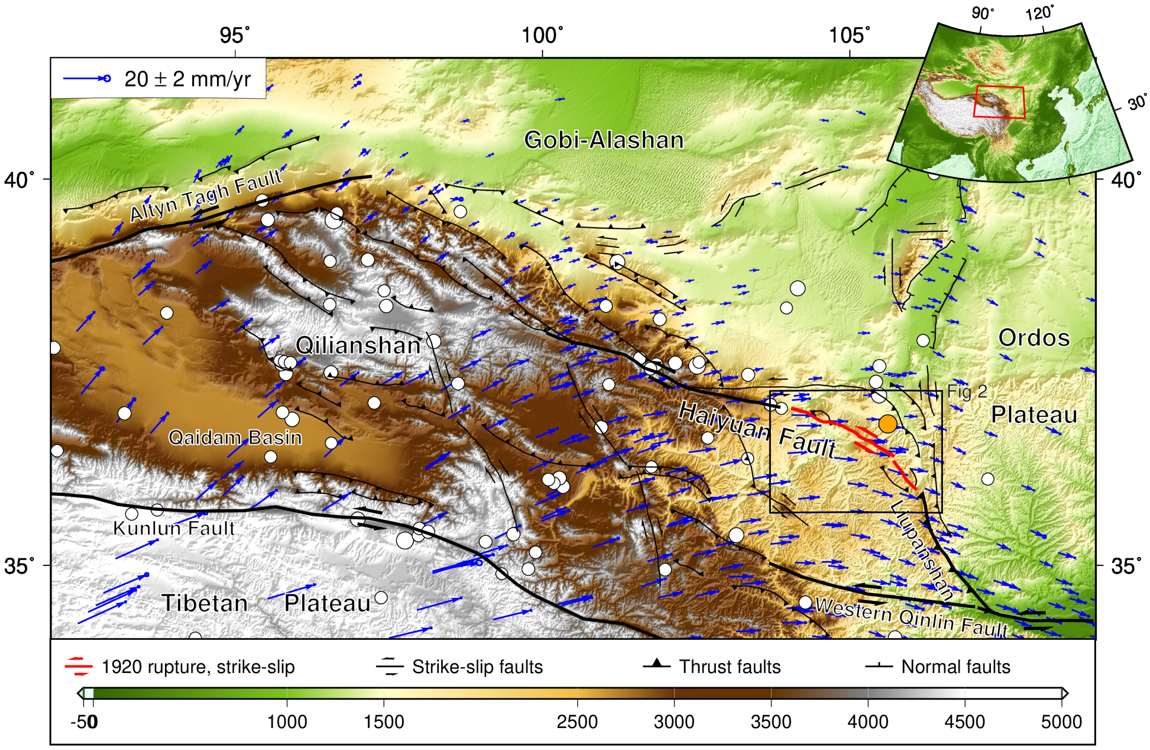

Figure 2.1: Tectonic overview of the northeast Tibetan Plateau, the location of which is given by the red box on the inset map. Blue arrows with error ellipses represent the Global Positioning System velocity field relative to the stable Eurasia (*Wang and Shen*, 2020). White circles are earthquakes between 1904 and 2015 with magnitude above 5.0 in the ISC-GEM catalogue (*ISC*, 2019), with size scaled to magnitude. The 1920 Haiyuan earthquake is highlighted in orange. The red lines show the extent of the rupture, with the western and middle sections mapped on Pleiades imagery, and the eastern section mapped on Google Earth with reference to the 1:50000 geological map in *IGCEA and NBCEA* (1990). Black box shows the extent of Fig 2.2.

The reason this magnitude is still unconfirmed is multi-fold. First, the data and measurements associated with Gutenberg-and-Richter's surface-wave magnitude M and body-wave magnitude m were not published (*Gutenberg and Richter*, 1941; *Gutenberg*, 1956), making the original seismological magnitudes unverifiable. Second, the coseismic slip distribution is still debated, thus a geomorphological moment magnitude has yet to be agreed (*IGCEA and NBCEA*, 1990; *Ren et al.*, 2016; *Zhang et al.*, 1987). Third, different M_W results ranging between 7.8 and 8.3 were obtained from the same set of spectral density measurements from the Uppsala and Riverview records (*Chen and Molnar*, 1977; *Deng et al.*, 1984; *Kanamori*, 1977) due to different focal mechanisms assumed in calculating the seismic moment M_o, making the usually trusted moment magnitude uncertain. Last but not least, due to the evolution of magnitude scales over the century, the meaning of the symbol M, and of the term "magnitude" itself, changed across the literature, making direct comparison difficult.

These uncertainties prompted us to revisit the Haiyuan earthquake to provide direct evidence for the magnitude of this earthquake. Seismologically, *Kanamori et al.* (2010), *Okal* (2015), *Kulikova and Krüger* (2015), *Kulikova et al.* (2016) and *Kulikova and Krüger* (2017) have shown that analogue seismograms can be obtained from various seismological archives to extract useful constraints. Likewise, recent advances in the availability of sub-metre resolution optical satellite imagery allows the identification and measurement of offsets along the surface rupture (*Kurtz et al.*, 2018; *Middleton et al.*, 2015; *Zhou et al.*, 2015a), *Zielke et al.* (2010). As a major earthquake that happened in the late historic, early instrumental era, the 1920 Haiyuan earthquake serves as a primary example of a large and rare event in order to compare different methods used in paleoseismological and modern seismological studies.

This study aims to first digitise analogue seismograms sourced from a wide range of global archives to relocate the epicentre (Section 2.2.2), invert for its focal mechanism (Section 2.2.3), model the waveforms for the moment magnitude M_W (Section 2.2.4), and verify the surface wave magnitude M_S and broadband body wave magnitude m_B (Section 2.2.5). Then, we measure horizontal offsets on orthorectified Pleiades satellite and unmanned aerial vehicle imagery to estimate the coseismic slip distribution and the average slip of the 1920 earthquake and hence calculate its moment magnitude M_W (Section 2.3). Finally, we reconcile the differences in reported magnitudes and shed light on how to interpret historical earthquake magnitudes (Section 2.4).

2.1.1 Tectonic Setting

The northeastern Tibetan Plateau is a tectonically active region bounded by the E-W trending strike-slip Haiyuan Fault, the Altyn Tagh Fault, the Western Qinlin Fault and the Kunlun Fault as well as the NW-SE trending thrust faults in the Qilian Shan and Liupanshan (Fig 2.1) (*Song et al.*, 2019; *Wang et al.*, 2014; *Zheng et al.*, 2016). The Qilian Shan and the Qaidam Basin absorb ∼10 mm/year of N-S shortening, ∼25% of the shortening between India and the Alashan block (*Wang et al.*, 2001). The combination of thrusts and strike-slip faults controls the elevation and eastward extrusion of the Tibetan Plateau in this NE part of the plateau (*Tapponnier et al.*, 1986; *Meyer et al.*, 1998; *Wang et al.*, 2001).

The ∼1000 km long Haiyuan Fault System is a major geomorphological structure in the NE Tibetan Plateau that accommodates oblique convergence with deformation partitioning between major left-lateral strike-slip faults and thrusts (*Gaudemer et al.*, 1995; *Tapponnier et al.*, 2001a). The 1920 Haiyuan earthquake ruptured the eastern end of the Haiyuan fault (Fig 2.1), between the creeping Laohushan section (*Jolivet et al.*, 2012) and the Liupanshan Thrust System (*Zheng et al.*, 2006) (Fig 2.2).

Estimated geological slip rates along the 1920 rupture range from 3.2 ± 0.2 mm/yr in the western section (*Matrau et al.*, 2019) to 4.5 ± 1.0 mm/yr in the middle section (*Li et al.*, 2009), which are consistent with the 5–6.3 mm/yr creep rate at Laohushan based on interferometric synthetic-aperture radar (InSAR) (*Cavalié et al.*, 2008; *Daout et al.*, 2016b; *Jolivet et al.*, 2012) and the 2.8–3.5 mm/yr overall slip rate absorbed by thrusting across Liupanshan based on measurements using the Global Navigation Satellite System (GNSS) (*Li et al.*, 2017a).

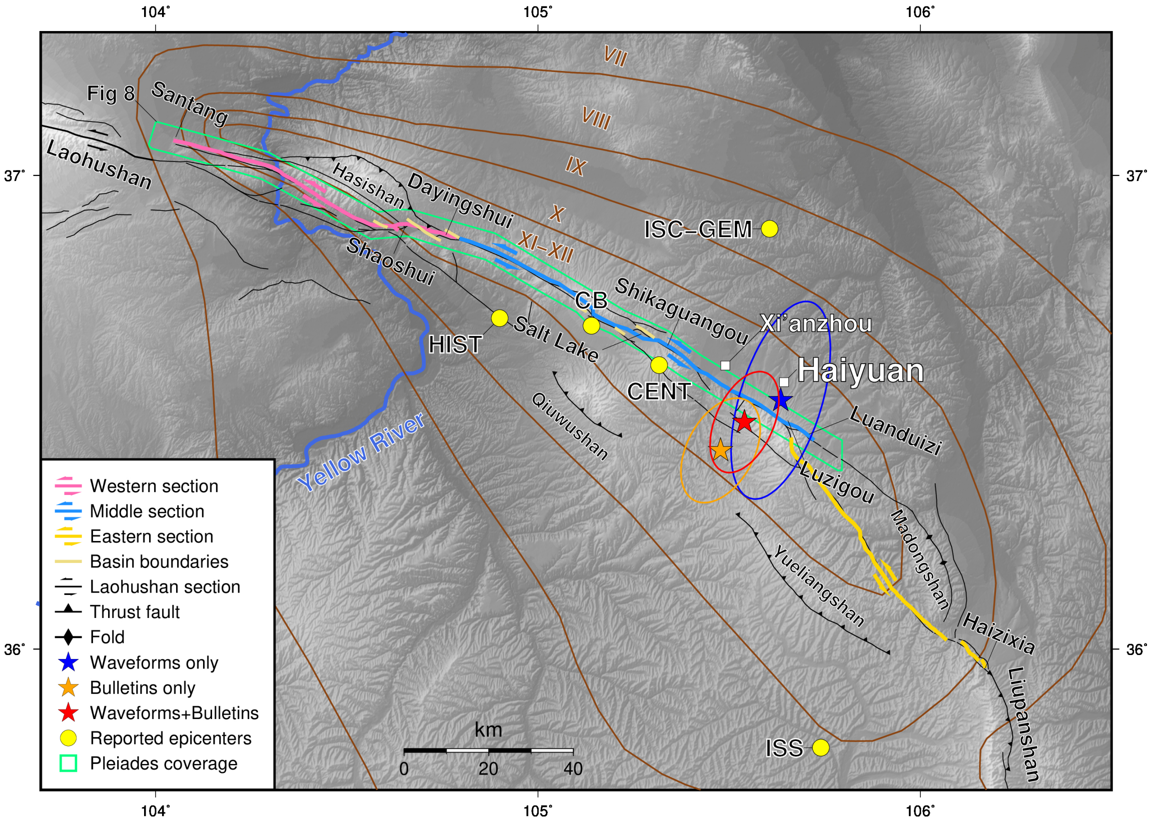

Figure 2.2: Map of the source area of the 1920 earthquake showing ruptured faults, inferred epicenters, and shaking intensity contours. The fault sections are divided following *Ren et al.* (2016). The isoseismal contours in brown are reproduced from *Zhuang et al.* (2018). Yellow dots show previously reported epicentres: HIST = Catalogue of historically felt earthquakes in China, preferred by *Xu et al.* (2019); CENT = Centennial catalogue (*Engdahl and Villaseñor*, 2002); ISC-GEM = International Seismological Centre - Global Earthquake Model catalogue (*ISC*, 2019); ISS = International Seismological Summary catalogue (*Villaseñor et al.*, 1997; *Villasenor and Engdahl*, 2005); CB = centre-bottom nucleation point used in the finite fault waveform modelling in Section 2.2.4. Stars show relocated epicentres in this study from phase arrival times from waveforms (blue), bulletins (orange) and waveforms and bulletins combined (red), with hypocentral depth fixed at 15 km; the orientations of the 1-standard-deviation error ellipses reflect the azimuthal distribution of the seismic stations available (Fig 2.3). The green box around the strike-slip portion of the fault rupture represents Pleiades data coverage in Fig 2.8a.

Overall, the Haiyuan fault is a near-vertical plane that dips steeply to the south (*Gaudemer et al.*, 1995; *Daout et al.*, 2016b). Seismic reflection profiles near Santang in the western section and the Salt Lake in the middle section suggested dips between 60° to 70° (*Fan et al.*, 2004; *Wang et al.*, 2012, 2014). A surface dip measurement of 67° was reported from a fault scarp at Haizixia in the eastern section (*IGCEA* *and NBCEA*, 1990). In addition, *Duan et al.* (2018) constrained, using the precise locations of small earthquakes, the dip of the 1920 Haiyuan rupture to be uniformly ∼80° above 8 km depth, and found that, below 8 km depth, the dip decreases from ∼80° to ∼45° from west to east.

The seismogenic thickness in this region is well-constrained. The current locking depth underneath the 1920 rupture, as inverted from InSAR, is 20 km (*Jolivet et al.*, 2012). Eighty nine percent of small earthquakes registered within 30 km of the 1920 rupture since 1976 occurred in the upper 22 km of the crust (*Xu et al.*, 2019). Aftershocks of the 2016 M_S 6.4 Mengyuan earthquake to the west of the 1920 rupture reached 19 km depth (*Li et al.*, 2016e,c). Although *Li et al.* (2016d) suggested shallow locking depth of 5 km below the 1920 rupture from GNSS measurements, they obtained similar locking depths of 22 km to the west of the Laohushan creeping section and 15-20 km at the Liupanshan. Therefore, even though the current locking depths under the 1920 rupture is still debated, we can assume that the locking depth of Haiyuan fault before the 1920 rupture was ∼20 km.

2.1.2 1920 Haiyuan Earthquake

The Haiyuan earthquake occurred at 12:05:55.42 UTC on 16 December 1920 (*ISC*, 2018). Described as “Where the Mountain Walked” because of extensive landslides (*Close and McCormick*, 1922), this event caused over 230,000 casualties, making it the second deadliest earthquake of the 20th century in China and in the world, only after the 1976 Tangshan Earthquake (*IGCEA and NBCEA*, 1990). The maximum intensity of shaking reached XII, with all buildings completely destroyed around the Salt Lake pull-apart basin and Xi’anzhou of Haiyuan County (Fig 2.2).

The previously reported seismological epicentres are scattered up to 30 km away from the rupture due to the sparse seismic network at the time and the coarser velocity model used (Fig 2.2). The epicentre inferred from macroseismic shaking observations is at the Salt Lake, very close to the epicenter in the Centennial catalogue (*IGCEA and NBCEA*, 1990). However, recent physics-based rupture models suggest an epicentre further west would better match the observed intensity of shaking pattern (*Xu et al.*, 2019).

Detailed field mapping in the 1980s reported 237 km of surface rupture (*Deng et al.*, 1986; *IGCEA and NBCEA*, 1990), which is now commonly divided into the western, middle and eastern section based on geometry and the slip pattern (*Ren et al.*, 2016; *Xu et al.*, 2019; *Zhang et al.*, 2005): the 70 km long 110° striking western section from Santang to the Dayingshui basin, the 90 km long 110°-120° striking middle section from east of the Dayingshui basin to Luanduizi and the 77 km long 145° striking eastern section from Luzigou to Haizixia (Fig 2.2) (*IGCEA and NBCEA*, 1990).

The maximum slip was first thought to be the 10 m offset at Shikaguangou in the middle section (*Deng et al.*, 1986; *IGCEA and NBCEA*, 1990) but this offset is now believed to be a cumulative offset (*Ren et al.*, 2016; *Xu et al.*, 2019). Dynamic rupture simulations predicted horizontal slip distributions that form bell-shaped curves on the three sections with a largest offset of 6.5 m near the centre of the middle section (*Xu et al.*, 2019).

2.1.3 A Brief History of Magnitude Scales

Following Richter's invention of the Californian local magnitude scale, M_L, 21 years after the 1920 earthquake, Gutenberg released the first global earthquake catalogue in terms of surface wave magnitude, M (*Gutenberg and Richter*, 1941). The M magnitude was derived from amplitudes of surface waves with periods around 20 s (*Abe*, 1981; *Bormann*, 2012; *Geller and Kanamori*, 1977; *Gutenberg*, 1945a). Realizing that surface waves of all deep earthquakes are relatively small, *Gutenberg* (1945b) developed the broadband body wave magnitude m, which later became known as

m_B (*Gutenberg and Richter*, 1956), and gave more uniform results across hypocentral depths. After the implementation of the World-Wide Standardized Seismograph Network in the 1960s, m_B was adapted to only measure 1 s P-wave amplitudes and became the narrow band m_b. It was only in the late 1970s that the moment magnitude, M_W, was introduced to scale with radiated energy and moment release (*Hanks and Kanamori*, 1979; *Kanamori*, 1977). Significant efforts were made to unify the different scales by applying corrections (*Pacheco and Sykes*, 1992) or choosing preferred scales according to magnitude range (*Engdahl and Villaseñor*, 2002). The reported magnitude of the 1920 Haiyuan earthquake varied from source to source as summarised in Appendix A.1.

2.2 Seismological Approach

2.2.1 Data Acquisition and Preparation

According to the International Seismological Centre (ISC) online bulletin (`http://www.isc.ac.uk/iscbulletin/search/bulletin/`), 78 stations reported phase readings for the 1920 Haiyuan Earthquake (*ISC*, 2018). However, many of these records are no longer to be found due to war damage, fire, misplacement and untracked lending over the years (*Okal*, 2015). Over one year of data hunting, we recovered 60 analogue seismograms recorded at 27 stations in 12 countries on 13 unique types of instruments (Fig 2.3, Appendix A.2, also see supplementary data set S1 for archive contacts). The only Chinese analogue seismogram of this event, recorded at the Zi-ka-wei station in Shanghai, was saturated upon the first P-wave arrival and the recording stylus was dislocated soon after, rendering it unusable.

The seismograms are preserved in a variety of formats. Whether a record is suitable for magnitude determination depends critically on the availability of a scale reference. Newly made scans from the original smoked papers are the best as they

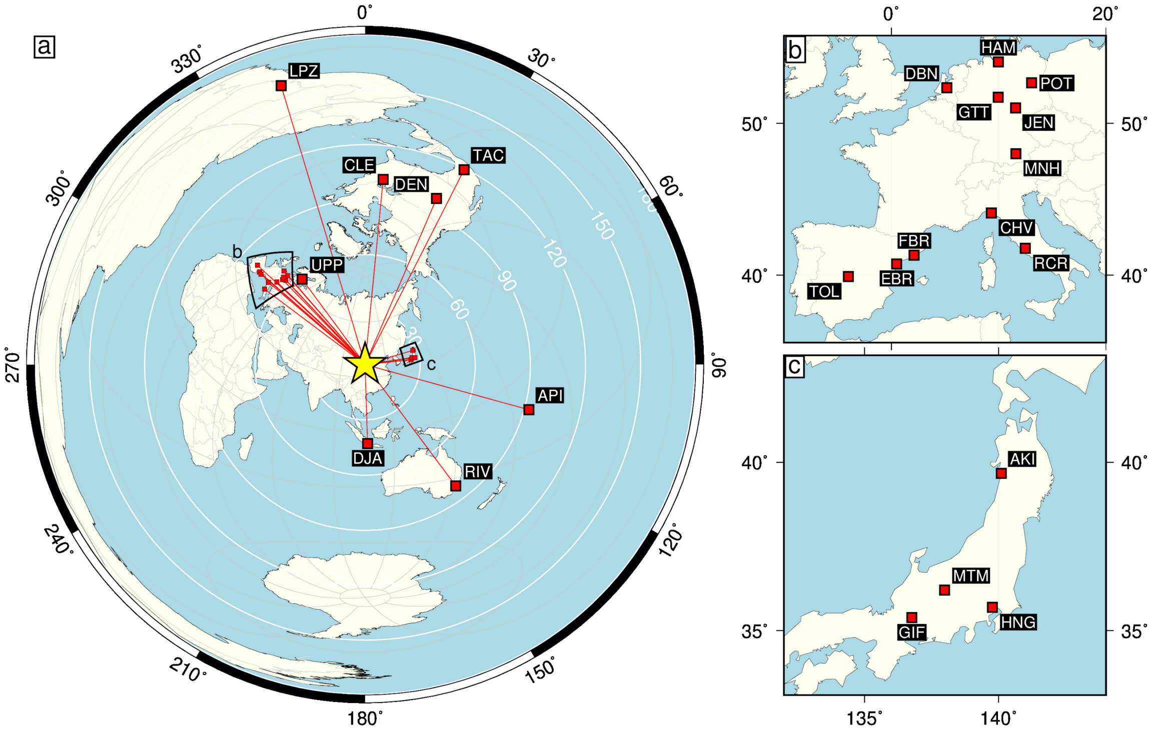

Figure 2.3: (a) Station distribution around the epicentre of the 1920 Haiyuan earthquake on an azimuthal equidistant projection. White concentric circles are epicentral distances. (b) and (c) show the station distribution for Europe and Japan respectively. The three-letter codes in the plot represent station names. When followed by a fourth character in the text, they represent waveforms. 'B', 'W', 'G' are used to differentiate Bosch-Omori, Wiechert and Gallitzin seismographs at those stations where multiple instruments were operational. 'H' stands for 'historical' when only one type of instrument was operational at the station (Table A.2).

retain the true dimensions. Photos have to be taken against a ruler placed in a way that minimises parallax error. Microfiches were usually carefully prepared with scale references. Microfilms, however, were scanned in the past at unknown resolution. If the microfilm did not contain a scale on the page, the record could only be used for epicenter relocation and focal mechanism determination, but not for amplitude measurements.

We first digitised the waveforms by hand as Bezier curves in version 2.10 of the GNU Image Manipulation Program (`http://www.gimp.org`). We digitised the traces starting from the beginning of the minute mark 3 minutes before the minute of first arrival and stopped where either a waveform becomes saturated, the trace breaks due to dislocation of the stylus, or at the edge of the seismogram if the left and right edges could not be reliably spliced together. As the seismograms were scanned at different resolutions, pixels-per-inch and pixels-per-minute values were both required to convert the digitised records into time series in units of millimetre and seconds (Fig 2.4a,b).

Due to the mechanical design of the seismographs, which involved a hinged stylus swinging on a rotating cylindrical drum, these analogue waveforms have unwanted curvature and slant (Fig 2.4a). To correct these geometric artifacts, we ran an inversion algorithm, developed at the University of Potsdam (see *Kulikova and Krüger* (2015)), to restore the symmetry of the waveforms based on the geometry of the instrument set-up described in *Čadek* (1987).

Instrument parameters including natural period, T_o, magnification factor, V_o, and either damping ratio, ϵ, or damping constant, h, were collated from the seismograms, scanned station bulletins, station specific literature, *Wood* (1921), and *McComb and West* (1931), in descending order of preference.

When neither damping constant, h, nor damping ratio, ϵ, was found in literature, we calculated them from the calibration pulse at the start of the seismogram, as in the case of records GIFH, RCRH, CHVH and TOLH, where the stylus was first set in motion after a change in paper and recorded a series of decaying oscillations (see equations 4.27, 4.31 in *Scherbaum* (2001)):

$$h = \frac{\ln(\epsilon)}{\sqrt{4\pi^2 + (\ln(\epsilon))^2}}, \quad \text{where} \quad \epsilon = \frac{a_k}{a_{k+2}} \tag{2.1}$$

where a_k and a_{k+2} are amplitudes one full wavelength apart in the calibration pulse.

If we could not find damping information in literature and the seismograms did not contain the calibration pulse (e.g., AKIH, LPZH and TACB), we chose as a best estimate the most common damping ratio of the same type of instrument in *Wood* (1921) or *McComb and West* (1931).

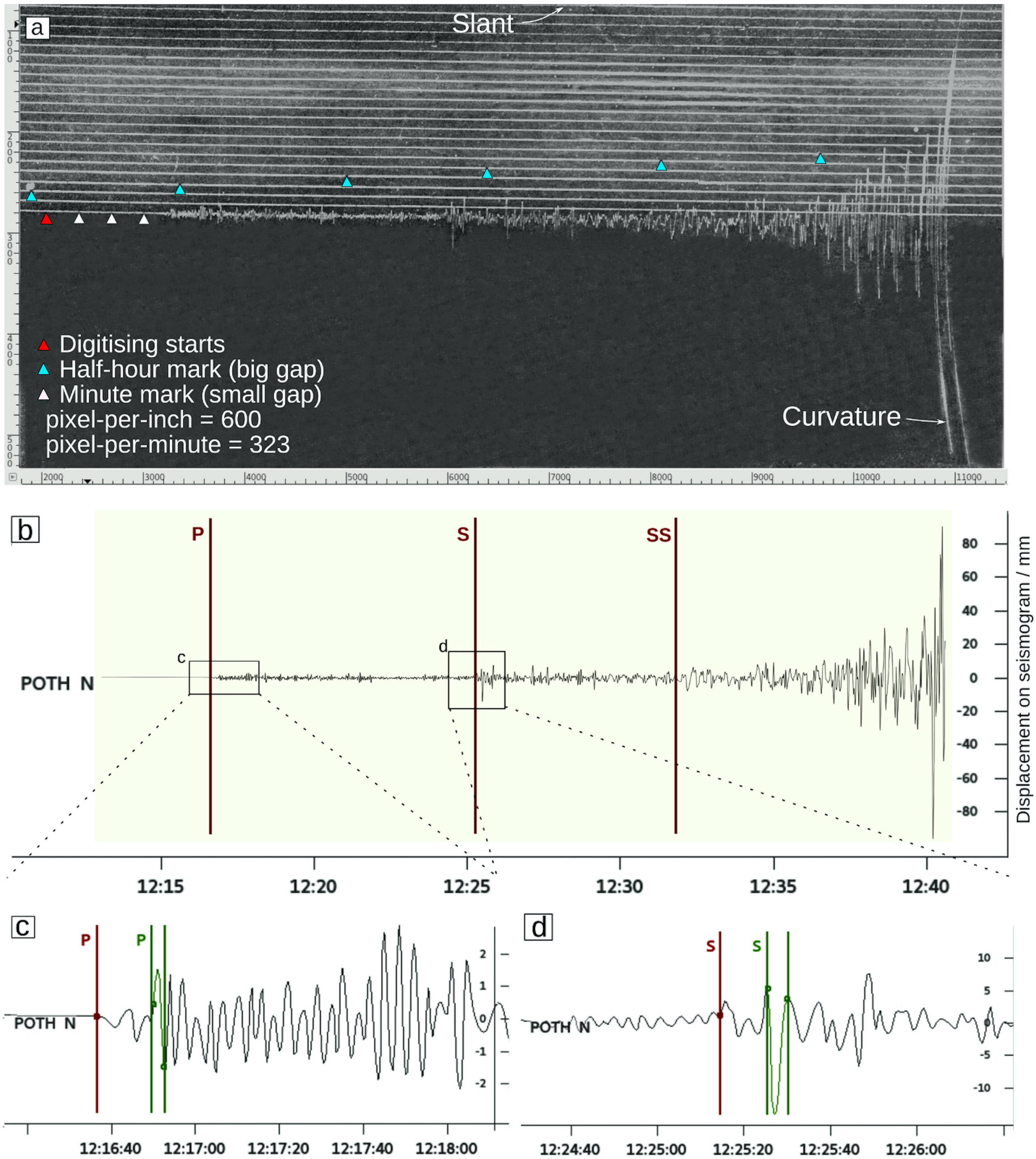

Figure 2.4: (a) Scanned seismogram from Potsdam Station in pixel coordinates. (b) Digitised waveform in mm as a function of time after curvature correction. Red markers with P, S and SS labels are the picked phase arrival times in the Snuffler browser of the Pyrocko toolbox (*Heimann et al.*, 2017). (c,d) Enlargements of the boxes in (b). Green markers highlight the amplitude (measured from zero) and period (crest-to-crest or trough-to-trough) measurements for m_B calculation in Section 2.2.5.

These parameters (Appendix A.2) were used to calculate the instrument specific transfer functions, $V(T)$, which is the key to converting between the recorded and the actual ground displacements (*Scherbaum*, 2001):

$$\begin{aligned}
&V(T) = V_o \frac{\omega^2}{(P_1 - i\omega)(P_2 - i\omega)}, \quad \text{where} \quad \omega = \frac{2\pi}{T}, \\
&P_{1,2} = -\omega_o(h \pm i\sqrt{1-h^2}), \quad \text{and} \quad \omega_o = \frac{2\pi}{T_o}, \\
&A_g = A_s/|V(T)| \times 1000
\end{aligned} \tag{2.2}$$

where $P_{1,2}$ are the poles of the low-pass filter that describes the frequency response of the seismograph, A_g is the ground displacement in micrometer and A_s is the recorded signal in millimetre on the seismogram.

The station books and local bulletins that we sourced from individual contacts and obtained from the the Istituto Nazionale di Geofisica e Vulcanologia's EUROSISMOS project webpage (`http://sismos.rm.ingv.it/en/index.php/bulletins`) also provided additional phase arrival data which we added to the ISC bulletins for epicentre relocation in section 2.2.2.

2.2.2 Epicentre Relocation

We first picked the arrival times of P, PP, PPP, S, SS, SSS and SP phases from the waveforms in the Snuffler browser of the Pyrocko toolbox (*Heimann*, 2019) (Fig 2.4b, see supplementary data set S2 for picked phase times). Since only one vertical component waveform was available, the P-type phase arrivals were preferentially picked on the horizontal component that forms the smaller angle with the radial direction from the source, and the S-type phase arrivals were picked on the component with the earlier onset. The interpretation of the onset typically involves a decision within a time range of a few wavelengths, especially in the cases of high frequency records (Table A.2). Considering this degree of subjectivity, our phase times are mostly accurate to ±10 s.

We then used version 6.0c of the Hyposat programme package (*Schweitzer*, 2001) to invert for the origin of the rupture based on the Crust 1.0 and AK135 velocity models (*Kennett et al.*, 1995; *Laske et al.*, 2013). The program used both onset times and travel time differences to iterate for the best fitting hypocenter. Phases with large time residuals were successively removed until all remaining phases had residuals below 30 s.

Three independent inversions were performed with arrival times from newly picked waveforms only, bulletins (previously published and newly added from station books readings) only, and the combined data respectively. Due to the lack of depth phases, we fixed the depth at 15 km assuming the rupture started near the bottom of the seismogenic layer (*Das and Scholz*, 1983). Changing the fixed depth shifts the epicentre along the major axes of the error ellipses. The resultant epicentres are all within 20 km of Haiyuan and fall within the XII intensity isoseismal contour (Fig 2.2, *Zhuang et al.* (2018)). We chose the epicentre derived from the combination of waveforms and bulletins (105.540 $\pm$ 0.251E, 36.481 $\pm$ 0.256N) as our best estimate to use for focal mechanism determination as it represents a balance of less numerous but more accurate, and more numerous but less accurate, data, and it lies closest to the known geomorphic trace of the fault rupture.

2.2.3 Focal Mechanism Determination

Considering the often unknown polarity and inconsistent minute-mark lengths of our waveforms, we could not use the first motions nor waveform modelling to determine the earthquake focal mechanism, so we determined the focal mechanism by fitting the radiation pattern in terms of the ratio between P- and S-phase amplitudes.

First, Green's functions assuming a point source were computed for a distance range between 1000 km (17.9°) to 18000 km (162.2°) at intervals of 20 km, a depth range between 0 and 40 km at intervals of 2 km and sampled at 2 Hz frequency. The calculation was based on the Qseis2006 code in the Fomosto tool of the Pyrocko package (*Heimann et al.*, 2017, 2019; *Wang*, 1999). The Green's functions were convolved with the instrument-specific transfer functions to generate synthetic seismograms in the same domain as the digitised records.

We then measured the amplitude of P, PP, PPP, S, SS, PS automatically by extracting the maximum absolute amplitude of each phase from time windows determined from theoretical travel times. The misfit, η, in the amplitude ratios between real and synthetic seismograms was calculated as:

$$\eta = \frac{1}{K}\sum_{k=1}^{K}\left(\sqrt{\frac{1}{N}\sum_{i,j}^{N}\left(\left(\frac{A_i}{A_j}\right)_{obs} - \left(\frac{A_i}{A_j}\right)_{syn}\right)^2}\right)_k, \tag{2.3}$$

$$\text{where } i/j = \begin{cases} \frac{P}{S} & \text{for } \Delta < 30^\circ, \\ \frac{P}{S}, \frac{PP}{S}, \frac{P}{SS}, \frac{PP}{SS} & \text{for } 30^\circ < \Delta < 50^\circ, \\ \frac{P}{S}, \frac{PP}{S}, \frac{PPP}{S}, \frac{P}{SS}, \frac{PP}{SS}, \frac{PPP}{SS} & \text{for } 50^\circ < \Delta < 100^\circ, \\ \frac{PP}{SS}, \frac{PP}{PS}, \frac{PPP}{SS}, \frac{PPP}{PS}, \frac{PS}{SS} & \text{for } \Delta > 100^\circ \end{cases}$$

where K is the number of waveforms and N is the number of epicentral distance dependent i/j phase combinations.

We performed a grid search through strikes between 80° and 160°, dips between 20° and 90°, rakes between -60° and 60° at steps of 10°, and centroid depths between 0 and 30 km, at steps of 2 km. Fig 2.5a shows the best-fit strike, dip and rake for each centroid depth suggesting the centroid depth is not well constrained. However, the focal mechanism is stable, with dip constrained between 80° and 90° and rake between -10° and 10° (Fig 2.5b). This range is consistent with our geological understanding that the 1920 Haiyuan earthquake was a shallow earthquake that slipped left laterally on a steeply dipping fault (*Deng et al.*, 1984; *Fan et al.*, 2004; *IGCEA and NBCEA*, 1990; *Wang et al.*, 2012, 2014).

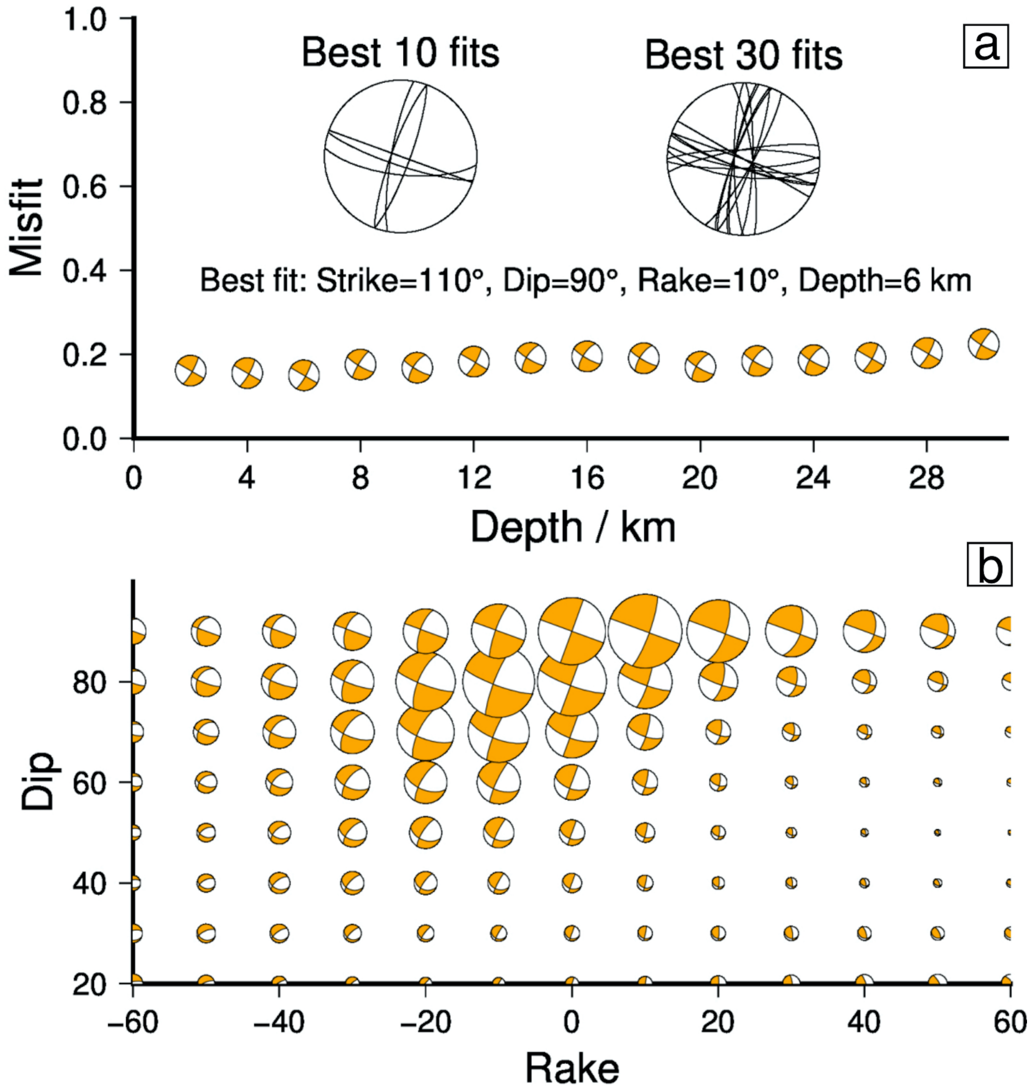

Figure 2.5: (a) The overall best 10 and 30 solutions, and the variation of the best-fit strike, dip and rake combination at each given centroid depth. (b) Solution misfit with changing rake and dip, with beach ball sizes proportional to the inverse of misfits with fixed strike of 110° and depth of 6 km.

2.2.4 Waveform Modelling for M_W

As the surface waves were clipped for the majority of our records, we only modelled the body wave portion of a subset of high quality records. The records had to be long enough to contain the full body wave trains, be well-damped and, more importantly, be of known polarity (*Kulikova and Krüger*, 2015; *Kulikova et al.*, 2016; *Kulikova and Krüger*, 2017). For stations within 30° epicentral distances, we defined a time window from 100 s before the theoretical P-wave arrival to 200 s after the theoretical S-wave arrival. For stations further away, we set the end of the time window to 200 s after the theoretical SS arrival. As the historical instruments mostly had narrow frequency bands, we band-pass filtered both digitised and synthetic waveforms to between 0.01 to 0.1 Hz in order to preserve the signals. To characterise the misfit, we correlated the real and synthetic waveforms for the time shift to keep them aligned, before cropping them again to only include the time window with overlapping data. The waveforms were then Butterworth filtered with a cosine taper of 10 s before the average relative misfit, γ, was calculated:

$$\gamma = \frac{1}{K}\sum_{k=1}^{K}\left(\frac{\sqrt{\sum_{n=1}^{N}(y_{obs}-y_{syn})^2}_n}{\sqrt{\sum_{n=1}^{N}(y_{obs}^2)_n}}\right)_k \tag{2.4}$$

where K is the total number of records being modelled, N is the total number of points sampled in the extracted time window and y_{obs} and y_{syn} are the real and synthetic waveforms sampled at 2 Hz (*Kulikova and Krüger*, 2015; *Kulikova et al.*, 2016; *Kulikova and Krüger*, 2017). The synthetic waveforms in the earlier steps were generated using point sources which means that all the seismic moment was released at once to create impulsive arrivals. However, with rupture velocities of 2.5 - 5.5 km/s, it would take about one minute to rupture a fault over 200 km. Therefore, in order to reproduce the moment rate embodied by the waveforms, we modelled the seismograms with a rectangular source. We initialised the fault as a single vertical plane that ruptures bilaterally, as indicated by our epicentral location near the central part of the rupture.

We tested the best-fitting focal mechanisms in Fig 2.5b through a range of fault lengths, widths, nucleation points, rupture velocities with magnitude fixed at an initial guess of M_W 8.0. The results suggested that the waveforms qualified for modelling preferred a dip of 90° (γ = 0.86–0.93) over 80° (γ = 0.92–1.01). As it is unlikely there would be a vertical slip component on a 90° dipping fault, we chose strike=110°, dip=90° and rake=0° as the focal mechanism for magnitude determination. Fault dimensions had the least significant effect on γ, so we fixed the fault length and width to be 240 km and 20 km, respectively, based on our geological understanding. With the nucleation point (centre bottom, CB in Fig 2.2) and rupture speed (3 km/s) selected based on misfit values from our limited data set, the synthetic magnitude was then varied to find the best-fitting M_W.

The magnitude with minimum misfit was M_W 7.8, with γ=0.86. However, the synthetic waveforms visibly underestimated the amplitudes, which we speculate resulted from the inconsistent minute mark lengths on our seismograms causing poor alignment between the synthetic and digitised waveforms. In order to avoid bias from misfits due to misalignment in the time domain, we used the root-mean-squared waveform displacement as a proxy for earthquake magnitude. The magnitude that provides the best match of the root-mean-square value of displacements sampled along the body-wave trains in the overlapping time window was chosen to be the best-fit magnitude for each station component. Fig 2.6 shows waveform fits at our final magnitude M_W 7.94, as averaged from the best M_W for each station in terms of the root-mean-squared displacement (Fig 2.7a). To check for consistency, a test with M_W 7.94 and varying source parameters was performed. The misfit with the above parameter set was $\gamma = 0.88$, only 0.1% larger than the minimum misfit found by grid searching the source parameters again, which happened at a rupture speed of 2.8 km/s with all other parameters unchanged.

The ability of the synthetic waveforms to fit the data varies between stations. One reason could be that the parameters we compiled from historical documents failed to accurately describe the instrument response on the day. Rarely could we find the full set of parameters in the same document. The parameters recorded in seismogram labels, bulletins, station books, *Wood* (1921) and *McComb and West* (1931) could

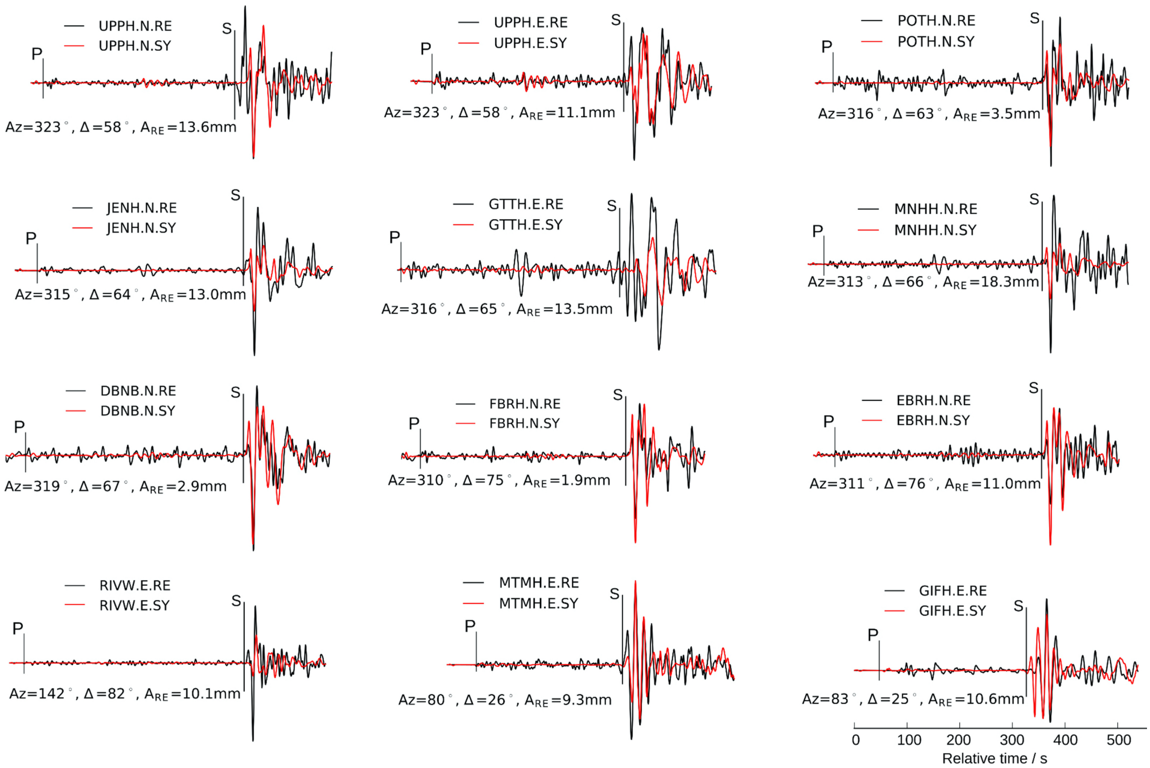

Figure 2.6: (a) Real and synthetic P-S waveforms for the overall best-fit magnitude of Mw 7.94.

also be different. Therefore, the values we tabulated in Table A.2 only represent a combination of values we trusted the most, based on the date of publication, associated elaborations and whether the values agree with what we observe on the seismograms. The fact that the synthetic waveforms tend to underestimate the P-wave train could be related to the background noise in the seismograms which sometimes have similar amplitudes as the recorded P-wave train. Therefore, we trust the S-wave trains more as they are more energetic.

2.2.5 m_B and M_S Determination

To check if we could reproduce the body wave and surface wave magnitudes obtained by *Gutenberg and Richter* (1954) and *Gutenberg and Richter* (1941) and to understand the differences between M_W and other types of magnitudes reported, we calculated m_B and M_S using our collected seismograms according to the following

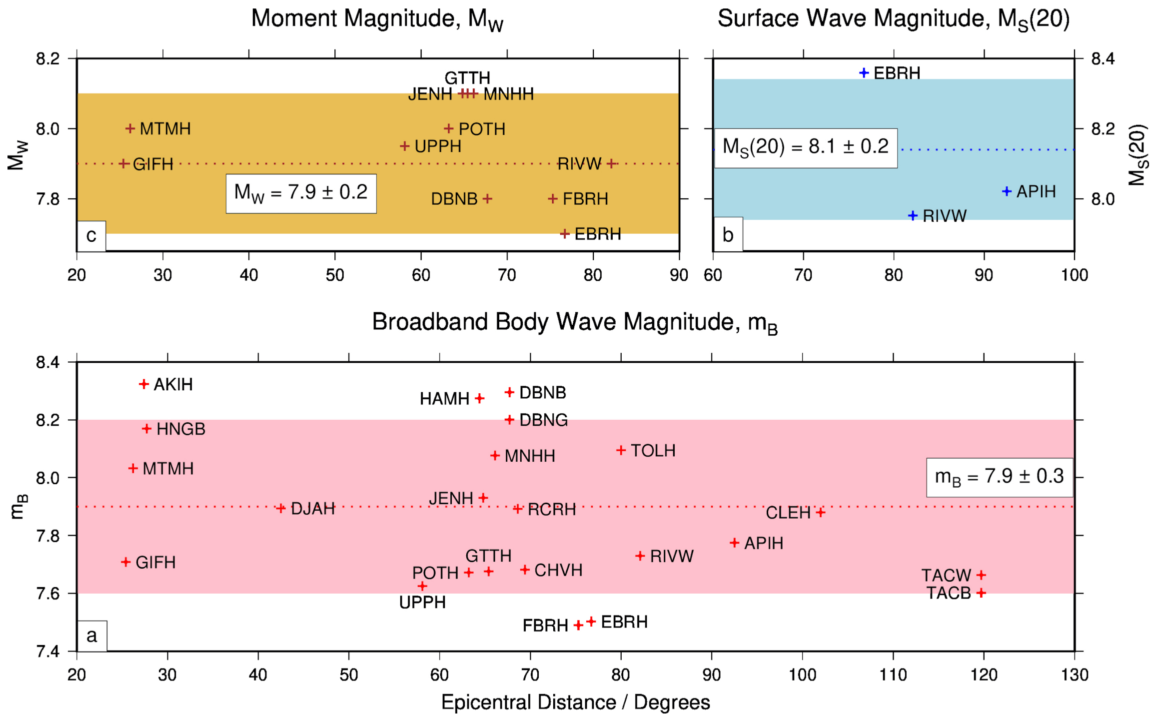

Figure 2.7: (a) M_W results from waveform modelling. (b) $M_S(20)$ and (c) m_B results from phase amplitude and period measurements. Dotted lines and coloured bands show the average and standard deviation of the station magnitudes.

definitions:

$$m_B = \log(\frac{A_H}{T})_{max} + Q(\Delta), \tag{2.5}$$

and

$$M_S(20) = \log(\frac{(A_H)_{max}}{T}) + 1.66 \log \Delta + 3.3, \tag{2.6}$$

where A_H is the vectorially combined horizontal phase amplitude in μm and T is the corresponding period in s. Δ is the epicentral distance, and Q is a distance- and phase-dependent calibration value tabulated in *Gutenberg and Richter* (1956).

The classical m_B, which is equivalent to the m in *Gutenberg* (1945b), is a medium-period broadband body-wave magnitude (*Bormann*, 2012). Unlike the more familiar narrow-band m_b, m_B accepts PH, PV, PPH, PPV or SH phase amplitudes with 2 s $< T <$ 20 s and only saturates at $\sim$8.5, hence was a popular choice for determining magnitudes of large earthquakes before the 1960s.

Due to the ambiguity in the meaning of and method for obtaining Gutenberg's surface-wave magnitude, M, we adopted the International Association of Seismology and Physics of the Earth's Interior (IASPEI) standard long-period teleseismic surface wave magnitude $M_S(20)$, which takes the highest phase amplitudes with 18 s $<$ T <22 s from stations with epicentral distance $20° < \Delta < 160°$ (*Bormann*, 2012).

For both m_B and $M_S(20)$, if the measured phases were within half a wavelength on the two orthogonal horizontal components and their periods differed by less than 1 s, we vectorially combined the amplitudes to give the true horizontal amplitude, A_H.

If vectorial combination was not possible, for m_B, we back-projected the body wave P, PP, S, SS phase amplitudes using the back-azimuth angle to obtain A_H trigonometrically, expecting the body waves to be polarised into radial and transverse components. For $M_S(20)$, we did not use the station if we could not find matching phases satisfying the requirements.

The amplitudes, A, and periods, T, were measured in the Snuffler seismogram browser (*Heimann*, 2019) (Fig 2.4c,d). The measured displacements A_s in mm were then converted to ground displacement A_g in μm through the transfer function, $V(T)$ (Equation 2.2).

The epicentral distances, Δ, and back-azimuth angles were calculated between our relocated epicentre and the latitudes and longitudes of historical stations in local bulletins or *Wood* (1921) using the $locdiff$ utility function of the Seismic Handler software package (*Stammler*, 1993).

In total, 123 phase amplitudes and periods were measured (see supplementary data sets S3 and S4) to obtain an average magnitude for each station (Fig 2.7b,c). The wide phase options, broadband period allowance and the back-azimuth method allowed us to retain 21 stations for body wave magnitude determination. The resultant magnitude is $m_B = 7.9 \pm 0.3$. Due to the strict requirements for $M_S(20)$, only three stations with long-period instruments fulfilled the criteria and gave a surface-wave magnitude of $M_S(20) = 8.1 \pm 0.2$.

2.3 Geomorphological Approach

Mapping of rupture length and continuity, combined with measurements of coseismic slip, are valuable for estimating moment release, as well as assessing the geometrical complexity of the rupture and phenomena related to the rupture process (*Clark et al.*, 2017; *Zhou et al.*, 2015a). For the 237 km long 1920 Haiyuan earthquake rupture, detailed field surveys along the entire rupture were performed in the 1980s (*Deng et al.*, 1986; *IGCEA and NBCEA*, 1990; *Zhang et al.*, 1987) (see supplementary data set S5 for their offset measurements), but their interpretation of the coseismic slip was challenged by *Ren et al.* (2016) based on 70 km of LiDAR data that partially covered the western and middle sections (pink patches in Fig 2.8a).

The 1980s field studies (*Deng et al.*, 1986; *IGCEA and NBCEA*, 1990; *Zhang et al.*, 1987) found that the surface slip distribution of the 1920 Haiyuan earthquake followed bell-shaped curves with peak offsets of 6 m, 10 m and 4 m at the centres of the western, middle and eastern sections (white squares in Fig 2.9a and Fig 2.10a). In contrast, *Ren et al.* (2016) observed clustering of 1.5–3.5 m offsets and 8–12 m offsets along about two-thirds of the western section (red error bars and grey bands in Fig 2.9a), hence classified the former as single-event displacements from the 1920 Haiyuan earthquake and the latter as cumulative displacements from 1920 and previous events. However, this classification leaves an ambiguity whether the offsets measured between 3.5 m and 8 m represent single-event or cumulative displacements. In the middle section, *Ren et al.* (2016) argued that the 10 m maximum offset reported by *Deng et al.* (1986) and *IGCEA and NBCEA* (1990) (circled in Fig 2.10a) is likely cumulative because there is a 5 m offset 20 m from the 10 m offset. However, *Ren et al.* (2016) also attributed 5.4–7.1 m offsets between Shikaguangou and Shao-

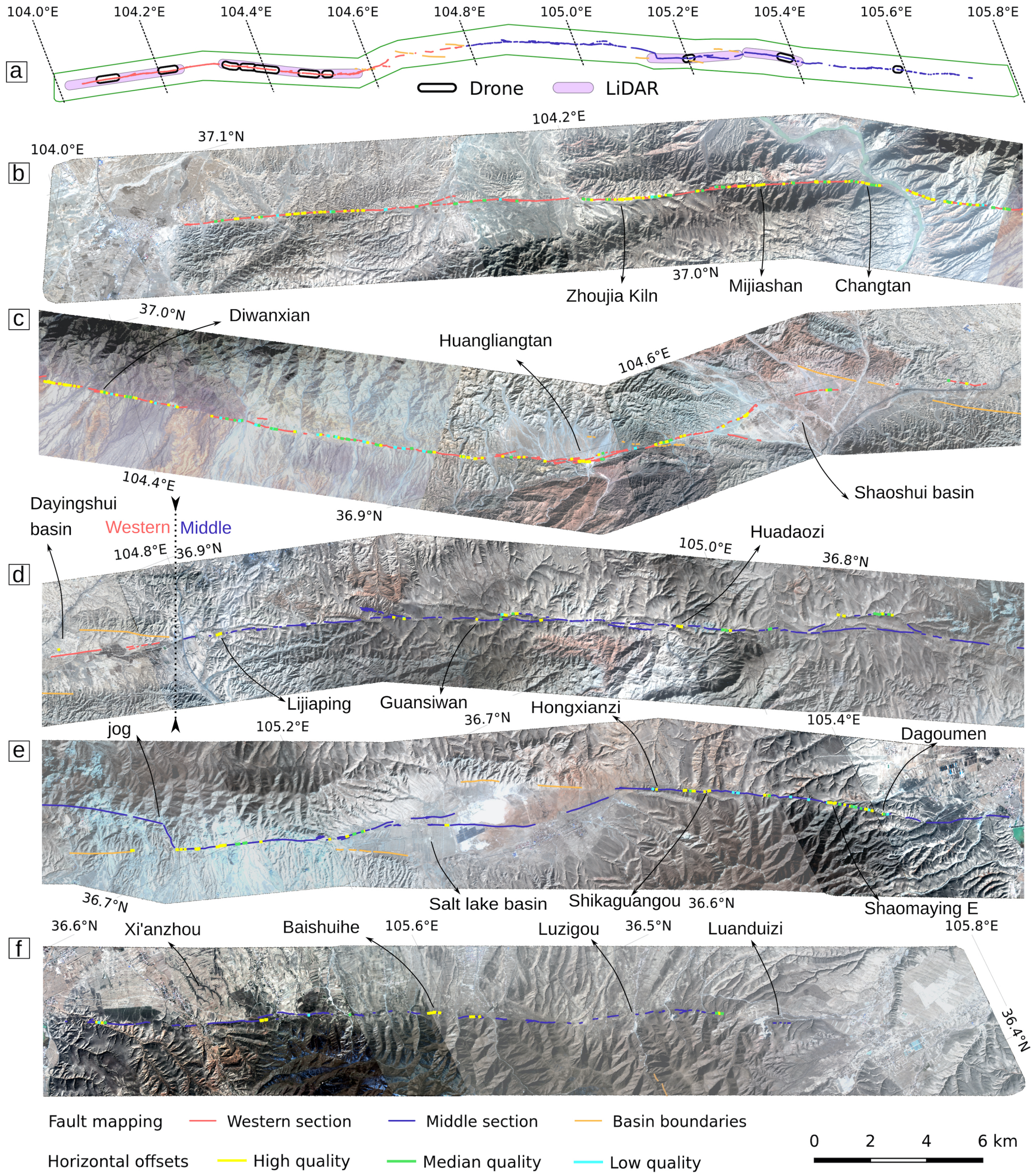

Figure 2.8: (a) Overview of data coverage by Pleiades imagery (green outline) and drone imagery (black) in this study and LiDAR DEMs (pink) in *Ren et al.* (2016). (b-f) Orthorectified multi-spectral Pleiades imagery with mapped fault traces and offsets from west to east.

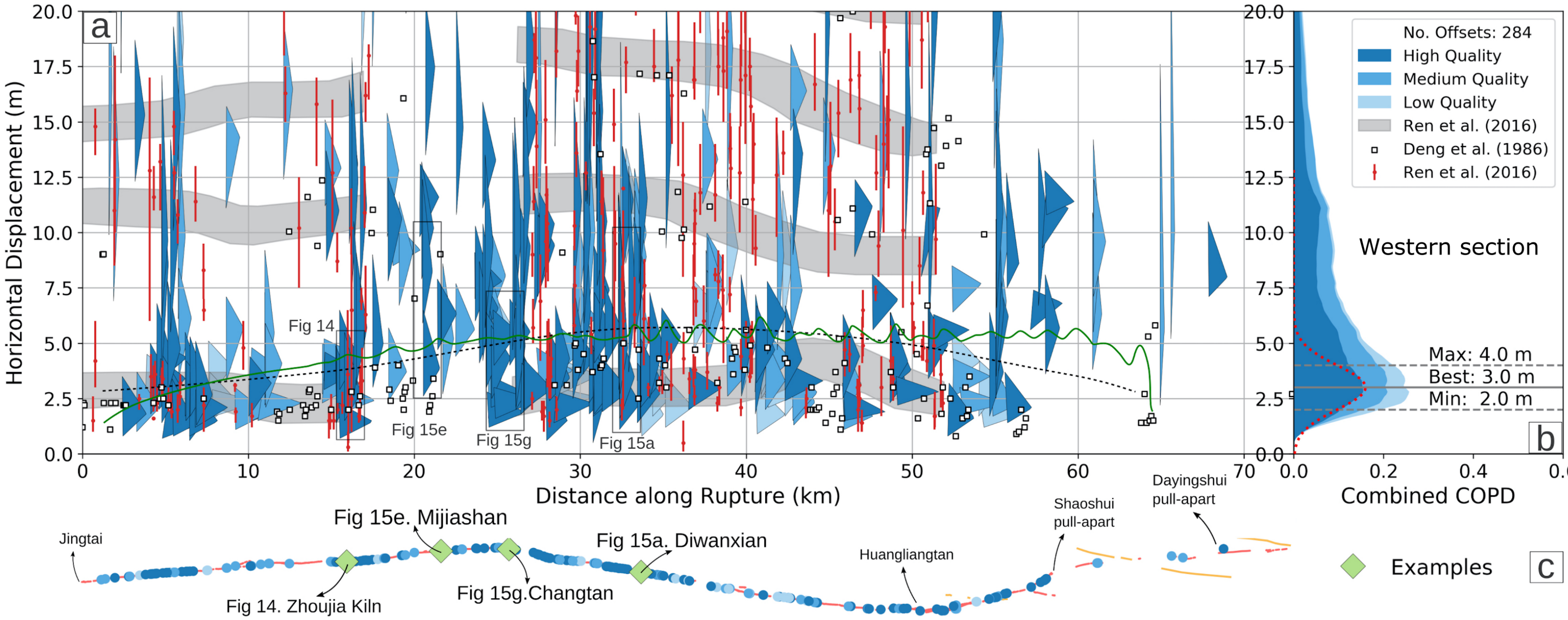

Figure 2.9: (a) Offsets along the western section measured from Pleiades and drone data (blue areas), LiDAR (red error bars, *Ren et al.* (2016)) and in the field (white squares, *Deng et al.* (1986); *IGCEA and NBCEA* (1990)). Grey bands are *Ren et al.* (2016)'s classification of cumulative offsets into past earthquakes. Different shades of blue represent high, medium and low quality offset features measured in this study. Black dotted line is the bell-curve slip distribution based on *Deng et al.* (1986). Green line is the simulated horizontal slip distribution by *Xu et al.* (2019). (b) Stacked cumulative offset probability density (COPD) from our measurements where the lowest peak represents the best-estimate of average slip from the 1920 earthquake. (c) Location of offsets along rupture with green diamonds marking example sites.

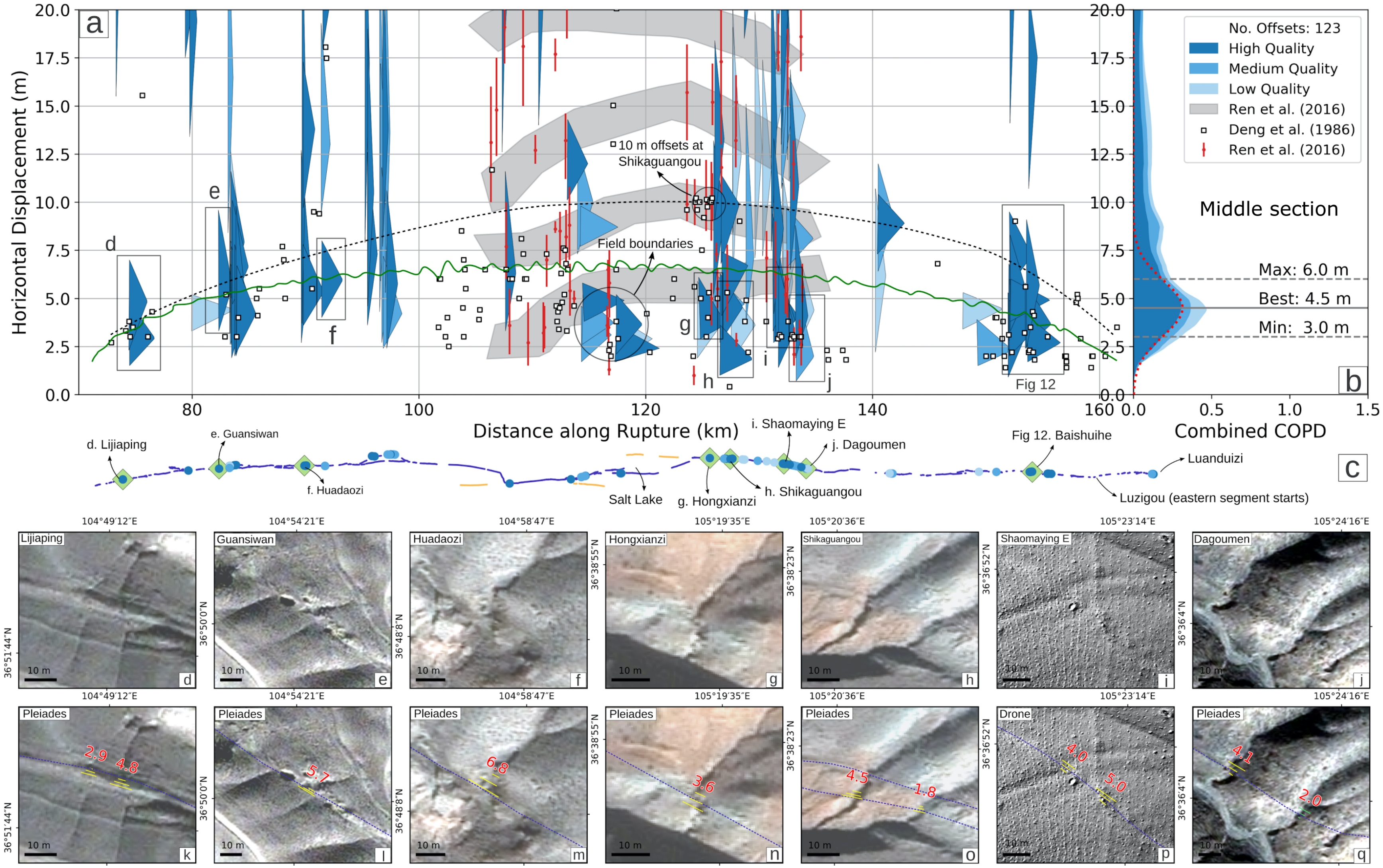

Figure 2.10: (a-c) Same as Fig 2.9(a-c), but for the middle section. (d-j) show example sites marked by the green diamonds in (c), with rupture and offset mapping labeled in (k-q).

maying as single-event offsets (grey bands in Fig 2.10a), despite the numerous 2–3 m offsets reported nearby (red error bars in Fig 2.10a), suggesting that the 5.4–7.1 m offsets could be cumulative, too. In addition, to the west of the Salt Lake basin, *Ren et al.* (2016) documented a step increase from 2.5–3.7 m to 5.0–6.2 m within 5 km (Fig 2.10a); if widely observed along the rupture, such slip variation would pose a challenge to moment magnitude estimation based on slip measurements.

These differences prompted us to revisit the mapping of offsets in order to see whether peak slip in excess of that measured by *Ren et al.* (2016) may have occurred in their data gap, to discriminate between the 3.5–8 m offset measurements in the western section and the scattered offsets in the middle section in order to interpret whether they were produced by the 1920 earthquake or represent more than one event. Finally, with a better understanding of the surface slip distribution along the entire length of the strike-slip western and middle sections and with the offsets reported by *IGCEA and NBCEA* (1990) on the eastern section, we estimate the seismic moment release M_o and hence moment magnitude M_W of the 1920 Haiyuan earthquake.

2.3.1 Image Processing and Field Acquisition

Twelve scenes of tri-stereo Pleiades optical imagery totalling over 1115 km^2 were acquired on cloud-free and snow-free days in the winter between November 2016 and January 2017, in order to minimise vegetation cover that would obscure the geomorphic features (Fig 2.8, see supplementary data set S6 for metadata). Each scene had three acquisitions from three different perspectives, with each acquisition consisting of a 0.7 m resolution panchromatic band and four 2 m resolution multi-spectral bands.

To orthorectify the imagery, we first processed the panchromatic imagery using the Leica Photogrammetry Suite module offered by ERDAS IMAGINE software following the methods described in *Zhou et al.* (2015a), *Middleton et al.* (2015) and *Ainscoe et al.* (2019). Tie points were computed based on satellite orbital information and then manually inspected to ensure even distribution and that they were away from shadows. We then used the Enhanced Automatic Terrain Extraction tool to extract point clouds based on relief displacement between images. The point clouds of all the possible combinations of images were combined to generate a raster DEM of 1 m resolution. After orthorectifying the multi-spectral and panchromatic imagery with the DEMs, we pan-sharpened the orthorectified multi-spectral imagery to the resolution of the orthorectified panchromatic imagery. The resultant ~0.7 m resolution orthorectified multi-spectral imagery allowed us to map fault traces in detail and to measure horizontal offsets in the QGIS software.

Fieldwork was undertaken in June 2017 and June 2018 to measure selected offsets with a tape measure and to conduct low-altitude photographic surveys over 10 sites (Fig 2.8a). Ground control markers were distributed evenly across the survey areas and their geographic coordinates determined using differential GNSS. Aerial photos were taken with a camera mounted on a DJI Phantom 4 quadcopter, which traversed the area at flying altitudes of ~100 m. Flight itineraries were programmed to ensure 60% overlap between tracks and 30% overlap along track between consecutive photos. Using the structure-from-motion method (*Westoby et al.*, 2012), we created orthophotos and a DEM from the aerial photos using the Agisoft Metashape software. The drone DEMs were of decimeter-resolution and served to validate measurements from the Pleiades imagery.

2.3.2 Offset Measurement

Surface rupture and horizontal offsets were mapped in QGIS software using the line feature tool (see supplementary data sets S7, S8 and S9 for the resultant .kml files and measurements). For each displaced stream, we measured the best offset between the thalwegs of channels, the minimum offset between the inner banks and the maximum offset between the outer banks, using the method of *Elliott et al.* (2015) (Fig 2.11). Measurements are summarised as blue triangular probability distributions in Fig 2.9a and Fig 2.10a.

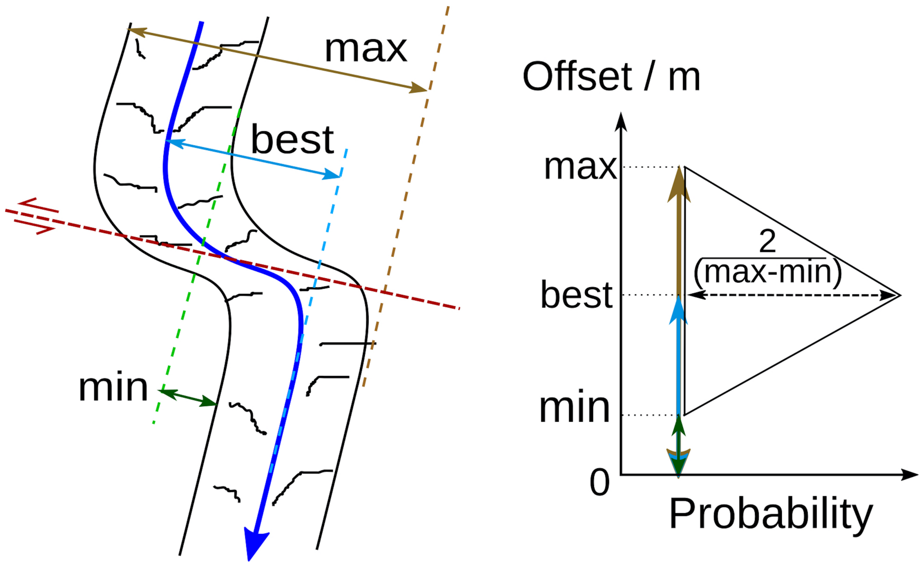

Figure 2.11: Schematic illustration of converting minimum, best and maximum offset measurements into a trianglar probability density function (PDF).

In areas with complex rupture patterns, we measured the total slip as the sum of displacements across all participating strands. For example, at the en-echelon faults at Baishuihe site (Fig 2.12), gullies 1, 2 and 3 are interpreted as being offset by one splay and gullies 4 and 5 by two splays. Hence, the summed best offsets measured are 3.3 m, 5.6 m and 5.6 m for gullies 1–3, 3.4 m and 7.2 m for the two beheaded downstream channels of gully 4, and 7.2 m for gully 5. In rupture zones where we could not resolve the offsets on individual strands, the offsets were not measured. In this way, we ensured that the offset obtained represents the total slip rather than a partial slip on each strand.

The measurements we made on the satellite and low-altitude photogrammetric data sets are well correlated (Fig 2.13a) and were corroborated with our field measurements (Fig 2.14). At Zhoujia Kiln, two streams 30 m from each other were

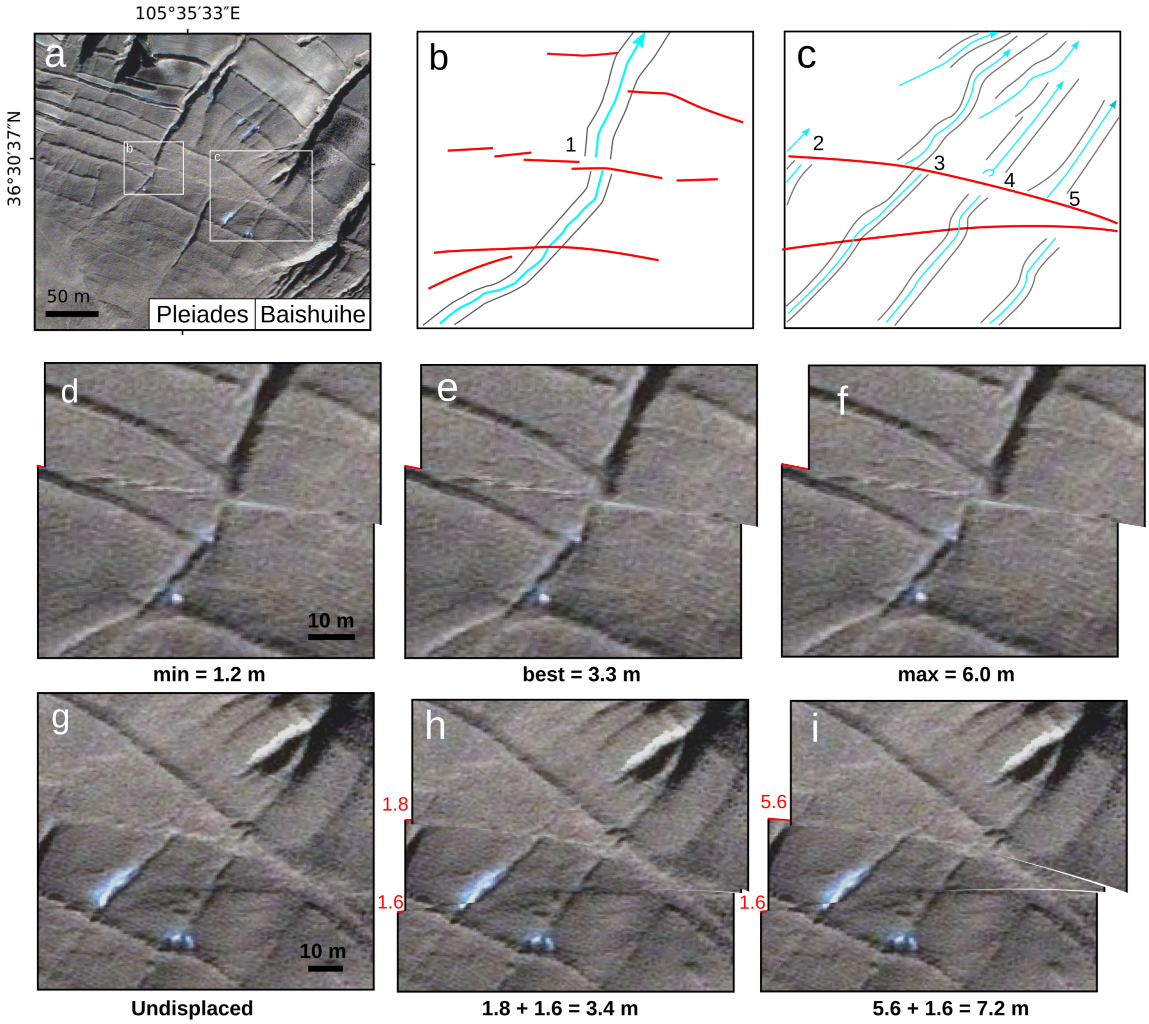

Figure 2.12: (a) Five gullies displaced by a series of en-echelon faults at Baishuihe site, see Fig 2.10a for location. (b,c) are geomorphic interpretation of the displaced channels. (d-f) shows the channel in (b) displaced by the minimum, best and maximum offsets measured. (c,g) show four gullies displaced by two fault splays and the offsets are measured as the sum of offsets on both rupture strands.

displaced. The offsets measured on them were 3.2 +3.2/−1.8 m and 1.5 +1.1/−0.9 m from the Pleiades imagery, 2.9 m +2.1/−1.6 m and 1.5 +0.9/−0.8 m on the drone DEM, and 2.8 +1.9/−0.7 m and 1.4 + 1.0/−0.4 m in the field, all consistent with each other. As drone DEMs have higher resolution than Pleiades imagery, the drone measurements were preferred and, when available, used in place of Pleiades measurements for subsequent analysis.

When we compared our measurements to those made by *Ren et al.* (2016), we

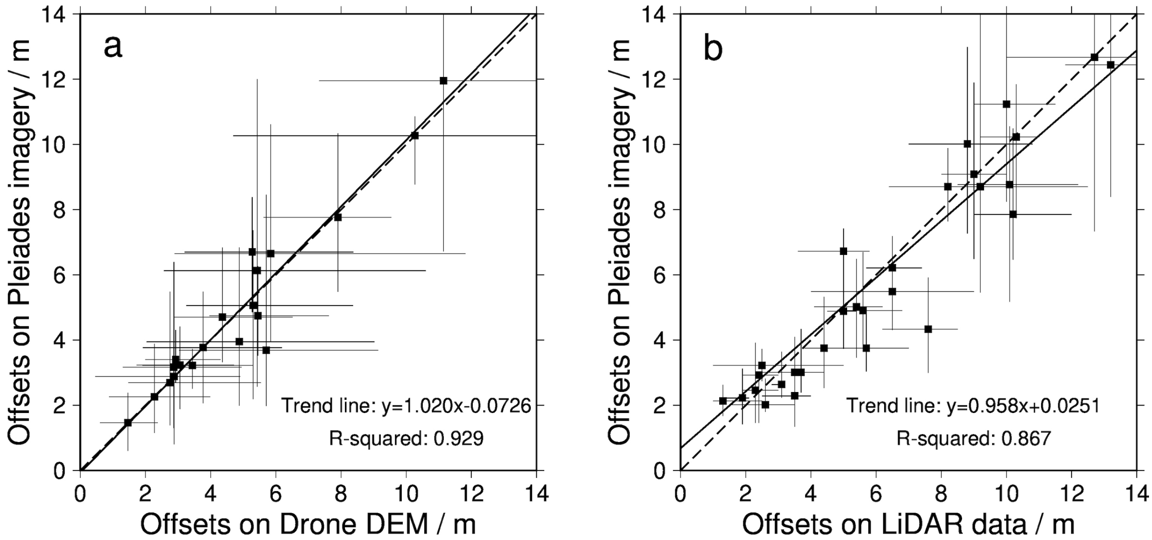

Figure 2.13: Comparison of offsets measured from (a) Pleiades imagery and drone DEM and (b) Pleiades imagery and LiDAR DEM, suggesting high-resolution satellite imagery can be as good as LiDAR data for offset measurement (*Zhou et al.*, 2015b).

find that the set of features we selected to measure are not always identical due to different interpretations and features being highlighted in different ways by the different data sets (Fig 2.15a-d). Sometimes, careful manual relocation of the measurements from *Ren et al.* (2016) was necessary to associate the measurements with the corresponding features. However, there is generally good agreement between the values, including similar uncertainties, obtained despite the different data sets employed and the different methods used to estimate offset (Fig 2.13b).

A quality rating was assigned to each offset measurement following *Scharer et al.* (2014). High quality was given to linear features that cross the fault at high angles ($> 60°$), with well-defined edges and sharp displacement. Medium quality was given to features that were sinuous or less well-defined or cut the surface rupture at smaller angles. Low quality was given to features that were poorly rated on at least two of the three factors mentioned above.

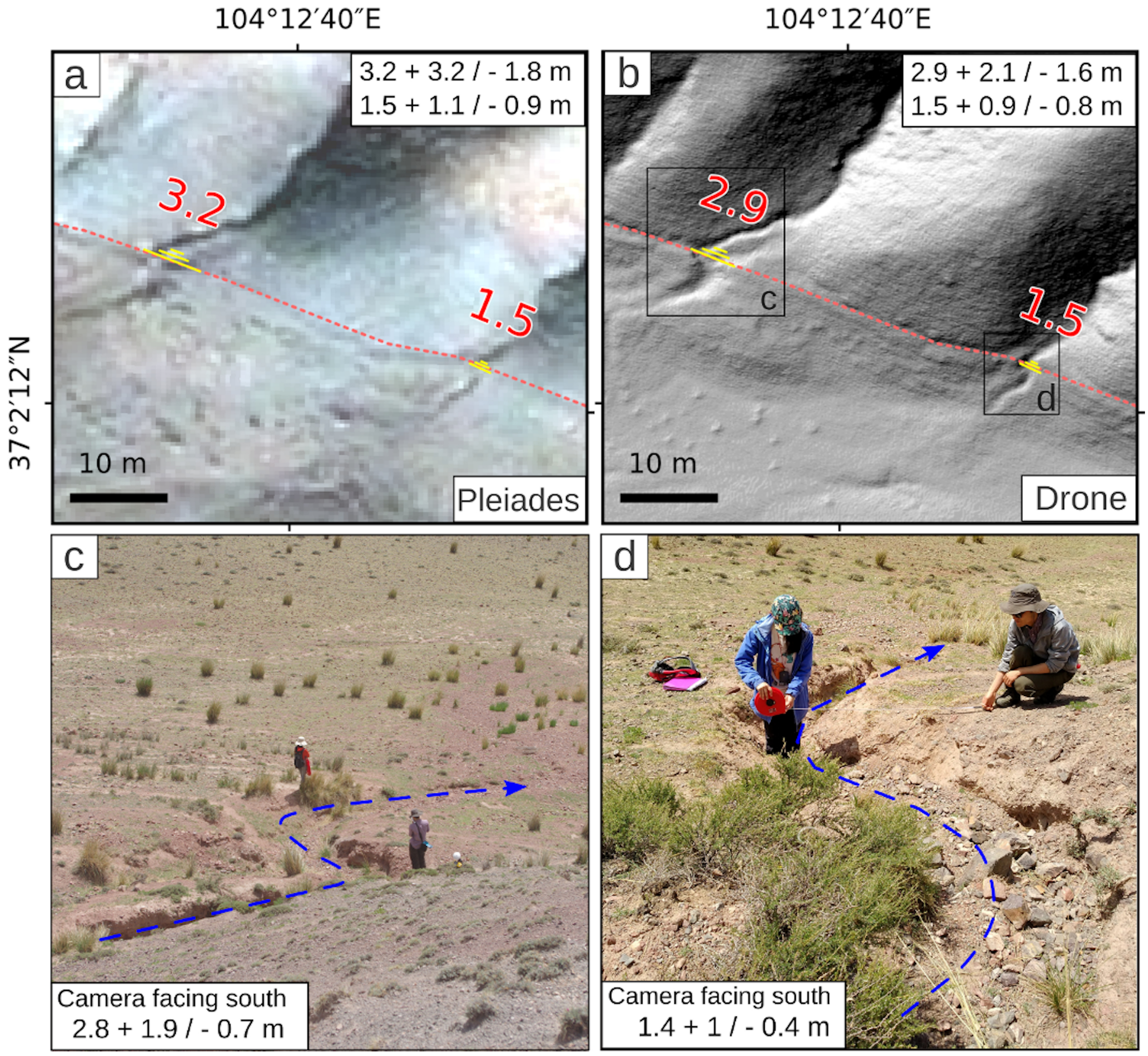

Figure 2.14: (a) Pleiades imagery and (b) shaded DEM derived from drone photos showing two displaced gullies 1 km east of Zhoujia Kiln (see Fig 2.8b and 2.9c). Red dotted line is the mapped fault rupture. The three yellow line segments against each offset stream are the measurements of minimum, best and maximum displacements from the Pleiades and drone DEMs respectively. Numbers in red are the best estimates, which are consistent with the tape measurements shown in (c-d).

2.3.3 Cumulative or Single Event Offsets?

It has been shown that slip variation over 100 m length scales is a real physical phenomena (*Gold et al.*, 2013). Therefore, the only times we can be certain that an offset is cumulative is when there is a smaller offset within 10s of meters from it. Thus, at Baishuihe site (Fig 2.12), we are confident that the offsets of gullies 2, 3 and

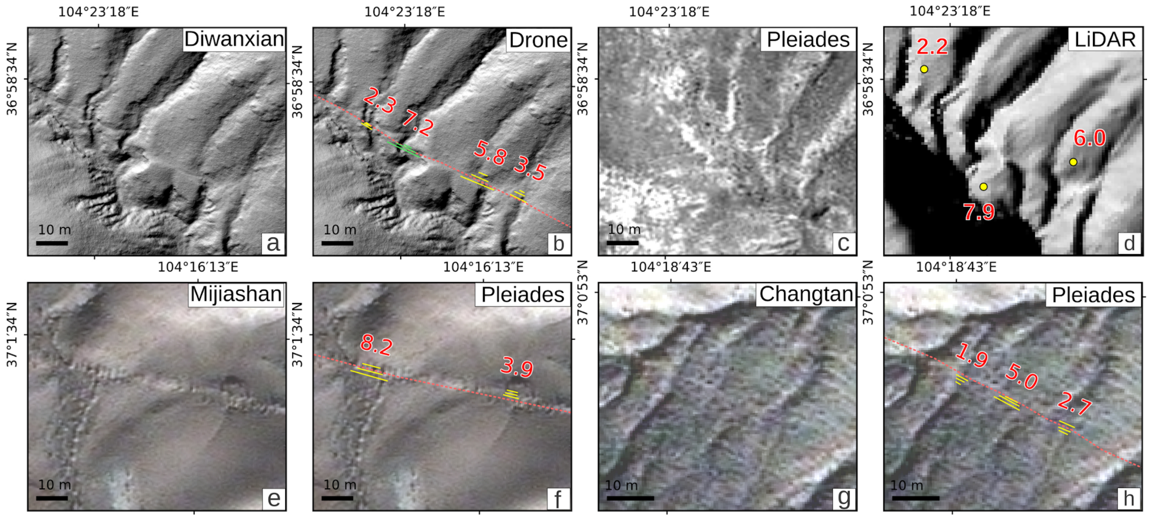

Figure 2.15: Diwanxian site shown in (a-b) ~0.1 m-resolution drone DEM, (c) ~0.7 m-resolution panchromatic Pleiades imagery and (d) ~0.5 m-resolution LiDAR DEM from *Ren et al.* (2016). (e-h) Pleiades imagery showing single event and cumulative offsets at Mijiashan and Changtan sites. See Fig 2.9c for locations.

5 are cumulative and the 3.3 m and 3.4 m from gullies 1 and 4 are likely single-event offsets from the 1920 earthquake. Similarly, at Mijiashan, Changtan and Diwanxian sites in the western section (Fig 2.15a-d), we see small offsets of 2-4 m juxtaposed against 5-9 m offsets, suggesting these larger offsets are cumulative offsets that could be attributed to 1920 and the previous event.

2.3.4 Surface Slip Distribution in the Middle Section

The middle section (Fig 2.10c) is characterised by a 35 km linear trace in the west that connects, through a 1 km wide right-stepping compressional jog, with a 20 km trace that penetrates the Salt Lake pull-apart basin, followed by another 35 km linear section, culminating with a series of en-echelon faults at the eastern end. In the westernmost linear trace, we observed a gentle increase of slip from 2.9 m and 4.3 m at Lijiaping, through 5.7 m at Guansiwan, to 6-7 m at Huadaozi (Fig 2.10d-f, k-m), following the same pattern reported by *Deng et al.* (1986) (Fig 2.10a). The section around the jog is now heavily altered by mining activity, hence we could not verify the scattered offsets measured in the 1980s, but we suspect the cluster of small offsets measured by *Ren et al.* (2016) could be related to the strike-slip-inhibiting effect of the restraining bend. In the Salt Lake basin, a series of field boundaries have been offset by 2-5 m, with the 5 m highlighted in *Ren et al.* (2016) as the best preserved (Fig 2.10a). From the east of the Salt Lake all the way to Dagoumen is classified as the area of maximum shaking intensity during the 1920 earthquake (*IGCEA and NBCEA*, 1990). Along this section, we found the <5 m good quality offsets identified by *Deng et al.* (1986) (Fig 2.10a, g-j) and verified that we could not find smaller offsets within 10s of meters of some 5.4 - 7.1 m offsets highlighted by the grey band in *Ren et al.* (2016) (Fig 2.10a). Therefore, we kept them all as single-event offsets. Further east, the surface rupture becomes less continuous and fractures into en-echelon splays with ∼3.3 m offset as shown in the Baishuihe site (Fig 2.12).

2.3.5 The Eastern Section

Along the eastern section, *Deng et al.* (1986) reported 25 horizontal offsets between 2.7 m and 4 m and one of 7.5 m (Fig 2.16a). The 7.5 m horizontal displacement was near a 1.0 m scarp height whereas two other 3.8 m and 4 m horizontal offsets were near a 0.5 m scarp height. Therefore, we interpret the 7.5 m as a cumulative offset. The average and standard deviation of the other horizontal measurements is 3.5 $\pm$ 0.5 m.

The scarp height measurements were all associated with a southwest dipping scarp on a northeast fault bounding the extensional Laohuyaoxian pull-apart basin. Therefore, they are formed by normal slip in a locally transtensional regime instead of the thrust motion that might be expected for an oblique convergent regime due to the fault bend. The other geomorphic features reported along the eastern section were tension cracks, landslides and southwestern dipping scarps that provide no hard evidence for any thrust motion.

If we were to be conservative in estimating the maximum possible slip on the eastern section, we could calculate the shortening across the fault due to the change of strike, α, of 20°, and hence the potential thrust motion on the fault that would result (Fig 2.16b). First, we can assume the slip vector is conserved between the middle and eastern sections, i.e., $d' = d = 5$ m, the strike-slip component parallel to the eastern section would be $D_{SS} = d' cos(\alpha) = 4.7$ m and the expected shortening across the fault would be $D_{SH} = d' sin(\alpha) = 1.7$ m. Taking a 70° dip on the eastern section (*Duan et al.*, 2018), we get $D_T = 5$ m for the thrust component of the slip, $D_V = 4.7$ m for the vertical displacement and $D = 6.9$ m for the total slip on the eastern section. We note that the expected $D_{SS} = 4.7$ m is larger than the 3.5 ± 0.5 m of horizontal offsets observed in the field (*Deng et al.*, 1986). However, the average magnitude of slip can vary from section to section as it does between the western and middle sections. If we assume that only the slip direction is conserved, but not the slip magnitude, then scaling values by 3.5/4.7 we obtain $D_{SH} = 1.3$ m, $D_T = 3.8$ m, $D_V = 3.6$ m and $D = 5.2$ m.

However, no such significant vertical displacements ($D_V = 4.7$ m or 3.6 m) were documented by *Deng et al.* (1986). A simple explanation could be that the stress field is modified by events on the thrusts around the eastern section at other times. Such partitioning of transpressional or transtensional strain between a main strike-slip and subparallel dip-slip faults have been observed at the Big Bend of the San Andreas Fault (*Daout et al.*, 2016a), the Denali Fault (*Bemis et al.*, 2015) and the Kunlun Fault (*King et al.*, 2005). If it is also the case along this section of the Haiyuan Fault, the slip on the eastern section in 1920 could indeed be purely strike slip.

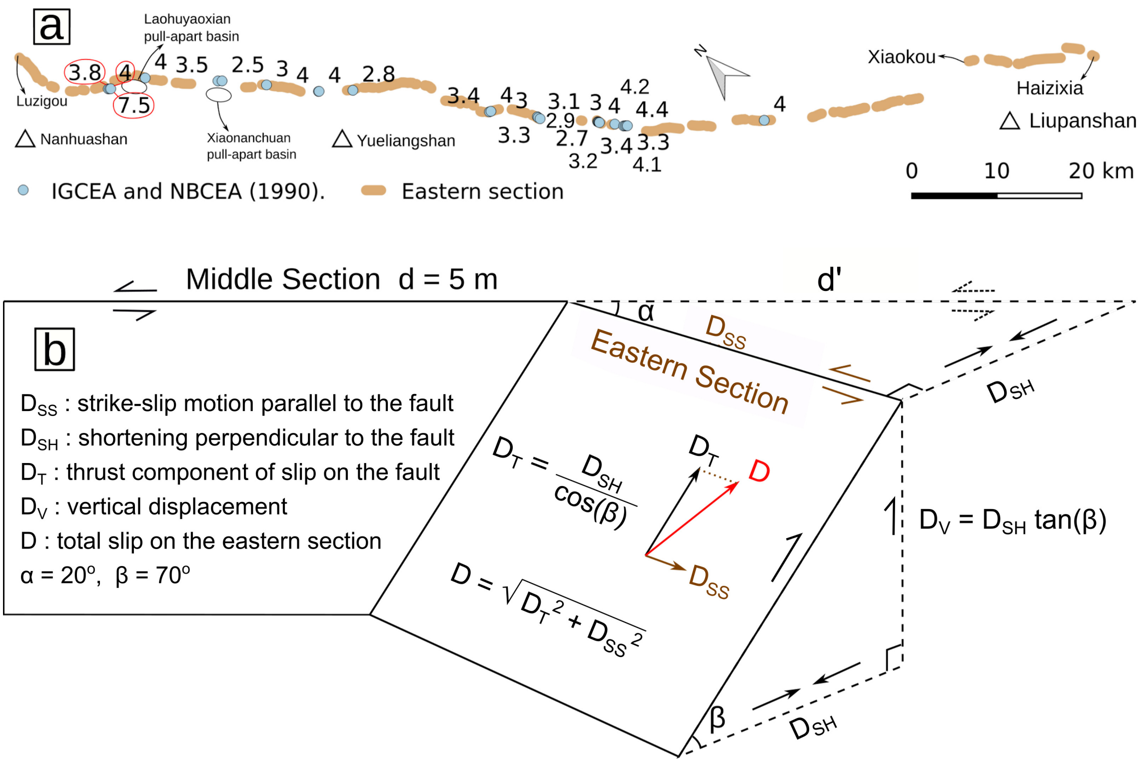

Figure 2.16: (a) Field measurements of horizontal offsets in meters reproduced from *IGCEA and NBCEA* (1990). The 3.8 m, 4 m and 7.5 m offsets, circled in red, are associated with 0.5 m, 0.5 m and 1.0 m vertical scarp heights respectively on the southwest dipping fault of the Laohuyaoxian pull-apart basin. Fault trace is digitised from the 1:50000 geological map of *IGCEA and NBCEA* (1990) and mapped from Google Earth. See Fig 2.2 for location. (b) Sketch showing the geometry used to estimate the expected thrust motion and vertical throw on the eastern section if the slip vector or slip direction was conserved between the middle and eastern sections.

2.3.6 Average Slip and M_W

The moment magnitude, M_W, can be calculated combining the moment release, M_o, from the three sections:

$$M_w = \frac{2}{3}(\log_{10} M_o - 9.1), \text{ where } \quad M_o = \mu DLW \tag{2.7}$$

where μ is the shear modulus of the seismogenic layer, D is the average slip along the fault, L is length of rupture and W is the down-dip width of the rupture (*Aki*, 1966; *Kanamori*, 1977).

To estimate the average slip, D, on each section, we stacked the triangular PDFs from the 284 and 123 offset measurements along the rupture length to obtain the cumulative offset probability density (COPD) of the western and middle section respectively (Fig 2.9b and Fig 2.10b). Assuming the offset population from each event follows a normal distribution, as was observed from, for example, the 1992 Landers earthquake (*Milliner et al.*, 2015), we fit a Gaussian curve to the bottom half of the lowest peak of high quality measurements, following *Klinger et al.* (2011), *Kurtz et al.* (2018), *Zielke et al.* (2010) and *Zielke et al.* (2015). We obtained the means and standard deviations of 3.0 $\pm$ 1.0 m for the western section and 4.5 $\pm$ 1.5 m for the middle section. These results agree with the single-event offsets we determined at Mijiashan (3.9 m), Changtan (1.9 m and 2.7m), Diwanxian (2.3 m and 3.5 m) in the western section and Baishuihe (3.4 m) at the eastern end of the middle section (Fig 2.15a-d and 2.12).

To assess the uncertainties in our offset measurements and their potential impact on the average slip, D, we performed 20 'blind' measurements at each of 8 example sites (two sites in Fig 2.14b and three high-quality (yellow) sites in Fig 2.15b from the western section, and two sites in Fig 2.10p and one site in Fig 2.12e from the middle section)(Fig S1). The measurements were carried out with the feature layer turned off in QGIS such that the line segments drawn to mark the offset lengths (see the yellow lines in Fig 2.14a,b) were invisible. Distances between the thalwegs, left banks and right banks of the streams were measured with the image zoomed to different magnifications. All but one site have the reported thalweg-to-thalweg distances inside the two sigma range from the average of the 20 blind measurements. All but one site have the maximum value of the 20 blind measurements smaller than the reported outer-bank distance and all sites have the minimum value of the 20 blind measurements larger than the reported inner-bank distance (Fig 2.11a). Therefore, our individual PDFs defined in Fig 2.11b cover 99% of the full range of possible measurements. The differences between the averages of 20 blind measurements and our reported thalweg-to-thalweg distances across 8 examples average to 0.1 m, insignificant compared to the 1 m and 1.5 m uncertainties associated with the average slips in the western and middle sections. Newly plotted COPDs based on measurements from *Ren et al.* (2016) and histograms based on measurements from *Deng et al.* (1986) also agree with our reported average slips (Fig S2-S8).

There are also other possible sources of errors due to locally varying dip and strike, channel erosion and scarp degradation that are unaccounted for, but given the steep fault dip and the near 0° rake constrained by our focal mechanism (Fig 2.5), we expect them to be negligible (*Mackenzie and Elliott*, 2017). Such uncertainties might be better assessed and the subjectivity of choosing the "best" marker further reduced in future studies by adopting a mathematical approach on high quality DEMs using a code such as that developed by *Stewart et al.* (2018).

Taking 70 km, 90 km and 77 km as the lengths, L, of each section, a width, W, of 20 km, and a shear modulus μ of 34 GPa based on local velocity profiles (*Chen et al.*, 2017b), we calculate the total M_o and obtain $M_W = 7.8 \pm 0.1$ (Table 2.1). Uncertainty of 2 GPa in μ, 20 km in L, or 1.5 km in W only increases the uncertainty of M_W by 0.02. As the average slip, D, is measured at the ground surface, it might be lower than the slip at depth, thus providing a lower bound on the moment estimate. The hypothetical case considered in Fig 2.16b, with a maximum possible slip of 6.9 m on the eastern section, gives $M_W = 7.9$ even with maximum slip on the western and middle sections. This conservative upper bound value gives us confidence that the moment contributed by this possible, but unproven, scenario will be limited, and its effect on M_W negligible.

Slip/m	Western	Middle	Eastern	M_o/Nm	M_W
Min	2.0	3.0	3.0	4.4E+20	7.69
Average	3.0	4.5	3.5	6.0E+20	7.78
Max	4.0	6.0	4.0	7.7E+20	7.86

Table 2.1: M_o and M_W calculations based on a width of 20 km, lengths of 70 km on the western section, 90 km on the middle section, 77 km on the eastern section, a shear modulus of 34 GPa, and assuming pure strike-slip motion on the eastern section as observed by *Deng et al.* (1986).

2.4 Discussion

2.4.1 Average M_W

For a direct comparison between the different estimates of the magnitude of the 1920 Haiyuan earthquake, we use the orthogonal regression relationships in *Bormann and Saul* (2008) and *Storchak et al.* (2012) to convert our m_B into $M_W = 8.1 \pm 0.4$ and our $M_S(20)$ into $M_W = 8.0 \pm 0.2$ (Table 2.2). As such, the M_W values in this study, including those from direct waveform modelling, those derived from measured offsets along the fault and M_S and m_B converted results, are all consistent within error. A simple average of the four M_W values give $M_W = 7.95 \pm 0.2$. If taking into account the uncertainties and excluding the $M_W = 8.0 \pm 0.2$ from $M_S(20)$, which is estimated from only 3 data points, the weighted average would be M_W 7.87 $\pm$ 0.2.

Our reestimated moment magnitude M_W 7.9 $\pm$ 0.2 agrees with the $M_W = 8$ estimated by *Deng et al.* (1984) using M_o derived from spectral densities first published by *Chen and Molnar* (1977). *Chen and Molnar* (1977) initially obtained M_W 8.3 instead of M_W 8.0 because they modelled the earthquake using a dip of 45° and a rake of -45°. However, as our focal mechanism inversion shows, this earthquake happened on a predominantly vertical fault plane and slipped with a rake close to 0°. Therefore, M_W 8.3, the current value in the ISC-GEM (*ISC*, 2019) and Centennial catalogue (*Engdahl and Villaseñor*, 2002), both based on *Chen and Molnar* (1977), is likely to be overestimated.

	This study	Equivalent M_W
Body wave magnitude (2-20s)	$m_B = 7.9 \pm 0.3$	$8.1 \pm 0.4^{*}$
Surface wave magnitude (∼20s)	$M_S(20) = 8.1 \pm 0.2$	$8.0 \pm 0.2^{**}$
Body wave modelling	$M_W = 7.9 \pm 0.2$	
Geomorphology	$M_W = 7.8 \pm 0.1$	
Mean of the best estimates:		$M_W = 7.95 \pm 0.2$
Mean inversely weighted by uncertainty:		$M_W = 7.90 \pm 0.2$
Weighted mean without $M_S(20)$:***		$M_W = 7.87 \pm 0.2$

* $M_W = 1.33 \times m_B - 2.36$ (Bormann and Saul , 2008)

** $M_W = exp(-0.22 + 0.23 \times M_S) + 2.86$ (Storchak et al.,2012)

*** $M_S(20)$ is determined by only 3 data points (Fig 2.7b).

Table 2.2: Summary of M_W estimates from this study and the equivalent M_W converted m_B and $M_S(20)$ using orthogonal regression relationships derived by *Bormann and Saul* (2008) and *Storchak et al.* (2012).

The moment magnitude M_W 7.9 and the rupture length of 230 km fit the scaling relationship for strike-slip earthquakes in *Wells and Coppersmith* (1994). With M_W 7.9, the 1920 Haiyuan earthquake is similar in magnitude to the 2001 M_W 7.8 Kokoxili earthquake (*Klinger et al.*, 2005; *Lasserre et al.*, 2005) and the 2008 M_W 7.9 Wenchuan earthquake (*Lin et al.*, 2009; *Liu-Zeng et al.*, 2009; *Xu et al.*, 2009) that also occurred within or on the boundary of the Tibetan Plateau.

2.4.2 m, m_B and M_W

Our m_B average from global records corroborates the m 7.9 determined by *Richter* (1958) using Pasadena records and supports our understanding that m_B and m are equivalent.

The regression relationship $M_W = 1.33 \times m_B - 2.36$ is associated with a standard deviation of $\sigma = \pm 0.18$ (*Bormann and Saul*, 2008), reflecting the scatter in the original catalogues. Considering the ∼0.2 uncertainty, the m_B-converted $M_W = 8.1 \pm 0.4$ is not inconsistent with the $M_W = 7.9 \pm 0.2$ from body wave modelling. This is reassuring as the moment magnitude was originally designed to scale well with m_B (*Kanamori*, 1977) and m_B later proved to be a good estimator of M_W (*Bormann and Saul*, 2008).

2.4.3 M_S and M

There are two IASPEI standards of M_S, a narrow-band $M_S(20)$ with period 20 $\pm$ 2 s, which we used, and a broad-band $M_S(BB)$ with periods 3–60 s (*Bormann et al.*, 2009; *Storchak et al.*, 2012). ISC recently obtained a broad-band surface wave magnitude $M_S(BB) = 8.06 \pm 0.11$ for this earthquake using amplitudes and periods reported in 9 station bulletins (*Di Giacomo*, 2020). The regression relationship $M_W = exp(-0.22 + 0.23 \times M_S) + 2.86$, derived for the median of all reported $M_S(20)$ and $M_S(BB)$ values for each event (*Storchak et al.*, 2012), converts $M_S(BB) = 8.06$ into $M_W = 7.98$, consistent with our $M_S(20)$ and M_W estimates.

Both our $M_S(20) = 8.1 \pm 0.2$ and ISC's $M_S(BB) = 8.06 \pm 0.11$ are lower in value than Gutenberg and Richter's M 8.5, suggesting these modern M_S and Gutenberg and Richter's M are not equivalent. In fact, *Abe* (1981) found that the original M is systematically larger than his reworked M_S by an average of 0.2 units, and in extreme cases, 0.9 units. This overestimation was most likely because Gutenberg vectorially combined the highest amplitudes of the N-S and E-W components which might not have occurred at the same time (*Bormann*, 2012; *Geller and Kanamori*, 1977).

2.4.4 M and M_W

A regression relationship between M and M_W has not been developed. Nevertheless, *Richter* (1958) introduced the relationship $m = 2.5 + 0.63M$ which would convert an M value of 8.6 to an m value of 7.9, the same as our m_B value as discussed above. Thus, when dealing with M of large shallow earthquakes between 1904 and 1952, it would be advisable to first convert M into m (m_B) which would then be comparable to M_W as discussed in Section 2.4.2.

In addition, values of M in some historical catalogues were assigned based on intensity of shaking. For example, *Gu* (1983) assigned the Haiyuan earthquake $M8\frac{1}{2}$ based on $I_\circ$ = XII. This conversion was made using the relationship $M = 0.58I_\circ + 1.5$ derived by *Li* (1960) using 35 Chinese earthquakes with both intensity ratings and magnitudes. In 1960, the only available magnitudes were Richter's local magnitude M_L and Gutenberg and Richter's M and m. The similarity between the M derived from intensities and the M obtained by Gutenberg for the Haiyuan earthquake suggests that the $M - I$ formula was likely based on Gutenberg and Richter's M, and the $M8\frac{1}{2}$ should, therefore, be converted to m in order to get the equivalent M_W.

2.4.5 Epicentre, Intensity and Surface Slip Distribution

Our relocated epicentres based on the 1-degree Crust 1.0 velocity model converge on the town of Haiyuan. The answer is stable whether we use the waveforms only, the bulletins only or these two data sets combined. With the large number of stations in Europe and Japan, the epicentre is better constrained along strike than perpendicular to strike. Therefore, we believe a location at this longitude is more accurate than those reported in previous catalogues.

Earthquakes have been observed to nucleate and terminate near geometrical discontinuities (compressional or extensional jogs, triple junctions and fault bend) (*King and Nábělek*, 1985). This phenomenon is observed for the 1976 Tangshan earthquake (*King and Nábělek*, 1985), the 1995 Tianzhu earthquake (*Lasserre et al.*, 2001) and the 2001 Kokoxili earthquake (*Klinger et al.*, 2005). The co-location of our epicentre and the junction between the middle section and the eastern splay (Fig 2.2) also supports this theory. We infer that the geometrical triple junction and the transition between the strike-slip and the transpression regimes could have concentrated stress near Haiyuan before the 1920 earthquake started (*Aki*, 1979; *King and Nábělek*, 1985).

As many 4–6 m offsets measured on the western section are actually cumulative, the average offset on the western section is only 3 ± 1 m, smaller than the 4.5 ± 1.5 m on the middle section and the 3.5 ± 0.5 m on the eastern section. Therefore, the surface slip distribution we obtained also correlates with the shape of the intensity contours which is narrower in the west and wider in the east (Fig 2.2).

2.5 Conclusion

Using digitised analogue seismograms, we have relocated the 1920 epicentre to 105.540E, 36.481N near Haiyuan, resolved the focal mechanism to be predominantly strike-slip on a vertical plane, and modelled the body waves to obtain $M_W = 7.9 \pm 0.2$. From horizontal offsets measured from the orthorectified Pleiades satellite imagery and DEM derived from aerial drone photos acquired by a quad-copter, we estimated $M_W = 7.8 \pm 0.1$ using the average slip and length of the rupture.

We also measured the phase amplitudes and periods of the waveforms to obtain broadband body wave magnitude $m_B = 7.9 \pm 0.3$ and the IASPEI standard surface wave magnitude $M_S(20) = 8.1 \pm 0.2$. The m_B is equal to the m and m_B previously reported by *Gutenberg and Richter* (1954) and *Abe* (1981). Converting m_B and M into M_W and averaging the best estimates from all four approaches, we constrain the magnitude of the 1920 Haiyuan earthquake to be $M_W = 7.9 \pm 0.2$, consistent within the uncertainty with the M_W 8.0 published by *Deng et al.* (1984). The $M_S(20)$ is smaller than the original M 8.5 by *Gutenberg and Richter* (1941), suggesting Gutenberg's definition of M is not compatible with that of the modern M_S and overestimates the size of earthquakes.

M reported based on intensity of shaking could be over-estimated as well, as in the case of the Haiyuan earthquake, the relationship was derived from Gutenberg's surface wave magnitude M (*Li*, 1960; *Gu*, 1983). Nevertheless, M can be converted into m using the relation given by *Gutenberg and Richter* (1956) and *Bormann and Saul* (2008). The m scale is later known as m_B and is a good proxy for the moment magnitude M_W within an uncertainty of $\sim \pm\, 0.2$ (*Bormann et al.*, 2013; *Kanamori*, 1977).

Chapter 3

Large-Scale InSAR Processing over the NE Tibetan Plateau

3.1 Introduction

Not only home to the deadly 1920 Haiyuan Earthquake, the tectonically active NE Tibetan Plateau has hosted over 20 large earthquakes with recorded magnitudes greater than 6.5 in the last century (Fig 3.1a), making it one of the most seismic prone regions in China. These earthquakes are either strike-slip events that occur on the major left-lateral strike-slip Haiyuan, Altyn Tagh and Kunlun Faults (e.g. *Deng et al.*, 1984; *Klinger et al.*, 2005), or thrust events in the convergent Qilianshan mountain range and the North Qaidam thrusts (e.g. *Liu et al.*, 2018; *Daout et al.*, 2019). Together, they release elastic strain being accumulated as the area deforms due to the tectonic forces associated with the collision of India with Eurasia that began ∼59 million years ago (*Hu et al.*, 2016).

Between the large active faults lives a thriving civilisation with the history of Silk Road and Hexi Corridor going back over 2000 years. Today, in between and around the mountains stand major cities of Lanzhou, Zhongwei, Wuwei, Zhangye, Jiuquan, Xining and Haidong, all with populations of the order of millions. Their presence makes seismic hazard assessment in the NE Tibetan Plateau particularly important.

Given the distributed nature of faulting in the continental interior, seismic hazard assessment will not only benefit from focused studies on the major faults, but also, and more importantly, from regional velocity and strain rate maps. Such velocity and strain rate maps can reveal previously unknown active faults (*Wicks et al.*, 2013), highlight regions of the fastest strain concentration (*Bird and Kreemer*, 2015; *Wang and Shen*, 2020), identify faults that are creeping at the surface (*Cavalié et al.*, 2008; *Jolivet et al.*, 2012), constrain the kinematics and frictional properties of faults (*Jolivet et al.*, 2013, 2015), and help discriminate between competing dynamic models (*Elliott et al.*, 2016). Geodetic tools, such as Global Navigation Satellite System (GNSS) and Interferometric Synthetic-Aperture Radar (InSAR), provide the ground deformation measurements from which fault slip rates and locking depths as well as regional velocity fields and strain rate maps can be derived.

The NE Tibetan Plateau is covered by a dense Global Navigation Satellite System (GNSS) network initially established in the late 1990s (Fig 3.1a) thanks to the Crustal Movement Observation Network of China (CMONOC) project (*Niu et al.*, 2005; *Gan et al.*, 2012). However, most of the GNSS sites are campaign stations that were surveyed only once every two years. After two decades of measurements, the accuracy of the horizontal velocities has reached 0.2 mm/yr (*Wang and Shen*, 2020) while the accuracy of the vertical velocity is ∼1.5 mm/yr (*Liang et al.*, 2013). Moreover, the long time interval between the GNSS campaigns means the data may not be able to capture transient motion such as the episodic creep observed by InSAR on the Laohushan section of the Haiyuan Fault (*Jolivet et al.*, 2015). Furthermore, GNSS are point measurements which, despite the already dense network, cannot effectively constraint over localised velocity variations near faults, which may help explain discrepancies between locking depths inverted from GNSS and InSAR data (e.g., *Jolivet et al.* (2012) and *Li et al.* (2016d)).

InSAR, on the other hand, has the advantages of wider and denser spatial coverage and more frequent data acquisition compared to the campaign GNSS data in the area. Previous InSAR studies covering the NE Tibetan Plateau have focused on deformation along the Haiyuan Fault, especially along the creeping section (*Cavalié et al.*, 2008; *Jolivet et al.*, 2012; *Daout et al.*, 2016b; *Song et al.*, 2019). Apart from *Jolivet et al.* (2012), which used data from both ascending (with sporadic acquisitions) and descending tracks, all other previous studies only used descending tracks. This is a combined result of the infrequent data acquisitions along the ascending tracks by the previous generation of satellites with free data (e.g., ERS and ENVISAT), and the steep prices of imagery provided by commercial satellites. In addition, earlier data processing techniques, where long strips of data were merged and processed together (*Wright et al.*, 2004; *Elliott et al.*, 2008; *Wang and Wright*, 2012; *Garthwaite et al.*, 2013; *Hussain et al.*, 2018), put strain on computing power, prohibiting routine large-scale processing for regional velocity and strain rate mapping.

After the launch of the constellation of Sentinel-1A and Sentinel-1B satellites by ESA in April 2014 and April 2016, respectively, the NE Tibetan Plateau has been imaged once every 24 days by each satellite, and from 2017 onwards, once every 12 days. This revisit time is shorter than the earlier Envisat and ERS satellites, which had a nominal revisit time of 35 days but often gaps of more than a few years are present in the time series. The Sentinel-1 satellites also acquire images over a larger area ($\sim 250 \times 250$ km^2 frames) at a higher resolution (5×20 m^2), which makes data processing more efficient for regional observation projects. The routine data acquisition along both the ascending and descending tracks enables the east and vertical velocities to be extracted from the two line-of-sight (LOS) directions, thus providing additional constraints for kinematic models.

With the computing power provided by the JASMIN servers, the Near Line

Archive (NLA) storage capacity, and the development of the Looking Into Continents from Space with Synthetic Aperture Radar (LiCSAR) automatic processing system (*Lazecký et al.*, 2020), it is now possible to process the large amount of data required for regional velocity and strain rate mapping (*Morishita et al.*, 2020; *Weiss et al.*, 2020). In the work detailed in Chapters 3–5, I process 5 years of Sentinel InSAR data over an area of 661322 km^2 to derive times series and velocity maps that reveal slip rates on various active faults and enhance our understanding of the distribution of interseismic strain accumulation in the NE Tibetan Plateau. The resultant velocity and strain rate maps will be the largest and highest resolution (100 m) to date for the NE Tibetan Plateau.

In this chapter, section 3.2 introduces InSAR principles including the latest processing techinques. Section 3.3 describes the Sentinel-1 data. Section 3.4 describes interferogram (IFG) creation with LiCSAR (section 3.4.1), atmospheric corrections with the Generic Atmospheric Correction Online Service (GACOS) (section 3.4.2), a network approach to ramp removal (section 3.4.3), data cleaning (section 3.4.4) and time series inversion using the New Small Baselines Subset (NSBAS) method (section 3.4.5). A new approach to frame-merging and velocity decomposition is presented in Chapter 4. The resultant strain rate maps and their implications on seismic hazard are discussed in Chapter 5.

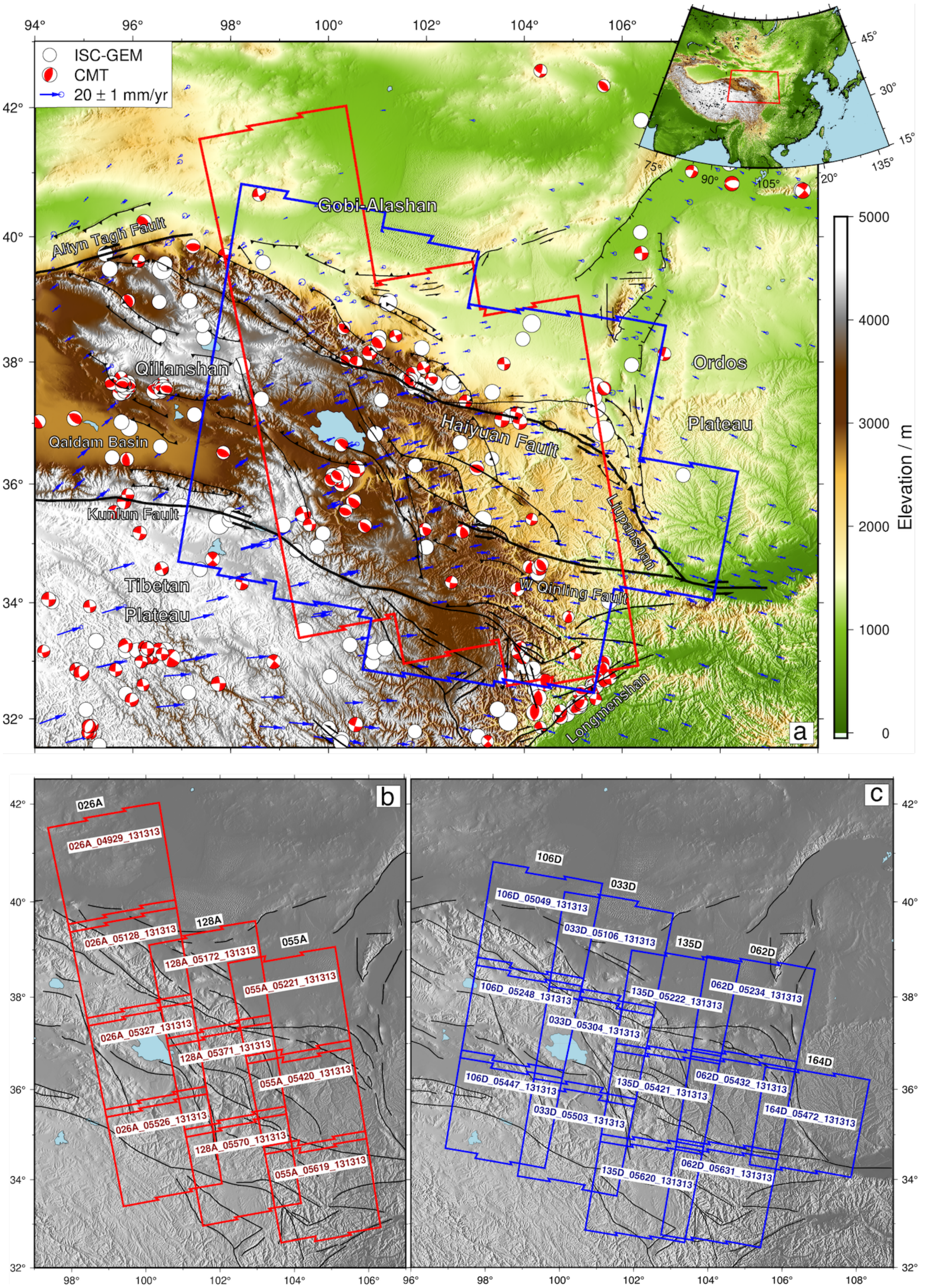

Figure 3.1: (a) Tectonic map of the NE Tibet with seismicity from ISC-GEM and CMT catalogues and GNSS velocities from *Wang and Shen* (2020). Red and blue polygons are the outlines of areas covered by ascending and descending Sentinel-1 InSAR frames, respectively. (b) Map of ascending frames. (c) Map of descending frames.

3.2 The InSAR Technique

As a synthetic aperture radar (SAR) bearing satellite travels around the Earth in a near-polar sun-synchronous orbit, its right-looking antenna sends a beam of electromagnetic radiation with a wavelength of a few centimetres to the Earth's surface and the phase and intensity of the returning pulse are recorded (Fig 3.2a). After repeated measurements at the same location over multiple orbiting cycles, the phase differences between any two acquisitions form an interferogram (IFG) which is wrapped over a cycle of 2π (Fig 3.2b). The wrapped phase differences across the IFGs can be unwrapped to form a continuous phase difference map, ϕ, with respect to a reference point of choice (Fig 3.2c). A correctly unwrapped IFG between two epochs should form a closed phase loop with two other IFGs made between these two epochs, A and B, and a third epoch, C, respectively, such that $\phi_{AB} + \phi_{BC} = \phi_{AC}$ (Fig 3.2d). By inverting the IFG network in Fig 3.2d for the incremental displacement over time and reconstructing the synthetic IFGs with the obtained phase increments, any unwrapping mistakes can be detected as step changes of multiples of 2π in the residual maps between the input and the reconstructed IFGs. After removing or correcting the IFGs with unwrapping mistakes, incremental and cumulative phase changes can be inverted from the network of IFGs and temporal functions (e.g. linear, logarithmic, etc.) can be fitted through the cumulative displacements to obtain the velocities of interest (Fig 3.2e).

Whether the surface velocity can be measured by InSAR or not depends on the signal-to-noise ratio of the time series data. The phase difference measured by each IFG can be regarded as the sum of the following components:

$$\phi = \phi_{def} + \phi_{orb} + \phi_{atm} + \phi_{DEM} + \phi_{bias} + \phi_{others} \tag{3.1}$$

where ϕ_{def} is the phase change due to movement of the crustal surface, ϕ_{orb} is

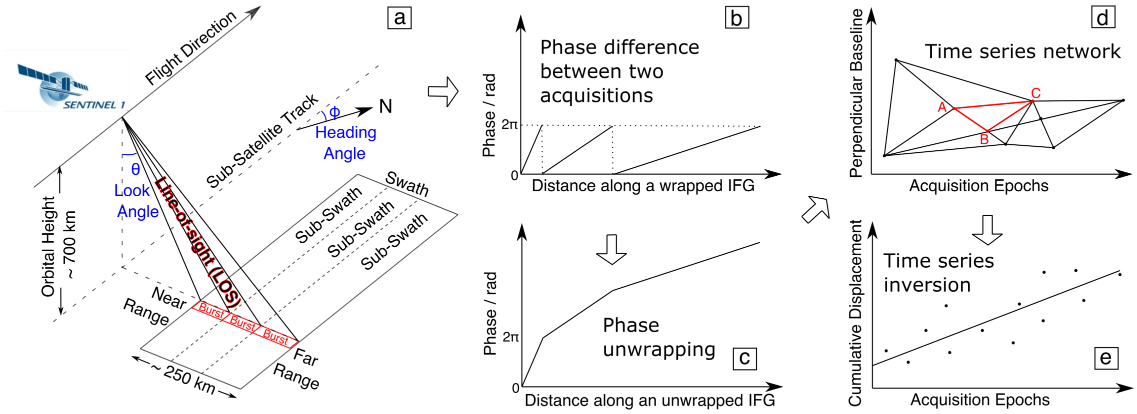

Figure 3.2: A cartoon illustrating the principle of the InSAR technique, modified from (*Massonnet and Souyris*, 2008). (a) Sketch of data acquisition by a synthetic aperture radar bearing satellite. (b) Schematic phase profile across a wrapped interferogram (IFG). (c) Schematic phase profile across a corretly unwrapped IFG. (d) A network of IFGs generated between acquisition epochs for time series inversion. The red triangle between epochs A, B and C serves as an example of a phase closure loop where it is expected that $\phi_{AB} + \phi_{BC} = \phi_{AC}$. (e) Fitting a temporal function (e.g., linear function) through the inverted cumulative displacement to obtain the velocity.

the residual phase from the inaccuracy of the satellite orbits, ϕ_{atm} is related to the phase delays resulted from the radar wave passing through the troposphere and the ionosphere, ϕ_{DEM} is the residual phase from inaccuracies of the DEM, (*Cavalié et al.*, 2008; *Hooper et al.*, 2004; *Elliott et al.*, 2016; *Yu et al.*, 2017; *Murray et al.*, 2019). ϕ_{bias} is a systematic bias introduced by multi-looked short temporal baseline IFGs (*Ansari et al.*, 2020), potentially due to high-frequency variations of the ground surface properties from vegetation growth, rain and snow. ϕ_{others} includes noise from all other sources such as unmodelled turbulent atmospheric delay, instrumental noise, decorrelation and unwrapping errors.

For Sentinel-1, good orbital control ensures that the satellites mostly travel within a 50 m radius tube which significantly reduces interferomatric decorrelation due to long perpendicular baselines, a problem that often affected InSAR data acquired by older-generation satellites. The small perpendicular baseline of the Sentinel-1 satellites also means the ϕ_{orb} and ϕ_{DEM}, which scale with the perpendicular baseline, are reduced accordingly (*Ducret et al.*, 2013). The bias from short temporal baseline

IFGs can be mitigated by introducing additional longer basline IFGs in the time series inversion (*Ansari et al.*, 2020; *Daout et al.*, 2020). In comparison to the L-band (24 cm) satellite data, the short wavelength (5.6 cm) of the C-band satellite makes the Sentinel-1 data relatively insensitive to the electron content of the ionosphere (*Bekaert et al.*, 2015). As a result, for short temporal baseline Sentinel IFGs over slowly deforming areas, the phase signals are often dominated by the wavelength-independent tropospheric delay, making it the most important component to try and remove in order to resolve the slow interseismic tectonic signals (*Elliott et al.*, 2016).

The tropospheric delay is composed of a stratified component that is correlated with topography and varies with seasonality and a turbulent component that is random in space and time (*Hanssen*, 2001). The stratified component can be further separated into a hydrostatic dry component that is related to temperature and dry air partial pressure, and a wet component that is related to temperature and the water vapour pressure (*Doin et al.*, 2009). Methods for correcting the tropospheric delays have evolved over the years from direct stacking of IFGs (*Wright et al.*, 2001) and time series methods (*Zebker et al.*, 1997; *Ferretti et al.*, 2001; *Hooper et al.*, 2004), to empirical correction based on phase-topography relationships (*Wicks et al.*, 2002; *Cavalié et al.*, 2007; *Elliott et al.*, 2008; *Bekaert et al.*, 2015), to using auxiliary data such as GNSS and meteorological models (*Onn and Zebker*, 2006; *Jolivet et al.*, 2011; *Walters et al.*, 2013; *Shen et al.*, 2019). The stacking method can effectively remove the turbulent component, but the resultant velocity may be biased by the stratified component which is not random (*Doin et al.*, 2009). Empirical correction based on a linear relationship between IFG phase and topography removes the stratified component, but may also remove topographically correlated tectonic signals (*Daout et al.*, 2018; *Shen et al.*, 2019). Power-law correction works on deforming regions but requires prior knowledge of the scale of deformation for selecting a spatial band uncontaminated by tectonic signals for parameter estimation (*Bekaert et al.*, 2015).

Continuous GNSS zenith delay measurements capture both the stratified and turbulent delays but the spatial resolution is limited by the distribution of stations (*Yu et al.*, 2017). Spectroradiometer and spectrometer data such as the Moderate Resolution Imaging Spectroradiometer (MODIS) by National Aeronautics and Space Administration and the Medium Resolution Imaging Spectrometer (MERIS) by European Space Agency are restricted to daytime and cloud-free conditions and they only detect the water vapour content and do not provide estimates of the hydrostatic dry delays (*Yu et al.*, 2018a; *Murray et al.*, 2019). The GACOS model (*Yu et al.*, 2017, 2018a,b), which uses the operational high-resolution European Centre for Medium-Range Weather Forecasts (HRES-ECMWF) weather model (*Dee et al.*, 2011, 2014), offers global coverage at $0.125° \times 0.125°$ horizontal resolution and availability under all time and weather conditions. GACOS corrections have been successfully applied to Sentinel-1 data by *Morishita et al.* (2020) and *Weiss et al.* (2020) to reduce the IFG standard deviations and differences with GNSS velocities by 20–30% in the studies of Japan and Turkey. *Murray et al.* (2019) and *Maubant et al.* (2020) find GACOS produces better correction results compared to other models, GNSS, water vapour data and empirical methods in the cases of the Central United States and Mexico. Therefore, the GACOS model can be considered as the state-of-the-art for atmospheric correction.

3.3 Data

In total, I processed 10 ascending frames and 13 descending frames of Sentinel-1A and -1B level-1 Single Look Complex (SLC) products acquired between October 2014 and December 2019 (Fig 3.1b,c) to generate 12480 IFGs (Fig 3.3). The temporal baselines between consecutive acquisitions are 24 days before November 2016 and 12 days afterwards. On average, 95 epochs are available for each frame over a span of 4.6 years (Fig 3.3). Statistical reduction of noise implies the uncertainty of the interseismic velocities derived from time series data, σ_v, is expected to follow:

$$\sigma_v = \frac{2\sqrt{3}\sigma_e}{N^{0.5}T} \tag{3.2}$$

where σ_e is the uncertainty of measured displacement per epoch, N is the number of epochs and T is the time span in years (*Zhang et al.*, 1997). Assuming a similar σ_e of ∼10 mm as in *Morishita et al.* (2020), based on the comparison between InSAR and GNSS time series data, the amount of data I processed would theoretically give an uncertainty, σ_v, of 0.77 mm/yr in the final velocity maps.

The Sentinel-1 data were mirrored from Copernicus SciHub to the Centre for Environmental Data Analysis (CEDA) Sentinel Mirror Archive (SMA) offered by the JASMIN infrastructure (*Lazecký et al.*, 2020). Data older than three months are stored in the Near Line Archive system (NLA) and were transferred to the CEDA archive before all SAR acquisitions from 2014 to 2019 are processed on a frame-by-frame basis.

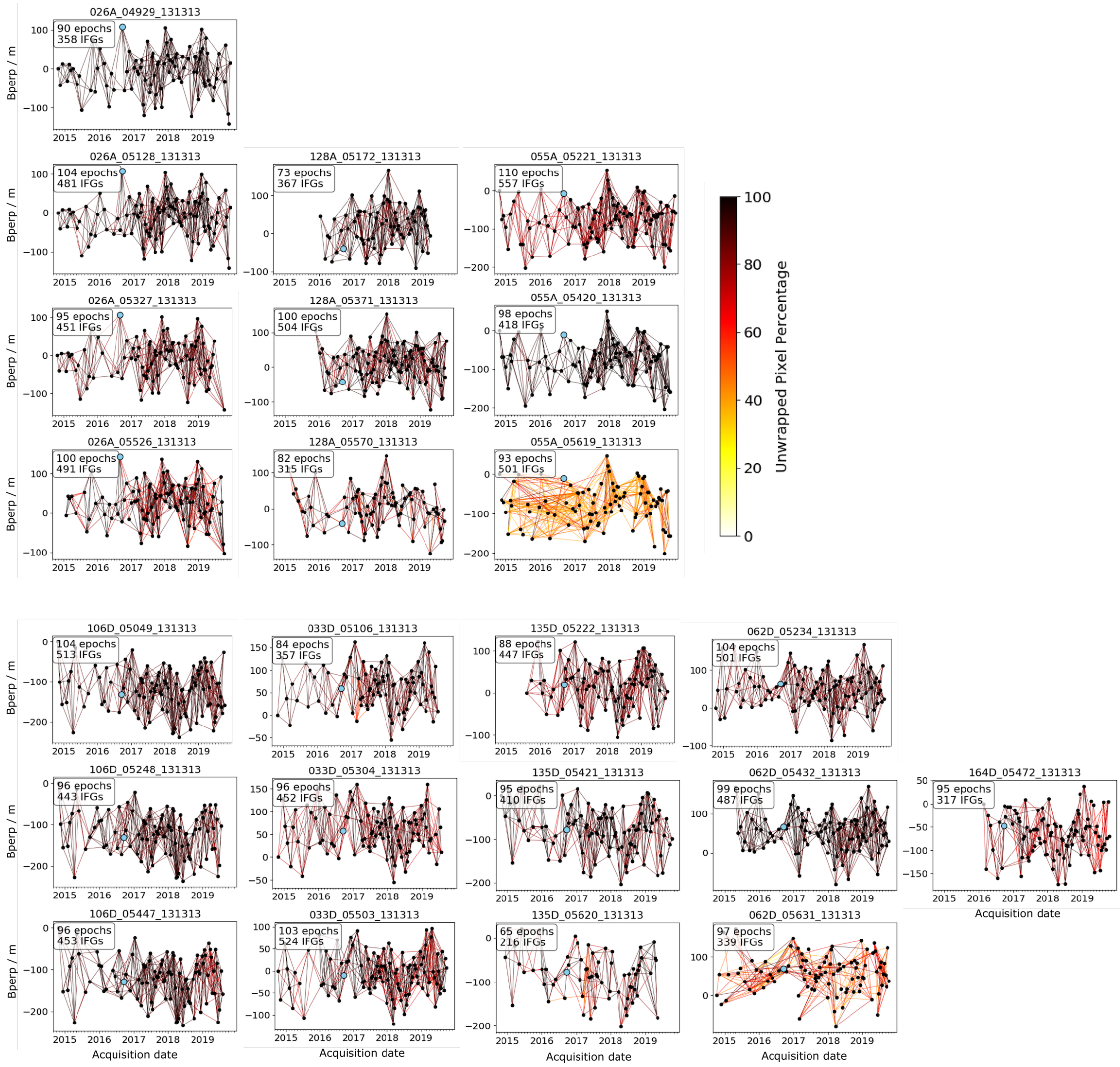

Figure 3.3: Perpendicular baseline plots for the final time series of each frame. Black dots represent all the acquisition dates with their perpendicular baseline. Blue dot in each frame represents the primary epoch to which imagery from other epochs are coregistered. Each line segment represents an interferogram (IFG) between two acquisition dates with a colour scale representing the percentage of pixels unwrapped out of all pixels in the frame.

3.4 Method

The procedure of InSAR data processing is illustrated in Fig 3.4 and involves generation of coherence files and unwrapped IFGs from Sentinel-1 Single Look Complex (SLC) data using the LiCSAR batch processing chain (*Lazecký et al.*, 2020) followed by atmospheric correction, ramp removal and time series inversion using NSBAS

(*Doin et al.*, 2011, 2015) and programs from the commercial software, GAMMA (*Wegnüller et al.*, 2016).

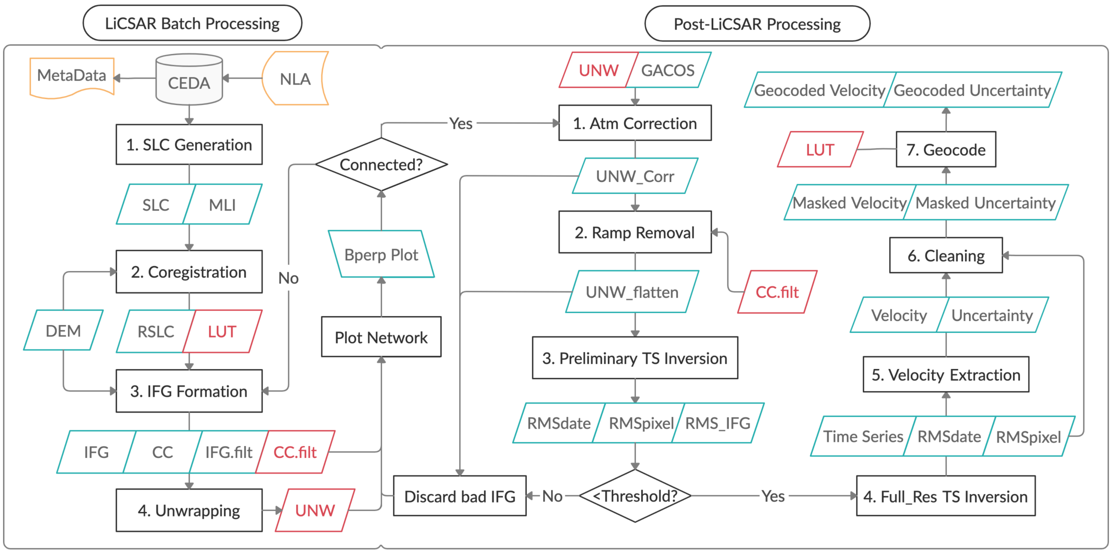

Figure 3.4: Summary of the InSAR processing workflow which begins with requesting Sentinel-1 data from the Near Line Archive (NLA) to the Centre for Environmental Data Analysis (CEDA) archive. It is followed by the LiCSAR processing chain which generates Single Look Complex (SLC) and Multilooked Intensity raster (MLI), coregisters the SLCs to the geometry of a single primary SLC to compute the look-up tables (LUT) and generate resampled SLCs (RSLCs). The RSLCs are paired to make interferograms (IFG) and coherence (CC) files with the topographic phase removed based on the digital elevation model (DEM). The unwrapped IFGs (UNW) are then produced from the filtered IFG and CC files. Once the network is checked to be complete, post-LiCSAR processing steps including atmospheric (Atm) correction, ramp removal, time series (TS) inversions are performed to extract velocities and associated uncertainties, which are cleaned and geocoded into the final map products.

3.4.1 LiCSAR processing

The IFGs were generated with the LiCSAR automatic processing package (*Lazecký et al.*, 2020). LiCSAR performs tasks from data unpacking, burst stitching, multi-looking, coregistration, IFG generation, filtering, phase unwrapping and geocoding in parallel batch jobs. The LiCSAR outputs I used for post-processing include filtered unwrapped IFGs and filtered coherence maps both in radar coordinates, a parameter file containing the primary multilooked intensity data (MLI), heading and incidence, angles, as well as refined look-up tables (LUT).

The batch LiCSAR processing jobs can fail at various stages due to errors associated with individual single look complex (SLC), resampled SLCs (RSLCs), raw and filtered IFGs. A good way of checking for data quality and completeness was to plot the perpendicular baselines (Bperp) such as those shown in Fig 3.3. If significant numbers of IFGs were not generated, the Bperp plots appear patchy and disconnected. In this case, the gaps are filled by creating additional interferograms until the Bperp plots are well connected. By default, LiCSAR generates IFGs between each epoch and three consecutive epochs both forwards and backwards in time. I changed the limit to six consecutive epochs to create redundancy and added IFGs with six-month and nine-month temporal baselines to provide further connections in order to reduce the impact of the potential bias from the short temporal baseline IFGs (*Ansari et al.*, 2020; *Daout et al.*, 2020).

After filtering the IFGs and their coherence files, LiCSAR only retains pixels with filtered coherence higher than 0.5 (*Lazecký et al.*, 2020). The colour of the Bperp plots represents the percentage of all pixels in the frame unwrapped (Fig 3.3). The 23 frames I processed have on average 86% pixels unwrapped, as expected from the high coherence of the data aided by the stable orbital control and short temporal baselines. The three frames with lower unwrapping percentages are frame 055A_05221_131313 which covers an unconsolidated desert, and frames 055A_05619_131313 and 062D_05631_131313 that suffer from the dense vegetation and tectonic complexity to the south of the West Qinling Fault and towards the east end of the East Kunlun Fault (Fig 3.1).

3.4.2 Atmospheric correction

Following *Morishita et al.* (2020) and *Weiss et al.* (2020), I use GACOS models for atmospheric correction. When GNSS data are available, GACOS incorporates estimated zenith total tropospheric delays (ZTD) from both the HRES-ECMWF weather model and GNSS. In the case of NE Tibetan Plateau, where GNSS ZTD data are not openly available, the GACOS model is just the ZTDs calculated from modelled HRES-ECMWF products (i.e., surface pressure, temperature and specific humidity), resulting in the correction of the stratified delays only (*Yu et al.*, 2018b).

The GACOS models are delivered in geographic coordinates and in unit of meters. In order to be applied to the IFGs, I first converted the GACOS data to radians and transformed the data into radar coordinates using the LUTs from LiCSAR. Then, I projected the ZTD to LOS phase delays using the incidence angles of the IFGs, and calculated the differences between phase delays from the same pairs of epochs as those making up the IFGs to generate the corresponding GACOS corrections. Finally, I set both the GACOS corrections and IFGs to the same zero reference area and subtracted the GACOS corrections from the IFGs to obtain the corrected IFGs (Fig 3.5a-c, e-g).

The reference area was chosen manually for each frame (grey boxes in Fig 3.5a-c, e-g), in an area that is expected to be temporally stable and away from active faults, vegetation, agriculture and desert. The reference window size was set to be 400×400 pixels^2, which is ∼30×30 km^2. This size is small enough to avoid tectonic signals and large enough to average over high-frequency turbulent atmospheric noise. The average of pixels in the reference window is subtracted from the IFGs and their corresponding GACOS models, so that both data sets have a common reference.

To evaluate the effectiveness of atmospheric correction using GACOS models, I plotted a point cloud of GACOS LOS against IFG (Fig 3.5d, h) for each IFG (*Yu et al.*, 2018b). Fig 3.5a-d show an example of an effective GACOS correction where the high correlation between GACOS and IFG LOS suggests the GACOS model successfully predicts the spatial pattern of the IFG. The steep gradient in Fig 3.5d shows GACOS also predicts the amplitude of the IFG accurately. Fig 3.5e-h represent an example of poor correction where the GACOS phase does not correlate with the IFG and results in higher post-correction variability. The point clouds are coloured by elevation to reveal the relationship between uncorrected phases and topography (inset of Fig 3.5d). The spatially variable degree of correlation with topography suggests the GACOS correction is indeed more suitable than empirical corrections for these IFGs.

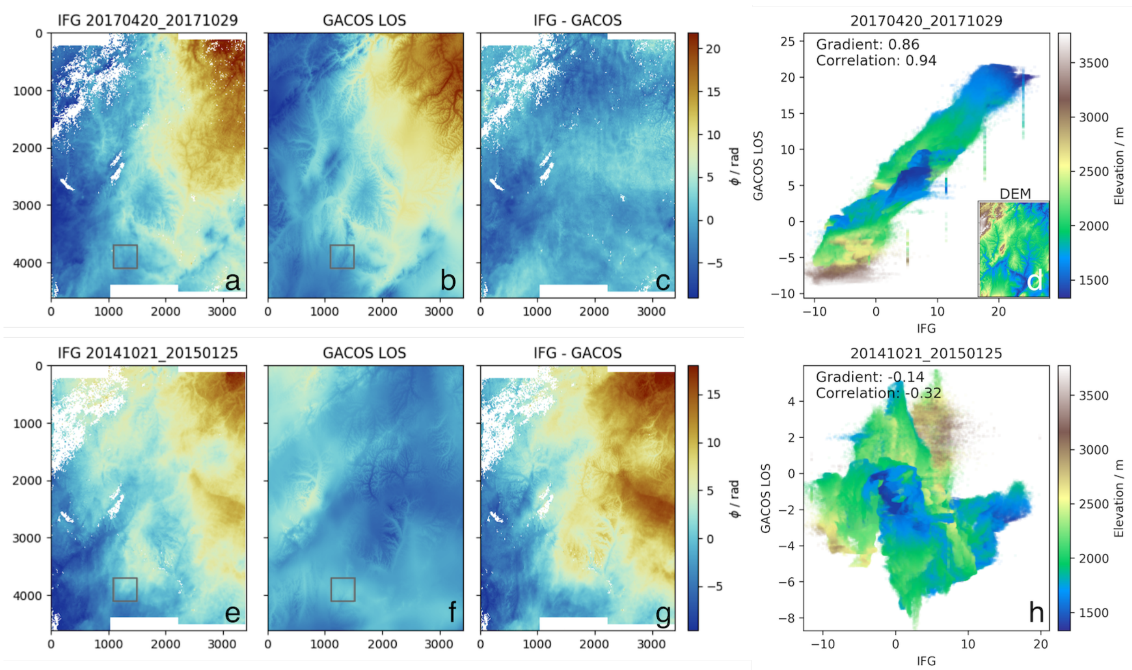

Figure 3.5: (a-c) An example of good GACOS correction where the GACOS model in (b) almost reproduced the IFG in (a), resulting in significantly reduced residual in (c). (d) shows the pixel comparison between the IFG and GACOS LOS with both correlation and gradient close to 1. (e-h) same as (a-d) but for an example where the GACOS model failed to predict the spatial pattern and amplitude of IFG. Both IFGs are from the frame 055A_05420_131313, with the DEM showing in the inset of (d). The grey boxes mark the chosen reference area where the average value of pixels in the box are subtracted from the IFG and the GACOS LOS so that two images have the same zero reference.

To assess the overall performance of GACOS, I plotted the best-fit gradient against the correlation between GACOS and IFG pixels as in Fig 3.5d for all IFGs in each frame (Fig 3.6). A positive relationship is observed between gradient and correlation, which can be explained by Fig 3.5d, where the gradient of the point cloud of a highly correlated pair is well-constrained and tends to be close to 1. On the contrary, the point cloud of a poorly correlated pair is less linear and the resultant gradient becomes less predictable. What is reassuring is the correlation between the phase range of the IFG and the quality of GACOS correction (Fig 3.6), as seen from the red points clustering towards the right hand side of the figures. This suggests that the larger the atmospheric signals, the better GACOS is at predicting them; the poorly corrected IFGs tend not to have a significant atmospheric component and could be related to low amplitude turbulent or water vapour changes. The statistics in each panel show the mode and standard deviation of the gradients and correlations for all IFGs in the frame. Overall, the frames have an average correlation of ∼0.65 and an average gradient of 0.55, suggesting that GACOS is better at predicting the spatial pattern of the IFGs than it is at predicting the amplitude of the correction. In most cases, GACOS underestimates the amplitude of the IFG, although the correction successfully removes more than half of the atmospheric delay.

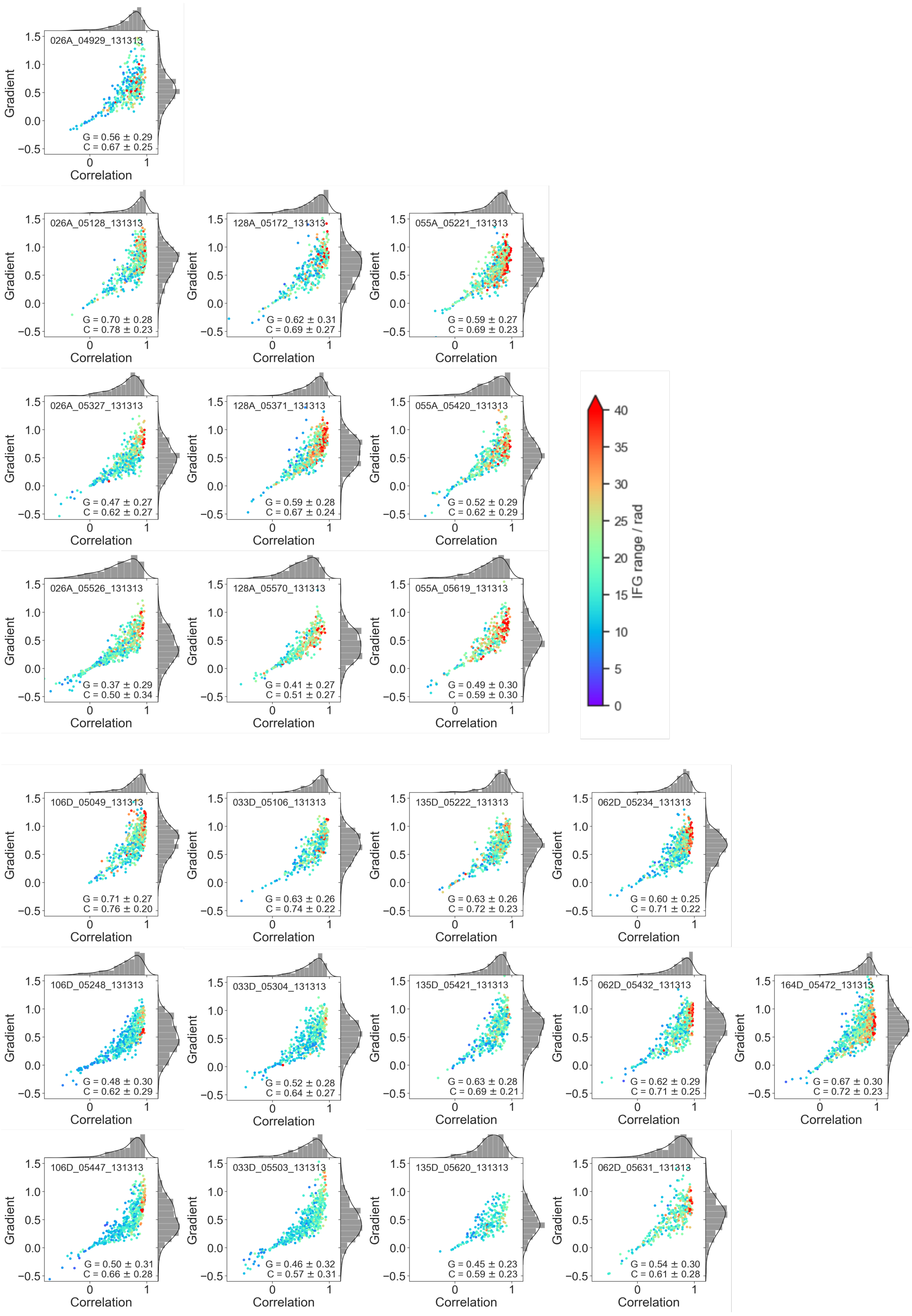

Figure 3.6: Joint plots between best-fit gradient and correlation from the scatter plots of GACOS LOS and IFG (as in Fig 3.5d,h) for each frame. The colour of the scatter points represent the amplitude range (difference between the 99.7 percentile and 0.03 percentile of the pixel values) of the corresponding IFG. The G and C labels in each panel stand for gradient and correlation with their mean and standard deviations.

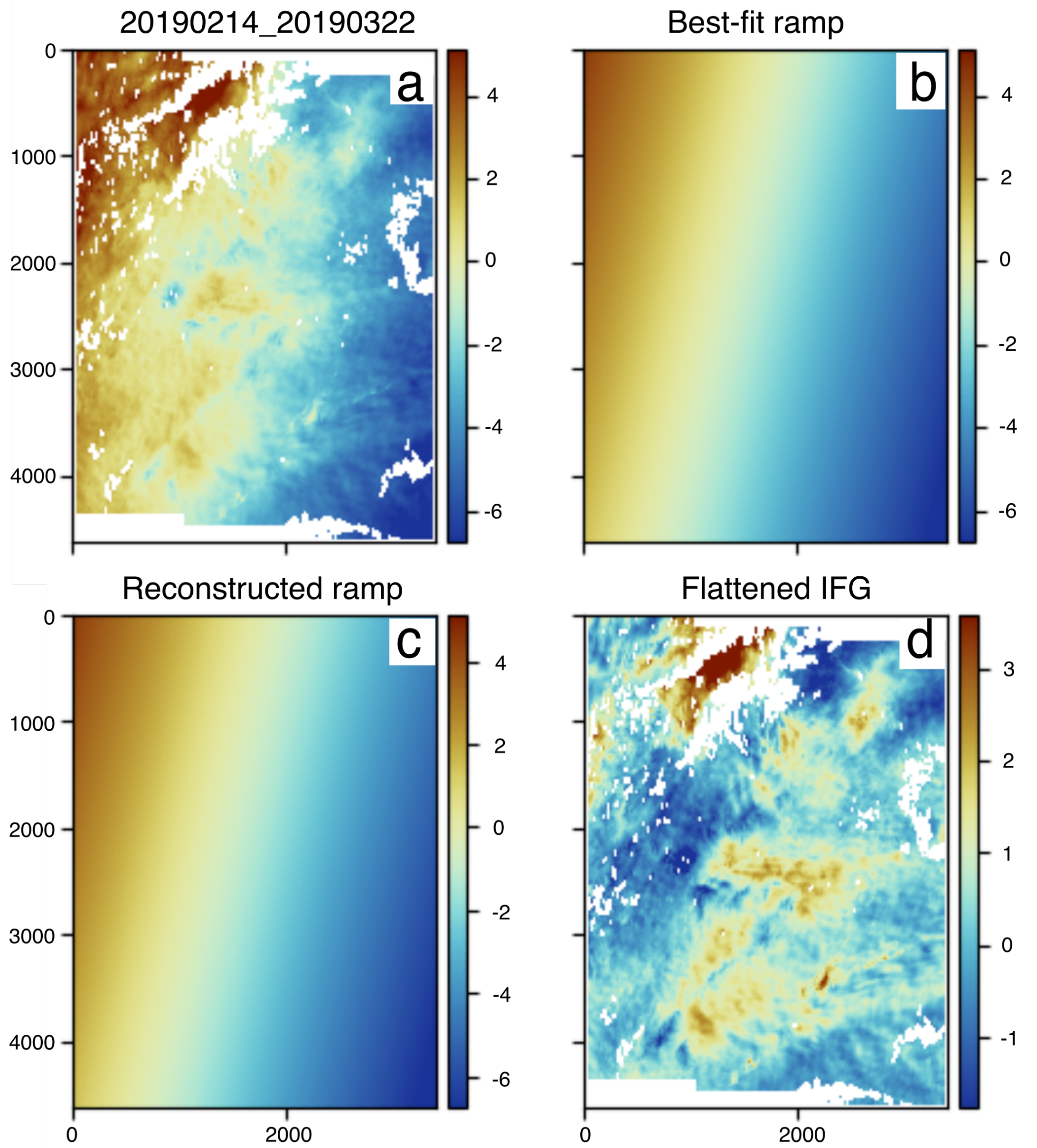

Figure 3.7: An example of ramp removal using a network approach. (a) Masked IFG with only pixels with coherence higher than 0.5; (b) Best-fitting linear ramp for (a); (c) Reconstructed ramp correction based on ramp parameters individually inverted from a network of ramp parameters; (d) Flattened IFG after removing the reconstructed ramp in (c).

3.4.3 Ramp removal

After the atmospheric correction, there are still some long-wavelength signals present in the corrected IFGs, with possible contributions from unmodelled tropospheric delays, ionospheric phases (*Gomba et al.*, 2017), orbital inaccuracies (*Fattahi and Amelung*, 2014) and solid earth tide (*Xu and Sandwell*, 2020). Such signals are undesired in measuring interseismic strain and make unwrapping mistakes harder to identify. To flatten the IFGs further, I used a network approach to remove a planar ramp from each IFG, following *Biggs et al.* (2007) and *Maubant et al.* (2020).

The ramp removal takes four steps: (1) Mask the IFG with the filtered coherence file from the LiCSAR outputs to only include pixels with coherence higher than 0.5 for ramp estimation (Fig 3.7a); (2) Estimating the best-fitting linear ramp parameters, a_{ij}, b_{ij}, c_{ij}, for each IFG between epoch i and j with an orbital ramp of the form $z_{ij} = a_{ij}x_{ij} + b_{ij}y_{ij} + c_{ij}$, where (x, y) are pixel positions in radar coordinates (Fig 3.7b) and calculate the pixel residuals; (3) Invert the three networks of parameters independently for the ramp parameters of each epoch, a_k, b_k, c_k, where $k \in i, j$, applying a weight based on both the temporal baseline of the IFG and the root-mean-square (RMS) of the pixel residuals (IFGs with shorter temporal baselines and lower RMS residuals are given higher weights); (4) Remove the reconstructed ramp for each IFG (Fig 3.7c), based on the inverted ramp parameters for both epochs of the corresponding IFG (Fig 3.7d). The exact formulation in step (3) is as follows:

$$\begin{bmatrix} \frac{1}{\sigma_{12}} \times m_{12} \\ \vdots \\ \frac{1}{\sigma_{ij}} \times m_{ij} \\ \vdots \\ \frac{1}{\sigma_{(k-1)k}} \times m_{(k-1)k} \end{bmatrix} = \begin{bmatrix} \frac{1}{\sigma_{12}} & (-1 & 1 & 0 & \dots & \dots & 0) \\ \vdots & \vdots & \vdots & \vdots & \vdots & \vdots & \vdots \\ \frac{1}{\sigma_{ij}} & (0 & \dots & -1 & 1 & \dots & 0) \\ \vdots & \vdots & \vdots & \vdots & \vdots & \vdots & \vdots \\ \frac{1}{\sigma_{(k-1)k}} & (0 & \dots & \dots & 0 & -1 & 1) \end{bmatrix} \times \begin{bmatrix} m_1 \\ m_2 \\ \vdots \\ m_i \\ m_j \\ \vdots \\ m_{k-1} \\ m_k \end{bmatrix} \tag{3.3}$$

$$\text{where} \quad \sigma_{ij} = \frac{1}{w_1} + \frac{1}{w_2}$$
$$w_1 = exp(\frac{-dt_{ij}}{2})$$
$$w_2 = exp(\frac{-rms_{ij}}{rms_{80}}) + 0.01$$

where m is a ramp parameter a, b, or c; dt is the temporal baseline of each IFG in decimal years, m_{ij} is a ramp parameter for an IFG between epochs i and j, m_k is a ramp parameter for epoch k and rms is the RMS of the residual after removing a best-fit linear ramp. rms_{80} is a constant equal to 80 percentile of the rms values of all IFGs, which ensures the partial weights, w_1 and w_2, have similar ranges.

The reconstructed ramps may have slightly different ramp parameters than the best-fitting ramps, but this step is necessary to ensure ramps removed do not introduce artificial phase misclosure in the network. In addition, it also avoids overfitting each IFG which could be biased from tectonic signals, turbulent tropospheric delays, decorrelation noise and unwrapping mistakes. After ramp removal, the flattened IFGs for all frames have an average pixel root-mean-squared (RMS) value of 2.16 rad (~4 cm two-way), which represents the amplitude of spatial variation of the data used in the times series.

3.4.4 Data cleaning

As I correct and flatten the IFGs in steps detailed in sections 3.4.2 and 3.4.3, sources of data problems can be revealed. Up to this stage, IFGs with at least three types of data problems can be visually identified and removed, after which, a preliminary time series inversion can be performed to statistically discard poor quality IFGs.

Mis-registration problem

Coregistration mistakes are typically caused by errors in spectral diversity calculation from overlapping bursts of primary and secondary SLCs (*Lazecký et al.*, 2020). This mistake appears in unwrapped IFGs as azimuthal partitions between subswaths, and/or burst-sized sharp or smooth ripply patterns within the subswaths (Fig 3.8a-c). The coregistration issue has been addressed in the latest version of LiCSAR whereby a method was developed to identify the coregistration mistake by extracting linear features from the image and remove such IFGs before publishing the products. However, before the LiCSAR update, this error identification was manual and required careful visual checking of all IFGs generated.

Incomplete data

IFGs can have missing bursts, or fractions of bursts, of data due to incomplete SLC data retrieval at the first stage of the LiCSAR processing chain (Fig 3.8d-f). Such data gaps in the SLCs do not prevent successful IFG making or unwrapping, and the pixels with values are still meaningful contributions to the time series. Whether these IFGs are retained depends on the location of the reference window chosen for the frame at the atmospheric correction stage (Sections 3.4.2). If the reference window contains no pixel, the IFG will not be properly corrected and will generate

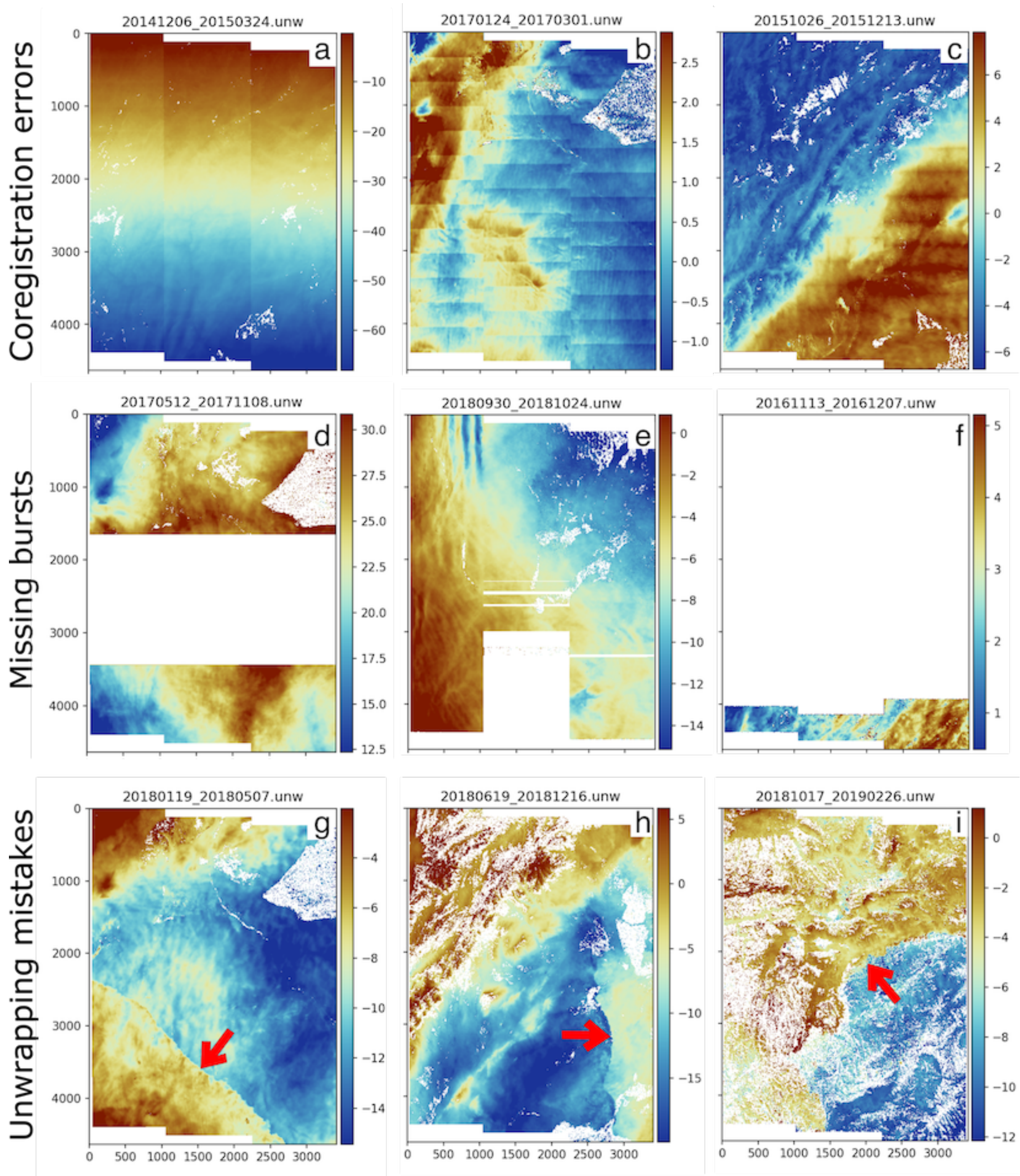

Figure 3.8: Examples of erroneous IFGs. (a-c) Mis-registration problems. (a) Mis-registration between subswaths. (b) Mis-registration between bursts. (c) Mis-registration giving smooth ripply pattern at burst level in only the bottom right half of the frame. (d-f) Incomplete data manifested as missing bursts or parts of bursts. (g-i) Unwrapping error, with the boundaries of phase jump mistakes pointed at by red arrows.

an empty file for the corrected IFG. If not discarded, the empty corrected IFG will cause the ramp removal network inversion to fail in Section 3.4.3. Hence, care was taken to remove such empty files after the GACOS correction.

Unwrapping error

Unwrapping mistakes are sharp phase jumps of multiples of 2π that are visible as geometrical boundaries (Fig 3.8g-i). Some phase jumps are already obvious in the uncorrected IFGs and others less so, especially in IFGs with severe atmospheric problems, hence large ranges of amplitude, that do not correlate with topography. The identification of such errors becomes easier as the IFGs were flattened with atmospheric correction and ramp removal, such that the phase jump becomes the most pronounced signal in the IFG. Manual removal of IFGs with unwrapping mistakes was carried out throughout the post-LiCSAR processing chain, although a final check with preliminary time series inversion was performed in low resolution to catch all remaining unidentified unwrapping mistakes before the proper time series was performed to obtain the velocity maps.

3.4.5 Time series inversion

Time series analysis (Fig 3.2d) was performed using the NSBAS program developed by *López-Quiroz et al.* (2009) and *Doin et al.* (2015). NSBAS solves for the temporal increments of phase changes, $\delta\phi_n$, per pixel and applies an overall temporal function defined by ϕ_k^s to regularize the problem in case of gaps in the network (*Doin et al.*, 2015):

$$\forall l \in [1, M] = \sum_{n=1}^{n=j-1} \delta\phi_n = \Phi_l \tag{3.4}$$

$$-\alpha W_1 \phi_1^s = 0 \tag{3.5}$$

$$\forall k \in [2, N] \quad \alpha W_k \left(\sum_{n=1}^{n=k-1} \delta\phi_n - \phi_k^s \right) = 0 \tag{3.6}$$

$$\forall k \in [1, N] \quad \gamma\omega_k \partial^2 \phi_k^s / \partial t^2 = 0 \tag{3.7}$$

where Φ_l is the lth IFG between epoch numbers $n = i$ and $n = j$; ϕ_k is the cumulative phase increment from the first epoch $\phi_1 = 0$ to ϕ_{k-1}. N is the total number of epochs; M is the total number of IFG. γ is the smoothing coefficient; ω_k is the average time interval between the 5 epochs used to calculate the second derivative. α is set small enough to only have an impact when there are missing links in the network. W_k can be changed at each iteration to weight the inversion differently. The method also has an option to downsample the data for faster computation.

The by-products generated, other than the time series, include (1) the overall RMS pixel map, $\phi_{RMS_{pixel}}$, which highlights outlines of unwrapping mistakes present in the network, (2) the deviation maps (between each IFG and the reconstructed IFG from network inversion) which highlight outlines of unwrapping mistakes per IFG, and the RMS value of all valid pixels in each deviation map, $\phi_{RMS_{ifg}}$, which helps shortlist the worst unwrapped IFGs, (4) the RMS map per epoch averaged from all associated deviation maps and the RMS value per epoch, $\phi_{RMS_{epoch}}$, which helps identify particular acquisitions that introduce mistakes in all IFGs associated with them.

Preliminary Time Series Inversion for data refinement

The purpose of the preliminary inversion is to identify IFGs with unwrapping mistakes with the help of NSBAS's statistical RMS products. Therefore, in this step, the IFG data set is inverted in low resolution with multilook factors of 5 both along range and along azimuth, without temporal smoothing or iteration. IFGs with the highest $\phi_{RMS_{ifg}}$ (Fig 3.9a) and IFGs made with acquisitions with the highest $\phi_{RMS_{epoch}}$ (Fig 3.9b) are discarded after visually confirming that the $\phi_{RMS_{ifg}}$ maps contain significant patches of unwrapping mistakes (Fig 3.9c).

Even with network redundancy to start with, the remaining network can become disconnected or sparsely connected after discarding the miscoregistered IFGs, the

IFGs with missing bursts over the reference area, and the IFGs with unwrapping mistakes. Therefore, new IFGs with longer temporal baselines were generated using LiCSAR to build up the network again. Some newly made IFGs can end up being discarded, too. So, this process was repeated until all the IFGs in a well-connected network (with at least 3 IFGs linking every epoch) have $\phi_{RMS_{ifg}}$ lower than ~2 rad (Section 3.4.3 and Fig 3.4), and no unwrapping mistakes appear in the overall $\phi_{RMS_{pixel}}$ map.

Full-resolution Time Series Inversion

A systematic signal in multilooked IFGs with short temporal baselines has been noted to bias velocity extracted from InSAR time series (*Ansari et al.*, 2020). To mitigate this effect, I removed all 12-day IFGs from the networks before the final time series inversion. According to *Daout et al.* (2020), the bias caused by the short-period (12 and 24 days) IFGs is negligible when the network is well-connected and contains many long-period (3 and 6 months) IFGs as in Fig 3.3. As the 12-day IFGs are only present in the post-2017 time series, removing them helps make the entire network from 2014 to 2019 based on IFGs with temporal baseline of 24 days and above. Removing them only before the final inversion allows me to capitalise on the coherent pixels in those 12-day IFGs for better ramp removal and error identification in the time series analysis.

The full-resolution inversion for the cumulative displacement time series is carried out in two iterations. The first iteration is weighted by the misfit from fitting each IFG with a planar ramp obtained from the previous ramp removal section such that the spatially noisier pixels are weighted less. The residuals between the input IFGs and reconstructed IFGs from the first iteration are used to weight the second iteration such that IFGs that fit poorly temporally into the network have less effect on the final time series. The resultant RMS maps are visually checked to confirm there are no remaining unwrapping mistakes. The RMS values are also typically smaller than those in the preliminary inversions (Fig 3.9d).

Finally, I extract a linear velocity, V, from the time series with $\phi_k = Vt_k$ also in two iterations, where t_k is the cumulative time from the first epoch *Daout et al.* (2018) (Fig 3.2e). The first iteration is weighted by $\phi_{RMS_{epoch}}$ from the time series inversion such that dates associated with IFGs that poorly fit the reconstructed IFGs have less effect on the linear velocity. Then, the misfit per pixel per epoch from the first iteration is used to weight the second iteration of inversion such that the epochs that deviate more from a linear velocity trend are weighted less. The uncertainty, $\sigma(V)$, associated with the final velocity, V, for each pixel is computed as the standard deviation of the residual between ϕ_k and the model prediction Vt_k. The resultant linear velocity and the uncertainty maps from the second iteration (Fig 3.10a,b) were cleaned, geocoded and had their units and signs converted for the final products (Fig 3.10c,d).

The cleaning step was done by masking the products using the $\phi_{RMS_{pixel}}$ map with a masking threshold of ~0.5 rad. Geocoding was done with the look-up table from LiCSAR using the geocode gamma command in the same way as the final step of LiCSAR processing. The product unit was converted from rad/yr to mm/yr, by dividing the velocity by 4π and multiplying the radar wavelength (speed of light divided by the radar frequency of 5.405 GHz). A negative sign was applied to follow the sign convention of positive velocity towards the satellite.

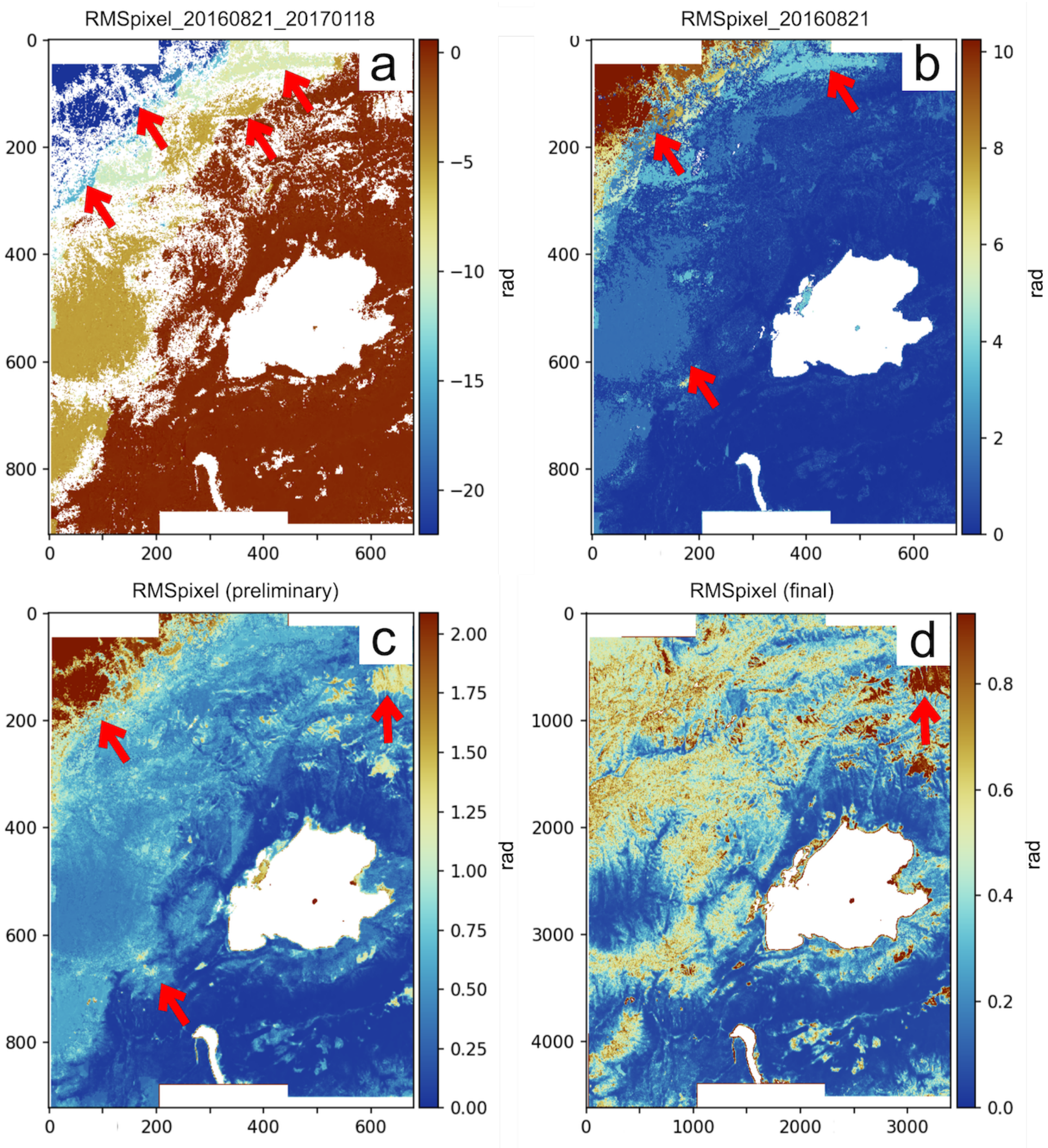

Figure 3.9: Example of unwrapping mistake identification (pointed at with red arrows) based on NSBAS time series inversion for frame 033D_05304_131313. (a-c) are products from the low resolution preliminary time series inversion. (a) An example of the ϕRMS_{ifg} map of the IFG with the highest RMS misfit in the network. (b) An example of ϕRMS_{epoch} map of the epoch with the highest average RMS misfit from all IFGs of which it constitutes one epoch of the interferometric pair. (c) Map of ϕRMS_{pixel} which highlights significant unwrapping errors present in IFGs in the network. (d) Map of ϕRMS_{pixel} from the full resolution final time series inversion with two iterations after IFGs with unwrapping mistakes have been removed. The final ϕRMS_{pixel} values are below 1 rad. The small patch of high RMS area was tolerated and the corresponding velocity was later masked out.

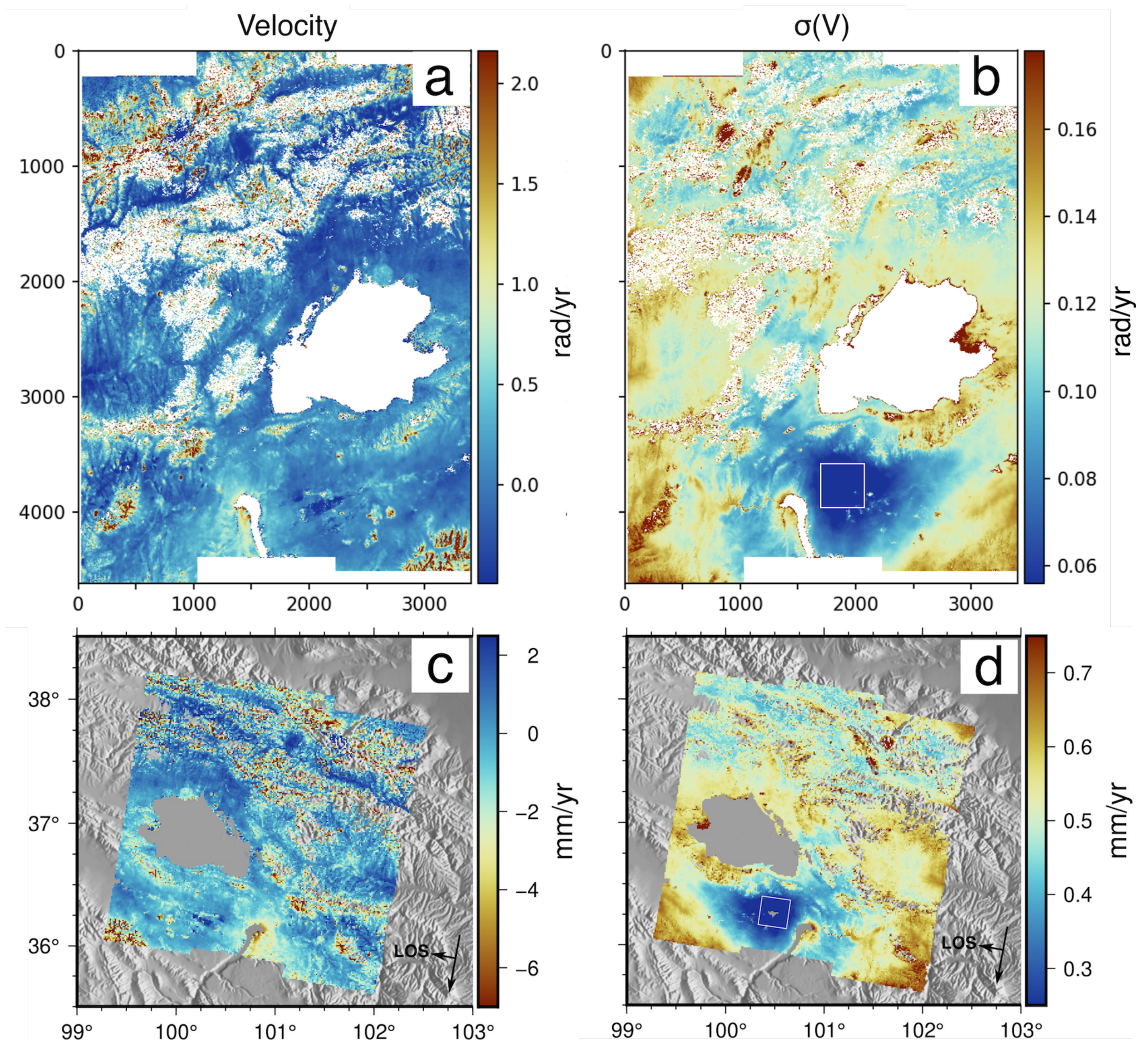

Figure 3.10: (a) Linear velocity in unit of rad/yr extracted from the time series for frame 033D_05304_131313. (b) Uncertainty associated with (a) with the white box showing the reference area. (c-d) Geocoded and cleaned version of (a) and (b) in units of mm/yr. The sign convention is positive towards the satellite.

3.5 Discussion

The post-LiCSAR processing chain outlined above proved effective on 21 out of 23 frames in my study area, with $\phi_{RMS_{ifg}}$ reduced to the threshold level (<2 rad) after at most 3 iterations of network refinement. However, two frames (055A_05619_131313 and 062D_05631_131313) covering an area enclosed by the West Qinling Fault, East Kunlun Fault and Longmenshan Fault have encountered the most difficulties (Fig 3.11).

These two frames suffer from severe unwrapping problems, potentially due to both the dense vegetation and the tectonic complexity of the area. During the network refinement, many IFGs were discarded due to their high $\phi_{RMS_{ifg}}$ values. As a result, more IFGs with longer temporal baselines had to be generated to form a connected network. In the worse case of the ascending frame 055A_05619_131313, over 12 iterations of IFG making, manual checking, preliminary time series inversion were performed to result in the final network with all $\phi_{RMS_{ifg}}$ below the threshold level (Fig 3.12). Yet, the ϕ_{RMS} map still shows high misclosure in the southwest corner of the frame where the East Kunlun Fault partitions into the oblique reverse Bailongjiang (BLJ) Fault and the sinistral Maqên-Maqu-Tazang (MMT) Fault (Fig 3.11) (*Li et al.*, 2020a).

To explore whether filtering and unwrapping parameters should be tailored for areas with heavy vegetation and steep relief, experiments with filtering window sizes (16×16 and 48×48), filtering strength (0.5 and 1.5) and the coherence threshold for unwrapping (0.4 and 0.6) that are different from the LiCSAR defaults (32×32, 1.0 and 0.5, respectively) were performed to generate different sets of IFG networks for the 055A_05619_131313 frame. However, series of preliminary time series inversion tests and network refinement did not show systematic improvements, and did not form complete working networks by the stage where the IFGs with the default LiCSAR parameters have obtained the final network. This comparison suggests that the default LiCSAR parameters are already optimal.

Due to the long temporal baselines of the IFGs used (average 200 days), the current networks for these two frames are formed with IFGs with low coherence values. As a result, the average percentage of pixels unwrapped is 64.01% for frame 055A_05619_131313 and 63.99% for frame 062D_05631_131313) (Fig 3.3). Further human-guided unwrapping methods, such as bridge making, should be explored next to specifically improve the unwrapping of the problematic IFGs (*Doin et al.*, 2011). Such a step could help retain more IFGs with shorter temporal baselines and more coherent pixels in the network, which will provide more constraint for the time series inversion.

In addition, these two frames both observed anomalies in the gradient against correlation plots at the atmospheric correction step (Fig 3.6). Some IFGs with the highest amplitudes (red dots) exhibit low gradients and correlations between the GACOS model and the IFGs. The reason for their occurrences requires further investigation. Potentially, gradients-correlation-range plots like those in Fig 3.6 could provide additional means of verifying the integrity of the IFGs in the network and could be used to filter out more bad IFGs.

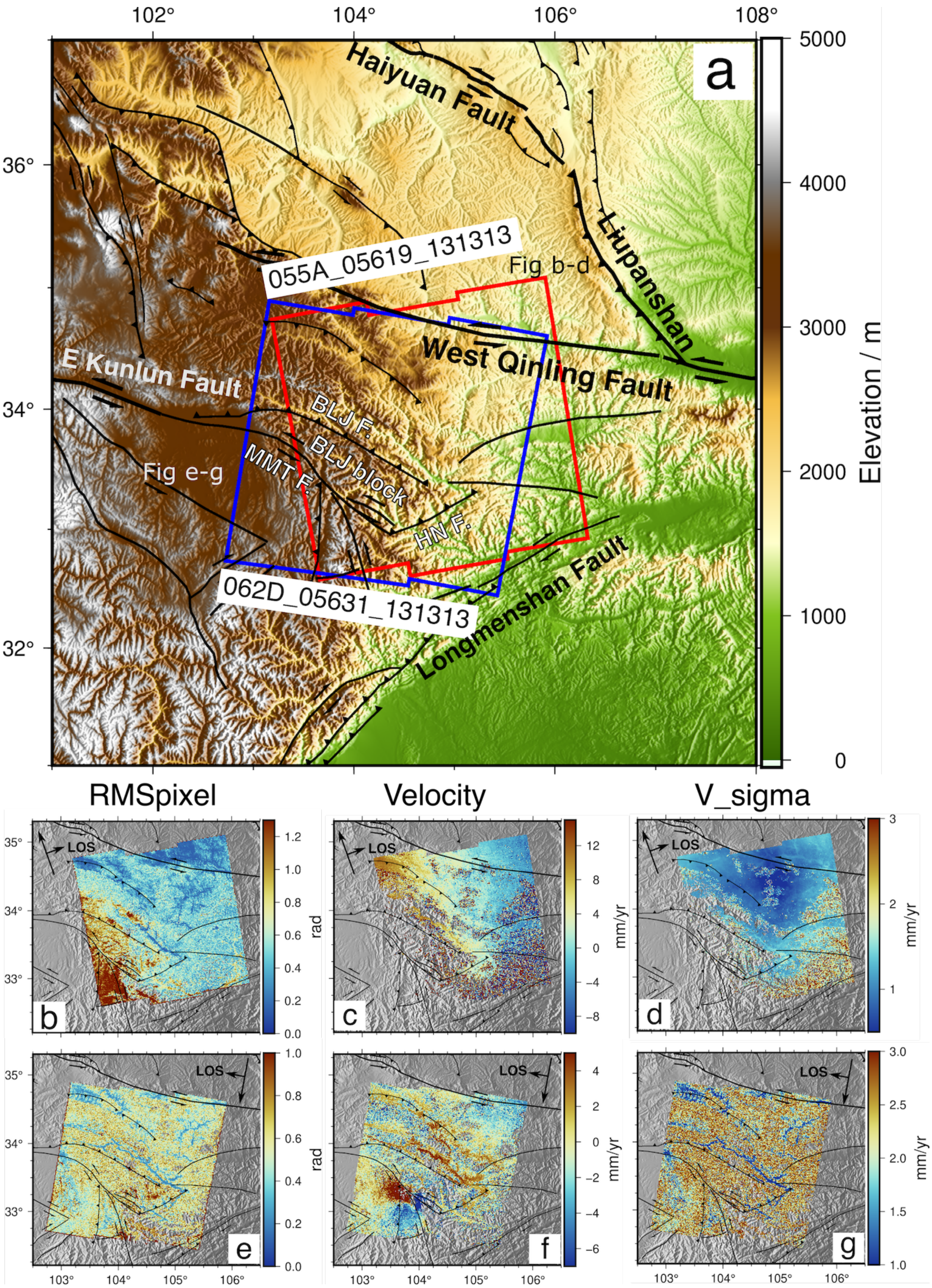

Figure 3.11: (a) Topography and tectonics of the area containing the two challenging frames 055A_05619_131313 and 062D_05631_131313. BLJ F. = Bailongjiang Fault; MMT F. = Maqên-Maqu-Tazang Fault; HN F. = Hanan Fault. (b) $\phi_{RMS_{pixel}}$ map, (c) velocity map and (d) uncertainty of velocity for frame 055A_05619_131313. (e-g) same as (b-d) but for frame 062D_05631_131313.

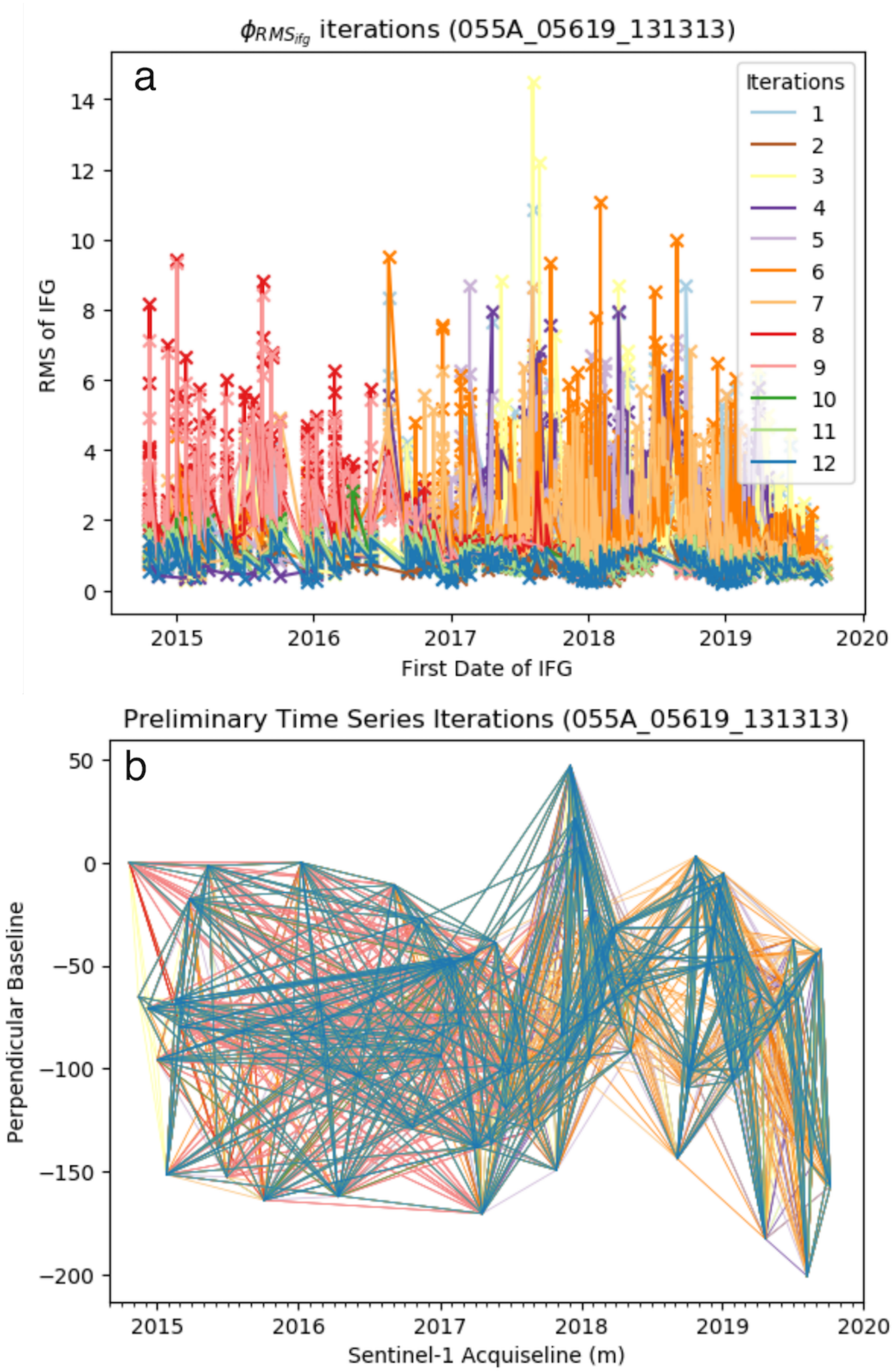

Figure 3.12: (a) $\phi_{RMS_{ifg}}$ of each preliminary time series iteration. (b) Network inverted at each preliminary time series iteration.

Chapter 4

Regional InSAR velocity maps

4.1 Introduction

The overall objectives of this InSAR study are to (1) create high-resolution regional velocity maps that can reveal motion along faults in the east and vertical directions (2) derive strain rate maps that can provide an overview of the distribution of strain rates, thus highlighting areas with higher seismic hazard. While LiCSAR enables large-scale automatic processing of the Sentinel-1 InSAR data, the resultant velocity maps are derived in pre-determined LiCS frames which do not always intersect tectonic features in ways that are easys to interpret. Therefore, I need to mosaic the frame-sized velocity maps to form coherent regional velocity maps prior to using the data for tectonic strain mapping, seismic hazard analysis and other scientific investigations.

Several challenges exist in the stitching of velocity maps: (1) The velocities in each LOS map are relative to that of a reference area within the frame, but the relative velocities between the different reference areas are unknown; (2) Due to the different IFG networks between frames and varying effectiveness of atmospheric correction in each IFG, the resultant velocity maps can be slightly tilted in space relative to each other; (3) The incidence angle of the line of sight (LOS) increases in the range direction creating steps in the LOS velocities where the near-range and far-range pixels of neighbouring tracks overlap.

In this chapter, I develop methods for stitching together the frame-sized velocity maps by solving for frame-specific ramps that shift the velocity maps to the same reference frame. An improved method of decomposing the ascending and descending LOS velocities into Cartesian components is also presented. These methodological advancements result in two continuous high resolution and high quality east (V_E) and up (V_U) velocity maps covering an extended area of the NE Tibetan Plateau.

4.2 Preliminary investigation

4.2.1 Simple merging of frame-sized velocity maps

To fully grasp the problem at hand, I perform a series of preliminary analyses of the velocity maps. A direct merging of the velocity maps, by overlaying southern frames on top of northern frames and then overlaying eastern tracks on top of western tracks, results in the regional LOS velocity maps shown in Fig 4.1. These maps are mostly flat due to the deramping step before time series inversion, but frame and track boundaries are discernible in many places, especially around frames that intersect with major faults. Not all steps at frame boundaries can be explained by the difference references which introduce constant offsets. One possible reason relates to removing the best-fitting planar ramps from IFGs across a fault, where the true LOS should exhibit a velocity step within the frame. As a result, the deramped velocity map may be tilted away from the true 'horizontal'.

4.2.2 Overlap offsets between frames

Calculating pixel offsets in the overlapping areas between frames along track reveals that the mode of the step sizes range from 0.14 to 4.84 mm/yr (Fig 4.2). Some

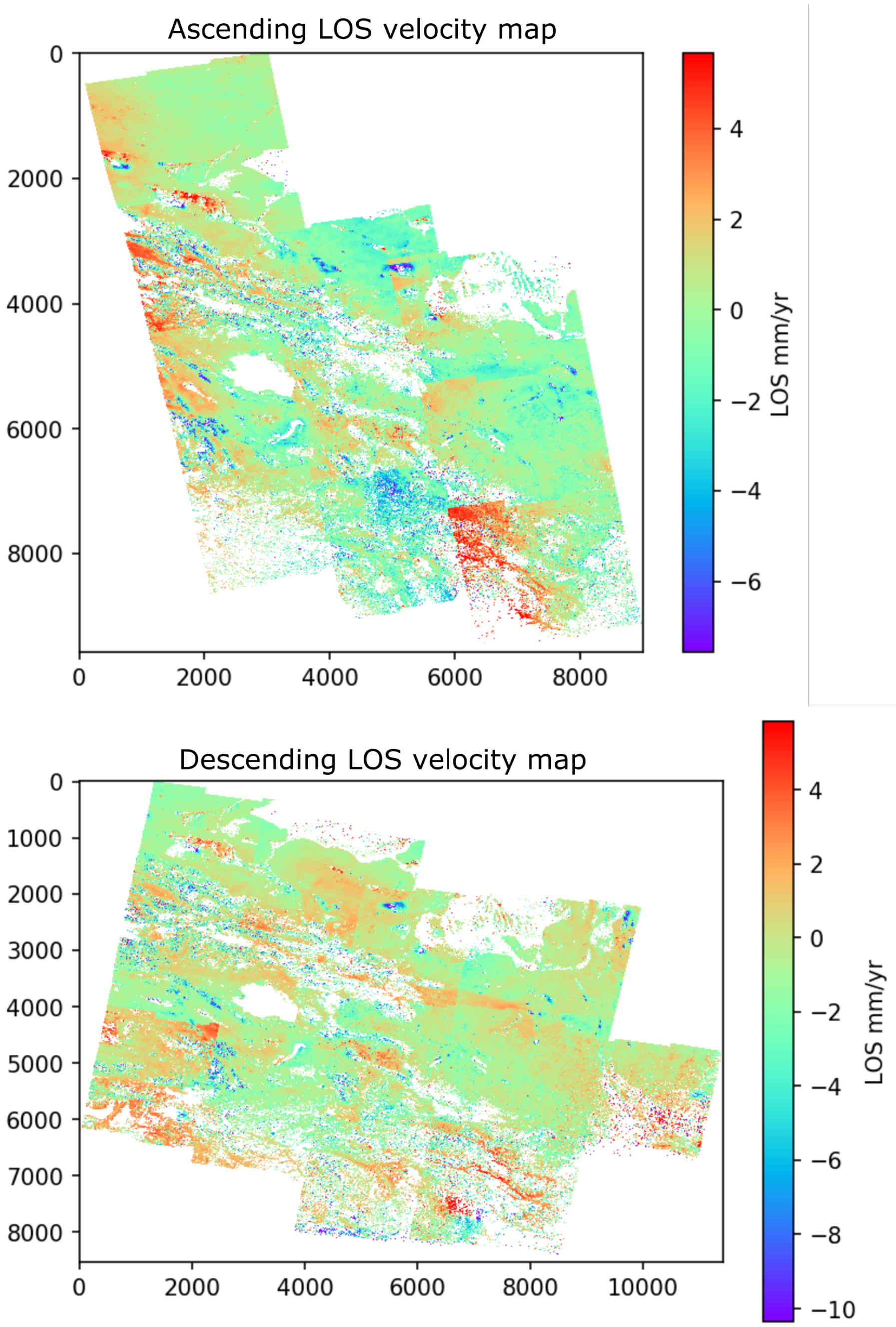

Figure 4.1: Merged velocity maps in pixel coordinates with direct output from time series inversion.

overlap offsets also show strong gradients from west to east, previding evidence for a relative tilt between the velocity maps. The overlap offsets with ramps all consist of one frame that crosses a fault. For example, Fig 4.2a, f and i are associated with the Altyn Tagh, Haiyuan and Kunlun Faults, respectively (Chapter 3 Fig 3.1).

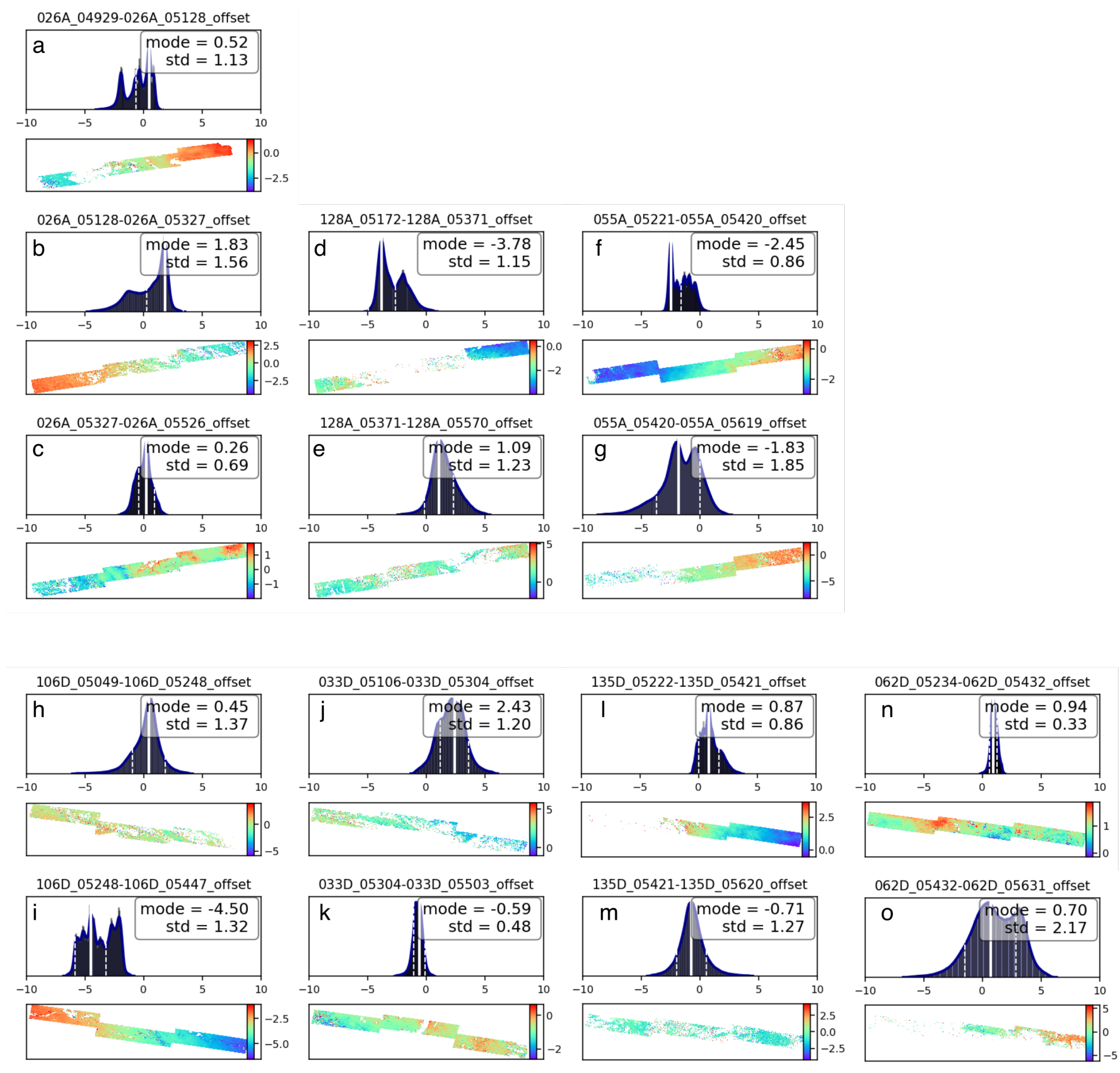

Figure 4.2: Histograms of pixel differences between overlap areas of frames along track. Solid white lines mark the mode of the histogram. Dotted white lines mark one standard deviation from the mode. Average mode = -0.318 mm/yr. Average standard deviation = 1.2 mm/yr. The colour scales for each panels are different. I choose to compare the mode values, instead of mean values, because after the inversion for ramp parameters in the later steps, the mean values of the residual offsets will all become zero, but the mode values can remain non-zero and serve as a proxy for the degree of non-Gaussian distributions of the offset values.

On average, the standard deviation of the overlap offsets along track is 1.2 mm/yr, which is approximately the order of magnitude expected from 5 years of continuous observation, as discussed in Chapter 3 Section 3.3. This is largely owning to the largest standard deviations associated with the ascending frame 055A_05619_131313 and the descending frame 062D_05631_131313, which both cover the tectonically active and densely vegetated area to the south of the West Qinglin Fault where IFGs suffer from low coherence and unwrapping errors.

4.2.3 Fitting ramps along range to the frame offsets

To understand how much of the variation in the overlap offsets can be accounted for by a planar ramp, I invert for the best-fitting ramp for each overlap for stitching the southern frame to the north and calculate the residuals. To avoid tilting the velocity map in the azimuth direction which is weakly controlled by the narrow strip of data that is elongated in the range direction, I invert for the ramp only in the range direction. This was achieved by rotating the coordinate axes by the heading angle of the satellite. After removing the ramps along range, the offset residuals have an average standard deviation of of 0.91 mm/yr (Fig 4.3), which is a 24% improvement. The previously scattered histograms associated with overlap offsets with obvious ramps also reduced to narrow Gaussian distributions (compare Fig 4.2 and Fig 4.3a-d,f,g,i,l), with the average of mode values reduced to -0.038 mm/yr, very close to the mean values of zero. The histogram for the offset between frames 106D_05248_131313 and 106D_05447_131313 is one example where the improvement is significant (compare Fig 4.2i and Fig 4.3i), suggesting the velocity maps for these two frames are actually of very high quality.

4.2.4 Overlap offsets between tracks

The ramps described above only have one degree of freedom in the along-range direction. Therefore, there might still be residual ramps in the azimuthal direction which cannot be constrained with the overlaps between frames. The presence of such azimuthal ramps are suggested by the offsets between tracks, where the frames in

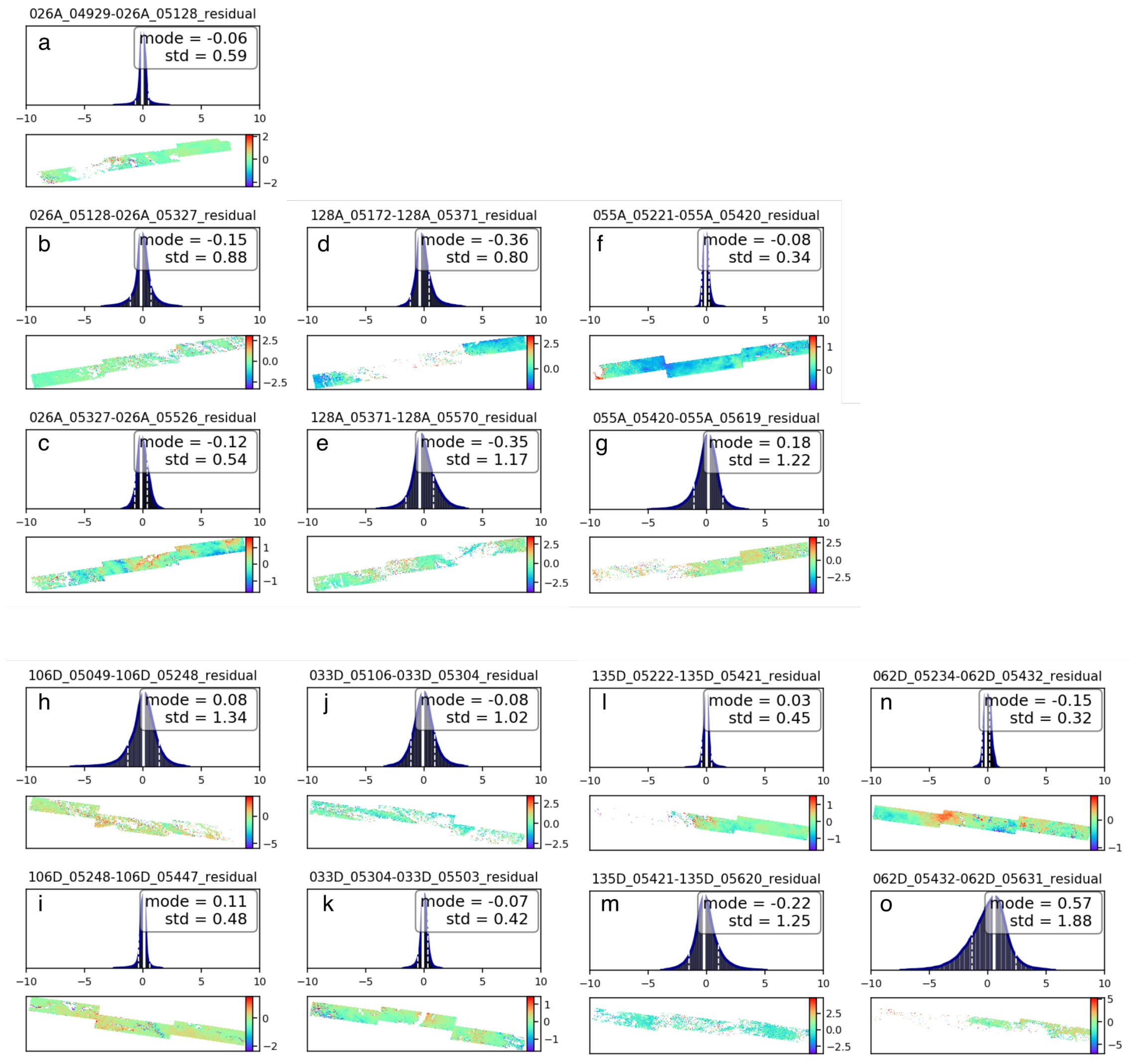

Figure 4.3: Histograms of pixel differences between overlap areas of frames along track after applying a ramp in the range direction to close the gaps between the frames. Solid white lines mark the mode of the histogram. Dotted white lines mark one standard deviation from the mode. Average mode = -0.038 mm/yr. Average standard deviation = 0.91 mm/yr.

each track have been stitched with ramps in range removed (Fig 4.4). However, the overlap offsets between tracks cannot be used to guide the frame or track stitching; the incidence angles are different at the near-range and far-range sides of the tracks, so the LOS velocities are not expected to be continuous between tracks. In fact, the offsets between tracks are expected to have steps across faults as explained in the cartoon in Fig B.1. Therefore, it is necessary to tie the InSAR velocity maps to an external reference frame, which can be defined using GNSS data.

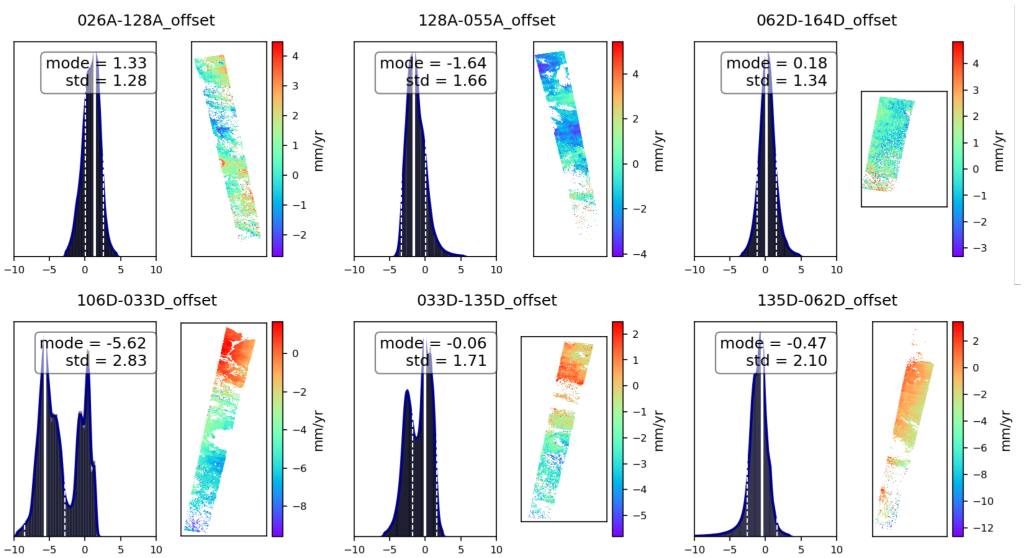

Figure 4.4: Histograms of pixel differences between overlap areas of merged tracks after applying ramps along the range direction to close the gaps between the frames. Solid white lines mark the mode of the histogram. Dotted white lines mark one standard deviation from the mode.

4.3 Projecting InSAR LOS to the GNSS reference frame

One previous attempt to merge the LiCSAR frame-sized velocity maps was done by *Weiss et al.* (2020), following the method of *Hussain et al.* (2018). They projected each InSAR LOS map onto a reference LOS map interpolated from GNSS velocities by subtracting a best-fitting second-order polynomial from the InSAR data. Their resultant overlaps between frames had an average standard deviation greater than 2 mm/yr, twice as large as the 1.2 mm/yr in my raw data set and the 0.91 mm/yr I obtained in the preliminary test. An explanation for their large overlap offsets could be that the interpolation of the spatially sparse GNSS points introduced large errors in the reference LOS maps, and adjusting InSAR LOS to fit the loosely controlled reference maps degraded the quality of the InSAR measurements. Therefore, a new frame-stitching method needs to be developed to preserve the precision of the InSAR data.

4.3.1 GNSS data in the NE Tibetan Plateau

Thanks to the two-phased installation of the CMONOC GNSS network in 1999 and 2009, the NE Tibetan Plateau is well covered by GNSS stations in terms of spatial density and distribution (*Gan et al.*, 2007; *Liang et al.*, 2013; *Wang and Shen*, 2020). Most stations in the area were installed in phase I of the project in 1999. Most of the stations in the area are campaign GNSS sites that have existed for almost 20 years. The sites were measured twice a year resulting in horizontal velocities with low uncertainties. *Wang and Shen* (2020) present the latest horizontal velocity field for the area, combining readings from continuous and campaign stations from both CMOMOC and regional networks. Their data are published in both ITRF2008 and a Eurasia-fixed reference frame (Fig 4.5a) and have an average uncertainty of 0.2 mm/yr. Vertical velocities are available from *Liang et al.* (2013) in both ITRF2008 and a stable northern neighbours reference frame (Fig 4.5b), with an average uncertainty of 1.5 mm/yr. The stable northern neighbours reference is relative to the average vertical velocity from three continuous stations in the stable Alashan, Ordos and Mongolia blocks to highlight the relative vertical motion within the Tibetan Plateau (*Liang et al.*, 2013). As the horizontal components are orthogonal to the vertical component and the reference frame transformations in the horizontal and vertical components are independent, I combine the horizontal components in the Eurasia-fixed reference frame from *Wang and Shen* (2020) with the vertical components in stable northern neighbours reference frame from *Liang et al.* (2013) to highlight the tectonic signals.

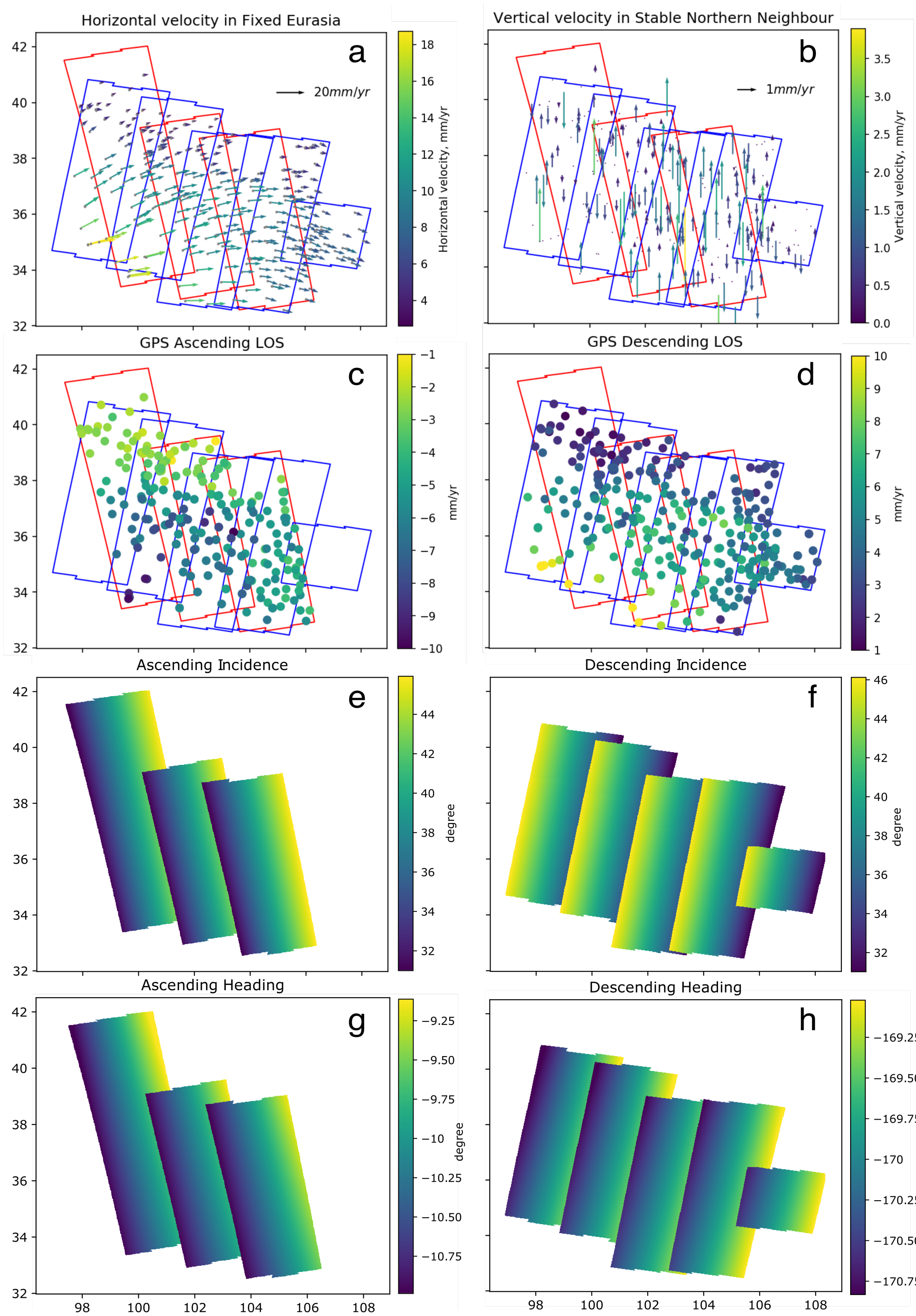

Figure 4.5: (a) Horizontal GNSS velocities in Fixed Eurasia reference frame from *Wang and Shen* (2020). (b) Vertical GNSS velocities in the Stable North Neighbour of Tibetan Plateau reference frame from *Liang et al.* (2013). Projected (c) ascending and (d) descending LOS velocities from the GNSS velocities in (a) and (b) based on their respective (e-f) incidence and (g-h) heading angles. Red polygons are ascending InSAR tracks and blue polgyons are descending InSAR tracks.

Not all stations with horizontal velocities have associated vertical velocities because *Liang et al.* (2013) discarded vertical measurements with uncertainty greater than 2.5 mm/yr and from stations in operation for less than 3 years. There are 282 stations with horizontal velocities in the area covered by the InSAR data and 169 of these have an associated vertical velocity (Fig 4.5a,b). All 23 frames contain at least 10 well-distributed stations and 20 have at least 8 stations with 3D velocities (Fig 4.6). Only three frames in the southwest, 026A_05526_131313, 106D_05447_131313 and 033D_05503_131313 (Fig 4.6d,m,p), have only 2 or 3 3D stations available, but all have good 2D station coverage.

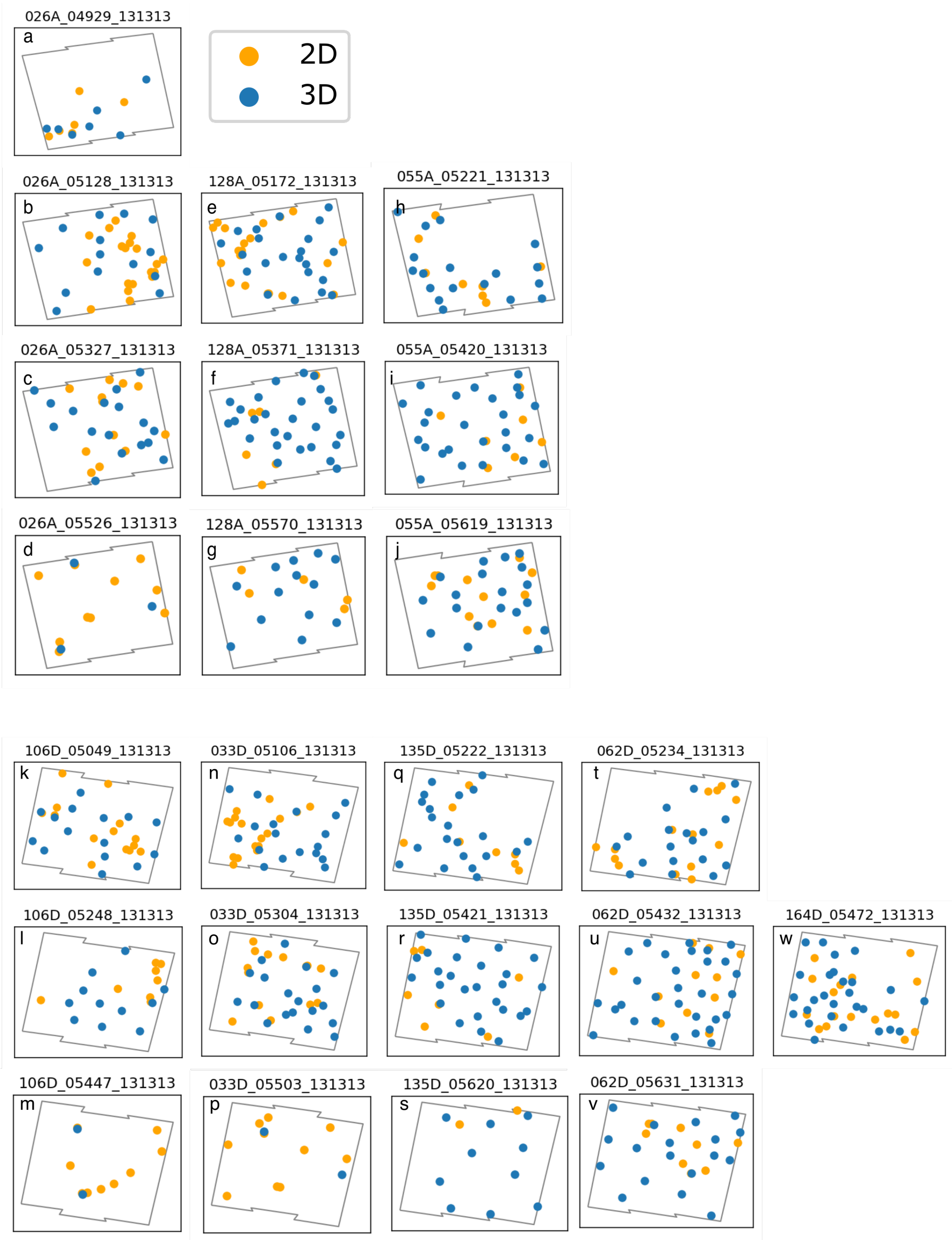

Figure 4.6: Distribution of 2D and 3D GNSS stations in the (a-j) ascending and (k-w) descending frames.

4.3.2 Method for calculating GNSS LOS and associated uncertainties

To avoid introducing errors in the space between GNSS stations, I only calculate the point data of GNSS LOS velocities from the three components of GNSS velocities and the heading and incidence angles information from the ascending and descending InSAR data (Fig 4.5c-h).

The convention of InSAR data processed using GAMMA tools is such that the heading angle, ϕ, is defined as positive clockwise from the north, and the incidence angle, θ, is defined as the angle between the LOS and the vertical down direction from the vantage point. As illustrated by Fig 4.7, in both the ascending and descending cases, the LOS velocity, V_{LOS}, and their associated uncertainty, σ_{LOS}, can be calculated as:

$$V_{LOS} = -V_E cos(\phi) sin(\theta) + V_N sin(\phi) sin(\theta) + V_U cos(\theta) \tag{4.1}$$

$$\sigma_{LOS} = \sqrt{(-\sigma_E cos(\phi) sin(\theta))^2 + (\sigma_N sin(\phi) sin(\theta))^2 + (\sigma_U cos(\theta))^2} \tag{4.2}$$

where V_E, V_N and V_U are velocity components in the east, north and vertical directions, and σ_E, σ_N and σ_U are their associated uncertainties.

The contributions to the GNSS LOS velocities and uncertainties from each of the east, north and vertical components can be analysed separately (Fig 4.8). Contributions from V_E dominate the LOS signals but with moderate uncertainties. The contributions from the N-S components are negligible, both in terms of velocities and uncertainties. The uncertainties from σ_U dominate the LOS uncertainties, σ_{LOS}, and dwarf the absolute values of the contributions from V_U to V_{LOS}.

Therefore, to strike a balance between quality and abundance of GNSS data points, I use only 3D stations (with east, north and vertical components) when there are more than ten in a frame. When there are fewer 3D stations available

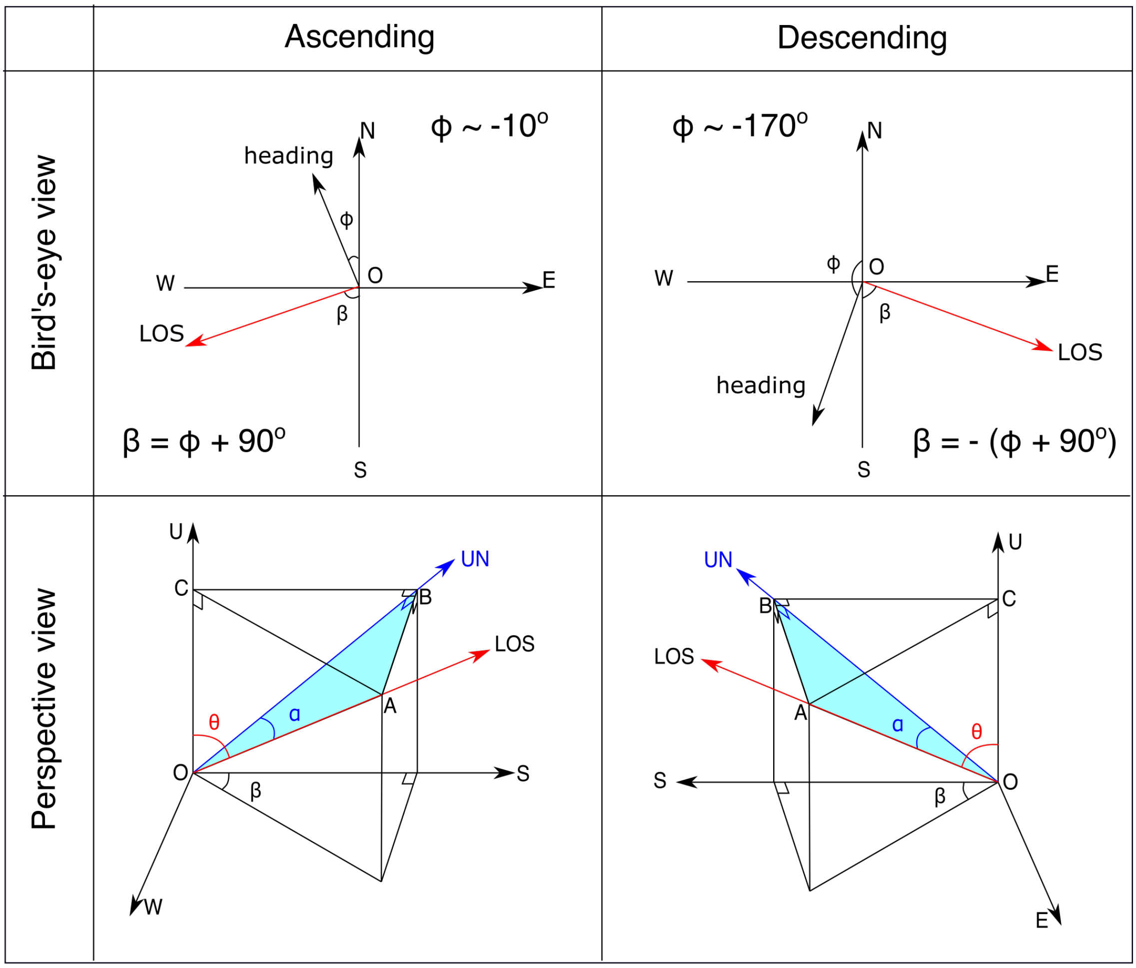

Figure 4.7: Geometry for calculating LOS from east, north and vertical velocity components. O=Ground pixel, N=North, E=East, S=South, W=West, LOS=Line-of-sight direction from the point of observation on the ground to the satellite, UN=Projection of LOS to the north-up plane. ϕ=heading angle, θ=incidence angle, α=angle between the LOS and the UN directions.

(Fig 4.6a,d,m,p), I include 2D stations (with only N-S and E-W components), assuming zero vertical velocity (V_U=0) from these stations. Given the near zero mean of the contribution to LOS from V_U and their almost equivalent-in-magnitude uncertainties, this is a reasonable assumption (Fig 4.8c,f,i,l). To reflect the lack of information on V_U at the 2D stations, I set the uncertainty in the vertical component, σ_U, to be the largest absolute value of the available V_U in the frame. As such, the magnitude of uncertainties associated with the GNSS LOS are comparable to that of the InSAR LOS, both at ~1 mm/yr level.

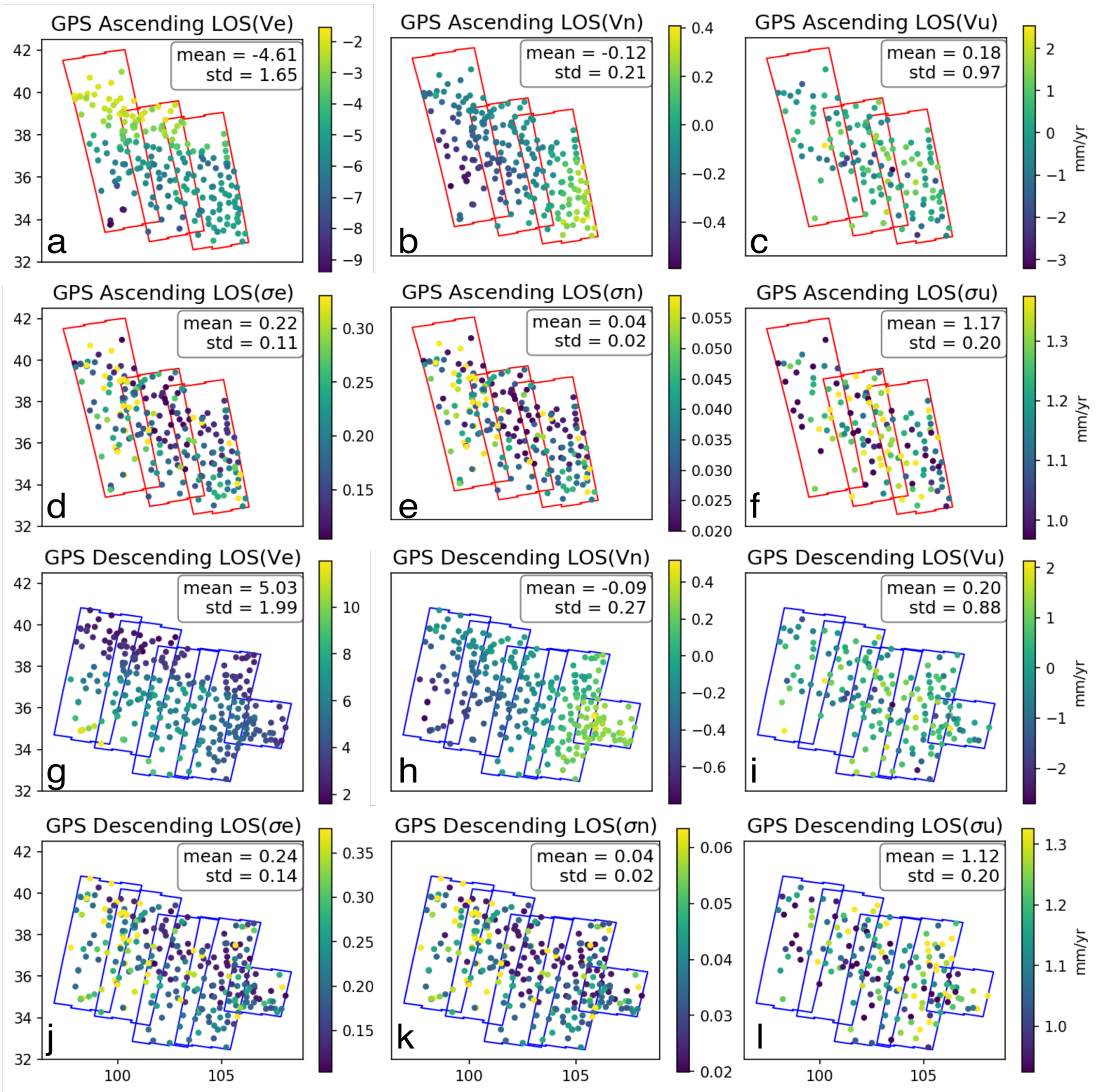

Figure 4.8: Contribution to (a-c) ascending and (d-f) descending LOS velocities from each of the east, north and vertical components. Contributions to the uncertainties of (g-i) ascending and (j-l) descending LOS velocities from each of the east, north and vertical components.

4.3.3 Method for projecting InSAR to GNSS LOS

There are two challenges associated with projecting InSAR LOS maps to point data. The first is how to handle local InSAR LOS variability. The second is how to avoid wasting GNSS points when the corresponding InSAR pixels are empty. To address these two problems, I calculate the weighted mean of the InSAR velocities based on their uncertainties in an n×n window surrounding the GNSS location. I initialise the size of the window as a 5×5 grid, and let it grow in steps of 2 until it finds at least 10 non-empty pixels from InSAR. All stations find enough InSAR pixels within a window size of 61×61, which is equivalent to an area of $\sim 4.3 \times 4.3$ km^2, smaller in dimension than short wavelength tectonic motions like creep would typically occur. The uncertainty associated with this weighted mean of InSAR velocity, σ_{InSAR}, is set to the standard deviation of the velocity pixels in the window. The total uncertainty of this GNSS-InSAR offset, σ_{offset}, is set to the root sum squares of σ_{InSAR} and σ_{GNSS}, where σ_{GNSS} is the σ_{LOS} in Equation 4.2. The σ_{offset} uncertainties are used to weight the ramp inversion as follows:

$$\begin{bmatrix} \frac{1}{\sigma_1} \times d_1 \\ \vdots \\ \frac{1}{\sigma_n} \times d_n \end{bmatrix} = \begin{bmatrix} \frac{1}{\sigma_1} & (x_1 & y_1 & 1) \\ \vdots & \vdots & \vdots & \vdots \\ \frac{1}{\sigma_n} & (x_n & y_n & 1) \end{bmatrix} \times \begin{bmatrix} a \\ b \\ c \end{bmatrix} \tag{4.3}$$

where $d_1 \ldots d_n$ are the n offsets between InSAR and GNSS LOS, $\sigma_1 \ldots \sigma_n$ are the corresponding σ_{offset}, $(x_1, y_1) \ldots (x_n, y_n)$ are the GNSS locations in the frame index, and $ax + by + c$ is the ramp to be inverted for. As the preliminary tests based on frame overlaps did not show compelling evidence for the need of higher order adjustments, and as a higher-order ramp could potentially remove tectonic signals, I continue to remove planar ramps to minimise alteration of the InSAR data. An example of projecting one frame of InSAR LOS map to the GNSS LOS points is shown in Fig 4.9.

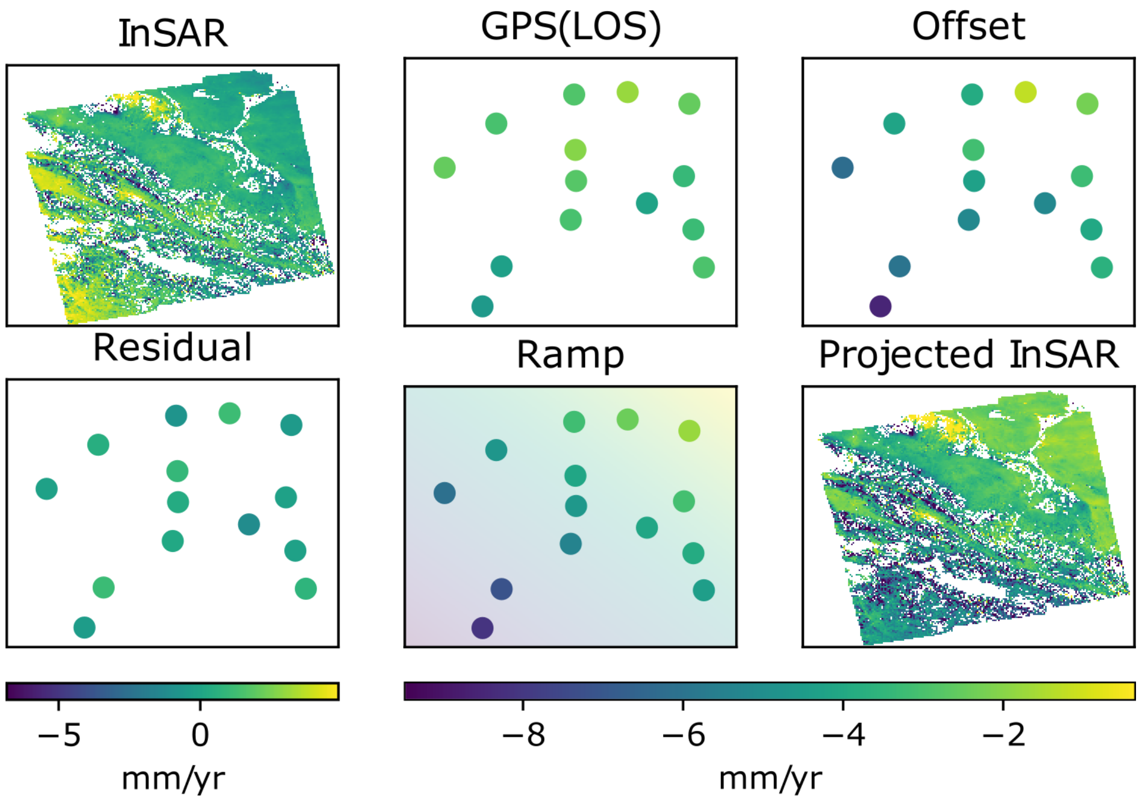

Figure 4.9: An example of projecting the InSAR LOS velocities to the 3D GNSS LOS velocities from the frame 026A_05128_131313 (Fig 4.6b). Offset = GNSS(LOS) - InSAR, Projected InSAR = InSAR + Ramp, Residual = Offset - Ramp. The semi-transparent background colour of the Ramp panel represents the ramp applied to the InSAR LOS map with the dots in full colour representing the ramp values at the GNSS locations.

Using this approach, I demonstrate the necessity of applying ramps in both range and azimuth by revealing an azimuthal ramp in the GNSS–InSAR LOS residuals after applying the planar ramp defined by GNSS–InSAR LOS offsets in the middle frame to the whole 128A track which was previously stitched with range ramps removed based on the frame overlaps (see Section B.2). Therefore, I fit a planar ramp to all frames and use this to adjust the InSAR LOS velocities. The residuals between the GNSS LOS and the adjusted InSAR LOS velocities give an average mode of -0.09 mm/yr and an average standard deviation of 1.60 mm/yr (Fig 4.10). The average mode of the overlap offsets between projected frames becomes 0.036 mm/yr, with the largest magnitude of the mode offset below the 1 mm/yr level (Fig 4.11), suggesting that projecting InSAR LOS velocities to GNSS LOS velocities is an effective way of stitching the InSAR velocity frames together. The resultant average standard deviation is 0.98 mm/yr, slightly higher than the 0.90 mm/yr from the preliminary test of fitting ramps along range, suggesting there is a trade-off between fitting the GNSS LOS and fitting the InSAR frame overlaps. Therefore, a joint inversion method aimed at simultaneously fitting the GNSS LOS and InSAR frame overlaps is suggested.

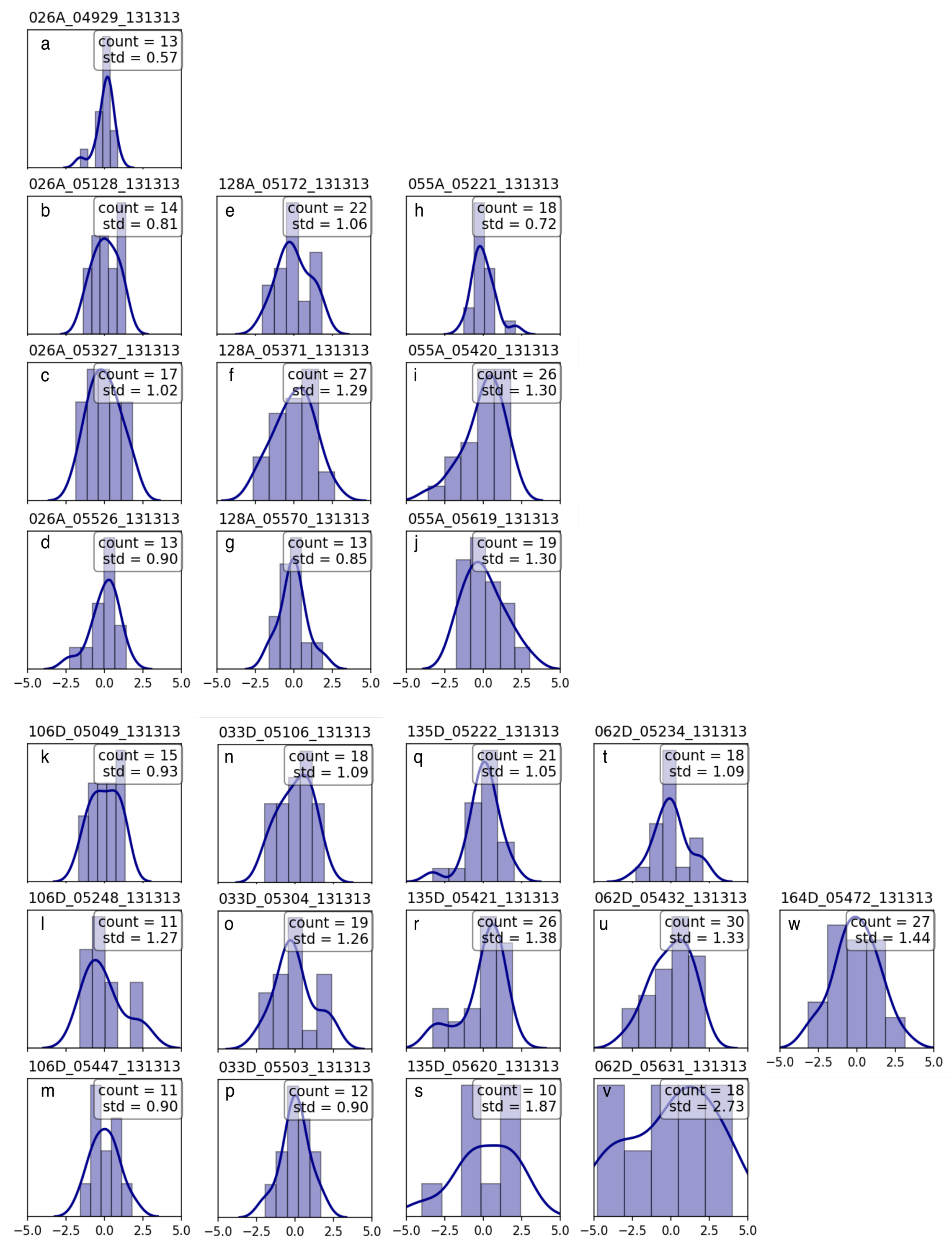

Figure 4.10: Histograms of residuals between the GNSS and the adjusted InSAR LOS velocities for all (a-j) ascending and (k-w) descending frames. By default, only 3D stations are used, except for cases when there are fewer than 10 3D stations in the frame (a,d,m,p), then 2D stations are also used.

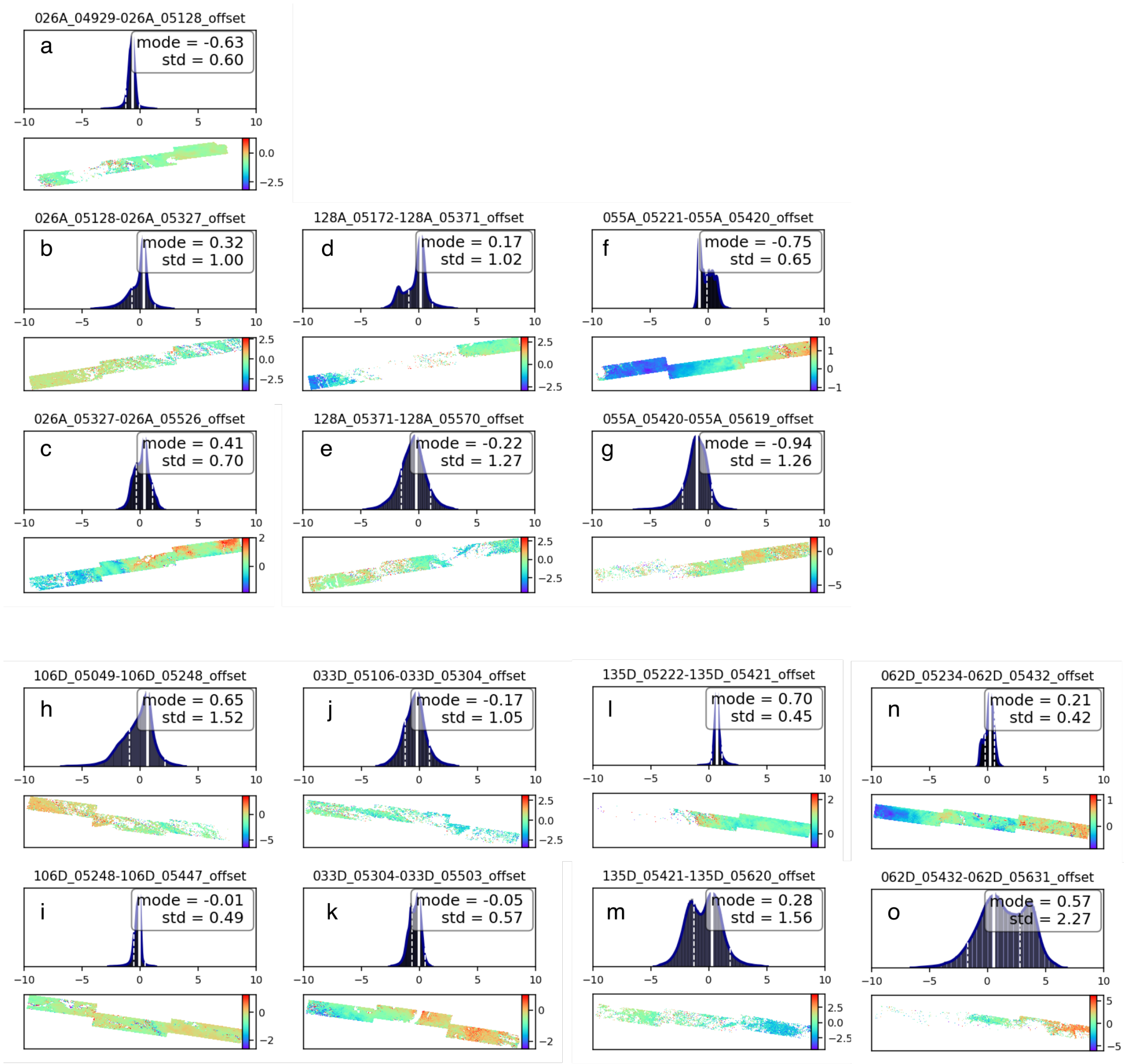

Figure 4.11: Histograms of pixel differences between overlap areas of frames along each track after projecting each frame to the GNSS LOS velocities. Solid white lines mark the mode of the histogram. Dotted white lines mark one standard deviation from the mode. Residual ramps are visible in multiple panels.

4.3.4 Joint inversion of InSAR frame overlaps and GNSS data

The key to the joint inversion lies in determining the relative weights between the InSAR overlaps and GNSS points. Without applying a weighting factor, the inversion is dominated by the InSAR points as there are many more of them. In order to determine the best balance between the effects of InSAR overlaps and GNSS data, a reference map was first created to guide the different weighting tests. This was done using a three-step approach: (1) Each frame is projected to the GNSS LOS; (2) The projected frames in the same track are stitched together by fixing the northernmost frame and fitting a ramp in range based on their frame overlaps successively to the south; (3) The merged track is projected to all the GNSS LOS in the track again to adjust for the along-range tilts applied in step (2) (Section B.3, Fig B.3-B.7).

A joint inversion without weighting introduced undesired tilts in the azimuth direction (Fig B.8), as the InSAR points in the narrow strips of InSAR overlap influence the ramp in the azimuth direction. Applying a weighting of the simple ratio between the number of InSAR points, m, and the number of GNSS points, n, weights the GNSS points too heavily and the ramps between the frame overlaps reappeared (Fig B.9). A solution is to apply a weighting of the square-root of the ratio, $\sqrt{m/n}$. This weighting minimises the sum of the average of the squared misfits from the InSAR-InSAR overlaps and the average of the squared misfits from the InSAR-GNSS offsets:

$$\begin{bmatrix} \frac{1}{\sqrt{\sigma^2(i1)+\sigma^2(i2)}}(I1-I2) \\ \frac{1}{\sqrt{\sigma^2(i2)+\sigma^2(i3)}}(I2-I3) \\ \frac{\sqrt{m/n}}{\sqrt{\sigma^2(i1)+\sigma^2(g1)}}(I1-G1) \\ \frac{\sqrt{m/n}}{\sqrt{\sigma^2(i2)+\sigma^2(g2)}}(I2-G2) \\ \frac{\sqrt{m/n}}{\sqrt{\sigma^2(i3)+\sigma^2(i3)}}(I3-G3) \end{bmatrix} = \begin{bmatrix} \frac{1}{\sqrt{\sigma^2(i1)+\sigma^2(i2)}}(x & y & 1 & -x & -y & -1 & 0 & 0 & 0) \\ \frac{1}{\sqrt{\sigma^2(i2)+\sigma^2(i3)}}(0 & 0 & 0 & x & y & 1 & -x & -y & -1) \\ \frac{\sqrt{m/n}}{\sqrt{\sigma^2(i1)+\sigma^2(g1)}}(x & y & 1 & 0 & 0 & 0 & 0 & 0 & 0) \\ \frac{\sqrt{m/n}}{\sqrt{\sigma^2(i2)+\sigma^2(g2)}}(0 & 0 & 0 & x & y & 1 & 0 & 0 & 0) \\ \frac{\sqrt{m/n}}{\sqrt{\sigma^2(i3)+\sigma^2(i3)}}(0 & 0 & 0 & 0 & 0 & 0 & x & y & 1) \end{bmatrix} \begin{bmatrix} a_1 \\ b_1 \\ c_1 \\ a_2 \\ b_2 \\ c_2 \\ a_3 \\ b_3 \\ c_3 \end{bmatrix} \tag{4.4}$$

where $I1 \ldots I3$ are successive InSAR frames along track, the $G1 \ldots G3$ are GNSS LOS velocities in the corresponding InSAR frames, $\sigma(in)$ and $\sigma(gn)$ are the uncertainties associated with the InSAR and GNSS measurements as previously defined in σ_{InSAR} and σ_{GNSS}, x and y are the column and row numbers in the merged pixel index frame and a_n, b_n, c_n are the ramp parameters to be inverted for the nth frame. The resultant LOS velocity maps are shown in Fig 4.12, very similar to the reference map in Fig B.6, thus proving $\sqrt{m/n}$ is a good choice for the relative weighting between the InSAR frame overlaps and the InSAR-GNSS overlaps.

There are several key features in the final LOS maps. (1) The step boundaries between frame overlaps that were present in the initial merged maps (Fig 4.1) disappeared in the final maps. (2) The step changes between the track boundaries become more obvious, reflecting the changes of incidence angles across the tracks. (3) The ascending LOS velocities become increasingly negative and the descending LOS velocities become increasingly positive from north to south, as expected from the increasing east-component velocities in the same direction (Fig 4.5a). (3) There are two areas of step changes in the LOS velocities, one in the northeast and one in the southwest, both striking ∼120°. These step changes correspond to the single-strand portions of the strike-slip Haiyuan and Kunlun Faults where the deformation style is relatively simple. (4) The velocity changes become more diffused and the measurements become noisier over the Qilianshan thrusts in the northwest and the multiple fault branches of the East Kunlun Fault in the south west where the tectonics is more complex.

The residuals between frame overlaps and between GNSS and InSAR LOS from the joint inversion are shown in Fig 4.13 and 4.14. The average standard deviations of 0.87 mm/yr between the frame overlaps is slightly higher than the 0.84 mm/yr in the 3-step approach and the average standard deviations of 1.27 mm/yr between the GNSS and InSAR LOS is slightly lower than the 1.36 mm/yr in the 3-step approach.

This is a result of the trade-off between fitting the two data sets. The joint inversion is preferred here because this approach treats the two data sets equally whereas the 3-step approach compromised the fits between the InSAR and GNSS LOS to preferentially fit the frame overlaps. The average of the mode values between the frame offsets is -0.054 mm/yr, very close to zero. The distributions of the InSAR-GNSS residuals, with an average of 45 GNSS points per track, also follow Gaussian shapes centred near zero. These are great results which demonstrate the effectiveness of this method.

The offsets between track overlaps (Fig 4.15) also become smaller in magnitude and follow more Gaussian distributions as compared to Fig 4.4. Note the negative sign in all the mode values after projecting the frame maps to the reference frame of the GNSS data (Fig 4.15). This is due to the order of subtraction, with the western track minus the eastern track, a reflection of the increases of LOS velocities at track boundaries from west to east (Fig B.6). This can be explained by the change of incidence angles across track, with a $\sim 10°$ decrease across the ascending track boundaries and a $\sim 10°$ increase across the descending track boundaries, both of which will produce a step increase of LOS velocities given the viewing geometries (Fig 4.5a and Fig 4.7). The exact magnitudes of the offsets between tracks will be a function of the relative velocities in different components and the incidence angles, as alluded by the simplified model for the pure strike-slip case in Fig B.1.

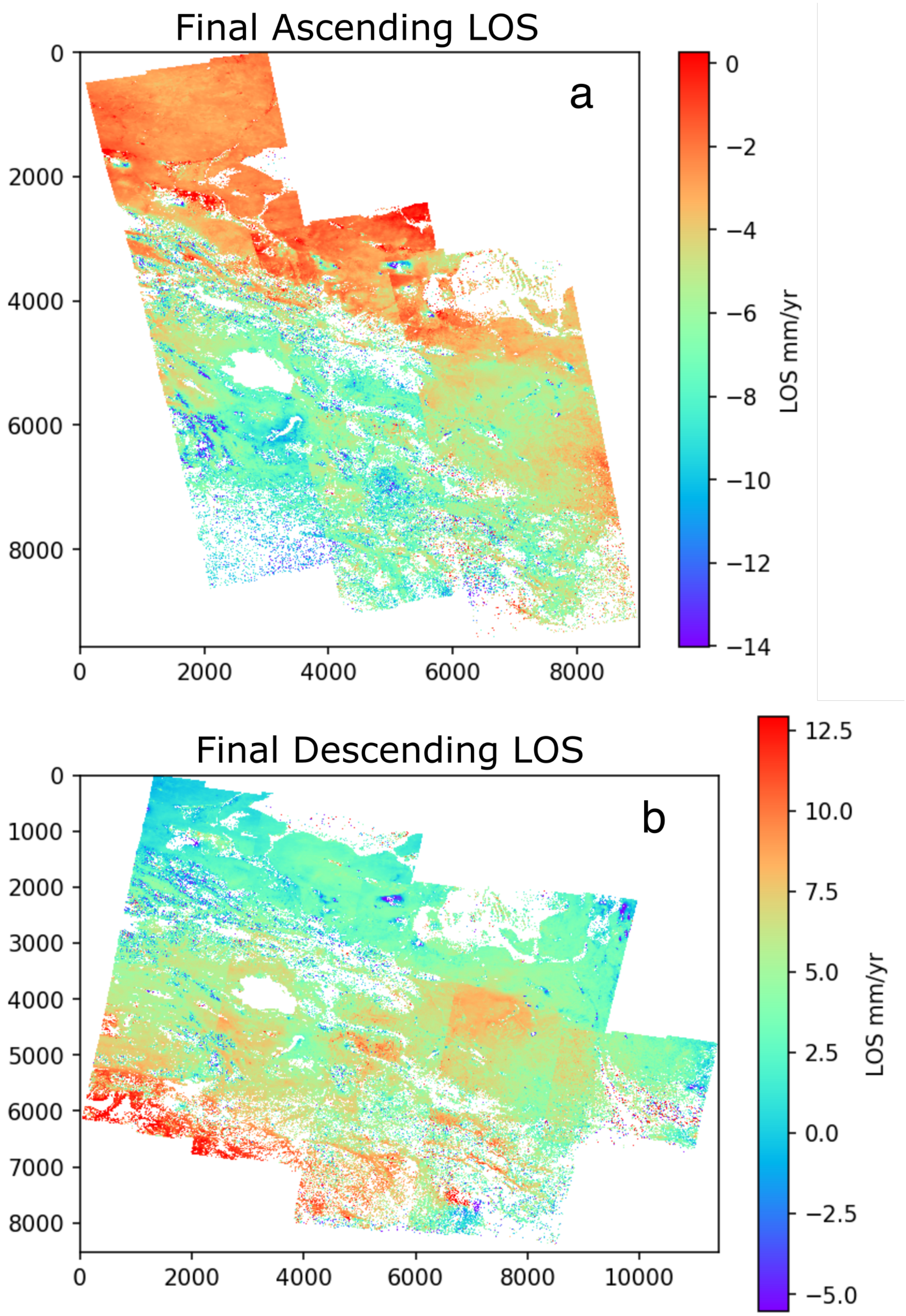

Figure 4.12: (a) Ascending and (b) descending LOS maps of joint inversion with weighting factor $\sqrt{m/n}$.

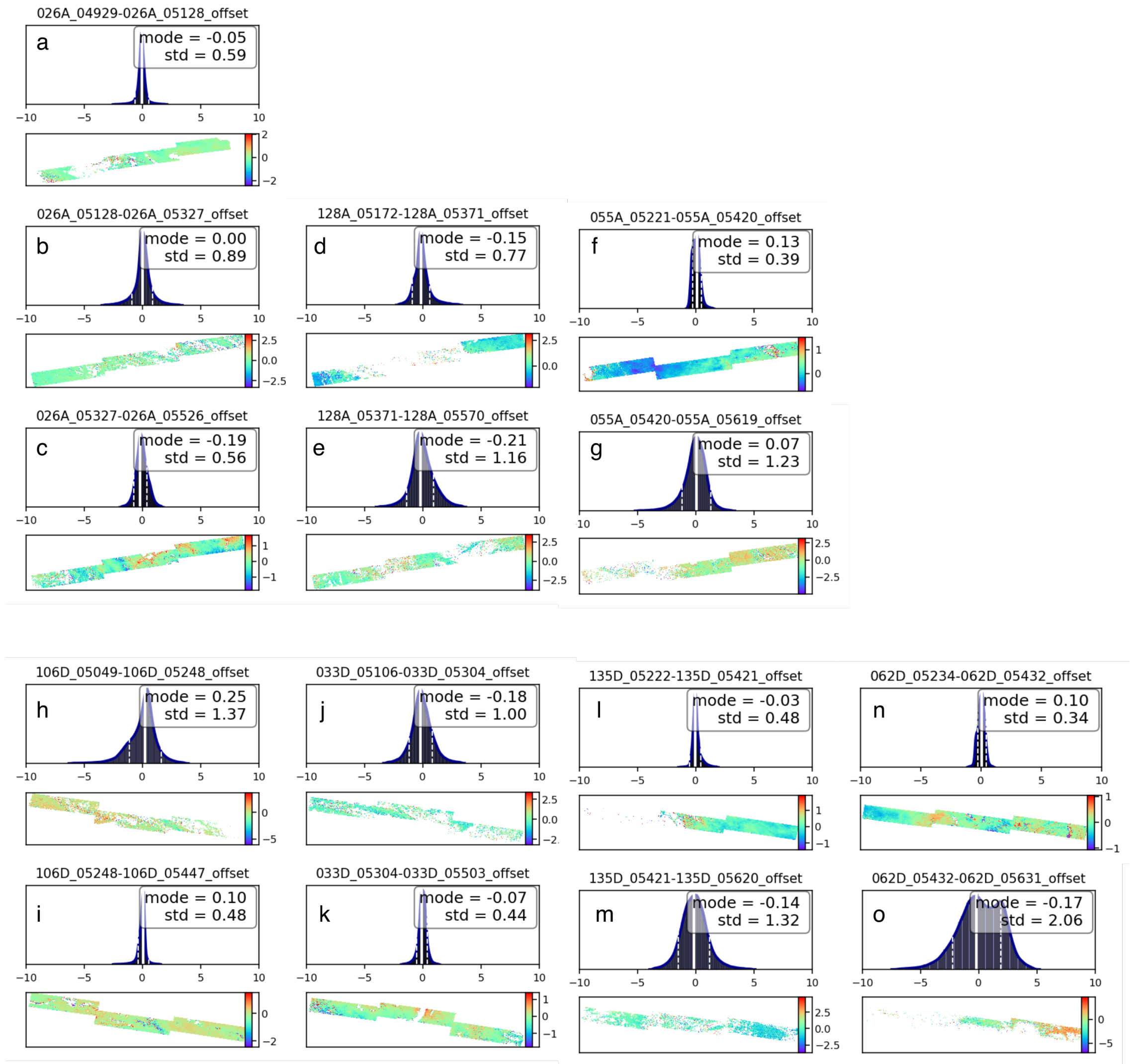

Figure 4.13: Histograms of pixel differences between frame overlaps after joint inversion with weighting factor $\sqrt{m/n}$.

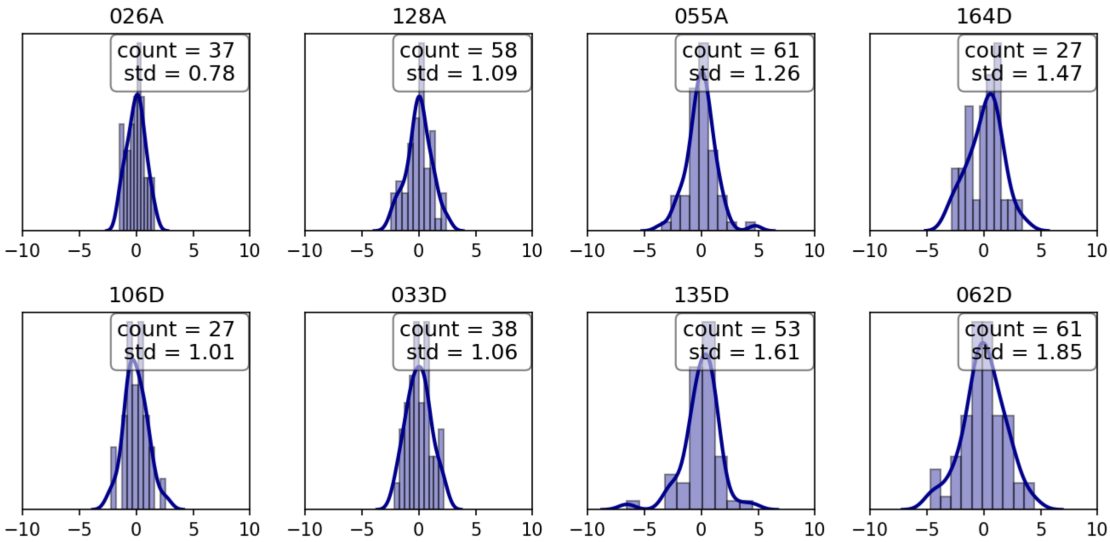

Figure 4.14: Histograms of residuals between GNSS LOS and InSAR LOS in each track after joint inversion with weighting factor $\sqrt{m/n}$.

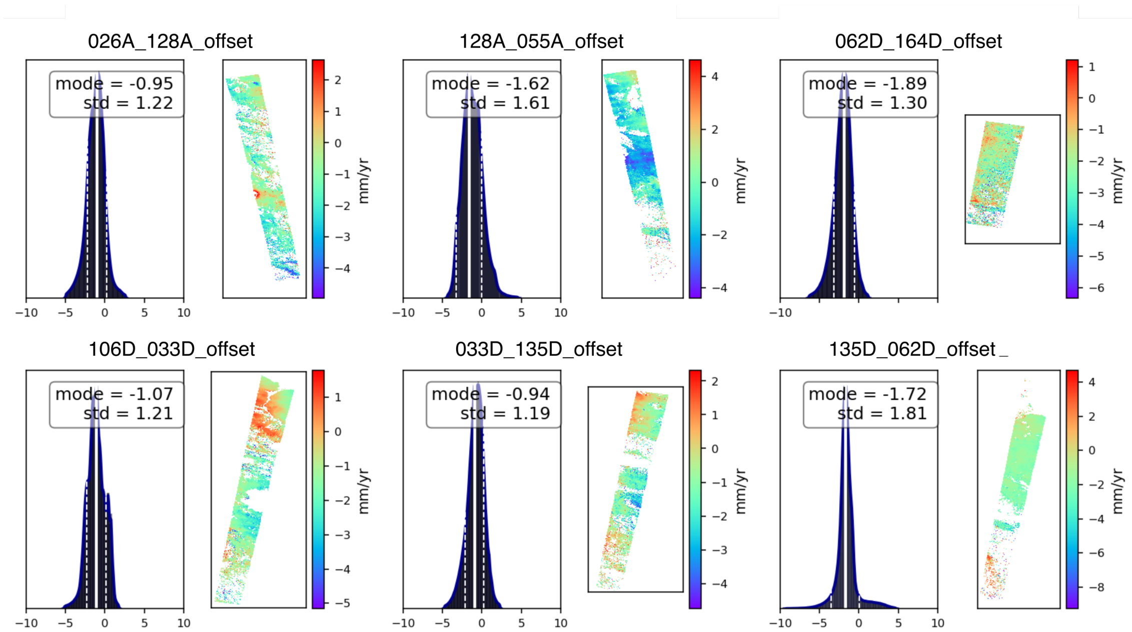

Figure 4.15: Histograms of pixel differences between track overlaps after joint inversion with weighting factor $\sqrt{m/n}$.

4.4 Velocity decomposition

The ascending and descending LOS velocity maps provide measurements in two directions. In order to decompose the two LOS velocities into standard 3-component velocities (east, north and vertical), a third constraint must be provided. When the area is small and the tectonic setting is uncomplicated (e.g., a local view of a pure strike-slip fault), it is common practice to assume one of the velocity components is zero (*Wang and Wright*, 2012). For regional velocity mapping in areas where this simple assumption does not hold, GNSS data are usually leveraged to provide the additional information needed.

Weiss et al. (2020) used the interpolated N-S velocities from GNSS data and the two LOS velocities to simultaneously solve for the east and vertical velocity components. This method may propagate the uncertainties of the interpolated GNSS north velocities into both the east and vertical components. Despite the already dense GNSS array in the NE Tibetan Plateau and the high precision of the individual GNSS horizontal velocities, the uncertainties associated with the interpolated GNSS field can be large. Here, I describe an alternative method, following a similar method developed by Lin Shen at the University of Leeds (personal communication), in which the velocities are decomposed in two stages to retain the quality of the InSAR data in the best-constrained east component.

4.4.1 Stage 1: Decompose into V_E and V_{UN}

Without introducing the GNSS measurements, the ascending and descending InSAR LOS allow two velocity components to be resolved. Given the geometry of the observations, the LOS is the most sensitive to V_E (Fig 4.8). Therefore, the choice is to first decompose the two LOS velocities into V_E and V_{UN} via:

$$LOS = -V_E \times cos(\phi)sin(\theta) + V_{UN} \times \sqrt{1 - sin^2(\theta)cos^2(\phi)} \tag{4.5}$$

where V_E is the east velocity and V_{UN} is the projection onto the north-up plane of the combined LOS contributions from the north and vertical components. ϕ is the heading angle and θ is the incidence angle. A mathematical proof of Equation 4.5 is provided in Figure B.10, which is based on the geometry in Fig 4.7.

In practice, this partitioning is done by performing weighted least square inversions for pixels covered by up to two ascending and two descending tracks. The general form of the inversion is as follows:

$$\begin{bmatrix} \frac{1}{\sigma(a_0)} \times LOS_{a_0} \\ \frac{1}{\sigma(a_1)} \times LOS_{a_1} \\ \frac{1}{\sigma(d_0)} \times LOS_{d_0} \\ \frac{1}{\sigma(d_1)} \times LOS_{d_1} \end{bmatrix} = \begin{bmatrix} \frac{1}{\sigma(a_0)} & (-cos(\phi_{a_0})sin(\theta_{a_0}) & \sqrt{1 - sin^2(\theta_{a_0})cos^2(\phi_{a_0})}) \\ \frac{1}{\sigma(a_1)} & (-cos(\phi_{a_1})sin(\theta_{a_1}) & \sqrt{1 - sin^2(\theta_{a_1})cos^2(\phi_{a_1})}) \\ \frac{1}{\sigma(d_0)} & (-cos(\phi_{d_0})sin(\theta_{d_0}) & \sqrt{1 - sin^2(\theta_{d_0})cos^2(\phi_{d_0})}) \\ \frac{1}{\sigma(d_1)} & (-cos(\phi_{d_1})sin(\theta_{d_1}) & \sqrt{1 - sin^2(\theta_{d_1})cos^2(\phi_{d_1})}) \end{bmatrix} \begin{bmatrix} V_E \\ V_{UN} \end{bmatrix} \tag{4.6}$$

where a_0, a_1, b_0 and b_1 are notations for the up to two possible overlapping ascending tracks and up to two possible overlapping descending tracks covering a pixel. σ is the LOS velocity uncertainty derived during the time series inversion discussed in Chapter 3, Section 3.4.5 Fig 3.10d. The number of rows in Equation 4.6 per pixel depends on the number of tracks covering the pixel with valid data. Only pixels with both ascending and descending LOS velocities are decomposed into V_E and V_{UN}, hence the resultant maps have the shapes of the overlapping area of the ascending and descending data coverage (Fig 4.16a-b).

Equation 4.6 can be written as $d = Gm$, where d is a vector whose components are the LOS input velocities, G is the transformation matrix and m is a vector with components V_E and V_{UN} that is to be solved for. The uncertainties, $\sigma(V_E)$ and $\sigma(V_{UN})$ associated with V_E and V_{UN} can be calculated from the uncertainties of the

LOS velocities through the covariance matrix:

$$cov(m) = [G^T cov(d)^{-1} G]^{-1} \tag{4.7}$$

where $cov(d)$ and $cov(m)$ are the covariance matrices of d and m, respectively. As the different LOS samples are independent, $cov(d)$ is a diagonal matrix with squares of the uncertainties of the LOS velocities used ($\sigma(a_0)$, $\sigma(a_1)$. $\sigma(d_0)$ and/or $\sigma(d_1)$). The diagonal terms of $cov(m)$ are the variance of V_E and V_{UN}, so taking square roots of the diagonal terms of $cov(m)$ gives the uncertainties $\sigma(V_E)$ and $\sigma(V_{UN})$ (Fig 4.16c-d).

The resolved V_{UN} is only an approximation of the true value as the exact value of V_{UN} is dependent on the track-specific heading and incidence angles which are different for the 2–4 tracks covering a pixel. Nevertheless, the differences in heading angles, ϕ, is at most $\sim 1°$, and the differences in incidence angles, θ, is at most $\sim 10°$ (Fig 4.5e-h). Thus, the error in the $\sqrt{1 - sin^2(\theta_{track}) cos^2(\phi_{track})}$ term of Equation 4.6 is at most 10%, and the largest errors will occur at the overlaps between tracks in the same orientation.

To understand the effect of difference in incidence angles on the uncertainty of V_{UN}, I perform a test to solve for V_E and V_{UN} per pair of overlapping ascending and descending tracks and calculate the offsets between the overlapping areas of the V_E and V_{UN} patches (Section B.6). The differences between all possible combinations of overlapping patches, which are the fragments of the track overlaps where the uncertainties are expected to be the largest, are 0.05 ± 1.12 mm/yr for V_E and -0.10 ± 0.89 mm/yr for V_{UN} (Fig B.11-B.14). Therefore, the uncertainty in the V_{UN} estimate because of the approximation made is at the same level as that in the velocity measurements.

Therefore, the V_{UN} in Fig 4.16b could be considered as a weighted mean of the 3–4 true V_{UN} values from different tracks covering a pixel. The quantitative effect

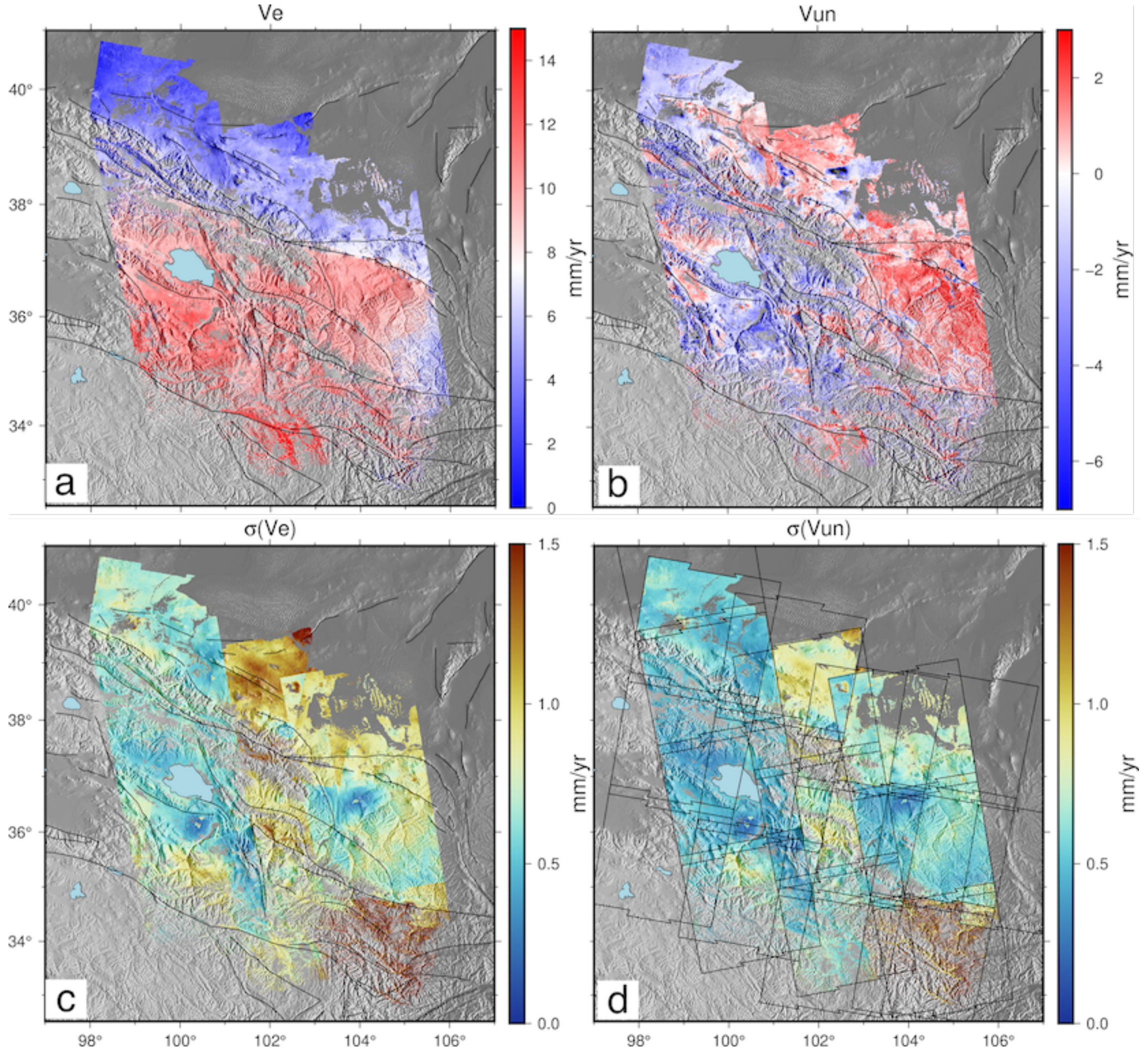

Figure 4.16: (a-b) Decomposed V_E and V_{UN} velocity maps and (c-d) their associated uncertainties.

of the approximation is cuptured by $\sigma(V_{UN})$ (Fig 4.16d) and will be reflected in the uncertainty in the V_U and V_N decomposition from V_{UN} in the next stage.

4.4.2 Stage 2: Decompose V_{UN} into V_U and V_N

By this stage, we have isolated V_E and are left with the estimates of the subvertical component V_{UN} which is related to the two as yet undetermined velocity components V_U and V_N. It is now necessary to introduce external constraints on the velocities, i.e., GNSS, to separate these two components. There are two reasons for interpolate

V_N instead of V_U from the GNSS. One is that InSAR LOS is insensitive to motion in the along track direction, which is close to north-south. Using interpolated V_N from GNSS velocities allows me to obtain the best possible V_U field. Second, not all GNSS stations have a vertical component and the horizontal velocity of GNSS is also better constrained than the vertical component; hence interpolating V_N from GNSS allows me to take advantage of the high-quality V_N velocities of the 2D GNSS stations that were not used when I projected the InSAR LOS to the common reference frame.

First, I interpolated the N-S component of the GNSS velocities from *Wang and Shen* (2020) and their associated uncertainties to obtain a map of V_N and a map of $\sigma(V_N)$ (Fig 4.17a,b) using the GMT *surface* command. The *surface* function finds the minimum curvature surface by fitting an elastic sheet under tension to the given points and I apply a high tension to ensure that maxima and minima can only occur at the control points. This may not be true, but best preserves the data. For the same reason, no pre-filtering of the GNSS velocities was performed. Any anomalies are associated with high uncertainties which are interpolated in the same way (Fig 4.17b).

For each track, k, that covers a pixel, a V_U and a $\sigma(V_U)$ can be calculated:

$$V_U = V_{UN} \times \frac{\sqrt{1 - sin^2(\theta_k)cos^2(\phi_k)}}{cos(\theta_k)} - V_N \times \frac{sin(\phi_k)sin(\theta_k)}{cos(\theta_k)} \tag{4.8}$$

$$\sigma(V_U) = \sqrt{\sigma^2(V_{UN}) \times \frac{1 - sin^2(\theta_k)cos^2(\phi_k)}{cos^2(\theta_k)} + \sigma^2(V_N) \times \frac{sin^2(\phi_k)sin^2(\theta_k)}{cos^2(\theta_k)}} \tag{4.9}$$

Hence, pixels in the overlapping areas can have up to four realisations of V_U and $\sigma(V_U)$. For the final result, weighted means of the V_U and $\sigma(V_U)$ are obtained for each pixel (Fig 4.17c,d). V_U is weighted by $1/\sigma(V_U)$ so the better constrained V_U is preferred. $\sigma(V_U)$ is weighted by itself so the larger $\sigma(V_U)$ is preferred, in an effort to account for the underestimated $\sigma(V_N)$ in the interpolated areas.

Given how the interpolation smooths the velocity field, it is unrealistic that V_N

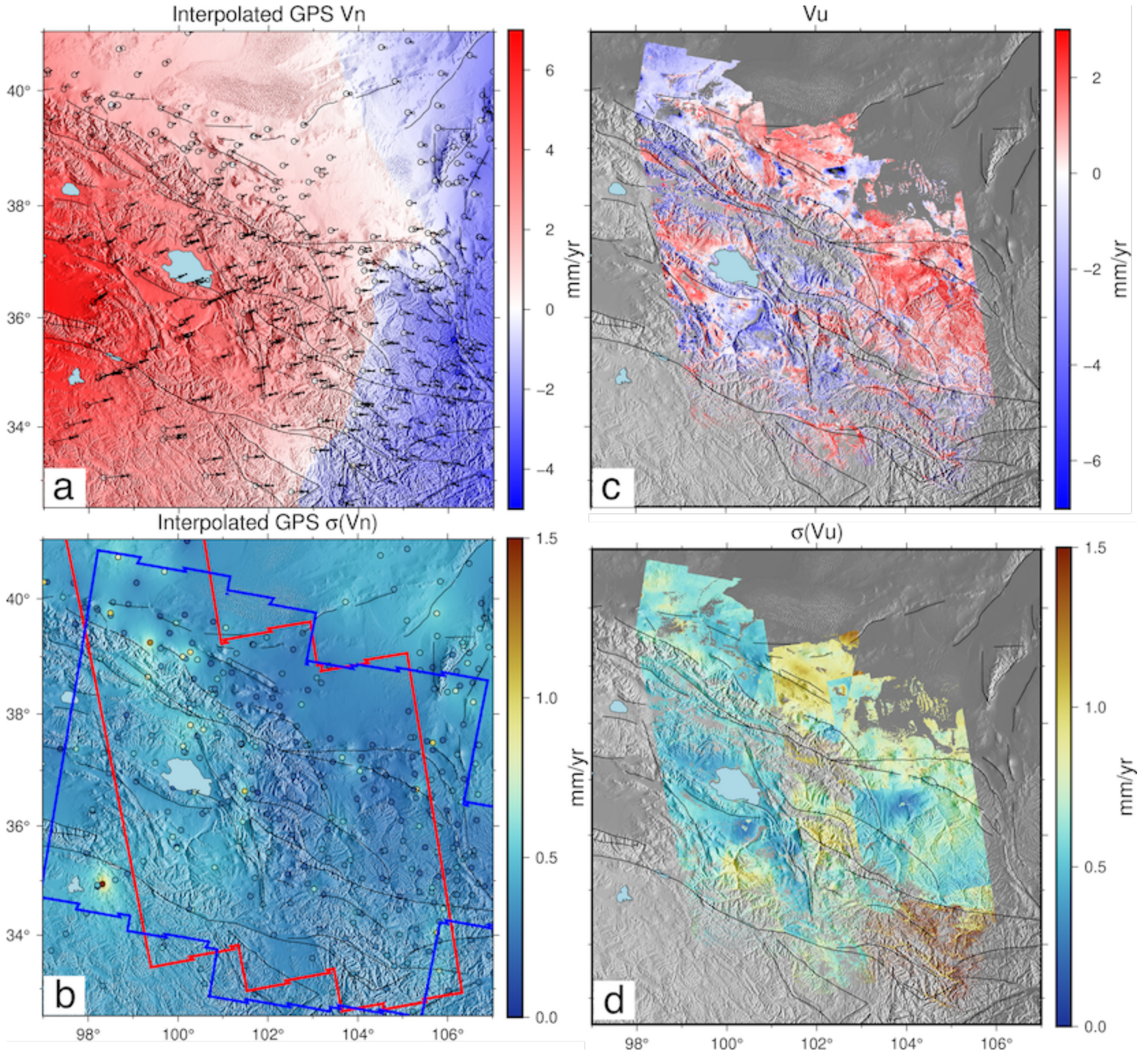

Figure 4.17: (a-b) Maps of V_N and $\sigma(V_N)$ as interpolated from GNSS velocities (*Wang and Shen*, 2020). (c-d) Resolved maps of V_U and $\sigma(V_U)$.

in the interpolated areas share the same levels of $\sigma(V_N)$ as the control points do. Nevertheless, based on Equation 4.9 and values of incidence and heading angles (Fig 4.5e-h), $\sigma(V_U)$ is the root sum squares of ~14% of $\sigma(V_N)$ and ~101% of $\sigma(V_{UN})$, suggesting the contribution from $\sigma(V_N)$ is relatively small. Comparing Fig 4.16d and Fig 4.17d reveals that $\sigma(V_U)$ is only slightly higher than $\sigma(V_{UN})$ and still below 1 mm/yr for most of the tracks, apart from the frame in the southeast which experienced difficulty in processing. Overall, $\sigma(V_U)$ is also smaller than $\sigma(V_E)$ (Fig 4.16c), suggesting the error coming from the approximation of V_{UN} is relatively small.

4.5 Regional V_E and V_U velocity maps

The aforementioned data analysis results in two regional velocity maps and associated uncertainties covering an area of 439254 km^2 with sampling of one point every 3 arcseconds (∼90 m) (Fig 4.18 to Fig 4.21). The V_E map (Fig 4.18) is decomposed from InSAR LOS only and is in the Eurasia-fixed reference frame. V_U (Fig 4.19) is derived from the V_{UN} from InSAR and the interpolated GNSS V_N and is in the stable north neighbour of the Tibetan Plateau reference frame. The maps provide a new, extensive view of the crustal motion of the NE Tibetan Plateau at an unprecedented resolution.

Remarkable agreement is observed between the InSAR and GNSS V_E velocities (Fig 4.18), the component in which the GNSS velocities are more precise (Fig 4.20). The one-to-one fit for V_E has a gradient of 0.98 and a R^2 of 1 (Fig 4.22a). It is encouraging to see the good agreement between InSAR and GNSS velocities even in the southwest frame (Fig 4.18) where InSAR uncertainties are the highest (Fig 4.20), which further exemplifies the high quality of the InSAR V_E map.

The V_U map is characterised by a high degree of variability, which would not have been captured by the GNSS points alone. While the InSAR-GNSS correlation for the V_U component is less impressive (Fig 4.22b), with a gradient of 0.31 and R^2 of 0.51, the fit is not expected to be good given the uncertainties associated with the GNSS V_U being almost as large as their absolute values. Nevertheless, there is still a positive correlation, albeit a weak one. Fig 4.21 highlights the advantage of using InSAR for measuring vertical motion as the uncertainty of the vertical component velocity map is significantly reduced to a level of about one third of that of GNSS velocity data.

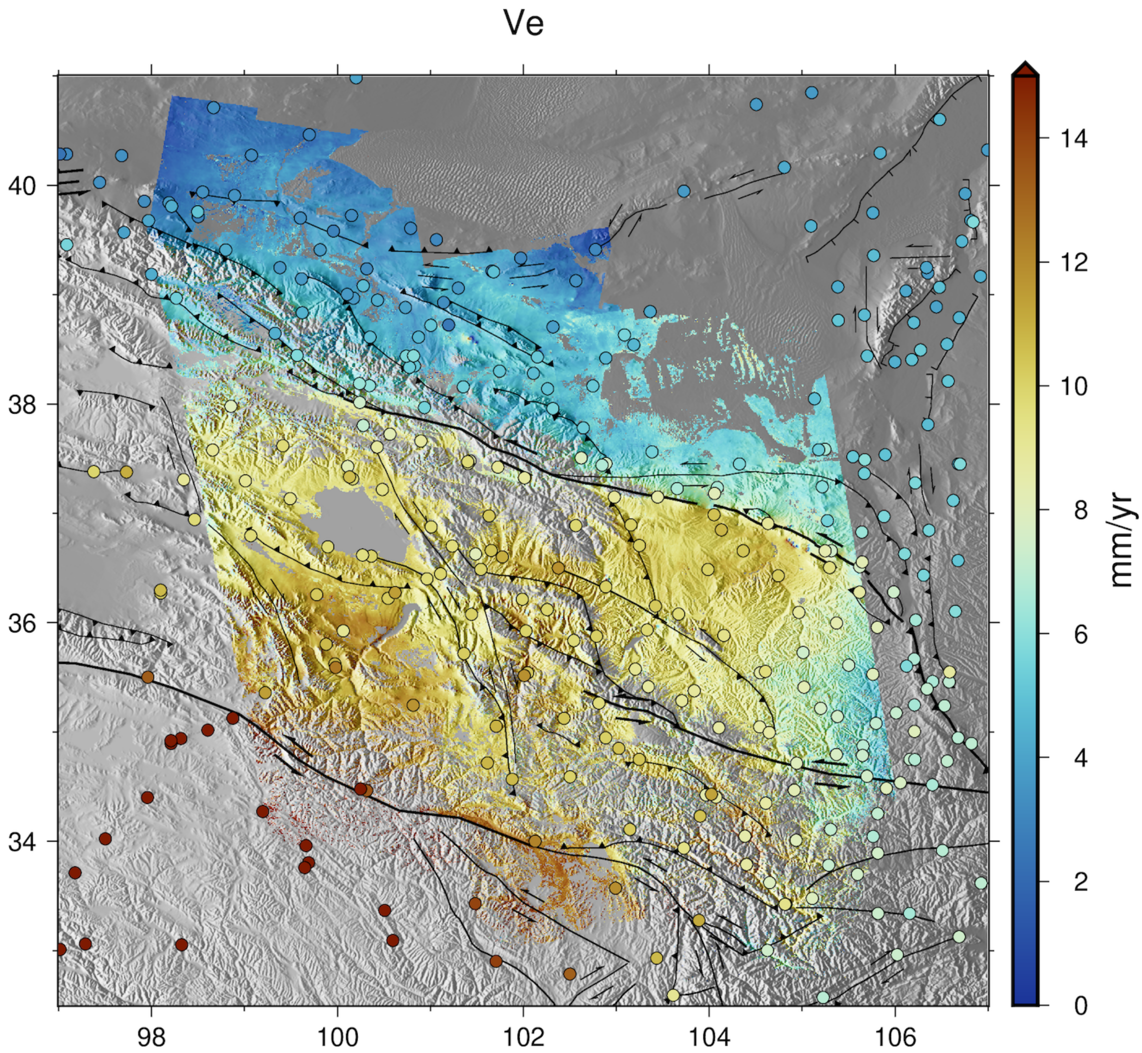

Figure 4.18: East-west velocity map of the NE Tibetan Plateau partitioned from the ascending and descending InSAR LOS velocities. Dots are GNSS measurements of E-W velocities.

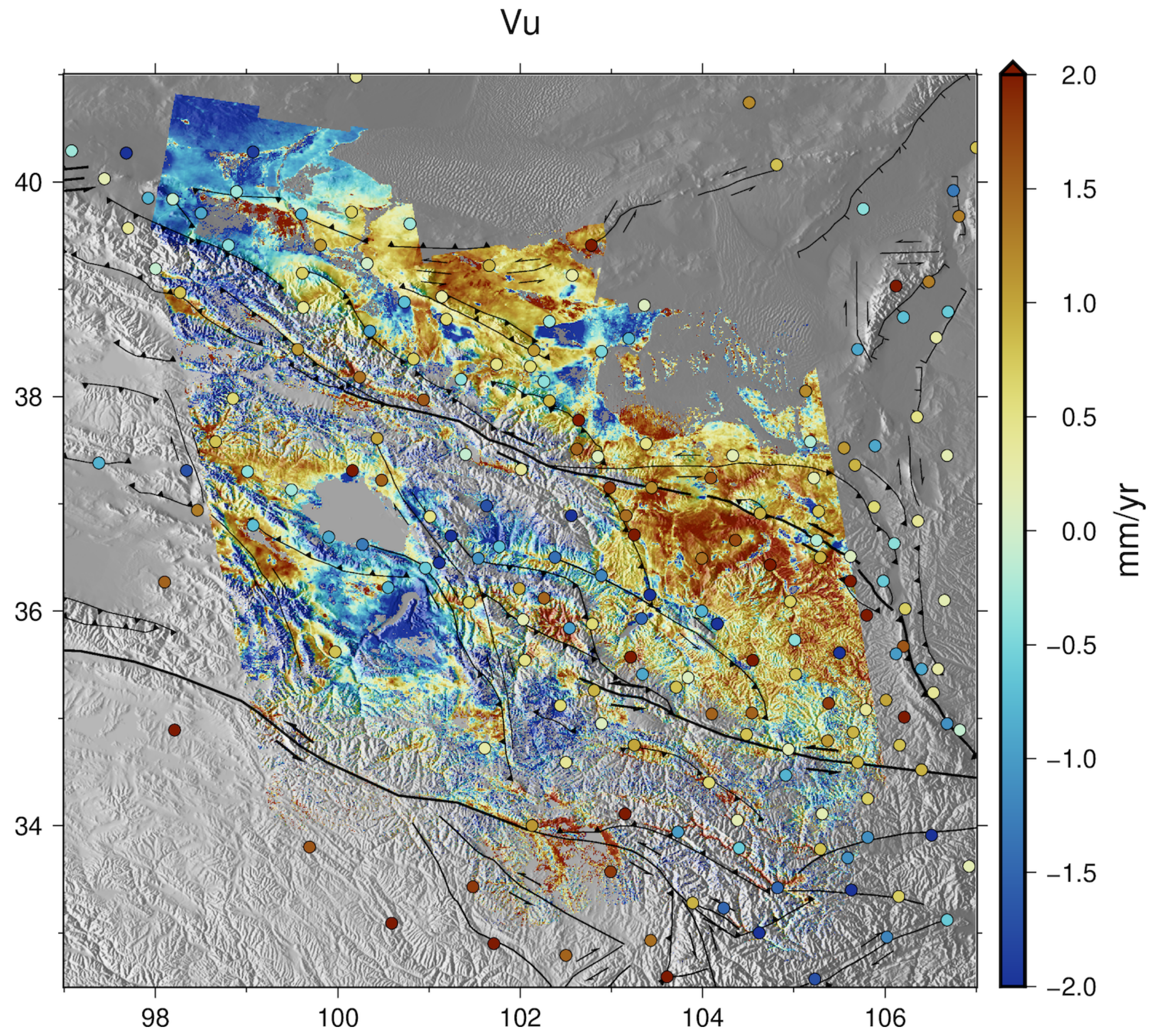

Figure 4.19: Vertical velocity map of the NE Tibetan Plateau derived from InSAR V_{UN} and the interpolated V_N map from GNSS points. Dots are GNSS measurements of vertical velocities.

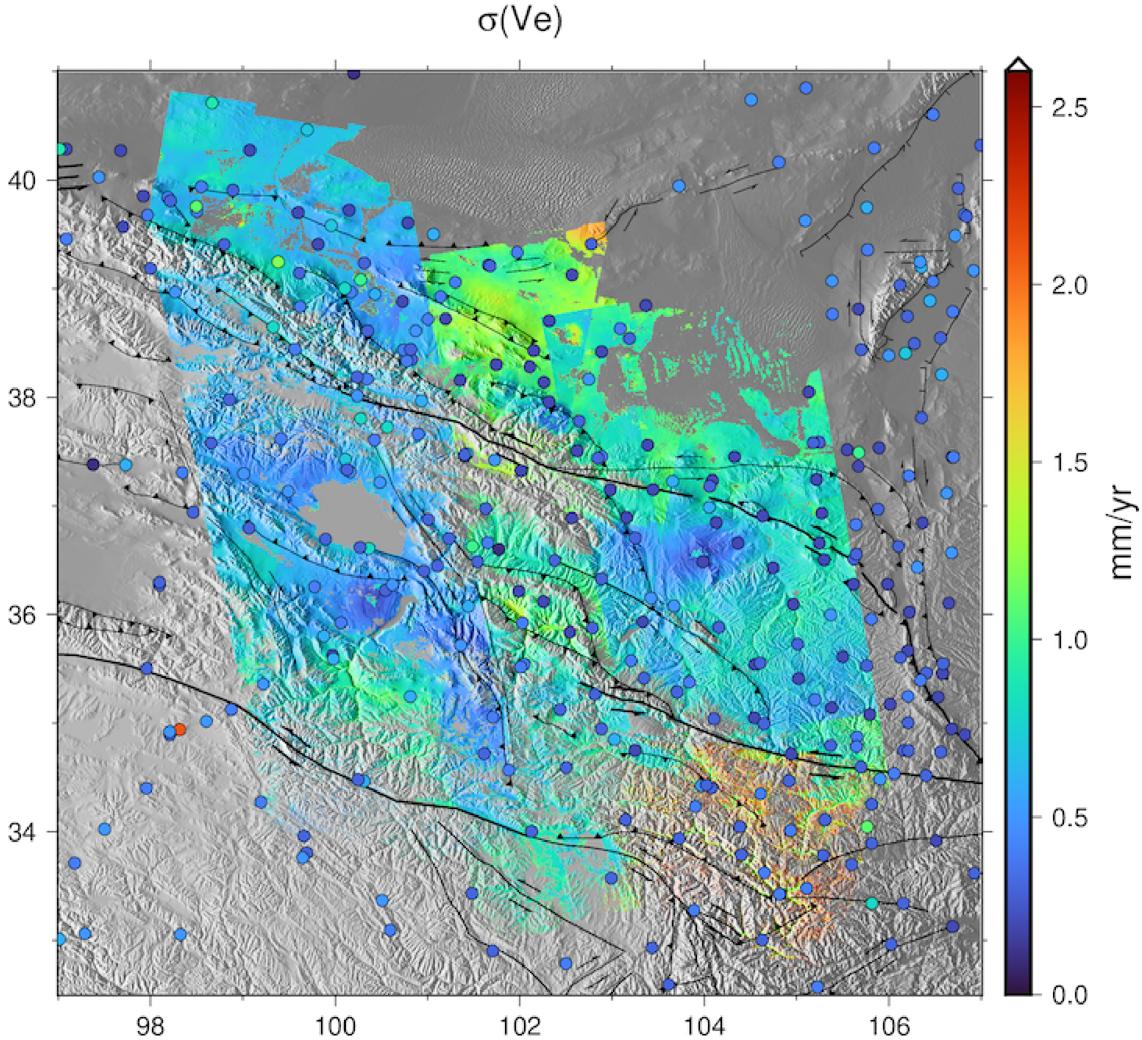

Figure 4.20: Uncertainties of the east-west velocity map of the NE Tibetan Plateau. Dots are corresponding GNSS uncertainties for comparison.

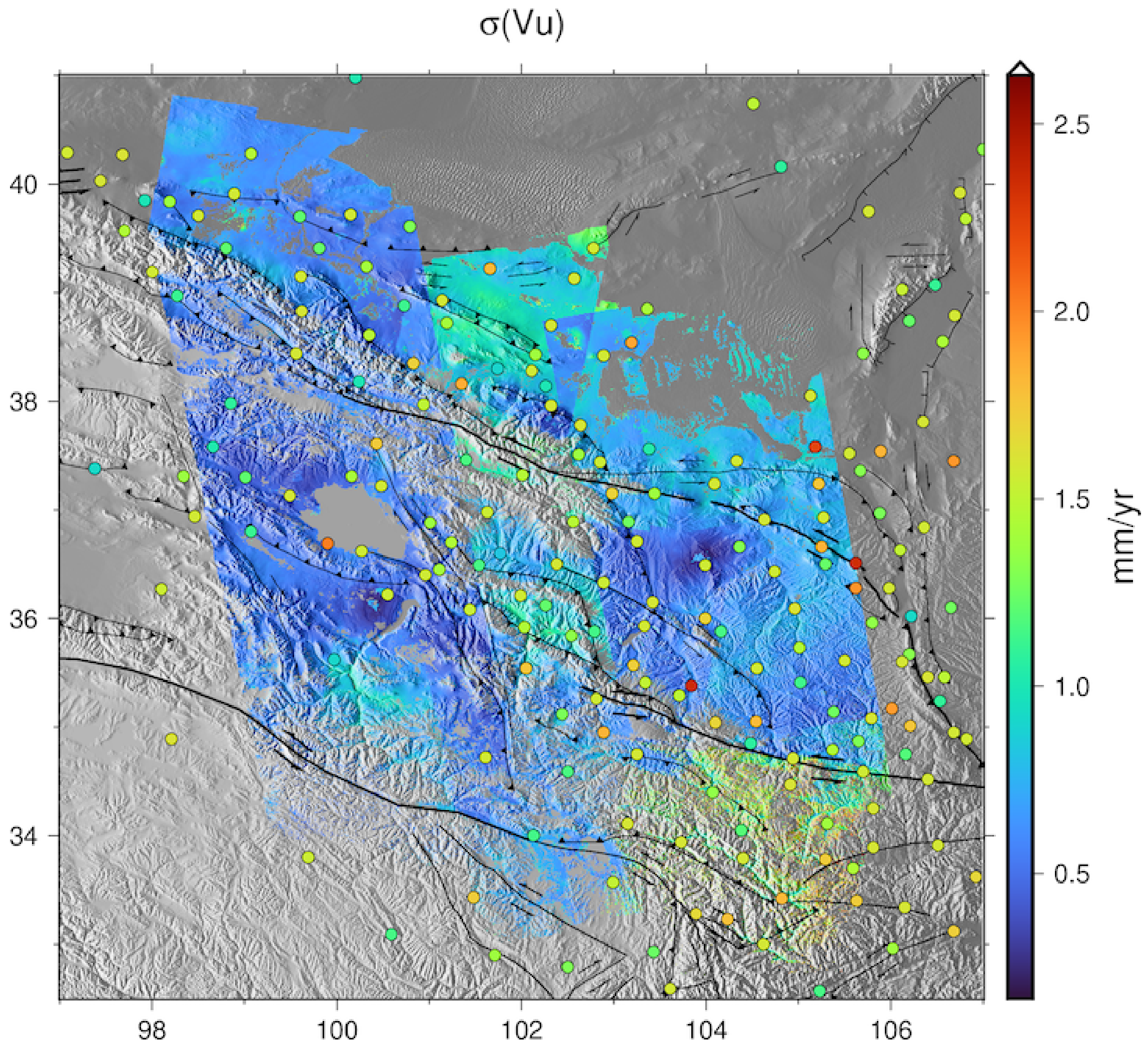

Figure 4.21: Uncertainties of the vertical velocity map of the NE Tibetan Plateau. Dots are corresponding GNSS uncertainties for comparison.

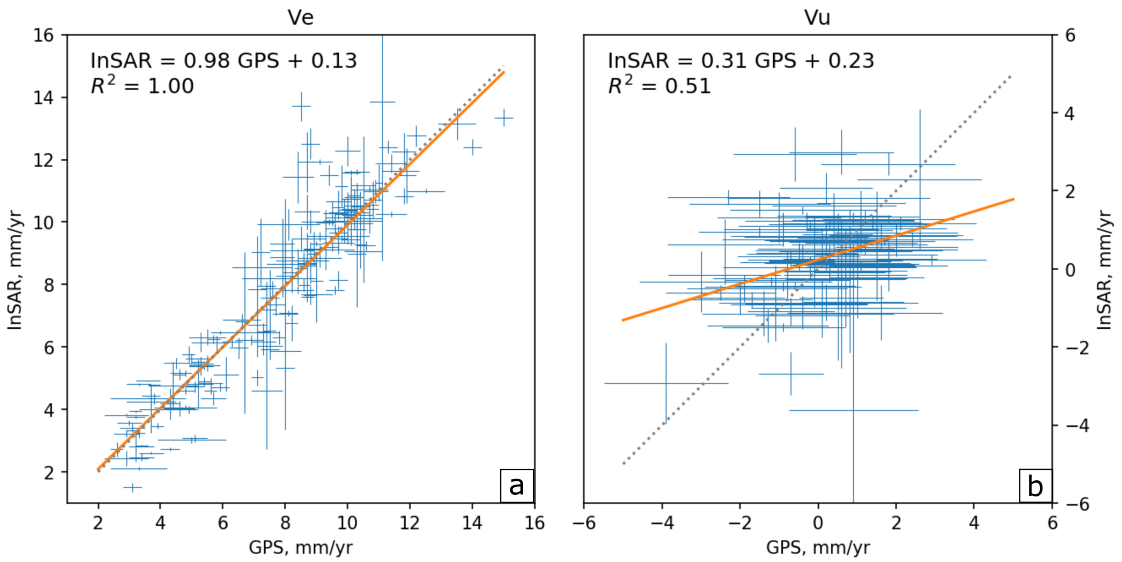

Figure 4.22: Comparison between InSAR and GNSS (a) V_E and (b) V_U velocities. Blue crosses = InSAR and GNSS velocities with uncertainties. Orange line = weighted best-fit line of the distribution labeled in text. Grey dotted line = one-to-one line for reference.

4.5.1 Uncertainty analysis

Several features are observed from the uncertainty maps in Fig 4.20 and Fig 4.21. (1) The highest uncertainties (1.5 – 3 mm/yr) come from the southeast frame where the IFGs suffer from decorrelation and unwrapping problems (Section 3.5). (2) The top frame of the middle track also show higher uncertainties (1.0 – 1.5 mm/yr) than the rest of the map because of the shorter time series covered by the data set (Fig 3.3). (3) There are areas with exceptionally low uncertainties, e.g., to the south of the Haiyuan Fault and to the south of the Qinghai Lake (Fig 3.10). These are resulted from the reference areas being chosen there during the time series processing, compounded by the effect of spatially correlated patterns in the IFGs. Referencing all IFGs in a frame to the mean phase in a reference area suppresses the scatter in the local time series, thus lowering the associated uncertainties in the reference area. Despite GACOS correction and ramp removal, the final IFGs still have spatially correlated structures, such as residual atmospheric patterns, residual orbital ramps and ground deformation patterns (*Jolivet and Simons*, 2018). This means the larger region that is spatially correlated with the reference area would also have uncertainties artificially reduced to below their true values.

In order to fully take into account the spatially dependent uncertainties, the standard approach is to calculate semi-variograms for each frame of the LOS velocity maps, from which three parameters are inverted to characterise the distance-dependent correlations per frame (*Sudhaus and Jónsson*, 2009; *Daout et al.*, 2016b; *Bagnardi and Hooper*, 2018; *Murray et al.*, 2019). From the three parameters, a variance-covariance matrice can be constructed to weight subsequent modelling steps such as projecting the InSAR velocity maps to the GNSS reference frame and decomposing the LOS velocities into V_E and V_U. Nevertheless, this approach can be computationally expensive, especially at the velocity decomposition step. If all the pixels are to be solved simultaneously, this could incur a variance-covariance matrix of the size $10^7 \times 10^7$ and become impractical to implement.

A simpler approach that is easier to implement would be to calculate the semi-variogram per frame of the LOS uncertainty map based on pixel distances to the reference centre. The inverted parameters from the semi-variograms can be used to calculate the theoretical scaling factor for scaling up uncertainties near the reference area to a theoretical value as if the reference point was not there. The uncertainty map after scaling can be considered as not influenced by the reference areas any more and can be used in Equation 4.4, Equation 4.6 and Equation 4.9 as before. The implementation of this scaling method and the above standard variance-covariance method will be tested in future work.

As it currently stands, the differences between InSAR and GNSS component velocities average to -0.03 mm/yr for V_E and -0.05 mm/yr for V_U showing no systematic bias in the results. The average absolute difference between InSAR and GNSS V_E is 0.78 mm/yr, 30% greater than the 0.59 mm/yr average vector sum of the V_E uncertainties from InSAR and GNSS. This difference is likely to reduce after the spatially correlated uncertainties are taken into account. The average absolute difference between InSAR and GNSS V_U is 1.03 mm/yr, a value in between the 0.38 mm/yr average uncertainty for InSAR V_U and the 1.49 mm/yr average uncertainty for GNSS V_U, suggesting that the poorly constrained GNSS V_U velocities are responsible for most of the differences in the vertical component.

4.5.2 Preliminary analysis of the velocity maps

The V_E map (Fig 4.23) shows a pattern that generally follows what we would expect from regional tectonics. The east velocity decreases northwards with sharp velocity changes localised on the single strand portions of the Haiyuan Fault and the Maqu section of the East Kunlun Fault. The sinistral motion on the Haiyuan Fault extends from eastern edge of the map to the interior of the Qilianshan, where it transitions

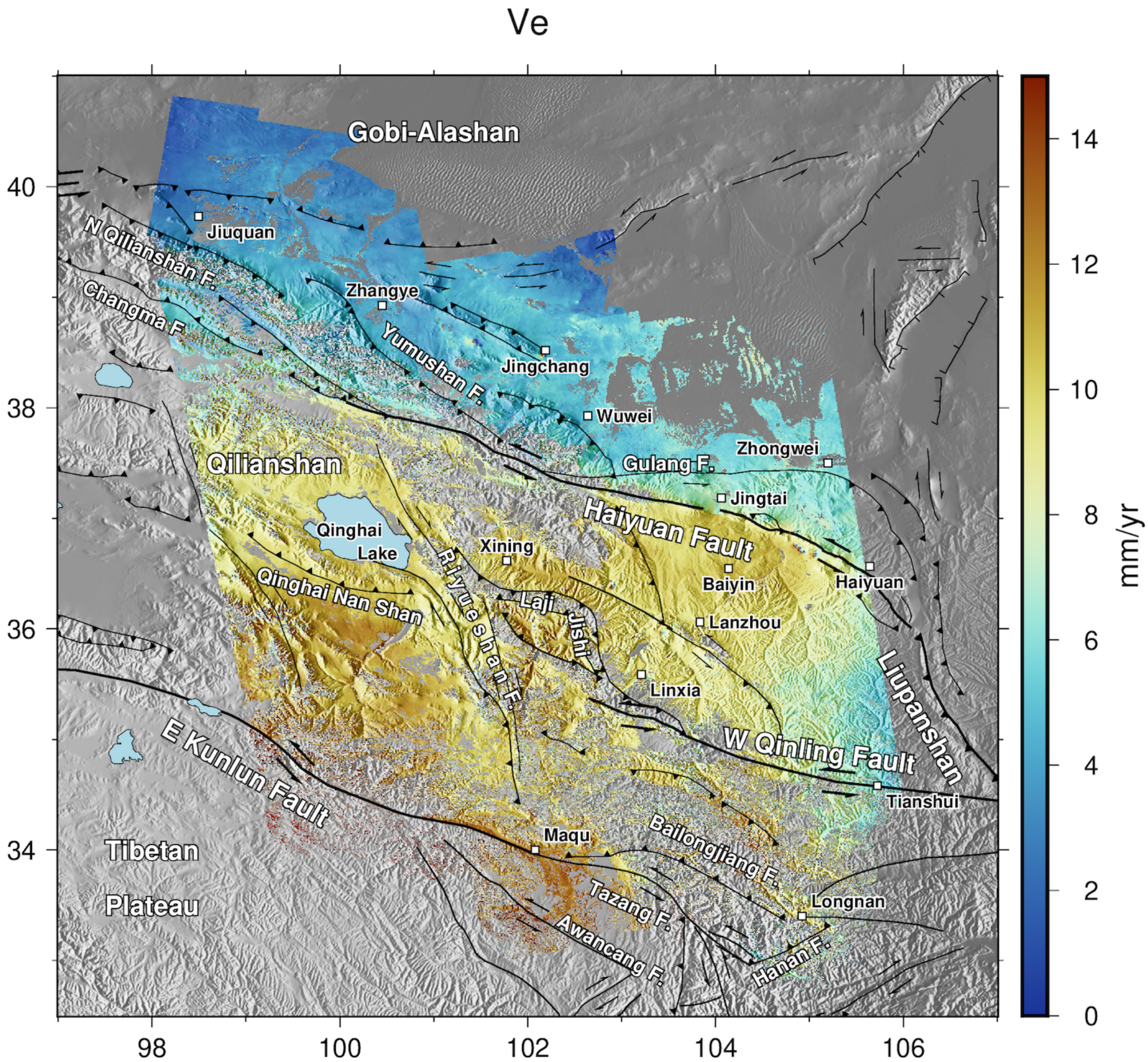

Figure 4.23: East velocity map from InSAR with fault and place labels.

into the Changma and North Qilianshan thrusts. In the interior of the Qilianshan, the velocity changes gradually over a broad region, suggesting distributed deformation. This is consistent with the GNSS result from **?**. The velocity gradient across the Gulang Fault is almost negligible, suggesting little slip partitioned by this structure. Similarly, no significant velocity step happens across the West Qingling Fault, implying its slow motion. However, a smooth west-to-east velocity gradient is present between the Haiyuan and West Qingling Faults, possibly a far field response to the thrust motion on the Liupanshan Fault where the sinistral motion on the Haiyuan

Fault transitions into east-west shortening. Although the motions around the arcuate Laji and Jishi thrusts are less clear due to the decorrelation in the mountains, the velocity change across the Qinghai Nan Shan is obvious, suggesting either fast thrust motion or a sinistral component on the thrust fault. A belt of low V_E is observed around the NNW-SSE trending Riyueshan Fault, consistent with the overall right-lateral motion. Nevertheless, the width of the low V_E region seems to suggest the deformation is likely distributed across a fault zone rather than a simple strike slip fault, especially around the southern segment of the Riyueshan Fault. The faults currently mapped in this area represents an amalgamation of the fault maps of *Yuan et al.* (2013) and *Li et al.* (2020a), but no studies were found on the detailed structures here. The velocity variation across the Kunlun Fault seems to be most localised across a short section near Maqu. As it branches into the Bailongjiang and Tazang Faults at the east end, the deformation becomes more partitioned with the enclosed Bailongjiang microblock slowing down as it approaches the Hanan Fault.

The V_U map (Fig 4.18) offers more surprises. The expected vertical velocity from the styles of faulting alone would be uplift in the Qilianshan thrusts, and minimal vertical motion across areas dominated by the strike slip faults. However, to the first order, there seems to be broad-scale relative uplift around the Haiyuan Fault and to the north of the Qilianshan and subsidence across most of the Qilianshan thrusts and to the east and south of the Qinghai Lake. Nevertheless, this pattern of general uplift in the lowlands in the northeast is also consistent with the slow and young reverse faulting along the Helishan to the north of Hexi Corridor (Fig 1.5), from which *Zheng et al.* (2013b) inferred an outward and northward growth of topography. Although it is surprising to see subsidence dominating the thrusting Qilianshan, this subsidence is interleaved with narrow lenses of uplift in the fault-parallel valleys. In fact, on smaller scales, this anticorrelation between topography and vertical motion is observed not only in the Qilianshan, but also to the west of the Qinghai Lake, at the centre of the

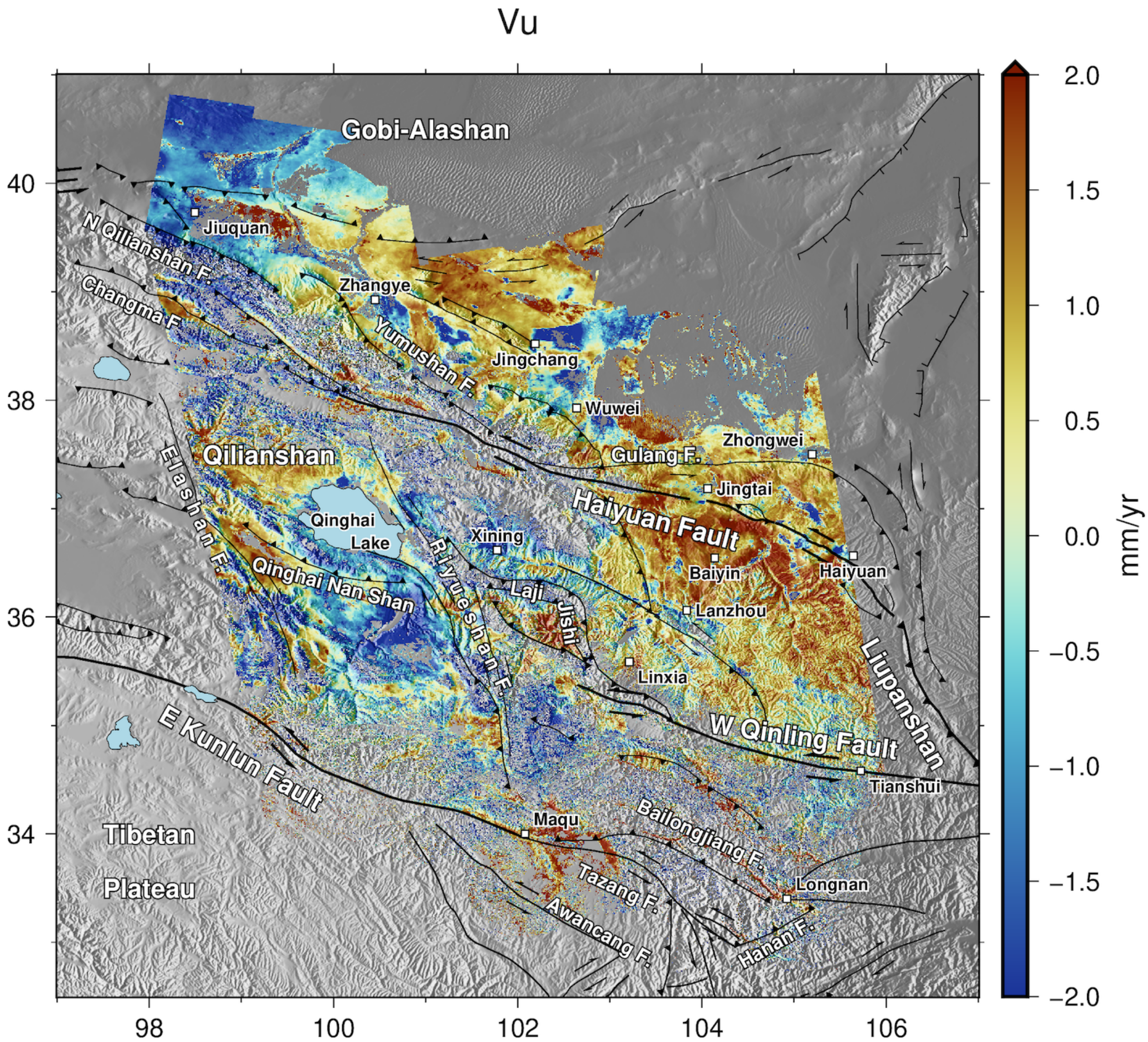

Figure 4.24: Vertical velocity map from InSAR with fault and place labels.

Laji and Jishan Shan and at the fault junction near Maqu (Fig 4.18 with enlarged views in Fig B.15 to Fig B.17). These areas are all within the predicted permafrost zones (*Gruber*, 2012) (Fig B.15 and Fig B.16); it is possible that the freeze-and-thaw cycles of the permafrost in the mountain peaks, as observed by *Daout et al.* (2017) and *Daout et al.* (2020) in western Qilianshan, could be operational across the whole region affected permafrost. If true, this mechanism could cause subsidence of the mountain peaks, due to the melting of permafrost, and uplift of the valleys, where the melt potentially accumulates, and introduce a higher amplitude climatic signal that overprints the tectonic signal here. Exceptions are observed to the south of the

West Qinling Fault, to the south of the Qinghai Nan Shan thrust (Fig 4.18) and at the various triangular patches near the cities to the north of the Qilianshan (Fig B.19). The moon-shaped empty patch to the south of the Qinghai Nan Shan thrust is the Longyangxia Reservoir (Fig B.16), which could potentially offer an explanation to the subsidence around it with gravitational loading of the water column. The various geometrical shapes of subsidence near the major cities to the north of the Qilianshan are likely anthropogenic as they follow closely the shapes of farmlands (Fig B.19), where it is not uncommon to pump up underground water for agriculture (*Zhou*, 1990). The uplift to the north of the Bailongjiang Fault could be of tectonic origin as it is consistent with the north-dipping Bailongjiang oblique thrust (*Li et al.*, 2020a), but the uplift here also coincides with the shape of the drainage basin, thus could also be related to hydrological processes (Fig B.18). The various potentially non-tectonic sources that could influence the vertical motions make the interpretation of the V_U map challenging. More work needs to be done to tease out the various component signals and find the sources of the vertical motions by separating the seasonal signal from the time series (*Daout et al.*, 2020), or by performing principle component analysis (*Daout et al.*, 2017). As the primary purpose of this thesis is the seismic hazard of the NE Tibet, I first focus on mapping the strain rate distribution and deriving the expected seismic rates for this region (Chapter 5).

Chapter 5

Strain Rate and Seismic Hazard Analysis

5.1 Introduction

Strain rate maps are able to highlight areas where deformation is concentrated. This information can be used to estimate the expected earthquake rate, hence informing seismic hazard models. Examples of tectonic estimates of the rates of global shallow seismicity are from *Bird et al.* (2010) and *Bird and Kreemer* (2015). These products are based on a smoothed strain rate map derived from a coarse global GNSS velocity field and global empirical relationships between strain rate and seismicity based on four classes of plate boundaries. With the higher-resolution InSAR velocity maps, such as those derived in Chapter 4, the seismic hazards in the continental interior, where deformation is more distributed and faulting styles more complex, can be investigated in more details. Therefore, this chapter aims to develop an InSAR-based high-resolution crustal strain map for the NE Tibetan Plateau and assess its implications for seismic hazard.

5.2 Crustal Strain of the NE Tibetan Plateau

5.2.1 Strain Rate Calculation

The strain rate tensor, $\dot{\varepsilon}$, is the symmetric part of the velocity gradient tensor, L:

$$L = \begin{bmatrix} \frac{\partial V_E}{\partial x} & \frac{\partial V_N}{\partial x} & \frac{\partial V_U}{\partial x} \\ \frac{\partial V_E}{\partial y} & \frac{\partial V_N}{\partial y} & \frac{\partial V_U}{\partial y} \\ \frac{\partial V_E}{\partial z} & \frac{\partial V_N}{\partial z} & \frac{\partial V_U}{\partial z} \end{bmatrix} \tag{5.1}$$

$$\dot{\varepsilon} = \begin{bmatrix} \dot{\varepsilon}_{xx} & \dot{\varepsilon}_{xy} & \dot{\varepsilon}_{xz} \\ \dot{\varepsilon}_{yx} & \dot{\varepsilon}_{yy} & \dot{\varepsilon}_{yz} \\ \dot{\varepsilon}_{zx} & \dot{\varepsilon}_{zy} & \dot{\varepsilon}_{zz} \end{bmatrix} = \begin{bmatrix} \frac{\partial V_E}{\partial x} & \frac{1}{2}(\frac{\partial V_E}{\partial y} + \frac{\partial V_N}{\partial x}) & \frac{1}{2}(\frac{\partial V_E}{\partial z} + \frac{\partial V_U}{\partial x}) \\ \frac{1}{2}(\frac{\partial V_N}{\partial x} + \frac{\partial V_E}{\partial y}) & \frac{\partial V_N}{\partial y} & \frac{1}{2}(\frac{\partial V_N}{\partial z} + \frac{\partial V_U}{\partial y}) \\ \frac{1}{2}(\frac{\partial V_U}{\partial x} + \frac{\partial V_E}{\partial z}) & \frac{1}{2}(\frac{\partial V_U}{\partial y} + \frac{\partial V_N}{\partial z}) & \frac{\partial V_U}{\partial z} \end{bmatrix} \tag{5.2}$$

where x, y, z represent east, north and up directions. The magnitude of strain rate is the second invariant of the strain rate tensor expressed as $\dot{\varepsilon}_{II} = \sqrt{\dot{\varepsilon}_{ij}^2}$, where $\dot{\varepsilon}_{ij}$ are the entries of the strain rate tensor with the index notation $i, j = 1 \ldots 3$ and the repeated indices are summed over with the Einstein summation notation.

The decomposed V_E, V_N and V_U velocity maps measured at the crustal surface allow me to derive the top two rows of the velocity gradient tensor, L. Without knowledge of the change of velocity with depth, the $\partial/\partial z$ terms of L are unknowns. Therefore, the full strain rate tensor, $\dot{\varepsilon}$, cannot be obtained. However, the four horizontal velocity gradients, i.e.,the top left four entries of L, can give the top left four entries of $\dot{\varepsilon}$, which are the components related to the horizontal strain rate. As the shear stress at the upper surface of the crust zero, the vertical axis has to be one of the principal component of the strain rate tensor at the surface, and thus the other two principal components will lie in the horizontal plane (*Bird et al.*, 2010; *Bird and Kreemer*, 2015). Therefore, I can follow *Sandwell and Wessel* (2016) and *Wang and Shen* (2020) to calculate the second invariant, or magnitude, of the horizontal strain rate as:

$$\dot{\varepsilon}_{II_h} = \sqrt{\dot{\varepsilon}_{xx}^2 + \dot{\varepsilon}_{xy}^2 + \dot{\varepsilon}_{yx}^2 + \dot{\varepsilon}_{yy}^2} = \sqrt{\dot{\varepsilon}_{xx}^2 + 2\dot{\varepsilon}_{xy}^2 + \dot{\varepsilon}_{yy}^2} \tag{5.3}$$

This formulation is not the same as that in *England and Mckenzie* (1982) or in VELMAP, a code developed by *Wang and Wright* (2012), where they calculate the second invariant of the full strain rate tensor, assuming incompressibility and invariability of the horizontal velocities with depth. The horizontal strain rate is preferred here as it is based on fewer assumptions.

For V_E and V_U, I have both the decomposed InSAR velocity maps and the GNSS point measurements. For V_N, only the GNSS measurements are available. Here, I first work with the V_E and V_U from InSAR and the V_N from GNSS to obtain the six components of L. In order to highlight tectonic features, I filter the velocity component data down to 1-, 5-, 10-, 15- and 20-arcminute resolutions using the GMT *blockmedian* tool. Using the weight option with the inverse of pixel uncertainties, I calculate for each window of a specified resolution a weighted median velocity where the sum of weights associated velocities below and above it are equal. GMT *surface*s are then fitted to the filtered GNSS V_N and InSAR V_E and V_U data to create the interpolated maps. The derivatives of the filtered velocity maps are calculated using the GMT *grdmath* tool with the -*M* option to turn the map units into distance units. The resultant filtered velocity maps and the related components of the velocity gradient tensor are shown in Fig 5.1, Fig 5.2 and Fig 5.3. It is noted that some high strain rates could be missed because of the use of the GMT *blockmedian* tool. In future work, a median filter on a finer discretization could be implemented to preserve the creep as a very narrow zone of very high strain rate.

As expected, the major E-W oriented strike-slip faults are the main feature of the $\partial V_E/\partial y$ distribution (Fig 5.1k-o). The NW-SE oriented Qilianshan thrusts are highlighted in both the $\partial V_U/\partial x$ and the $\partial V_U/\partial y$ plots (Fig 5.2f-j and k-o). Due to the sparse GNSS control points compared to the grid spacing, the filtered V_N velocity

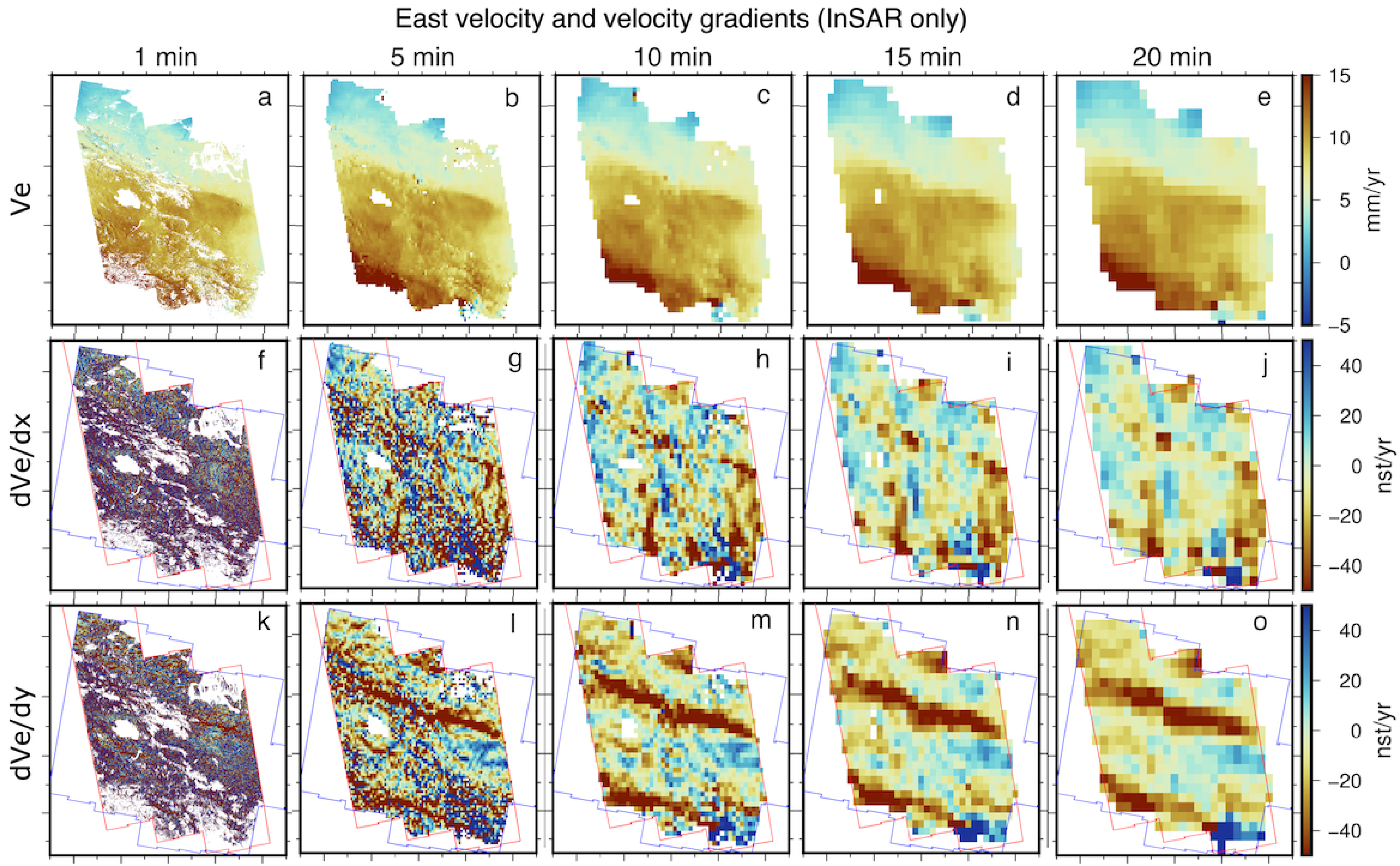

Figure 5.1: East InSAR velocity maps filtered at resolutions of (a) 1 arcminute, (b) 5 arcminutes, (c) 10 arcminutes, (d) 15 arcminutes and (e) 20 arcminutes. (f-i) are the derivatives of (a-e) in the east direction. (k-o) are the derivatives of (a-e) in the north direction.

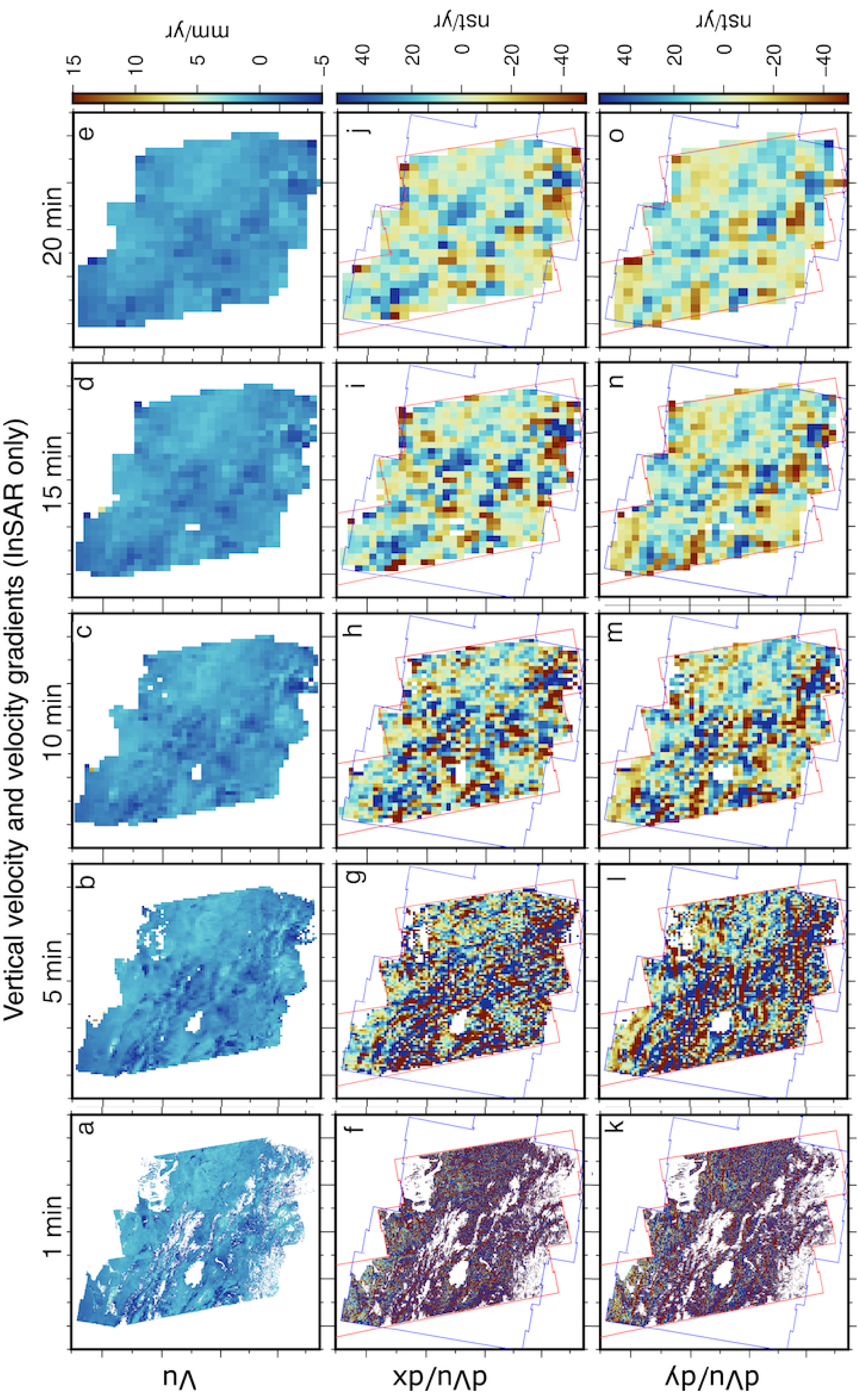

Figure 5.2: Vertical InSAR velocity maps filtered at resolutions of (a) 1 arcminute, (b) 5 arcminutes, (c) 10 arcminutes, (d) 15 arcminutes and (e) 20 arcminutes. (f-i) are the derivatives of (a-e) in the east direction. (k-o) are the derivatives of (a-e) in the north direction.

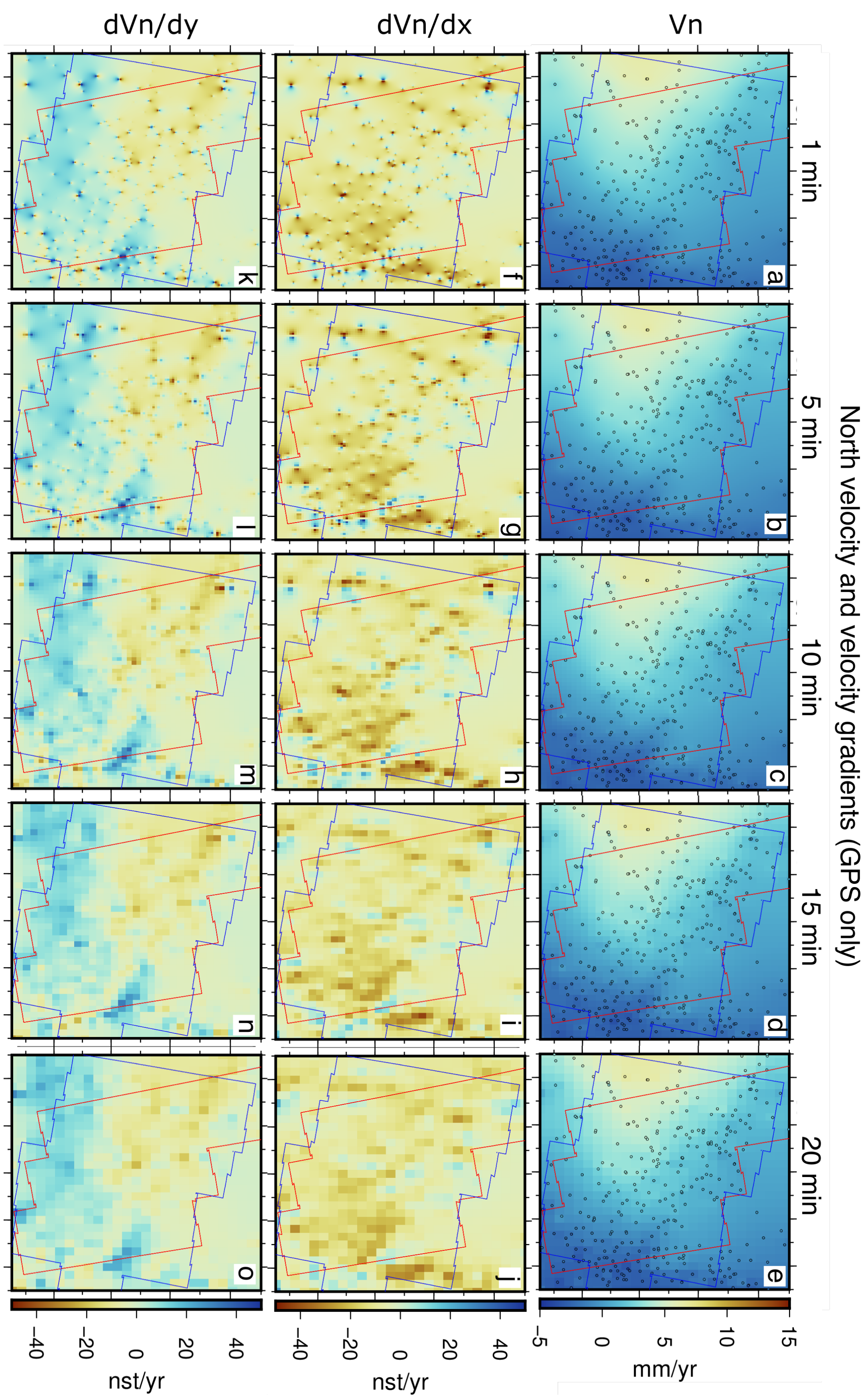

Figure 5.3: North velocity maps based on GMT *surface* fitted to the GNSS velocities and filtered at resolutions of (a) 1 arcminute, (b) 5 arcminutes, (c) 10 arcminutes, (d) 15 arcminutes and (e) 20 arcminutes. (f-j) are the derivatives of (a-e) in the east direction. (k-o) are the derivatives of (a-e) in the north direction.

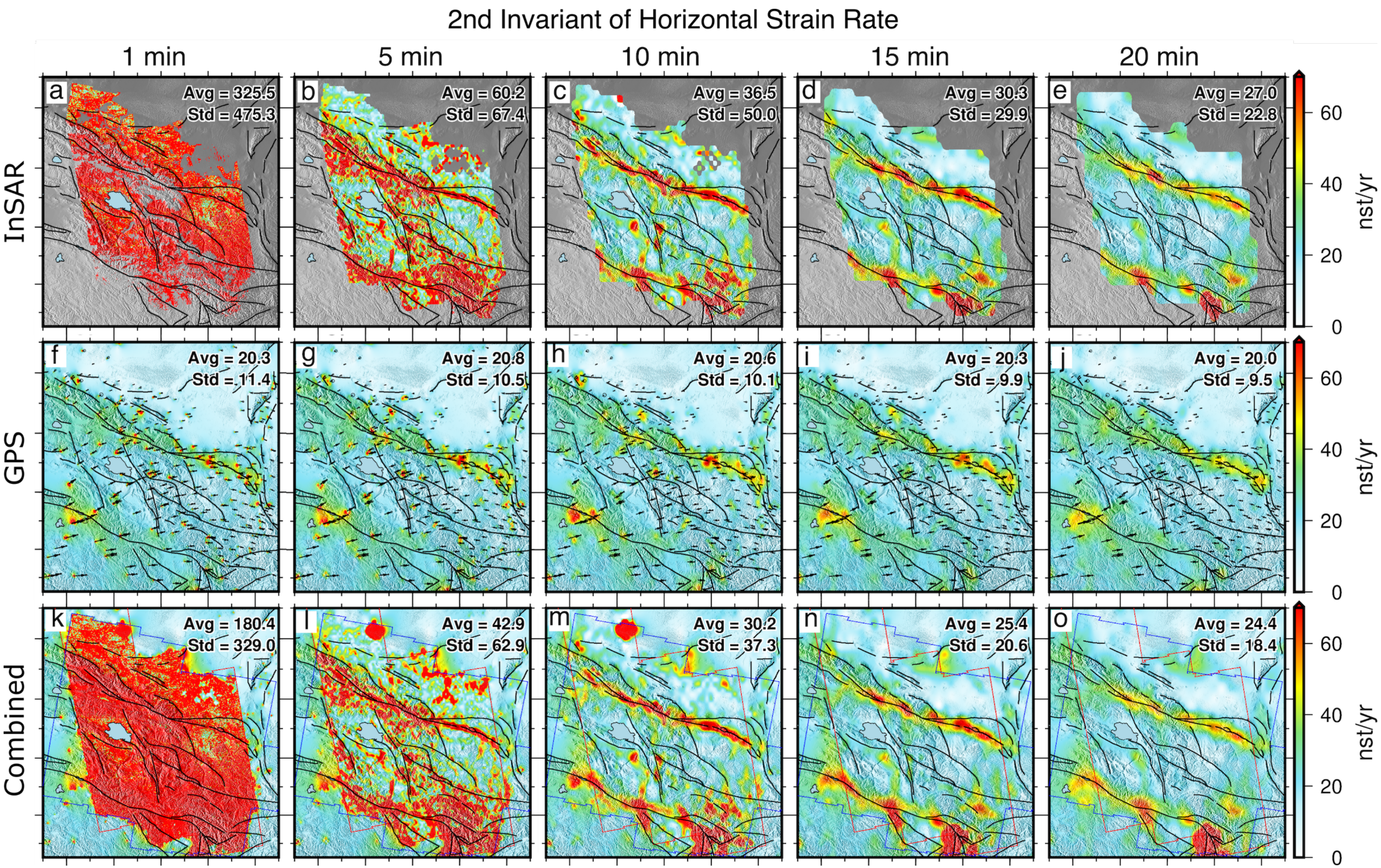

Figure 5.4: Second invariant of horizontal strain rates using velocity maps filtered at resolutions of (a) 1 arcminute, (b) 5 arcminutes, (c) 10 arcminutes, (d) 15 arcminutes and (e) 20 arcminutes. (f-i) are the same as (a-e) but from the GNSS data only. (k-o) are the same as (a-e) but from the combined data set with InSAR and GNSS velocities. The average and standard deviations of the pixel values are labeled on the top right of each panel.

maps do not vary significantly with the *blockmedian* resolution (Fig 5.3a-e) and their $\partial V_N/\partial x$ and $\partial V_N/\partial y$ derivatives are of much lower magnitudes (Fig 5.3f-j, k-o). In contrast, the InSAR derived velocity gradients are very sensitive to the blockmedian resolution, with 1-arcminute maps completely dominated by noise (Fig 5.1f,k and Fig 5.2f,k) and the 15-arcminute and 20-arcminute $\partial V_E/\partial y$ maps doing better jobs in highlighting just the major strike-slip Haiyuan and Kunlun Faults.

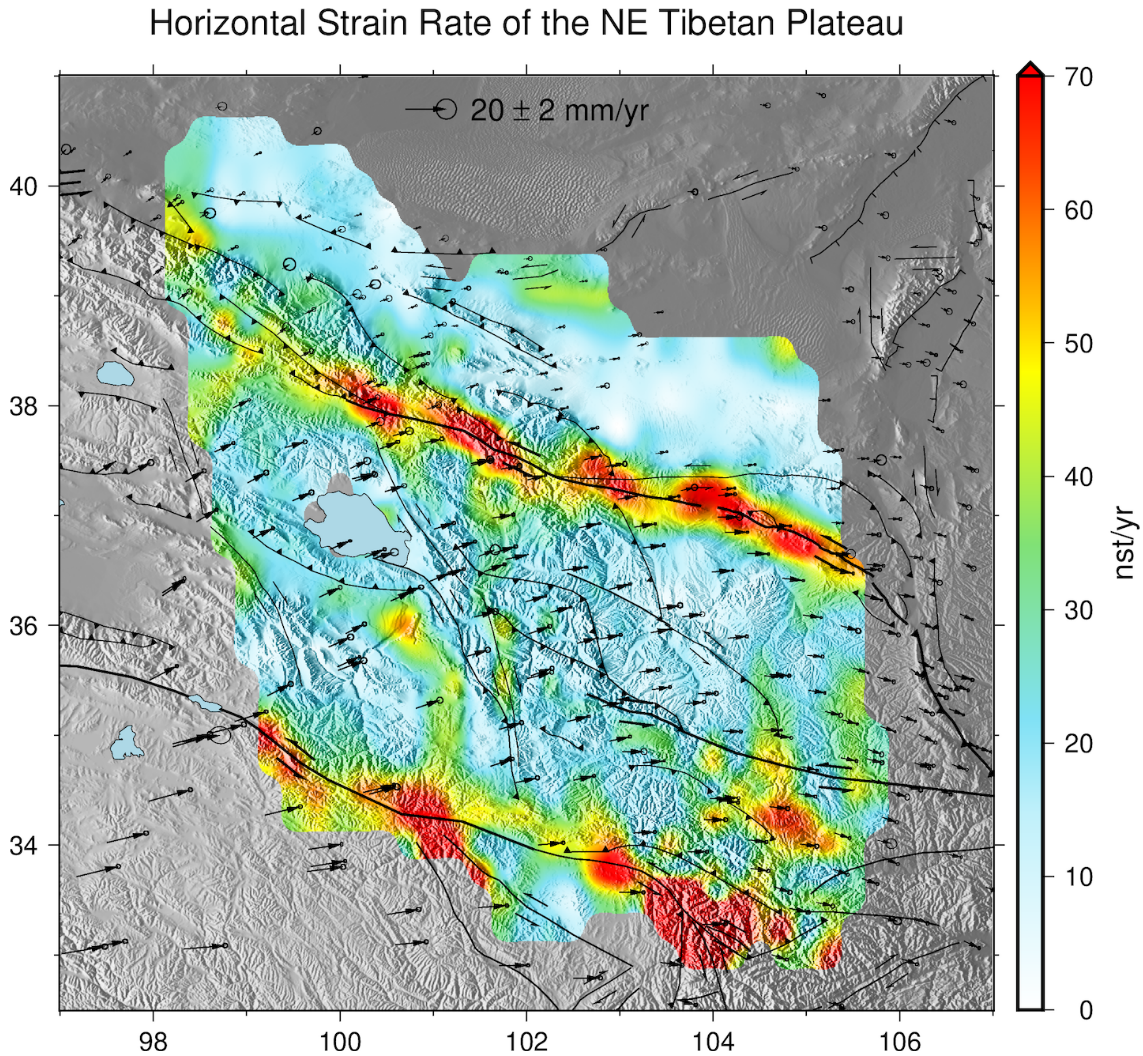

Figure 5.5: The chosen horizontal strain rate solution derived from V_E from InSAR and interpolated V_N from GNSS filtered at 15-arcminute resolution.

Horizontal strain rate maps based on Equation 5.3 and the four horizontal velocity gradient components of different resolutions are given in Fig 5.4a-e. Comparing the strain rate maps, it can be seen that most of the signals in the 1-arcminute resolution are of short wavelengths and fade with increasing levels of filtering. The persistent features are the continuous high strain rates along the Haiyuan and Kunlun Faults, which are the remaining features in the 15- and 20-arcminute resolution maps (Fig 5.4d,e). The 10-arcminute resolution map contains some features such as the strain between the thrust faults of the Qilianshan that could be real but are smoothed out in the lower resolution maps; yet it also contains features that are likely artefacts such as the strain on the north edge of the map, which is absent in the GNSS-based maps (Fig 5.4f,i) and disappear with stronger filtering. The average pixel value and standard deviation across the map are labeled in each panel. Both values decrease rapidly from 1-arcminute to 5-arcminute and gradually stabilise afterwards. The cross-over between the average and standard deviation of strain rates happens at 15-arcminute, suggesting the tectonic signal has beaten down the noise and further smoothing is likely to remove the desired signal. Both the visual judgement and the statistics seem to favour the 15-arcminute map which I, therefore, choose as the cleanest and sharpest solution for the magnitude of the horizontal strain rate of the NE Tibet (Fig 5.5).

5.2.2 InSAR Strain Rate Versus GNSS Strain Rate

I further compare the chosen strain rate map (Fig 5.5) with that derived from GNSS velocities alone (Fig 5.6). To derive the GNSS strain rate, I fit a GMT *surface* to the east component of the GNSS velocities which are filtered to the five different resolutions in the same way I derived the GNSS V_N maps (Fig C.1). The resultant second invariant of the horizontal GNSS strain rate maps are shown in Fig 5.4f-j, with the product at the same 15-arcminute resolution enlarged in Fig 5.6.

In the GNSS-derived map(s), regions of high strain rates appear as diffused hot spots. The locations of the strain hot spots also tend to be associated with regions

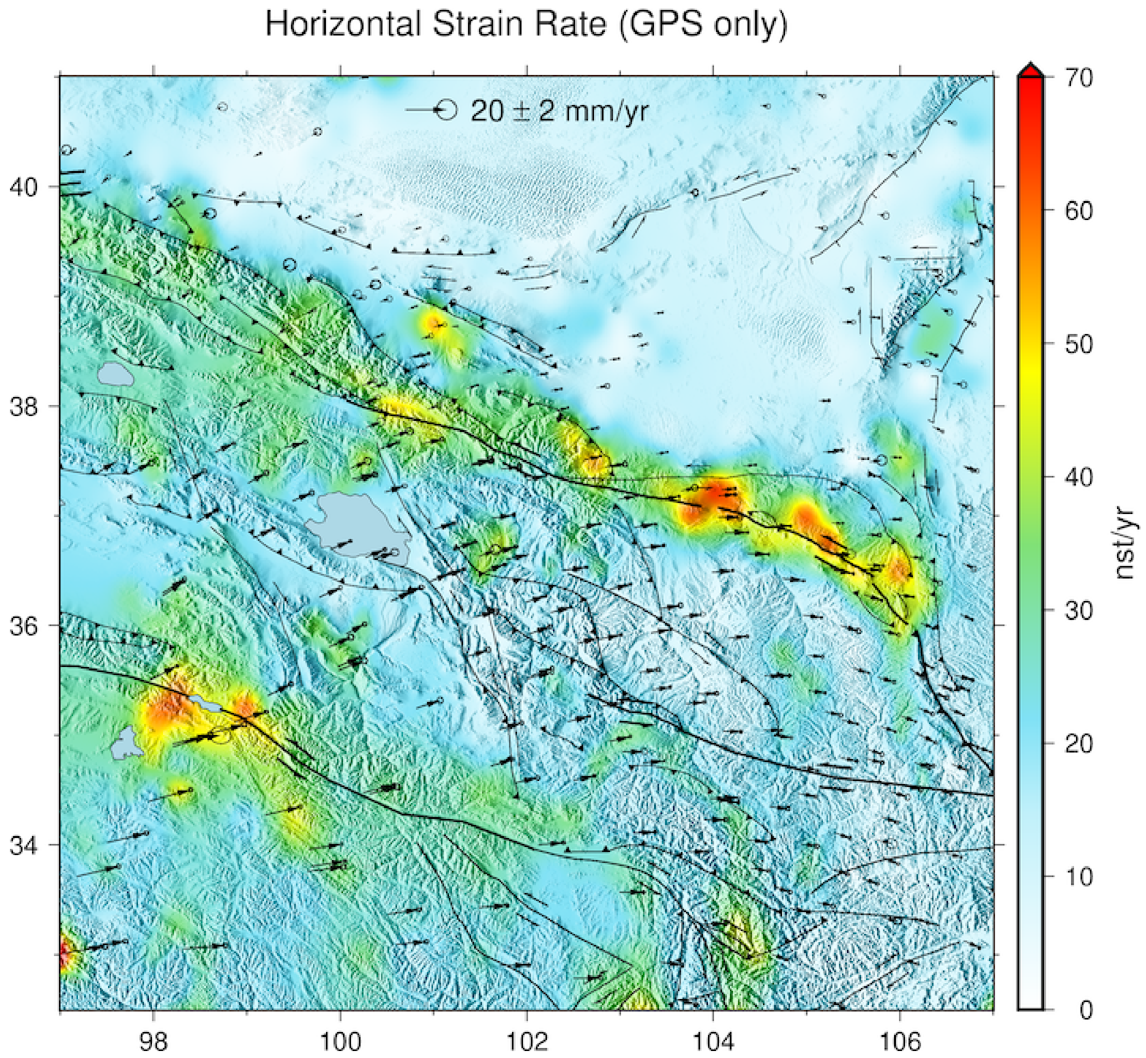

Figure 5.6: The 15-arcminute resolution horizontal strain rate map derived from the GNSS horizontal velocities shown as arrows.

with clustered GNSS measurements, as most clearly illustrated in Fig 5.4f and by how the pattern evolves with the filtering resolution (Fig 5.4g-j). This implies that such high strain could be caused by local variation of measurement quality. In particular, the strain concentration on the East Kunlun Fault is co-located with a measurement with high uncertainty (Fig 4.17b and Fig 4.20 of Chapter 4), suggesting the high strain rate there is probably not real. Furthermore, the magnitude of strain rate derived from GNSS velocities is also smaller than that of the preferred strain rate map (Fig 5.5). This is possibly due to the sparsity of the GNSS stations, thus, a lack of closely positioned stations to reveal secular velocity differences. Therefore, strain rate derived from only GNSS velocities could be underestimated.

In contrast, the chosen strain rate map derived from InSAR V_E highlights continuous features of strain concentration in the shapes of the geological faults (Fig 5.5). This suggests that strain is accumulating along most stretches of the faults, rather than concentrated on local hot spots as implied by the GNSS-derived strain rate map. In particular, the highest strain concentration seems to co-locate with junctions between strike-slip and thrust faults, or differently oriented strike-slip faults. This makes sense as relative movement at triple junctions induces a volume change and intense local deformation is required to avoid a gap opening or material overlap (*Andrews*, 1994). These geometrical discontinuities being barriers to sliding, also hinder potential aseismic slip that could happen on smoother portions of the fault (*Sagiya et al.*, 2004), causing relative concentration of strain at the fault junctions. This result is consistent with observations of rupture initiations and terminations at geometrical discontinuities along faults (*King and Nábělek*, 1985) and reinforces our understanding of strain concentration related to slip partitioning in complex systems of faults (*Gaudemer et al.*, 1995).

5.2.3 Sources of High Strain

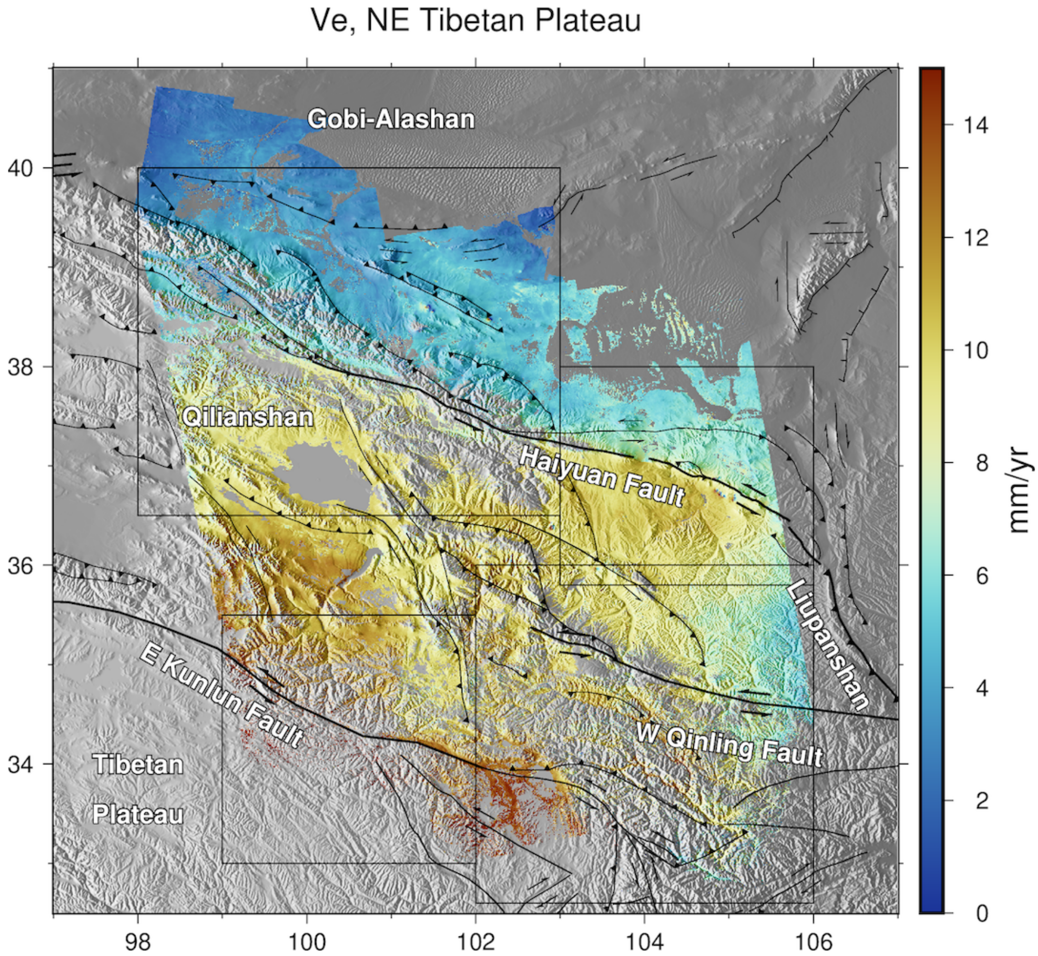

Figure 5.7: East velocity map from InSAR with boxes showing the extent enlarged in Fig 5.8 to Fig 5.11.

The root of the high strain rate in the InSAR-derived map can be further investigated from the profiles along the V_E InSAR velocity map (Fig 5.7 to Fig 5.11). It can be seen that areas highlighted in the chosen strain rate map are indeed where the velocity changes the most rapidly.

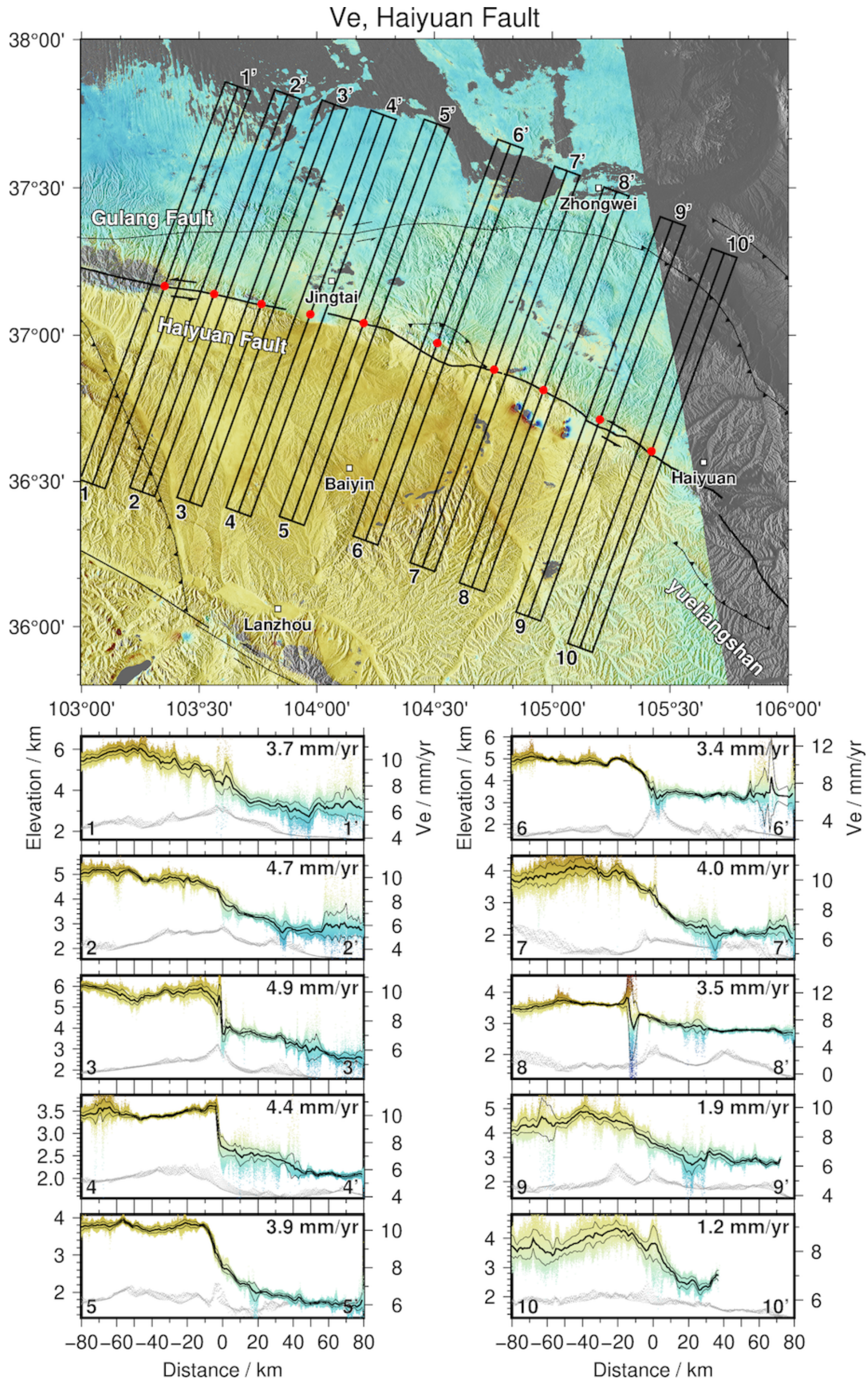

Figure 5.8: Profiles along the Haiyuan and Gulang Faults. Red dots in the map are the centres of profile where distance is 0 km. Coloured dots are pixel values along profile distance extracted from the 30-arcsecond resolution V_E map. Thick black line = mean value per 1 km bin; thin black lines = standard deviation per 1 km bin. The difference between the mean values at the ends of profiles are labeled in each panel. Grey dots are topography along profile.

In Fig 5.8 across the Haiyuan and Gulang Faults, the velocity step is well-imaged along the entire stretch. The sharp velocity step in profiles 3–3' and 4–4' show evidence of creep. In particular, profile 4–4' not only highlights the creeping motion along the Haiyuan Fault, but also reveals a smaller velocity step across the Gulang Fault, which is not obvious in the other profiles. This feature is captured in the strain rate map with a bulge of high strain area to the north of the Haiyuan Fault (Fig 5.5). The velocity steps in profiles 7–7' to 10–10' are of smaller magnitude and stretch over longer fault-perpendicular distances, which support a relatively smaller strain rate as in Fig 5.5. Therefore, the elevated strain concentration in the GNSS-derived strain rate map in the same location is probably an artefact due to the distribution of GNSS stations (Fig 5.6).

In the Qilianshan region (Fig 5.9), the far-field velocity gradient is evident in both the profiles and the map. However, it is worth noting that areas of high strain rate (profiles 3–3', 4–4' and 5–5') corresponds to not only fault junctions but also locations where velocity pixels are retained immediately on both sides of the Haiyuan Fault, which enable the sharp velocity step, hence the high strain rate, to be revealed. On the contrary, some medium strain areas (e.g., on both sides of profile 6–6') have more empty pixels against the fault. Therefore, the variation between the high strain and medium strain areas in the Qilianshan could potentially also be a result of the InSAR pixel distribution. A more interesting view of the strain distribution is offered by the 10-arcminute solution of the strain rate map (Fig 5.4c) where the short-wavelength dip in V_E, as captured by profile 1–1', is also highlighted. In all six profiles, there is a correlation between peaks in the V_E velocity and peaks in topography. Some of the correlations are positive whereas others are negative, but all are associated with wide scatter of V_E measurements. Further work is required to understand the mechanism behind this correlation, but these features tend to be local and are smoothed out in the filtered strain rate maps.

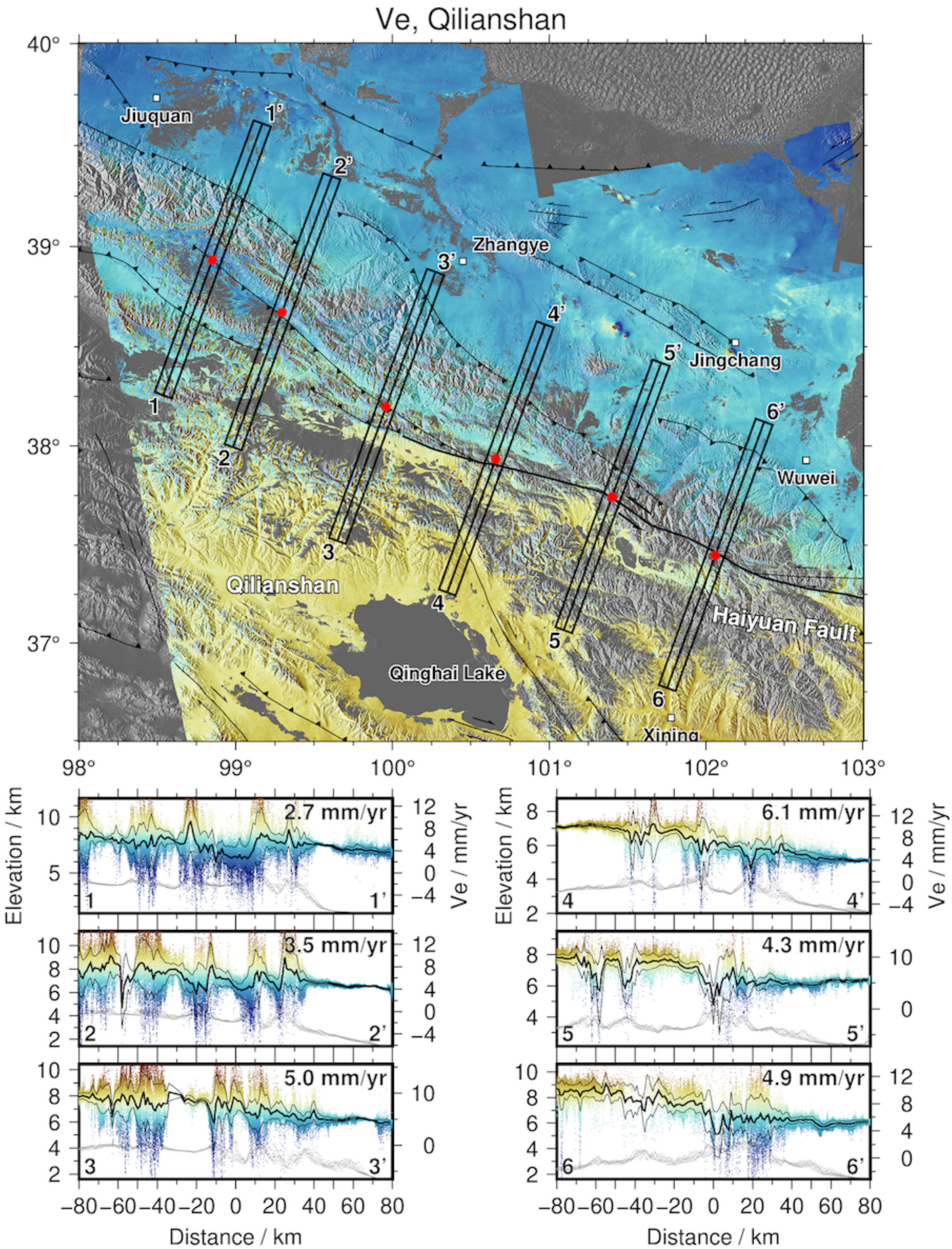

Figure 5.9: Same as Fig 5.8 for the Qilianshan.

Along the East Kunlun Fault, the velocity step across fault happens across a single fault strand in the west (Fig 5.10) and becomes partitioned over branches in

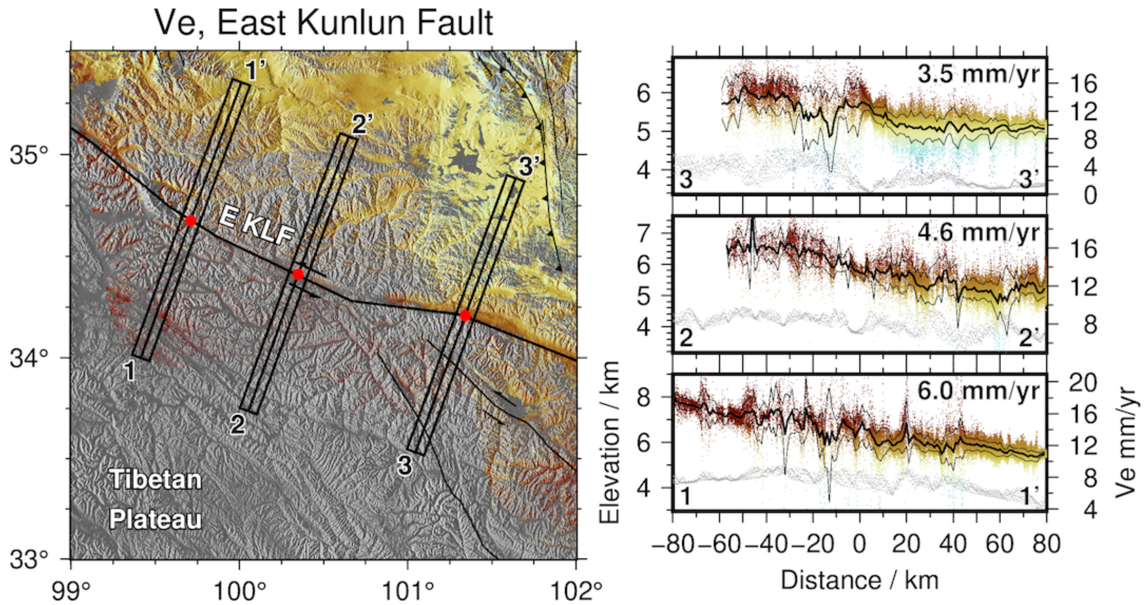

Figure 5.10: Same as Fig 5.8 for the East Kunlun Fault.

the east (Fig 5.11), mostly in the sense expected of the left-lateral strike-slip motion. However, the step in the V_E velocity in profile 3-3', in the opposite sense as the other profiles, suggests the micro-block enclosed by the Bailongjiang (BLJ), Maqên-Maqu-Tazang (MMT) and Hanan (HN) Faults is constrained from moving eastwards at the same rate as its surrounding crust. Therefore, there is a big patch of high strain rate in and around this micro-block (Fig 5.5). The fact that the high strain rate does not fill the entire micro-block is owning to the lack of pixels immediately to the south of the Bailongjiang Fault which are masked out due to their high RMS_{pixel} values. Profile 5-5' of Fig 5.11 does not reveal a step change at zero distance, explaining the slow strain rate near the West Qinling Fault (Fig 5.5).

5.2.4 Strain Rate Map with Both InSAR and GNSS

An attempt was made to combine InSAR and GNSS data to calculate the strain rate for the whole map area. The InSAR grid was first converted to a table of (longitude, latitude, V_E) triplets, which are combined with the GNSS data and filtered together

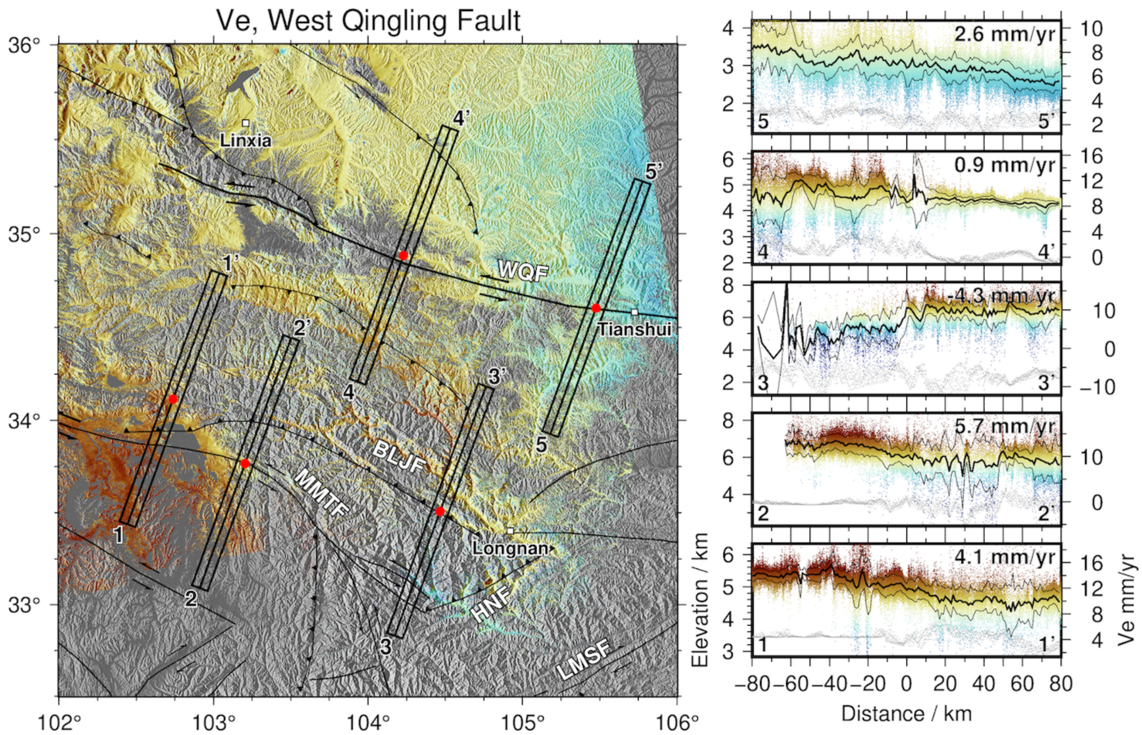

Figure 5.11: Same as Fig 5.8 for the West Qingling Fault and the east end of the East Kunlun Fault which branches into the Bailongjiang (BLJ) and Maqên-Maqu-Tazang (MMT) Faults which terminate at the Hanan (HN) Fault.

with GMT *blockmean*. A GMT *surface* was then fitted to the filtered data set. The resultant velocity gradients are shown in Fig C.2 and the second invariant of the horizontal strain rates are shown in Fig 5.4k-o. The contrast in resolution and magnitude between the InSAR-covered area and the GNSS-only area is obvious. Nevertheless, there is spill-over of strain rate from the InSAR measurements to the GNSS-only areas, which results in some artificially high strain rate at the edges of the InSAR area that might not be true. In order to suppress such aliasing effect, different filtering methods should be investigated in future work.

Another way of combining InSAR and GNSS data for the strain rate is through VELMAP (*Wang and Wright*, 2012; *Wang et al.*, 2019). VELMAP divides the region into an irregular triangular mesh and solves for components of the strain rate at the centre of each triangle that fit the input velocity data (*Savage et al.*, 2001). Jonathan

Weiss of the University of Potsdam helped run VELMAP with the combined dataset of my stitched LOS InSAR track data and 3D GNSS data, and produced solutions using average mesh spacings of distances of 20 km and 30 km (Fig C.3 and C.4, respectively). This method does a better job at integrating the InSAR and GNSS data in comparison to my solutions, as seen from the absence of artificial strain at the InSAR track boundaries. However, the areas with high strain rates in both solutions appear as smudged hot spots that do not follow the geological structures as closely as the chosen solution in Fig 5.5. The magnitude of strain rate obtained from VELMAP is also lower than that in Fig 5.5 because VELMAP implements the thin-sheet 3D strain rate equation from *England and Mckenzie* (1982) without the $\sqrt{2}$ term, assuming a definition of second invariant as $\dot{\varepsilon}_{II} = \sqrt{\frac{1}{2}\dot{\varepsilon}_{ij}^2}$ instead of $\dot{\varepsilon}_{II} = \sqrt{\dot{\varepsilon}_{ij}^2}$. With another factor of $\sqrt{2}$, VELMAP's result would be of comparable magnitude to my result, although the spatial distribution of strain rate will stay the same. Therefore, Fig 5.5 is still the preferred solution.

5.2.5 Full Strain Rate, Dilatation and Maximum Shear

For completeness, I calculate other strain products. The first is the second invariant of the full strain rate tensor as defined in *England and Mckenzie* (1982):

$$\dot{\varepsilon}_{II} = \sqrt{2(\dot{\varepsilon}_{xx}^2 + \dot{\varepsilon}_{yy}^2 + \dot{\varepsilon}_{xy}^2 + \dot{\varepsilon}_{xx}\dot{\varepsilon}_{yy})} \tag{5.4}$$

This formulation assumes incompressibility of the lithosphere ($\dot{\varepsilon}_{zz} = -(\dot{\varepsilon}_{xx} + \dot{\varepsilon}_{yy})$) and invariability of horizontal velocities with depth ($\dot{\varepsilon}_{xz} = \dot{\varepsilon}_{zx} = \dot{\varepsilon}_{yz} = \dot{\varepsilon}_{zy} = 0$). The second invariant of the 3D strain rate tensor has the same distribution pattern as that of the 2D horizontal strain rate tensor, but with a ∼10% increase in magnitude across the map (Fig 5.12a-c). This similarity is surprising as one would expect a higher increase in strain rate magnitude in the thrusting region than in the strike-slip region due to the added vertical motion, as suggested by the $\partial V_U/\partial x$ and $\partial V_U/\partial y$ maps (Fig 5.2f-j and k-o). There are three potential explanations for this discrepancy. One is that the thrusting region is not actually increasing in height, thus the crust there is not thickening relative to the strike-slip region, as hinted by the V_U map in Chapter 4 (Fig 4.19). The second is that the low resolution of the V_N velocity provided by the GNSS data gives smaller magnitudes in the associated $\partial V_N/\partial x$ and $\partial V_N/\partial y$ components (Fig 5.3k-o), thus underestimating the terms of $\dot{\varepsilon}_{yy}$ and $\dot{\varepsilon}_{xy}$ in Equation 5.3. The third is that the data resolution is too fine for the thin sheet model, a very smoothed crustal rheology model that describes the far-field view of the deformation style across the whole orogeny and hence explicitly ignores the strain localisation along faults. Given the high magnitudes and variations in $\partial V_U/\partial x$ and $\partial V_U/\partial y$ (Fig 5.2f-j and k-o), it is hard to imagine the same level of variation in the $\partial V_E/\partial z$ and $\partial V_N/\partial z$ terms in order for the $\dot{\varepsilon}_{xz} = \dot{\varepsilon}_{yz} = 0$ condition to hold.

Next, I calculate the dilatation rate (Fig 5.12d-f) and the maximum shear strain rate (Fig 5.12g-i) as defined in *Savage et al.* (2001) and *Wang and Shen* (2020). The dilatation rate is formulated as $\dot{\varepsilon}_{dil} = \dot{\varepsilon}_{xx} + \dot{\varepsilon}_{yy}$, which is equal in magnitude but opposite in sign to $\dot{\varepsilon}_{zz}$ (*England and Mckenzie*, 1982). The maximum shear rate is formulated as $\dot{\varepsilon}_{shear} = \sqrt{\dot{\varepsilon}_{xy}^2 + (\dot{\varepsilon}_{xx} - \dot{\varepsilon}_{yy})^2/4)}$. The dilatation rate and maximum shear rate maps are useful in revealing the two components that contribute to the second invariant of the horizontal strain rate maps. Comparing Fig 5.12d-i with Fig 5.5, we see the maximum shear rate dominating the horizontal strain rate, as noted by *Wang and Shen* (2020). Contractions tend to happen at fault junctions which also corroborates with our understanding of the roles of fault geometries in strain concentration (*King and Nábělek*, 1985).

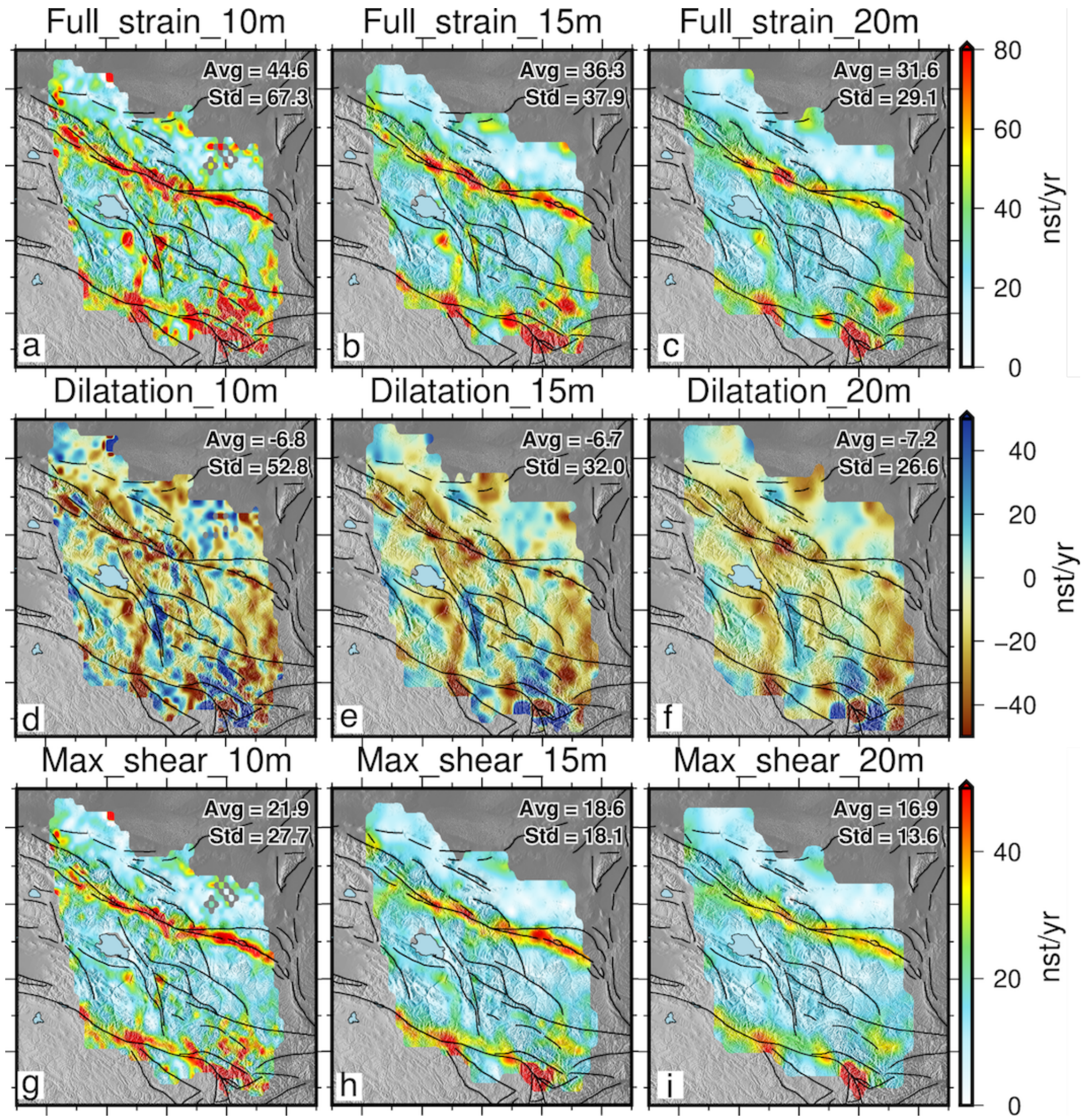

Figure 5.12: (a-c) Second invariant of the 3D strain rate tensor based on Equation 5.4 using velocity gradients filtered at 10-, 15- and 20-arcminutes, respectively. (d-f) Dilation rate calculated as $\dot{\varepsilon}_{xx}+\dot{\varepsilon}_{yy}$. (g-i) Maximum shear rate calculated as $\sqrt{\dot{\varepsilon}_{xy}^2 + (\dot{\varepsilon}_{xx} - \dot{\varepsilon}_{yy})^2/4}$.

5.3 Seismic Hazard Analysis

Based on the elastic rebound hypothesis (*Reid*, 1910), the strain energy accumulated in the crust would eventually be released as seismic moment during earthquakes. It follows that on the long term average, the seismic moment build-up rate from the elastic deformation of the crust should equal the rate of seismic moment release from the collection of earthquakes of various sizes.

Following *Bird et al.* (2015), the seismic moment build-up rate, $\dot{M}_o$, can be calculated from the measured strain rate, $\dot{\varepsilon}_{II}$, if there are no aseismic processes, using:

$$\dot{M}_o = \alpha \mu D A \dot{\varepsilon}_{II} \tag{5.5}$$

where α is a dimensionless geometric factor which scales the horizontal motion to the slip on the fault plane, μ is the shear modulus, D is the coupled seismogenic thickness and A is the pixel area. As in Chapter 2, I use 34 GPa for the shear modulus and use 20 km for the coupled seismogenic thickness.

The geometric factor, α, depends on the tectonic regime. Based on the regional distribution of focal mechanisms in the Global Centroid Moment Tensor Catalog (*Dziewonski et al.*, 1981; *Ekström et al.*, 2012), I divide the study area into two purely strike-slip areas containing the Haiyuan and Kunlun Faults, and one thrusting region including the mountain ranges stretching from the Qilianshan in the northwest to the terminating branches of the East Kunlun Fault in the southeast (Fig 5.13a). For the strike-slip region, I use $\alpha = 1$ as the faults are near vertical and the slip direction is along the maximum shear direction (Fig 5.12). For the thrusting region, I assume an average fault dip of 45° and set $\alpha = \sqrt{2}$, as only $cos(45°)$ of the slip on the faults contributes to crustal shortening, which is measured by the horizontal strain rate tensor to sum over. The strain rate map after scaling with the geometric factors is shown in Fig 5.13b.

The 45° angle is a theoretical value based on the assumption that a fault should bisect the angle between the maximum and minimum principle stress vectors. In fact, the faults in the Qilianshan are likely steeper, thus requiring more slip to produce the shortening. However, there should also be an left-lateral oblique component in their slip vector, which more efficiently releases the horizontal shear. These two factors trade off with each other in terms of the required slip rate to balance the strain rate.

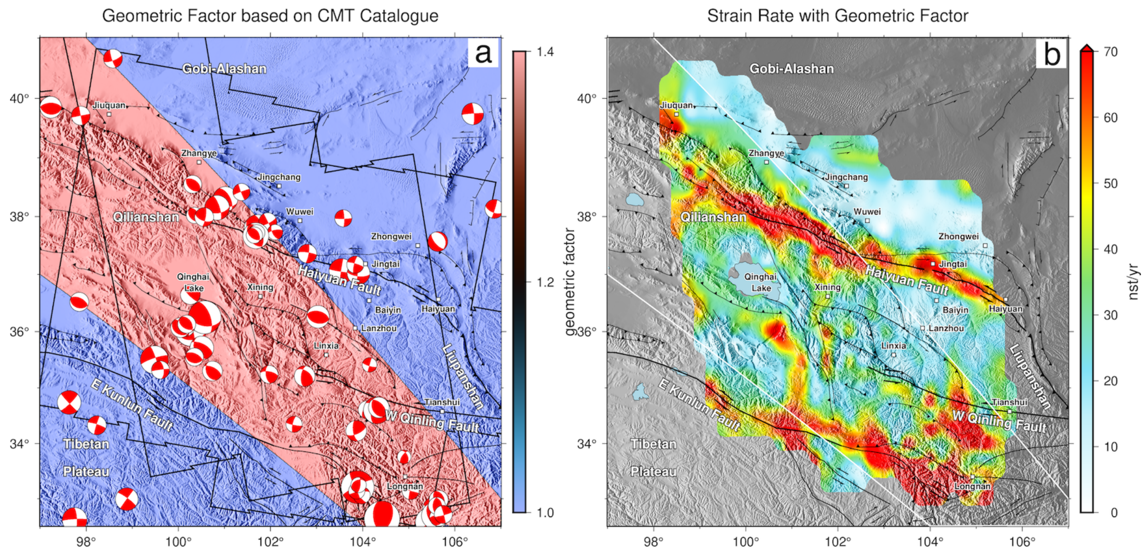

Figure 5.13: (a) Division of the region into a strike-slip only region (blue) and a thrust only region (pink) based on the focal mechanisms recorded by the CMT catalogue, with assigned geometric factor of 1 and $\sqrt{2}$, respectively. (b) The product of second invariant of horizontal strain rate (Fig 5.5) and the geometric factor in (a).

A proper treatment would require balancing the sum of earthquake seismic moment tensors with the strain rate tensor, which is beyond the scope of this thesis.

Fig 5.13b provides a view of where we expect higher earthquake rates as compared to areas where we expect lower earthquake rates. In order to estimate the seismic hazard of the whole region instead of at each pixel, I sum the $\dot{M}_o$ over the entire map to obtain the overall budget of the seismic moment rate of 1.1×10^{19} Nm/yr. This value will be 0.92×10^{19} Nm/yr or 1.4×10^{19} Nm/yr if I take 30° or 60° instead of 45° as the dipping angle for calculating the geometric factor of the thrusting area, or 0.94×10^{19} Nm/yr or 1.3×10^{19} Nm/yr if I choose a smoother (20-arcminute) or less smooth (10-arcminute) horizontal second invariant solution. Therefore, I take 1.1×10^{19} Nm/yr as my best estimate, 0.9×10^{19} Nm/yr as a lower bound and 1.4×10^{19} Nm/yr as an upper bound for the total seismic moment build-up rate in the area. This estimation does not take into account the uncertainties on the shear modulus and seismogenic depth, including which will further widen the uncertainty bounds.

The conversion from seismic moment rate to earthquake rate relies on the Gutenberg-Richter relationship (*Gutenberg and Richter*, 1954) which stipulates a log-linear frequency and magnitude relationship:

$$log(N) = a - bM \tag{5.6}$$

where M is the magnitude of earthquakes, N is the total number of earthquakes in any given region and time period of at least that magnitude, and a and b are constant parameters. Parameter a scales with the total moment rate. Parameter b defines the relative abundance of small versus large earthquakes.

Equation 5.6 can also be expressed in terms of seismic moment by assuming the magnitude concerned is the moment magnitude, M_W, which relates to the seismic moment by $M_W = \frac{2}{3}log(M_o - 9.1)$, such that:

$$N(M_o) = \alpha M_o^{-\beta} \quad \text{where} \quad \alpha = 10^{a+6.07b} \quad \text{and} \quad \beta = \frac{2}{3}b \tag{5.7}$$

where $N(M_o)$ is the number of earthquakes with seismic moment equal to or greater than M_o per unit time. Integrating Equation 5.7 from zero moment to the maximum moment that can be released in a single event, $M_{o(max)}$, we have the total seismic moment release rate, M_o^{tot}, as:

$$M_o^{tot} = \int_0^{M_{o(max)}} M_o \left(-\frac{dN}{dM_o}\right) dM_o \tag{5.8}$$

$$= \int_0^{M_{o(max)}} \alpha\beta M_o^{-\beta} dM_o \tag{5.9}$$

$$= \frac{\alpha\beta}{1-\beta} M_{o(max)}^{1-\beta} \tag{5.10}$$

$$\text{such that,} \tag{5.11}$$

$$\alpha = \frac{(1-\beta)M_o^{tot}}{\beta M_{o(max)}^{1-\beta}} \tag{5.12}$$

as derived in *England and Bilham* (2015). It is often found that the b value is $\sim$1 (*Hutton et al.*, 2010; *England and Bilham*, 2015), thus $\beta \sim \frac{2}{3}$.

The Equation 5.12 above by *England and Molnar* (2005) corrected a previous derivation by *Molnar* (1979) which, by forcing the number of $M_{o(max)}$ earthquakes to equal the number of earthquakes greater and equal to $M_{o(max)}$, artificially introduced a Dirac delta function in the single frequency distribution $(-\frac{dN}{dM_o})$ at $M_{o(max)}$ and thus underestimated the frequencies of lower magnitude earthquakes. *Rollins and Avouac* (2019) introduced a tapered form as an integration of the single frequency distribution predicted by *England and Molnar* (2005) between 0 and $M_{o(max)}$. This tapered form has a more physical feature of the cumulative frequency tailing off to zero at the maximum magnitude. However, it contradicts the original definition of the Gutenberg-Richter relationship in a sense that the largest earthquake never occurs. This conundrum faced by the tapered form in *Rollins and Avouac* (2019) can be resolved by considering $M_{o(max)}$ as a continuous range of seismic moment that could round to the exact moment given by the maximum M_W in a discretised catalogue. In this case, the frequency will only go to zero at half a step size greater than the maximum M_W, and the maximum M_W will have a non-zero frequency.

Nevertheless, for a catalogue shorter than a full seismic cycle, the largest earthquake either has occurred, and deflects the high-magnitude tail of the cumulative frequency to a region near the straight line as in the form by *England and Molnar* (2005), or has not occurred, and ends the cumulative frequency before the largest magnitude. Only in the rare instances when the catalogue spans an integer number of seismic cycles would the tapered form of *Rollins and Avouac* (2019) be fit by real catalogue data. In future work, the degree of tailing off at $M_{o(max)}$ could be explored as a measure of the ratio between the catalogue length and the length of a seismic cycle. Appropriate weights can also be applied in relevant modelling work to reflect the robustness of the frequencies derived from catalogues based on the ratio between the catalogue lengths and the inferred recurrence periods at different magnitudes. In this thesis, I adopt the linear cumulative frequency distribution of *England and Molnar* (2005), as defined in Equation 5.7 and Equation 5.12, considering the 1920 Haiyuan earthquake, which is likely to be the largest earthquake for this region, has already occurred in the seismic cycle covered by the catalogues.

Whether the the 1920 Haiyuan earthquake represents the largest earthquake that has ever occurred or will ever occur in the NE Tibetan Plateau is a big unknown. Across the world, the largest known intra-continental earthquake is the 1905 M_W 8.3–8.5 Bunay earthquake which broke through strong crystalline rocks (*Okal*, 1977; *Rizza et al.*, 2015). This would be approximately the magnitude if the whole 600 km Qilian-Haiyuan Fault were to rupture together with an average slip of 10 m. Looking beyond the instrumental record, the largest historical earthquakes recorded in the NE Tibetan Plateau in the China Historical Strong Earthquakes Catalogue (*CEA-PBED*, 1995) are three M 8 events that occurred in years 1654, 1739 and 1879. These magnitudes are derived from intensity of shaking and are rounded to the nearest 0.25, so the M 8 events could be of M 7.875–8.125. Ignoring other sources of uncertainties, if the conversion suggested in Section 2.4.4 is performed, these events could be of moment magnitude M_W 7.6–7.8, comparable or slightly smaller than the 1920 Haiyuan Earthquake.

Assuming the largest single release of seismic moment is approximately that in the 1920 Haiyuan earthquake, based on the magnitude reestimated in Chapter 2 ($M_W = 7.9 \pm 0.2$), I have $M_{o(max)} = 8.9 \times 10^{20}$ Nm for the best estimate, $M_{o(max)} = 4.5 \times 10^{20}$ Nm for the minimum and $M_{o(max)} = 17.8 \times 10^{20}$ Nm for the maximum. Taking the best estimates from both the strain rate and seismic moment of the 1920 Haiyuan Earthquake, I expect an event of the size of the 1920 Haiyuan Earthquake once every ∼160 years in the region covered by the strain rate map (red star in Fig 5.14a). A lower bound of 64 years is provided by the maximum estimate of strain rate and minimum estimate of the seismic moment of the 1920 Haiyuan Earthquake; an upper bound of ∼400 years is provided by the minimum estimate of strain rate and the maximum estimate of the seismic moment of the 1920 Haiyuan Earthquake (red dashed line in Fig 5.14).

These results are assuming all the measured strain will be released seismically, which may not be true given the secular creep along the Laohushan Section of the Haiyuan Fault which has been shown to persist in the past three decades (*Cavalié et al.*, 2008; *Jolivet et al.*, 2013, 2015) (Fig 5.8, profile 4-4'). Further work is required to quantify the amount of strain that is being released by aseismic slip, as well as inelastic deformation that builds the topography. If 25% of aseismic strain release is assumed as in *Rollins and Avouac* (2019), an event like the 1920 Haiyuan Earthquake will happen every ∼220 years in the area, with a minimum of 86 years and maximum of ∼530 years (blue star and dashed line in Fig 5.14). Using the six estimates of α in Table 5.1, with minimum, best and maximum for the two cases of 100% and 75% seismic strain release, respectively, I calculate the expected earthquake rates and their uncertainties in the frequency magnitude plot as stipulated by the Gutenberg-Richter relationship (red and blue solid lines and coloured bands in Fig 5.14).

α	Min	Best	Max
100%	3.71×10^{11}	5.72×10^{11}	9.13×10^{11}
75%	2.78×10^{11}	4.29×10^{11}	6.85×10^{11}

Table 5.1: The minimum, best, maximum estimates of α for the NE Tibetan Plateau based on the minimum, best, maximum estimates of the strain rates paired with the $M_{o(max)}$ calculated from the maximum, best and minimum estimates of the seismic moment release of the 1920 Haiyuan Earthquake, respectively, for the cases of 100% or 75% strain release by earthquakes.

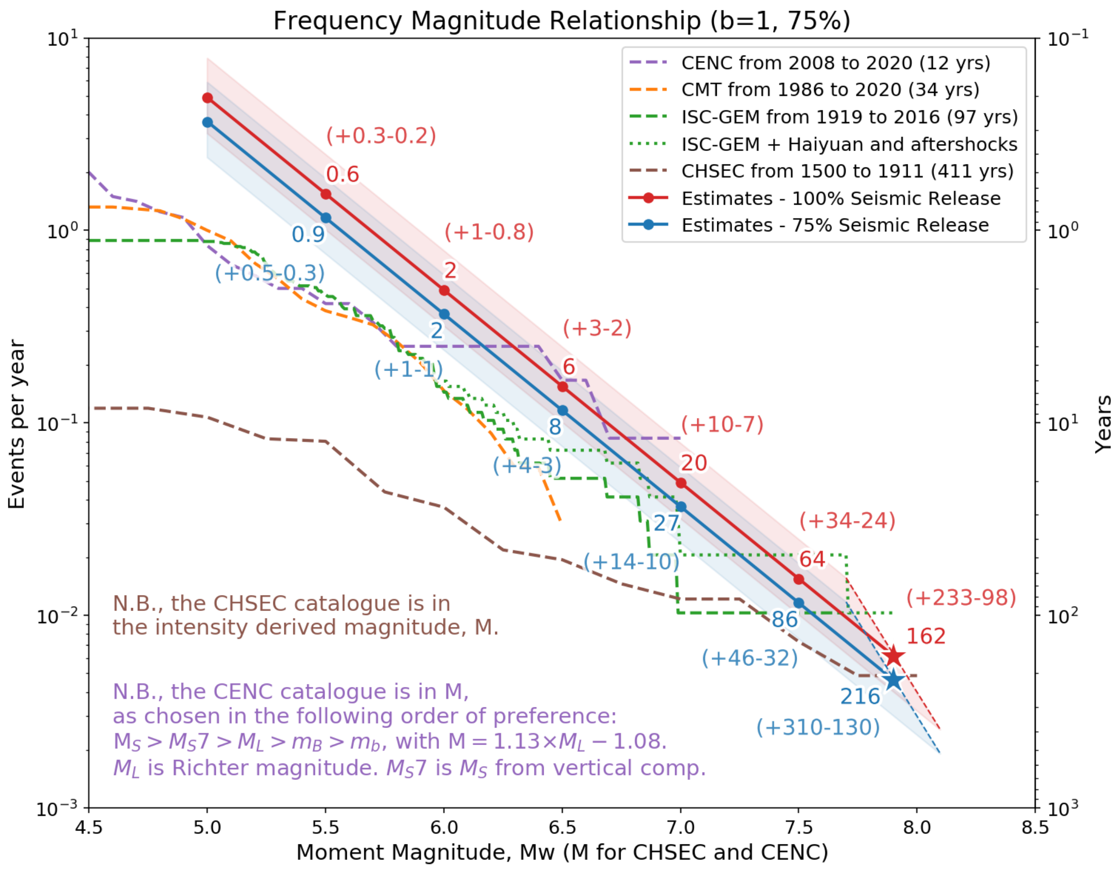

Figure 5.14: Frequency-magnitude relations between the number per year of events of magnitudes equal or greater than the given magnitude on the horizontal axis. The corresponding recurrence periods of such earthquakes are labeled on the secondary vertical axis on the right. Solid lines with coloured bands are the tectonic estimates of FMR based on $b = 1$ and the best, min and max estimates of α for cases of 100% (red) and 75% (blue) strain release by earthquakes, respectively (Table 5.1). The best estimates for the recurrence intervals for events of greater than or equal to every whole number M_W (red and blue dots) and the maximum M_W (red and blue stars) are labeled in the same colour with their associated uncertainties in brackets. The relationships derived from earthquake in the strain map area (Fig 5.15) from the ISC-GEM Global Instrumental Earthquake Catalogue (green dashed) (*ISC*, 2018, 2019), the Global Centroid Moment Tensor Catalogue (CMT) (orange dashed) (*Dziewonski et al.*, 1981; *Ekström et al.*, 2012), the China Earthquake Networks Center Catalogue (CENC) (purple dashed) (`http://www.csi.ac.cn/`, see *Dai et al.* (2019) for methodology and see *Li et al.* (2017b) for definitions of M_S and M_S7) and the China Historical Strong Earthquakes Catalogue (From 23 Century B.C. to 1911) (CHSEC) (brown dashed) (*CEA-PBED*, 1995) are plotted for comparison. Dotted green line shows the relation for the ISC-GEM if the 1920 Haiyuan Earthquake and two of its aftershocks, the recorded epicentres of which just fall out of the strain map area, are also included. The durations for each catalogue labeled in the legend are time periods with earthquakes recorded in the region defined by the strain rate map in Fig 5.13b.

I then plot the frequency magnitude relations (FMR) derived from events recorded in the ISC-GEM Global Instrumental Earthquake Catalogue (green dashed) (*ISC*, 2018, 2019), the Global Centroid Moment Tensor Catalogue (CMT) (orange dashed) (*Dziewonski et al.*, 1981; *Ekström et al.*, 2012), the China Earthquake Networks Center Catalogue (CENC) (purple dashed) (`http://www.csi.ac.cn/`, *Dai et al.* (2019)) (Fig 5.15a) and the China Historical Strong Earthquakes Catalogue (From 23 Century B.C. to 1911) (CHSEC) (brown dashed) (Fig 5.15b) (*CEA-PBED*, 1995) in Fig 5.14. Care is taken to only include events with epicentres inside the area where I have strain results (see elements in full colours versus in semi-transparent colours in Fig 5.15c-f). Although the CMT catalogue started in the 1976, it only recorded 2 events between 1976 and 1986, which is probably incomplete as the ISC-GEM catalogue recorded 10 events in the same period for the same area. Therefore, I used post-1986 events from the CMT catalogue to calculate the FMR over the 34 years from 1986 to 2020, during which time the temporal density of the recorded events is more consistent and a good agreement with the ISC-GEM catalogue is observed (Fig 5.15a). Similarly, the pre-1500 record in the CHSEC catalogue is also patchy in terms of temporal distribution. Therefore, I selected the post-1500 events for plotting the FMR (Fig 5.14).

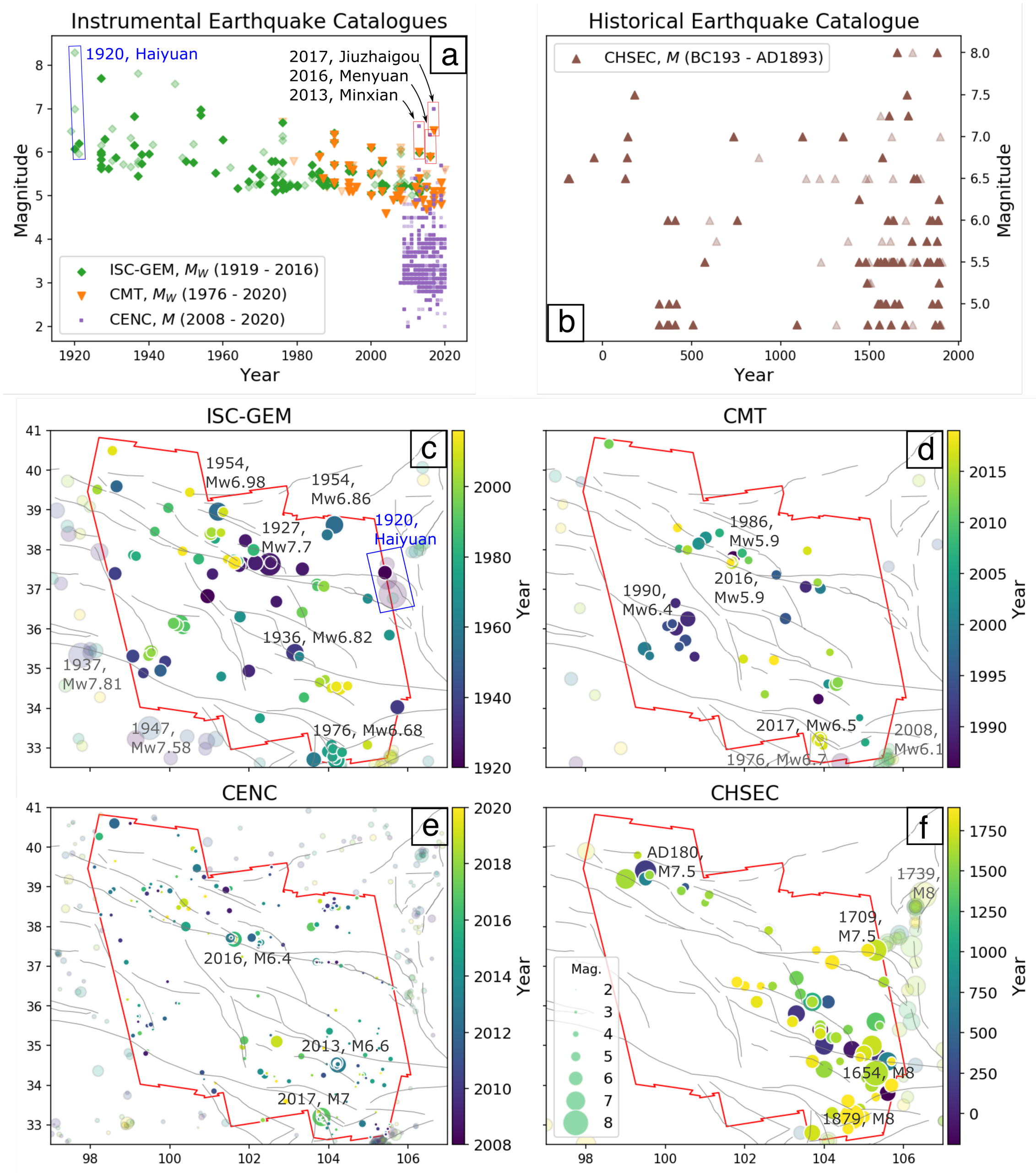

Figure 5.15: (a) Earthquake magnitude versus year plots for events recorded in the CENC (purple), ISC-GEM (green) and CMT (orange) catalogues. (b) Earthquake magnitude versus year plot for events recorded in the CHSEC catalogue. The year ranges in the legends of (a) and (b) represent full durations spanned by the catalogues, although for CMT and CHSEC, only earthquakes in a subset of the time period were used for calculating the frequency magnitude relations. (c-f) Map of earthquakes in ISC-GEM, CMT, CENC and CHSEC catalogues, respectively, coloured by years of earthquake occurrences. Bubble sizes represent magnitudes following the bubble scale in panel (f). The magnitudes used are moment magnitude, M_W, for ISC-GEM and CMT, the 'unified magnitude', M, for CENC, and the intensity derived magnitude, M, for CHSEC. For all panels, semi-transparent colours represent earthquakes in the map frame but outside the strain map area defined by the red polygon; full colours represent earthquakes in the strain map area, which are used to plot the frequency-magnitude relations in Fig 5.14. The year and magnitude of some of the largest earthquakes in each catalogues are labeled in text, with dark grey for earthquakes in the strain map area and light grey for earthquakes out of the red polygon.

Comparing the FMRs from the four catalogues, that of the CHSEC catalogue is the most different and predicts the lowest earthquake rates for earthquakes of M_W 7 and below. This is expected as the CHSEC is a historical catalogue based on compilation of historical literature, with magnitudes derived from the intensity of shaking estimated from recorded damages. Given the high elevation, hence, low population density, of the area and the far distance from the historical capitals, the literary records of damage in the NE Tibetan Plateau is likely incomplete, as reflected by the spatial distribution of the events (Fig 5.15f). As a result, the historical catalogue is dominated by the large and damaging earthquake. In other words, the magnitude of completeness, M_c, for the FMR of CHSEC is high, so the low rates for lower magnitude earthquakes are understood. It is interesting to note that the high end of the FMR of CHSEC meets the tectonic predictions spot on, which is encouraging as this constraint does not come easily from modern instrumental catalogues as the instrumental era is too short in comparison to the recurrence time of such large earthquakes. However, the magnitude in the CHSEC catalogue is the intensity derived M, which, as discussed in Chapter 2 Section **??**, tends to be higher in number than M_W. This means that, if corrected to M_W, the brown line will shift to the left. In addition, as the CHSEC ends in 1911, it just missed the 1920 Haiyuan Earthquake. If the CHSEC were extended for another 9 years, it would have captured 3 great earthquakes in the span of 420 years, hence will shift the brown line up which probably will still meet the tectonic predictions.

The ISC-GEM is the second longest out of the four, spanning 97 years from 1919 to 2016. As plotted in the standard manner, the green dashed line just missed the tectonic prediction on the lower bound apart from the range M_W 7.5–8 where it is within the lower bound. It is worth noting that the recorded epicentres of the 1920 Haiyuan Earthquake and two of its aftershocks fall just outside the strain map region (Fig 5.15c). If choosing my relocated epicentre of 105.540E, 36.481N for the main shock (Chapter 2 Fig 2.2), the 1920 earthquake would have just entered the polygon. Moreover, as most of the displacement from the 1920 event is within the strain map, this event did release accumulated strain from the mapped area. The aftershocks, currently plotted north of the Haiyuan Fault (Fig 5.15c) are likely mislocated as well, as the smaller-amplitude waveforms would have been registered by fewer stations and fewer arrival times would have been reported for epicentre inversion. Thus, the uncertainties on the locations of the aftershocks are likely larger than that of the main shock, which was already mislocated by 30 km from the responsible fault. If including the main shock and the two aftershocks (boxed and labeled in blue in Fig 5.15a,c), the modified FMR in the green dotted line of Fig 5.14 intersects with the tectonic prediction from M_W 6.5 to M_W 8.

The CMT catalogue is not consistent with the long term average model. Comparing the CMT and ISC-GEM catalogues through time (Fig 5.15a), the CMT catalogue seems to have covered a relatively quiescent 34 years. While the ISC-GEM registered four $M_W > 7$ earthquakes in the first 30 years of the catalogue (the 1920 Haiyuan Earthquake, the 1927 Gulang Earthquake (M_W 7.7), the 1937 Dulan Earthquake (M_W 7.81, out of the strain area) and the 1947 Dari Earthquake (M_W 7.58, out of the strain area)), no events of magnitude greater than M_W 6.5 happened in this area in the latest 34 years. The 1976 Pingwu Earthquake was M_W 6.7 and is just south of the polygon. However, including one M_W 6.7 earthquake and an extra 10 years does not significantly change the frequency. There is also a series of aftershocks of the 2008 Wenchuan Earthquake of magnitude up to M_W 6.1 just outside the polygon. Including them might lift the curve to intersect with the tectonic prediction, but the responsible fault, the Longmenshan Fault, was completely outside the strain rate map, so the inclusion would not be justified.

The FMR from the 12-year-long CENC agrees with the tectonic prediction between M_W 6–7 which is surprising given the short duration of recording. Comparing the three largest events recorded in both CENC and CMT catalogues, the 2017 Jiuzhaigou, 2013 Minxian and 2016 Menyuan Earthquakes, it is found that the CENC catalogue produce higher magnitudes for all three events (Fig 5.15a). As the CENC catalogue reports a unified M magnitude by taking the first available value in the order of $M_S > MS7 > M_L > m_B > m_b$ (*Dai et al.*, 2019), this discrepancy suggests that CENC's M_S value tend to be larger than M_W. A one-to-one comparison between events in both CENC and CMT catalogues reveals that CENC's M values systematically deviate from CMT's M_W values with a relationship of $CMT = 0.64 \times CENC + 1.85$, giving larger M for earthquakes above M_W 5 and smaller M for earthquakes below M_W 5 (Fig 5.16 inset). Thus, once the unified M is converted to M_W, this agreement with the tectonic prediction will no longer hold.

As such, it seems that the three instrumental catalogues agree well between M_W 5–6 and all fall below the tectonic prediction in this range. This suggests that the assumptions used in calculating the earthquake rates may not be good enough. In order to fit the instrumental catalogues better in the smaller magnitude range, I tested b values of 0.9, 0.8 and 0.7, which successively fit better smaller magnitude ranges. However, the predicted rates still sit above the FMRs of the catalogues. Therefore, I further lowered the percentage of strain release by seismicity, and find optimal parameter pairs of (b = 0.9, 40%), (b = 0.8, 50%) and (b = 0.7, 60%) (Fig C.5). Out of the three, the (b = 0.7, 60%) model seems to fit the instrumental catalogues the best in the M_W 5–6 range, a sweet spot where the longer-running ISC-GEM and CMT catalogues are close to complete and the shorter CENC catalogue has seen enough repeats of events of such magnitudes to give moderately reliable frequency estimates.

Therefore, the model with $b = 0.7$ and 60% seismic strain release represents my preferred tectonic earthquake rate estimates (Fig 5.16). In this model, an event of magnitude M_W 7 and above is predicted to happen in the region every 27 (+21-12)

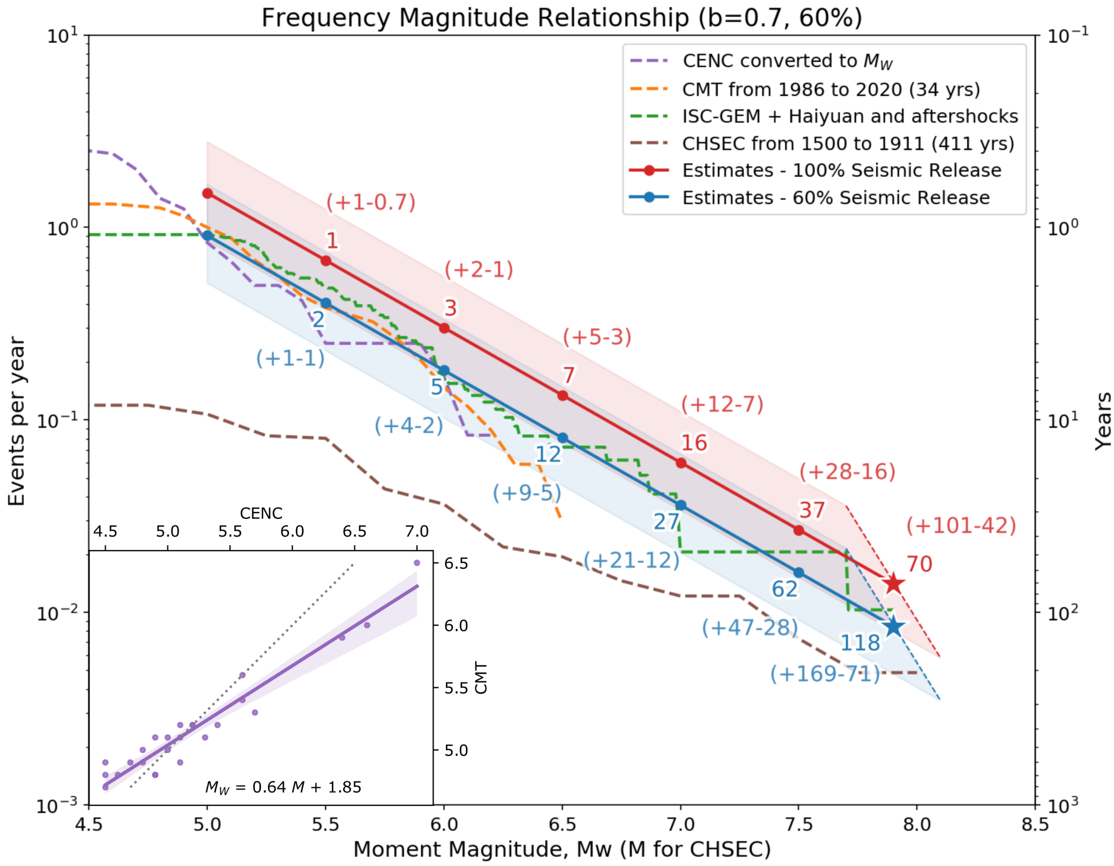

Figure 5.16: Preferred frequency magnitude relation estimated from tectonic strain with the assumption of b=0.7 and 60% seismic strain release. Only the preferred catalogues are plotted: CENC has been converted to M_W using relation derived in the inset (dots = events that appear in both CMT and CENC catalogues; purple line and band = linear regression of the dots; grey dotted line marks the 1-to-1 line); ISC-GEM includes the main shock and aftershocks of the 1920 Haiyuan Earthquake; CMT and CHSEC are the same as in Fig 5.14.

years, which agrees well with the records in the ISC-GEM catalogue. An event of the size of the 1920 Haiyuan Earthquake is expected to happen in the region every 118 (+169-71) years, which warrants caution compared to the 100 years lapsed since the 1920 Haiyuan Earthquake. Although the preferred blue line now sits above the CHSEC historical catalogue, as discussed above, if the CHSEC was 9 years longer, it would have captured the Haiyuan Earthquake which would then be raised closer to the tectonic prediction.

The 60% seismic strain release required by this model is on the lower end, but within error, of the seismic couplings of $0.72^{+0.28}_{-0.34}$ for Continental Transform Fault (CTF) zones and $1^{+0}_{-0.49}$ for Continental Convergent Boundary (CCB) zones estimated globally by *Bird and Kagan* (2004) and used in *Bird and Kreemer* (2015). Yet, 60% is the same as the fault coupling of 0.6 for the Qilianshan and Haiyuan Fault area, though lower than the 1.0 for the East Kunlun Fault, as estimated by *Rong et al.* (2020) for the smaller blocks. Nevertheless, it is important to compare the fault coupling values in view of the seismogenic thicknesses assumed in different studies. *Bird and Kagan* (2004) adopted shallow seismogenic thicknesses of 12 km with 0.72 coupling for CTF and 13 km with 1.0 coupling for CCB. *Rong et al.* (2020) assumed a deeper 25 km down-dip width with 0.6 coupling for the Qilianshan thrusts and a 15 km down-dip width with 1.0 coupling for the East Kunlun Fault. These results give a range of coupled seismogenic thickness between 8.64 and 15 km, which encloses the 12 km I can obtain from the 20 km seismogenic thickness and 60% seismic strain release.

Ultimately, the preferred rate estimates are constrained by the FMRs of the catalogues, hence carries significant weight for seismic hazard assessment. Therefore, the NE Tibetan Plateau needs to be well prepared for M_W 7 and larger earthquakes as their expected recurrence periods are well within the life expectancy of typical engineering projects. Based on the strain distribution in Fig 5.13b, such large to great earthquakes are more likely to happen along the extension of the Haiyuan Fault into the Qilianshan, as well as where the East Kunlun Fault branches into a series of strike-slip and reverse faults on the eastern end. Therefore, in these key areas, it is of paramount importance to make sure the building codes are up to date and preventative measures, such as building retrofitting and reinforcement, regular earthquake drills and early warning systems, are in place where possible, such that when a big event does strike, the life and economic losses are minimised.

Chapter 6

Conclusions

6.1 Summary of research outcomes

With the purpose of assessing the seismic hazard of the NE Tibetan Plateau, I have reestimated the magnitude of the 1920 Haiyuan Earthquake (Chapter 2) and generated the InSAR velocity and strain rate maps to provide estimates of earthquake rates for the NE Tibetan Plateau (Chapter 3-5).

Apart from the new magnitude of $M_W 7.9 \pm 2$ for the Haiyuan Earthquake, Chapter 2 brings attention to the possibility that the magnitudes of historical earthquakes in China could be systematically overestimated because of the overestimation of Gutenberg and Richter's surface wave magnitudes in the early instrumental era.

Chapter 3 used a combination of LiCSAR data processing, GACOS atmospheric correction and NSBAS time series analysis to produce 23 frame-sized velocity maps of ~100 m resolution and 1 mm/yr uncertainty from 5 years of Sentinel-1 data. Chapter 4 presented a frame-stitching method suitable for areas with good GNSS coverage. A 2-step velocity decomposition resulted in an east and a vertical velocity map which are of the highest resolution to date for the NE Tibetan Plateau. The east velocity reveals localised velocity change on most of the Haiyuan and the Maqu section of the East Kunlun Fault and distributed deformation across the Qilianshan, the Riyueshan Fault and the east end of the East Kunlun Fault.

Chapter 5 produced horizontal strain rate maps from the derivatives of the InSAR east and GNSS north velocity maps. Fast strain rates are revealed along the Haiyuan and Kunlun Faults, with strain concentration on the fault junctions. The dilatation and maximum shear strain components echo the style of faulting. With the total strain rate in the mapped area and the reestimated magnitude of the 1920 Haiyuan Earthquake, I derived the expected earthquake rates for the NE Tibetan Plateau. Frequency magnitude relationship with b value of 1 and 75% seismic strain release captures the CENC, ISC-GEM and CHSEC catalogues in the $M_W > 6.5$ range and overestimates the catalogues in the smaller magnitude range. A b-value of 0.7 and 60% seismic strain release would fit all three catalogues more closely in the $M_W > 5$ range. In the latter model, an event of $M_W >7$ is expected to happen in the mapped region every 15 to 48 years and an earthquake of the size of the 1920 Haiyuan Earthquake is expected to happen every 50 to 290 years.

6.2 Upcoming Results

Apart from implications on seismic hazard, the high resolution V_E and V_U InSAR velocity maps and their time series data contain a wealth of information that could be further extracted to improve our understanding of the regional tectonics.

6.2.1 Creeping Section of the Haiyuan Fault

The spatial and temporal evolution of the aseismic slip along the creeping section of the Haiyuan Fault can be revealed from the 5-years of time series data. This result can join existing observations in the 1990s and 2000s to reveal its 30-years of kinematic evolution and infer frictional properties (*Cavalié et al.*, 2008; *Jolivet et al.*, 2013, 2015).

6.2.2 Slip Rates and Locking Depths of the Haiyuan and Kunlun Faults

Slip rates and locking depths along the Haiyuan and Kunlun Faults can be obtained from the velocity maps. Comparing geodetic slip rates with geological slip rates would be useful for discriminating between contradictory geological slip rate results (*Lasserre et al.*, 1999, 2001) and assessing the activity of the faults over different time scales. Locking depths along the major faults can help resolve the discrepancies between the InSAR and GNSS-derived locking depths on the Haiyuan Fault (*Jolivet et al.*, 2012; *Li et al.*, 2017c), and estimate the proportion of expected seismic release of the measured strain rate, hence the seismogenic potential of the major faults.

6.2.3 Seismic Hazard of the Bailongjiang Microblock

Geodetic slip rates can be measured from the velocity maps over the micro-block enclosed by the terminating branches of the East Kunlun Fault. The Bailongjiang microblock is known to have great seismogenic potential, with a M 7.2-7.5 earthquake that occurred in 186 B.C. along the Bailongjiang Fault (*Yuan et al.*, 2007), a M 8.0 earthquake that occurred in 1879 A.D. along the Hanan Fault (*Deng et al.*, 2003; *Hou et al.*, 2005), but quiescence ever since. Comparing geodetic slip rates with geological slip rates and comparing current strain rate with historical seismicity will help assess the seismic hazard around the Bailongjiang microblock.

6.3 Pending Methodological Improvements

6.3.1 Digitising the Historical Seismic Archive

Digital seismic recording only began in the 1970s, but analogue seismograms have been recording the Earth's shaking for more than 100 years (*Okal*, 2015). What have been preventing people from tapping into this ocean of knowledge are the less-portable formats in which the analogue seismograms are stored and the non-standardised designs of the instruments that recorded them. Tools have been designed to digitise the waveforms from image scans (*Bogiatzis and Ishii*, 2016), with the latest upgrade aiming to semi-automatically pick the right path when waveforms overlap. The effectiveness of such tools awaits testing with differently formatted seismograms. The instrumental parameters are also largely available in historical literature (*Wood*, 1921; *McComb and West*, 1931). Digitizing them into a searchable online catalogue would be another important step for promoting the usage of this decaying and irreplaceable data archive.

6.3.2 Interferogram Unwrapping in Challenging Areas

Unwrapping in LiCSAR (*Lazecký et al.*, 2020) is performed using the SNAPHU version 2 method (*Chen and Zebker*, 2002), where a large IFG is divided into smaller tiles which are individually unwrapped before they are merged to form the full unwrapped IFG. Although this method is effective for 21 out of 23 frames in the NE Tibetan Plateau, difficulty was encountered over the vegetated Bailongjiang area where multiple fault branches exist in one frame. My current approach, which involves discarding IFGs with unwrapping mistakes and creating new IFGs of longer temporal baselines, results in low pixel coverage and large uncertainties of the final velocity maps. *Hussain et al.* (2016) developed an iterative unwrapping method which uses phase closure information to guide version 1 of SNAPHU unwrapping where a full IFG is unwrapped at once (*Chen and Zebker*, 2001). It may be worth implementing the iterative phase unwrapping algorithm with version 2 of SNAPHU for challenging areas in the future.

6.3.3 Frame Stitching in Areas with Poorer GNSS Coverage

I was lucky to have chosen an area with a good coverage of GNSS which provided constraints for stitching the velocity frames. Lin Shen at the University of Leeds worked on the Altyn Tagh Fault where GNSS points are scarce. Her method of frame stitching involves finding planar ramps that simultaneously fit all the ascending and descending data, track overlaps and available GNSS LOS. It was possible because she processed the InSAR data in tracks to start with. If used in my area with 23 frames, the inversion will involve over 70 free parameters which can be computationally expensive. An approach, probably by combining our methods, needs to be developed for large areas without good GNSS coverage, such as the interior of the Tibetan Plateau. Ways of quantifying uncertainty from this lack of GNSS control also need to be devised, as the projected velocity maps would carry uncertainty not only from InSAR measurements, but also from the uncertainty in the ramps applied.

6.4 Towards Better Seismic Hazard Assessment

A recurrent theme that emerged from this thesis is discrepancies in literature. This did not only happen to the magnitudes in earthquake catalogues but also appeared in strain, moment, and earthquake rate calculations. In a move towards large-scale strain rate mapping and seismic hazard assessment, it would be beneficial to reach a consensus as a community so that seismic hazard can be analysed in a systematic way.

6.4.1 Bridging Historical and Instrumental Catalogues

So far, most efforts in magnitude unification involve calculating regression relationships between magnitudes of common events in both catalogues within a certain period of time (*Zhang et al.*, 1999; *Cheng et al.*, 2017). An implicit assumption on this approach is that the magnitudes in each catalogue are obtained in the same way throughout the time period of concern. Although this assumption is probably true for more recent catalogues where both instruments and methods for magnitude determination are standardised (*Bormann and Saul*, 2008), it may not hold during the early instrumental age.

For example, *Abe and Noguchi* (1983b) found that the phase amplitudes measured by Gutenberg and Richter from an undamped Milne instrument for earthquakes between 1910 and 1912 are twice as large as the standard. *Abe and Noguchi* (1983a) found a temporal drift of Gutenberg and Richter's M in comparison with the 'real' M_S, with the former overestimating by 0.5 units between 1904 and 1906, 0.4 in 1907, 0.3 between 1908 and 1909 and 0.0 between 1910 and 1912. Although *Abe* (1981) did not think the magnitude of the 1920 Haiyuan Earthquake was overestimated, my result in Chapter 2 shows Gutenberg and Richter's M for this event not only overestimated M_W but also overestimated M_S.

Therefore, the magnitudes of as many earthquakes in the early instrumental period as possible should be reevaluated using analogue seismograms and crossed checked with geological evidence if possible. Nevertheless, this approach may only be practical for some large shallow earthquakes of that time as seismograms of events with $M_W 7$ were preferentially preserved (*Okal*, 2015) and earthquakes that are deep or small might not have left surface evidence that can still be traced today. As such, the conversion between intensity and magnitudes based on early 1900s earthquakes is unreliable and a revision may not be easy.

An alternative approach could be to derive a relationship between intensity and moment magnitude based on modern earthquakes (post 1960s), if the evolving approaches to intensity assignments can be unified. In this way, we circumvent all the magnitude conversion steps in between and could potentially obtain historical moment magnitudes that are more reliable.

6.4.2 From Strain Rate to Earthquake Frequency

Different approaches have been proposed for the various steps in the strain rate and earthquake frequency conversion. Due to the factor of 2 difference between engineering strain and scientific strain (*Wang and Wright*, 2012; *Hussain et al.*, 2018; *Weiss et al.*, 2020) and different simplifications made based on assumptions about deformation styles (*England and Mckenzie*, 1982; *Walters et al.*, 2014), strain results have been reported in different expressions of the second invariant of strain rate as well as other scalar quantities. Whilst all expressions are invariant with respect to coordinate transformation (*Tape et al.*, 2009), and all show relative high and low strain rate distributions, their absolute values start to matter when we try to scale the strain rate for earthquake rate calculations.

Although this ambiguity can be avoided by directly relating the strain rate tensor to moment rate tensor using Kostrov summation (*Kostrov and Riznichenko*, 1974), the inherit assumption of Kostrov summation is that the strain is irrotational, which requires deformation to occur on orthogonal conjugate faults or in a fault zone with randomly orientated fault planes (*Molnar*, 1979). As revealed by the InSAR V_E map (Fig 5.7) and the strain rate map (Fig 5.5), the deformation in the NE Tibetan Plateau is partitioned between the localised strike-slip motion on the Haiyuan and Kunlun Faults and the distributed shortening over the parallel reverse faults in the Qilianshan. Both areas mimic the tectonic setting with a single major fault or with a consistent slip vector across parallel faults, where according to *Chen and Molnar* (1977) and *Molnar* (1979), the expression from (*Brune*, 1968) is more suitable. The only area that can more aptly approximate to a continuum, as required for the Kostrov summation, would be the central area between the conjugate Riyueshan Fault and the Qinghai Nan Shan, Laji and Jishi thrusts. The choice between these two settings would introduce a multiplicative constant difference.

Bird and Liu (2007) and *Bird and Kreemer* (2015) avoid this choice by calculating the minimum moment rate from the largest principal strain rate, but have to calibrate against regional seismicity for each tectonic zone.

In addition, *England and Bilham* (2015), *Molnar* (1979) and *Avouac* (2015) disagree on how the Gutenberg-Richter relationship should be applied to convert total moment rate to seismicity rate. A choice between these would again introduce a constant factor difference.

Careful decisions need to be made in each of these steps to ensure the conversions are made in a consistent fashion. Ultimately, the total strain measured should tally with the sum of seismic and aseismic strain release. If the assumption of the 1920 Haiyuan Earthquake being the largest possible earthquake is correct, the onus is on the geodetic data to explain the proportion of aseismic deformation predicted by the frequency-magnitude relations given by geodesy and seismicity. If, however, the measured aseismic deformation is not enough to close the gap, the other explanation would be that the Haiyuan Earthquake is not yet the largest event for the NE Tibetan Plateau. In that case, we would have a bigger problem to worry about.

Bibliography

Abe, K. (1981), Magnitudes of large shallow earthquakes from 1904 to 1980, *Physics of the Earth and Planetary Interiors*, *27*(1), 72–92, doi:10.1016/0031-9201(81)90088-1. 2.1.3, 2.4.3, 2.5, 6.4.1, A.1

Abe, K., and S. Noguchi (1983a), Revision of magnitudes of large shallow earthquakes, 1897-1912, *Physics of the Earth and Planetary Interiors*, *33*(1), 1–11, doi:10.1016/0031-9201(83)90002-X. 6.4.1

Abe, K., and S. Noguchi (1983b), Determination of magnitude for large shallow earthquakes 1898 — 1917, *Physics of the Earth and Planetary Interiors*, *32*, 45–59. 6.4.1

Ainscoe, E. A., K. E. Abdrakhmatov, S. Baikulov, A. S. Carr, A. J. Elliott, C. Grützner, and R. T. Walker (2019), Variability in surface rupture between successive earthquakes on the Suusamyr Fault, Kyrgyz Tien Shan: Implications for palaeoseismology, *Geophysical Journal International*, *216*(1), 703–725, doi:10.1093/gji/ggy457. 2.3.1

Aki, K. (1966), Generation and Propagation of G Waves from the Niigata Earthquake of June 16, 1964.: Part 2. Estimation of earthquake moment, released energy, and stress-strain drop from the G wave spectrum, *Bulletin of the Earthquake Research Institute, University of Tokyo*, *44*(1), 73–88. 2.3.6

Aki, K. (1979), Characterization of barriers on an earthquake fault, *Journal of Geophysical Research: Solid Earth*, *84*(B11), 6140–6148, doi:10.1029/JB084iB11p06140. 2.4.5

Amante, C., and B. W. Eakins (2008), ETOPO1 1 arc-minute global relief model: Procedures, data sources and analysisRep. (document), 1.2

Andrews, D. J. (1994), Fault geometry and earthquake mechanics, doi:10.4401/ag-4136. 5.2.2

Ansari, H., F. De Zan, and A. Parizzi (2020), Study of Systematic Bias in Measuring Surface Deformation with SAR Interferometry, *IEEE Transactions on Geoscience and Remote Sensing*, (December), 1–12, doi:10.1109/TGRS.2020.3003421. 3.2, 3.4.1, 3.4.5

Avouac, J., and P. Tapponnier (1993a), Kinematic model of active deformation in central Asia, *Geophysical Research Letters*, *20*(10), 895–898, doi:10.1029/93GL00128. 1.3

Avouac, J.-P. (2015), From Geodetic Imaging of Seismic and Aseismic Fault Slip to Dynamic Modeling of the Seismic Cycle, *Annual Review of Earth and Planetary Sciences*, *43*(1), 233–271, doi:10.1146/annurev-earth-060614-105302. (document), 1.4, 1.9, 6.4.2

Avouac, J. and P. Tapponnier (1993b), Kinematic model of active deformation in central Asia, *Geophysical Research Letters*, *20*(10), 895–898, doi:10.1029/93GL00128. 1.2

Bagnardi, M., and A. Hooper (2018), Inversion of Surface Deformation Data for Rapid Estimates of Source Parameters and Uncertainties: A Bayesian Approach, *Geochemistry, Geophysics, Geosystems*, *19*(7), 2194–2211, doi:10.1029/2018GC007585. 4.5.1

Bekaert, D. P., A. Hooper, and T. J. Wright (2015), A spatially variable power law tropospheric correction technique for InSAR data, *Journal of Geophysical Research: Solid Earth*, *120*(2), 1345–1356, doi:10.1002/2014JB011558. 3.2

Bemis, S. P., R. J. Weldon, and G. A. Carver (2015), Slip partitioning along a continuously curved fault: Quaternary geologic controls on Denali fault system slip partitioning, growth of the Alaska Range, and the tectonics of south-central Alaska, *Lithosphere*, *7*(3), 235–246, doi:10.1130/L352.1. 2.3.5

Biggs, J., T. Wright, Z. Lu, and B. Parsons (2007), Multi-interferogram method for measuring interseismic deformation: Denali Fault, Alaska, *Geophysical Journal International*, *170*(3), 1165–1179, doi:10.1111/j.1365-246X.2007.03415.x. 3.4.3

Bird, P., and Y. Y. Kagan (2004), Plate-tectonic analysis of shallow seismicity: Apparent boundary width, beta, corner magnitude, coupled lithosphere thickness, and coupling in seven tectonic settings, *Bulletin of the Seismological Society of America*, *94*(6), 2380–2399, doi:10.1785/0120030107. 5.3

Bird, P., and C. Kreemer (2015), Revised Tectonic Forecast of Global Shallow Seismicity Based on Version 2.1 of the Global Strain Rate Map, *Bulletin of the Seismological Society of America*, *105*(1), 152–166, doi:10.1785/0120140129. 1.4, 3.1, 5.1, 5.2.1, 5.3, 6.4.2

Bird, P., and Z. Liu (2007), Seismic Hazard Inferred from Tectonics: California, *Seismological Research Letters*, *78*(1), 37–48. 6.4.2

Bird, P., C. Kreemer, and W. E. Holt (2010), A Long-term Forecast of Shallow Seismicity Based on the Global Strain Rate Map, *Seismological Research Letters*, *81*(2), 184–194, doi:10.1785/gssrl.81.2.184. 1.4, 5.1, 5.2.1

Bird, P., D. D. Jackson, Y. Y. Kagan, C. Kreemer, and R. S. Stein (2015), GEAR1: A Global Earthquake Activity Rate Model Constructed from Geodetic Strain Rates and Smoothed Seismicity, *Bulletin of the Seismological Society of America*, *105*(5), 2538–2554, doi:10.1785/0120150058. 5.3

Bogiatzis, P., and M. Ishii (2016), DigitSeis: A new digitization software for analog seismograms, *Seismological Research Letters*, *87*(3), 726–736, doi:10.1785/0220150246. 6.3.1

Bormann, P. (2012), Magnitude calibration formulas and tables, comments on their use and complementary data, *Tech. rep.*, doi:10.2312/GFZ.NMSOP-2$_DS_3$.1. 2.1.3, 2.2.5, 2.4.3

Bormann, P., and J. Saul (2008), The New IASPEI Standard Broadband Magnitude mB, *Seismological Research Letters*, *79*(5), 698–705, doi:10.1785/gssrl.79.5.698. (document), 2.4.1, 2.2, 2.4.2, 2.5, 6.4.1

Bormann, P., R. Liu, Z. Xu, K. Ren, L. Zhang, and S. Wendt (2009), First application of the new IASPEI teleseismic magnitude standards to data of the China national seismographic network, *Bulletin of the Seismological Society of America*, *99*(3), 1868–1891, doi:10.1785/0120080010. 2.4.3

Bormann, P., J. W. Dewey, I. Gabsatarova, S. Gregersen, A. A. Gusev, W. Y. Kim, H. J. Patton, B. W. Presgrave, L. Ruifeng, J. Saul, D. Storchak, R. A. Uhrammer, S. Wendt, P. Firbas, J. Havskov, K. Klinge, and K. Veith (2013), Summary of Magnitude Working Group Recommendations on Standard Procedures for Determining Earthquake Magnitudes from Digital Data, *Tech. rep.* 2.5

Brune, J. N. (1968), Seismic Moment, Seismicity and Rate of Slip along Major Fault Zones, *Journal of Geophysical Research*, *73*(2). 6.4.2

Čadek, O. (1987), Studying earthquake ground motion in Prague from Wiechert seismograph records, *Gerlands Beiträge zur Geophysik*, *96*(5), 438–447. 2.2.1

Cavalié, O., M. P. Doin, C. Lasserre, and P. Briole (2007), Ground motion measurement in the Lake Mead area, Nevada, by differential synthetic aperture radar interferometry time series analysis: Probing the lithosphere rheological structure, *Journal of Geophysical Research: Solid Earth*, *112*(3), 1–18, doi:10.1029/2006JB004344. 3.2

Cavalié, O., C. Lasserre, M. P. Doin, G. Peltzer, J. Sun, X. Xu, and Z. K. Shen (2008), Present-day deformation across the Haiyuan fault (Gansu, China), measured by SAR interferometry, *European Space Agency, (Special Publication)*, (655). 1.2, 1.3, 1.4, 2.1, 2.1.1, 3.1, 3.2, 5.3, 6.2.1

CEA-PBED, C. E. A. E. D. P. B. (1995), China Historical Strong Earthquake Catalogue (BC23-AD1911). (document), 1.1, 1.4, 1.8, 5.3, 5.14, 5.3

Chen, C. W., and H. A. Zebker (2001), Two-dimensional phase unwrapping with use of statistical models for cost functions in nonlinear optimization, *Journal of the Optical Society of America A*, *18*(2), 338, doi:10.1364/josaa.18.000338. 6.3.2

Chen, C. W., and H. A. Zebker (2002), Phase unwrapping for large SAR interferograms: Statistical segmentation and generalized network models, *IEEE Transactions on Geoscience and Remote Sensing*, *40*(8), 1709–1719, doi:10.1109/TGRS.2002.802453. 6.3.2

Chen, L., F. A. Capitanio, L. Liu, and T. V. Gerya (2017a), Crustal rheology controls on the Tibetan plateau formation during India-Asia convergence, *Nature Communications*, *8*(May), 1–8, doi:10.1038/ncomms15992. 1.2

Chen, W., and P. Molnar (1977), Seismic moments of major earthquakes and the average rate of slip in Central Asia, *Journal of Geophysical Research*, *82*(10), doi:10.1029/JB082i020p02945. 2.1, 2.1, 2.4.1, 6.4.2, A.1

Chen, Y., Y. Wang, and Y. Zhang (2017b), Crustal velocity structure of central Gansu Province from regional seismic waveform inversion using firework algorithm, *Earthquake Science*, *30*(2), 81–89, doi:10.1007/s11589-017-0184-5. 2.3.6

Cheng, J., Y. Rong, H. Magistrale, G. Chen, and X. Xu (2017), An Mw-Based Historical Earthquake Catalog for Mainland China, *Bulletin of the Seismological Society of America*, *107*(5), 2490–2500, doi:10.1785/0120170102. 6.4.1

CIESIN, C. f. I. E. S. I. N. C. U. (2018), Gridded Population of the World, Version 4 (GPWv4): Population Density Adjusted to Match 2015 Revision UN WPP Country Totals, Revision 11. (document), 1.2, 1.3

Clark, K. J., E. K. Nissen, J. D. Howarth, I. J. Hamling, J. J. Mountjoy, W. F. Ries, K. Jones, S. Goldstien, U. A. Cochran, P. Villamor, S. Hreinsdóttir, N. J. Litchfield, C. Mueller, K. R. Berryman, and D. T. Strong (2017), Highly variable coastal deformation in the 2016 MW7.8 Kaikōura earthquake reflects rupture complexity along a transpressional plate boundary, *Earth and Planetary Science Letters*, *474*, 334–344, doi:10.1016/j.epsl.2017.06.048. 2.3

Clark, M. K., J. W. Bush, and L. H. Royden (2005), Dynamic topography produced by lower crustal flow against rheological strength heterogeneities bordering the Tibetan Plateau, *Geophysical Journal International*, *162*(2), 575–590, doi:10.1111/j.1365-246X.2005.02580.x. 1.2

Close, U., and E. McCormick (1922), Where the Mountains Walked, *The National Geographic Magazine*, *41*(5), 445–464. 2.1.2

Copley, A. (2012), The formation of mountain range curvature by gravitational spreading, *Earth and Planetary Science Letters*, *351-352*, 208–214, doi:10.1016/j.epsl.2012.07.036. 1.2

Copley, A. (2017), The strength of earthquake-generating faults, *Journal of the Geological Society*, *175*, jgs2017—-037, doi:10.1144/jgs2017-037. 1.2

Cowgill, E., R. D. Gold, X. Chen, X. F. Wang, J. R. Arrowsmith, and J. Southon (2009), Low Quaternary slip rate reconciles geodetic and geologic rates along the Altyn Tagh fault northwestern Tibet, *Geology*, *37*(7), 647–650, doi:10.1130/G25623A.1. 1.3

Dai, G., C. Miao, and L. Zhai (2019), Unified Earthquake Cataloging of China Seismographic Network, *Earthquake Research in China*, *35*(1), 192–203. (document), 5.14, 5.3, 5.3

Daout, S., S. Barbot, G. Peltzer, M. P. Doin, Z. Liu, and R. Jolivet (2016a), Constraining the kinematics of metropolitan Los Angeles faults with a slip-partitioning model, *Geophysical Research Letters*, *43*(21), 11,192–11,201, doi:10.1002/2016GL071061. 2.3.5

Daout, S., R. Jolivet, C. Lasserre, M. P. Doin, S. Barbot, P. Tapponnier, G. Peltzer, A. Socquet, and J. Sun (2016b), Along-strike variations of the partitioning of convergence across the Haiyuan fault system detected by InSAR, *Geophysical Journal International*, *205*(1), 536–547, doi:10.1093/gji/ggw028. 1.3, 2.1.1, 3.1, 4.5.1

Daout, S., M. P. Doin, G. Peltzer, A. Socquet, and C. Lasserre (2017), Large-scale InSAR monitoring of permafrost freeze-thaw cycles on the Tibetan Plateau, *Geophysical Research Letters*, *44*(2), 901–909, doi:10.1002/2016GL070781. 4.5.2

Daout, S., M.-P. Doin, G. Peltzer, C. Lasserre, A. Socquet, M. Volat, and H. Sudhaus (2018), Strain Partitioning and Present-Day Fault Kinematics in NW Tibet From Envisat SAR Interferometry, *Journal of Geophysical Research: Solid Earth*, *123*(3), 2462–2483, doi:10.1002/2017JB015020. 3.2, 3.4.5

Daout, S., H. Sudhaus, T. Kausch, A. Steinberg, and B. Dini (2019), Interseismic and Postseismic Shallow Creep of the North Qaidam Thrust Faults Detected with a Multitemporal InSAR Analysis, *Journal of Geophysical Research: Solid Earth*, *124*(7), 7259–7279, doi:10.1029/2019JB017692. 3.1

Daout, S., B. Dini, W. Haeberli, M. P. Doin, and B. Parsons (2020), Ice loss in the Northeastern Tibetan Plateau permafrost as seen by 16 yr of ESA SAR missions, *Earth and Planetary Science Letters*, *545*, 116,404, doi:10.1016/j.epsl.2020.116404. 3.2, 3.4.1, 3.4.5, 4.5.2

Das, S., and C. H. Scholz (1983), Why large earthquakes do not nucleate at shallow depths, *Nature*, *305*(5935), 621–623, doi:https://doi.org/10.1038/305621a0. 2.2.2

Dee, D. P., S. M. Uppala, A. J. Simmons, P. Berrisford, P. Poli, S. Kobayashi, U. Andrae, M. A. Balmaseda, G. Balsamo, P. Bauer, P. Bechtold, A. C. Beljaars, L. van de Berg, J. Bidlot, N. Bormann, C. Delsol, R. Dragani, M. Fuentes, A. J. Geer, L. Haimberger, S. B. Healy, H. Hersbach, E. V. Hólm, L. Isaksen,

P. Kållberg, M. Köhler, M. Matricardi, A. P. Mcnally, B. M. Monge-Sanz, J. J. Morcrette, B. K. Park, C. Peubey, P. de Rosnay, C. Tavolato, J. N. Thépaut, and F. Vitart (2011), The ERA-Interim reanalysis: Configuration and performance of the data assimilation system, *Quarterly Journal of the Royal Meteorological Society*, *137*(656), 553–597, doi:10.1002/qj.828. 3.2

Dee, D. P., M. Balmaseda, G. Balsamo, R. Engelen, A. J. Simmons, and J. N. Thépaut (2014), Toward a consistent reanalysis of the climate system, *Bulletin of the American Meteorological Society*, *95*(8), 1235–1248, doi:10.1175/BAMS-D-13-00043.1. 3.2

Deng, Q., F. Sung, S. Zhu, M. Li, T. Wang, W. Zhang, B. Burchfiel, P. Molnar, and P. Zhang (1984), Active faulting and tectonics of the Ningxia-Hui Autonomous Region, China, *Journal of Geophysical Research*, *89*(10), 4427–4445, doi:10.1029/JB089iB06p04427. 2.1, 2.2.3, 2.4.1, 2.5, 3.1, A.1

Deng, Q., S. Chen, F. Song, S. Zhu, Y. Wang, W. Zhang, D. Jiao, B. Burchfiel, P. Molnar, L. Royden, and P. Zhang (1986), Variations in the geometry and amount of slip on the Haiyuan (Nanxihaushan) Fault zone, China and the surface rupture of the 1920 Haiyuan earthquake, in *Haiyuan Fault Zone*, pp. 169–182, doi:10.1029/GM037p0169. (document), 2.1, 2.1.2, 2.3, 2.3, 2.9, 2.3.4, 2.3.5, 2.3.6, 2.1

Deng, Q., P. Zhang, Y. Ran, X. Yang, W. Min, and L. Chen (2003), Active tectonics and earthquake activities in China, *Earth Science Frontiers*, *10*(z1), 66–73. 6.2.3

Di Giacomo, D. (2020), ISC-GEM solution for the Haiyuan earthquake of 16 December 1920, *ISC Seismological Dataset Repository*, p. 1, doi:https://doi.org/10.31905/8IZMESGK. 2.4.3, A.1

Di Giacomo, D., I. Bondár, D. A. Storchak, E. R. Engdahl, P. Bormann, and J. Harris (2015a), ISC-GEM: Global Instrumental Earthquake Catalogue (1900–2009), III. Re-computed MS and mb, proxy MW, final magnitude composition and completeness assessment, *Physics of the Earth and Planetary Interiors*, *239*, 33 – 47, doi:https://doi.org/10.1016/j.pepi.2014.06.005. A.1

Di Giacomo, D., J. Harris, A. Villaseñor, D. A. Storchak, E. R. Engdahl, and W. H. Lee (2015b), ISC-GEM: Global Instrumental Earthquake Catalogue (1900–2009), I. Data collection from early instrumental seismological bulletins, *Physics of the Earth and Planetary Interiors*, *239*, 14 – 24, doi:https://doi.org/10.1016/j.pepi.2014.06.003. A.1

Di Giacomo, D., E. R. Engdahl, and D. A. Storchak (2018), The ISC-GEM Earthquake Catalogue (1904–2014): status after the Extension Project, *Earth System Science Data*, *10*(4), 1877–1899, doi:10.5194/essd-10-1877-2018. A.1

Doin, M.-P., C. Lasserre, G. Peltzer, O. Cavalié, and C. Doubre (2009), Corrections of stratified tropospheric delays in SAR interferometry: Validation with global atmospheric models, *Journal of Applied Geophysics*, *69*(1), 35 – 50, doi:https://doi.org/10.1016/j.jappgeo.2009.03.010. 3.2

Doin, M.-P., F. Lodge, S. Guillaso, R. Jolivet, C. Lasserre, G. Ducret, R. Grandin, E. Pathier, and V. Pinel (2011), Presentation of the small baseline NSBAS processing chain on a case example: the Etna deformation monitoring from 2003 to 2010 using Envisat data, *Proceedings of the ESA 'Fringe 2011 Workshop', Frascati, Italy*, pp. (19–23). 3.4, 3.5

Doin, M. P., C. Twardzik, G. Ducret, C. Lasserre, S. Guillaso, and S. Jianbao (2015), InSAR measurement of the deformation around Siling Co Lake: Inferences on the lower crust viscosity in central Tibet, *Journal of Geophysical Research: Solid Earth*, *120*(7), 5290–5310, doi:10.1002/2014JB011768. 3.4, 3.4.5

Duan, H., S. Zhou, and R. Li (2018), Estimation of dip angle of Haiyuan faults based on seismic data, *Acta Geophysica Sinica*, *61*, 3713–3721, doi:10.6038/cjg2018L0601. 2.1.1, 2.3.5

Ducret, G., M. P. Doin, R. Grandin, C. Lasserre, and S. Guillaso (2013), DEM corrections before unwrapping in a small baseline strategy for InSAR time series analysis, *IEEE Geoscience and Remote Sensing Letters*, *11*(3), 696–700, doi:10.1109/LGRS.2013.2276040. 3.2

Dupont-Nivet, G., P. C. Lippert, D. J. van Hinsbergen, M. J. Meijers, and P. Kapp (2010), Palaeolatitude and age of the Indo-Asia collision: Palaeomagnetic constraints, *Geophysical Journal International*, *182*(3), 1189–1198, doi:10.1111/j.1365-246X.2010.04697.x. 1.3

Duvall, A. R., M. K. Clark, E. Kirby, K. A. Farley, W. H. Craddock, C. Li, and D. Y. Yuan (2013), Low-temperature thermochronometry along the Kunlun and Haiyuan Faults, NE Tibetan Plateau: Evidence for kinematic change during late-stage orogenesis, *Tectonics*, *32*(5), 1190–1211, doi:10.1002/tect.20072. 1.3

Dziewonski, A. M., T.-A. Chou, and J. H. Woodhouse (1981), Determination of earthquake source parameters from waveform data for studies of global and regional seismicity, *Journal of Geophysical Research: Solid Earth*, *86*(B4), 2825–2852, doi:10.1029/JB086iB04p02825. (document), 5.3, 5.14, 5.3

Ekström, G., M. Nettles, and A. Dziewoński (2012), The global CMT project 2004–2010: Centroid-moment tensors for 13,017 earthquakes, *Physics of the Earth and Planetary Interiors*, *200-201*, 1 – 9, doi:10.1016/j.pepi.2012.04.002. (document), 5.3, 5.14, 5.3

Elliott, A., M. Oskin, and Y. Shao (2015), Rupture termination at restraining bends: The last great earthquake on the Altyn Tagh Fault, *Geophysical Research Letters*, *42*, 2164–2170, doi:10.1002/2015GL063107. 2.3.2

Elliott, J. R., J. Biggs, B. Parsons, and T. J. Wright (2008), InSAR slip rate determination on the Altyn Tagh Fault, northern Tibet, in the presence of topographically correlated atmospheric delays, *Geophysical Research Letters*, *35*(12), doi:10.1029/2008GL033659. 1.3, 3.1, 3.2

Elliott, J. R., R. J. Walters, P. C. England, J. A. Jackson, Z. Li, and B. Parsons (2010), Extension on the Tibetan plateau: recent normal faulting measured by InSAR and body wave seismology, *Geophysical Journal International*, *183*(2), 503–535, doi:10.1111/j.1365-246X.2010.04754.x. 1.3

Elliott, J. R., R. J. Walters, and T. J. Wright (2016), The role of space-based observation in understanding and responding to active tectonics and earthquakes, *Nature Communications*, *7*, 1–16, doi:10.1038/ncomms13844. 1.2, 1.4, 3.1, 3.2

Engdahl, E. R., and A. Villaseñor (2002), Global seismicity: 1900-1999, *International Geophysics*, *81*, 0–12, doi:10.1016/S0074-6142(02)80244-3. (document), 2.2, 2.1.3, 2.4.1

England, P., and R. Bilham (2015), The Shillong Plateau and the great 1897 Assam earthquake, *Tectonics*, *34*, 1792–1812, doi:10.1002/2015TC003902. 5.3, 6.4.2

England, P., and G. Houseman (1985), Role of lithospheric strength heterogeneities in the tectonics of Tibet and neighbouring regions, *Nature*, *315*(6017), 297–301, doi:10.1038/315297a0. 1.2

England, P., and J. Jackson (2011), Uncharted seismic risk, *Nature Geoscience*, *4*(6), 348–349, doi:10.1038/ngeo1168. 1.4

England, P., and D. Mckenzie (1982), A thin viscous sheet model for continental deformation, *Geophysical Journal International*, *70*(2), 295–321. 1.2, 5.2.1, 5.2.4, 5.2.5, 5.2.5, 6.4.2

England, P., and P. Molnar (2005), Late Quaternary to decadal velocity fields in Asia, *Journal of Geophysical Research: Solid Earth*, *110*(12), 1–27, doi:10.1029/2004JB003541. 1.2, 5.3

England, P., and P. Molnar (2015), Rheology of the lithosphere beneath the central and western Tien Shan, *Journal of Geophysical Research : Solid Earth*, *120*, 3803–3823, doi:10.1002/2014JB011733. 1.2

EUODP, E. O. D. P. (2020), Global administrative boundaries. (document), 1.2

Fan, J.-c., S.-l. Li, X.-k. Zhang, and M.-j. Liu (2004), Geometric form of Haiyuan fault zone in the crustal interior and dynamics implications, *Acta Seismologica Sinica*, *17*(S1), 43–51, doi:10.1007/s11589-004-0065-6. 2.1.1, 2.2.3

Fattahi, H., and F. Amelung (2014), InSAR uncertainty due to orbital errors , *Geophysical Journal International*, *199*(1), 549–560, doi:10.1093/gji/ggu276. 3.4.3

Feng, C., T. J. Liu, and H. P. Hong (2020), Seismic hazard assessment for mainland China based on spatially smoothed seismicity, *Journal of Seismology*, *24*(3), 613–633, doi:10.1007/s10950-020-09918-3. 1.4

Ferretti, A., C. Prati, and F. Rocca (2001), Permanent scatterers in SAR interferometry, *IEEE Transactions on Geoscience and Remote Sensing*, *39*(1), 8–20, doi:10.1109/36.898661. 3.2

Fu, J., Z. Li, H. Meng, J. Wang, and X. Shan (2019), Performance Evaluation of Low-Cost Seismic Sensors for Dense Earthquake Early Warning: 2018–2019 Field Testing in Southwest China, *Sensors*, *19*, 1999, doi:doi:10.3390/s19091999. 1.1

Gan, W., P. Zhang, Z. K. Shen, Z. Niu, M. Wang, Y. Wan, D. Zhou, and J. Cheng (2007), Present-day crustal motion within the Tibetan Plateau inferred from GPS measurements, *Journal of Geophysical Research: Solid Earth*, *112*(8), 1–14, doi:10.1029/2005JB004120. 1.2, 4.3.1

Gan, W., Q. Li, R. Zhang, and H. Shi (2012), Construction and application of tectonics and environmental observation network of mainland China, *J. Eng. Stud*, *4*(4), 324–331. 3.1

Gao, M. (2003), New national seismic zoning map of China, *Acta Seismologica Sinica English Edition*, *16*(6), 639, doi:10.1007/s11589-003-0048-z. 1.4

Gao, M. (2015), *Publicizing Materials of GB 18306-2015 Chinese Ground Motion Parameter Zoning Map*, 264 pp., China Standard Press, Bejing. 1.1

Garthwaite, M. C., H. Wang, and T. J. Wright (2013), Broadscale interseismic deformation and fault slip rates in the central Tibetan Plateau observed using InSAR, *Journal of Geophysical Research: Solid Earth*, *118*(9), 5071–5083, doi:10.1002/jgrb.50348. 3.1

Gatinsky, Y. G., and T. V. Prokhorova (2014), Superficial and Deep Structure of Central Asia as Example of Continental Lithosphere Heterogeneity, *Universal Journal of Geoscience*, *2*(2), 43–52, doi:10.13189/ujg.2014.020202. 1.2

Gaudemer, Y., P. Tapponnier, B. Meyer, G. Peltzer, G. Shunmin, C. Zhitai, D. Huagung, and I. Cifuentes (1995), Partitioning of crustal slip between linked, active faults in the eastern Qilian Shan, and evidence for a major seismic gap, the 'Tianzhu gap', on the western Haiyuan Fault, Gansu (China), *Geophysical Journal International*, *120*(3), 599–645, doi:10.1111/j.1365-246X.1995.tb01842.x. 1.3, 2.1.1, 2.1.1, 5.2.2

Geller, R. J., and H. Kanamori (1977), Magnitude of great shallow earthquakes from 1904 to 1952, *Bulletin of the Seismological Society of America*, *67*(3), 587–598. 2.1.3, 2.4.3

Gold, P. O., M. E. Oskin, A. J. Elliott, A. Hinojosa-Corona, M. H. Taylor, O. Kreylos, and E. Cowgill (2013), Coseismic slip variation assessed from terrestrial lidar scans of the El Mayor-Cucapah surface rupture, *Earth and Planetary Science Letters*, *366*, 151–162, doi:10.1016/j.epsl.2013.01.040. 2.3.3

Gold, R. D., E. Cowgill, J. R. Arrowsmith, J. Gosse, X. Chen, and X. F. Wang (2009), Riser diachroneity, lateral erosion, and uncertainty in rates of strikeslip faulting: A case study from Tuzidun along the Altyn Tagh Fault, NW China, *Journal of Geophysical Research: Solid Earth*, *114*(4), 1–24, doi:10.1029/2008JB005913. 1.3

Gold, R. D., E. Cowgill, J. R. Arrowsmith, X. Chen, W. D. Sharp, K. M. Cooper, and X. F. Wang (2011), Faulted terrace risers place new constraints on the late Quaternary slip rate for the central Altyn Tagh fault, northwest Tibet, *Bulletin of the Geological Society of America*, *123*(5), 958–978, doi:10.1130/B30207.1. 1.3

Gold, R. D., E. Cowgill, J. R. Arrowsmith, and A. M. Friedrich (2017), Pulsed strain release on the Altyn Tagh fault, northwest China, *Earth and Planetary Science Letters*, *459*, 291–300, doi:10.1016/j.epsl.2016.11.024. 1.3

Gomba, G., F. Rodriguez Gonzalez, and F. De Zan (2017), Ionospheric phase screen compensation for the Sentinel-1 TOPS and ALOS-2 ScanSAR modes, *IEEE Transactions on Geoscience and Remote Sensing*, *55*(1), 223–235, doi:10.1109/TGRS.2016.2604461. 3.4.3

Gong, X., Y. Liu, Y. Jiao, B. Wang, J. Zhou, and H. Yu (2015), A Novel Earthquake Education System Based on Virtual Reality, *IEICE TRANSACTIONS on Information and Systems*, *E98-D*(12), 2242–2249, doi:10.1587/transinf.2015EDP7165. 1.1

Gruber, S. (2012), Derivation and analysis of a high-resolution estimate of global permafrost zonation, *Cryosphere*, *6*(1), 221–233, doi:10.5194/tc-6-221-2012. (document), 4.5.2, B.15

Gu, G. (1983), *Chinese Earthquake Catalogue*, Seismological Press, Beijing. 2.4.4, 2.5, A.1

Gutenberg, B. (1945a), Amplitudes of Surface Waves and Magnitudes of Shallow Earthquakes, *Bulletin of the Seismological Society of America*, *35*(1), 3–12. 2.1.3, A.1

Gutenberg, B. (1945b), Amplitudes of P, PP, and S and Magnitude of Shallow Earthquakes*, *Bulletin of the Seismological Society of America*, *35*(2), 57–69. 2.1.3, 2.2.5

Gutenberg, B. (1956), Great earthquakes 1896-1903, *Eos, Transactions American Geophysical Union*, *37*(5), 608–614, doi:10.1029/TR037i005p00608. 2.1, A.1

Gutenberg, B., and C. Richter (1941), *Seismicity of the Earth*, special papers, number 34 ed., 1–126 pp., Geological Society of America, New York, doi:10.1130/SPE34-p1. 2.1, 2.1.3, 2.2.5, 2.5, A.1

Gutenberg, B., and C. F. Richter (1954), *Seismicity of the earth and associated phenomena*, Princeton University Press, Princeton, N.J. 1.4, 2.2.5, 2.5, 5.3

Gutenberg, B., and C. F. Richter (1956), Magnitude and energy of earthquakes, *Annali di Geofisica*, *9*(1), doi:10.4401/ag-5590. 2.1.3, 2.2.5, 2.5

Hanks, T. C., and H. Kanamori (1979), A moment magnitude scale, *Journal of Geophysical Research B: Solid Earth*, *84*(B5), 2348–2350, doi:10.1029/JB084iB05p02348. 2.1.3

Hanssen, R. F. (2001), *Radar Interferometry:Data Interpretation and Error Analysis*, 308 pp. 3.2

Harkins, N., E. Kirby, X. Shi, E. Wang, D. Burbank, and F. Chun (2010), Millennial slip rates along the eastern Kunlun fault: Implications for the dynamics of intracontinental deformation in Asia, *Lithosphere*, *2*(4), 247–266, doi:10.1130/L85.1. 1.3

He, J., P. Vernant, J. Chéry, W. Wang, S. Lu, W. Ku, W. Xia, and R. Bilham (2013), Nailing down the slip rate of the Altyn Tagh fault, *Geophysical Research Letters*, *40*(20), 5382–5386, doi:10.1002/2013GL057497. 1.2, 1.3

Heimann, S. (2019), Snuffler - seismogram browser and workbench — Pyrocko v2019.06.06 Manual. 2.2.2, 2.2.5

Heimann, S., M. Kriegerowski, M. Isken, S. Cesca, S. Daout, F. Grigoli, C. Juretzek, T. Megies, N. Nooshiri, A. Steinberg, H. Sudhaus, H. Vasyura-Bathke, T. Willey, and T. Dahm (2017), Pyrocko - An open-source seismology toolbox and library, doi:http://doi.org/10.5880/GFZ.2.1.2017.001. (document), 2.4, 2.2.3

Heimann, S., H. Vasyura-Bathke, H. Sudhaus, M. P. Isken, M. Kriegerowski, A. Steinberg, and T. Dahm (2019), A python framework for efficient use of pre-computed green's functions in seismological and other physical forward and inverse source problems, *Solid Earth*, *10*(6), 1921–1935, doi:10.5194/se-10-1921-2019. 2.2.3

Hooper, A., H. Zebker, P. Segall, and B. Kampes (2004), A new method for measuring deformation on volcanoes and other natural terrains using InSAR persistent scatterers, *Geophysical Research Letters*, *31*(23), 1–5, doi:10.1029/2004GL021737. 3.2

Horton, B. K., G. Dupont-Nivet, J. Zhou, G. L. Waanders, R. F. Butler, and J. Wang (2004), Mesozoic-Cenozoic evolution of the Xining-Minhe and Dangchang basins, northeastern Tibetan Plateau: Magnetostratigraphic and biostratigraphic results, *Journal of Geophysical Research: Solid Earth*, *109*(B4), 1–15, doi:10.1029/2003jb002913. 1.3

Hou, J. J., M. K. Han, B. L. Chai, and H. Y. Han (1998), Geomorphological observations of active faults in the epicentral region of the Huaxian large earthquake in 1556 in Shaanxi Province, China, *Journal of Structural Geology*, *20*(5), 549–557, doi:10.1016/S0191-8141(97)00112-0. 1.1

Hou, K., Z. Lei, F. Wan, L. Li, and Z. Xiong (2005), Research on the 1879 southern Wudu M8.0 earthquake and its co-seismic ruptures, *Earthquake Research in China*, *21*(3), 295–310. 6.2.3

Hu, X., E. Garzanti, J. Wang, W. Huang, W. An, and A. Webb (2016), The timing of India-Asia collision onset – Facts, theories, controversies, *Earth-Science Reviews*, *160*, 264–299, doi:10.1016/j.earscirev.2016.07.014. 3.1

Hussain, E., A. Hooper, T. J. Wright, R. J. Walters, and D. P. Bekaert (2016), Interseismic strain accumulation across the central North Anatolian Fault from iteratively unwrapped InSAR measurements, *Journal of Geophysical Research: Solid Earth*, *121*(12), 9000–9019, doi:10.1002/2016JB013108. 6.3.2

Hussain, E., T. J. Wright, R. J. Walters, D. P. S. Bekaert, R. Lloyd, and A. Hooper (2018), Constant strain accumulation rate between major, *Nature Communications*, *9*(1392), 1–9, doi:10.1038/s41467-018-03739-2. 1.4, 3.1, 4.3, 6.4.2

Hutton, K., J. Woessner, and E. Hauksson (2010), Earthquake Monitoring in Southern California for Seventy-Seven Years (1932 – 2008), *Bulletin of the Seismological Society of America*, *100*(2), 423–446, doi:10.1785/0120090130. 5.3

ICGC (2019), Institut Cartogràfic i Geològic de Catalunya. (document)

IGCEA, and (Institute of Geology, China Earthquake Administration Ningxia Bureau of China Earthquake Administration). NBCEA (1990), *Active Haiyuan Fault Zone Monograph* , 286 pp., Seismological Publishing House, Beijing, China. (document), 2.1, 2.1.1, 2.1.2, 2.2.3, 2.3, 2.3, 2.9, 2.3.4, 2.16

INGV (2019), Istituto Nationale di Geofisica e Vulcanologia. (document)

ISC, (International Seismological Centre). (2018), On-line Bulletin, https://doi.org/10.31905/D808B830. (document), 2.1.2, 2.2.1, 5.14, 5.3

ISC, (International Seismological Centre). (2019), ISC-GEM Earthquake Catalogue, http://doi.org/10.31905/D808B825. (document), 1.1, 1.2, 1.4, 1.4, 1.8, 2.1, 2.1, 2.2, 2.4.1, 5.14, 5.3

JCUMSO (2019), John Carroll University Meteorological and Seismological Observatory, 1920, Seismogram of the December 16, 1920, earthquake in Ningxia Provence, China, from John Carroll University Historic Seismogram Collection: Columbus, Ohio Department of Natural Resources, Division of Geological Survey Archival Collection, Accession2017_006. (document)

Jolivet, R., and M. Simons (2018), A Multipixel Time Series Analysis Method Accounting for Ground Motion, Atmospheric Noise, and Orbital Errors, *Geophysical Research Letters*, *45*(4), 1814–1824, doi:10.1002/2017GL076533. 4.5.1

Jolivet, R., R. Grandin, C. Lasserre, M. P. Doin, and G. Peltzer (2011), Systematic InSAR tropospheric phase delay corrections from global meteorological reanalysis data, *Geophysical Research Letters*, *38*(17), 1–6, doi:10.1029/2011GL048757. 3.2

Jolivet, R., C. Lasserre, M.-P. Doin, S. Guillaso, G. Peltzer, R. Dailu, J. Sun, Z.-K. Shen, and X. Xu (2012), Shallow creep on the Haiyuan Fault (Gansu, China) revealed by SAR Interferometry, *Journal of Geophysical Research*, *117*, doi:10.1029/2011JB008732. 1.3, 2.1.1, 2.1.1, 3.1, 6.2.2

Jolivet, R., C. Lasserre, M. P. Doin, G. Peltzer, J. P. Avouac, J. Sun, and R. Dailu (2013), Spatio-temporal evolution of aseismic slip along the Haiyuan fault, China: Implications for fault frictional properties, *Earth and Planetary Science Letters*, *377-378*, 23–33, doi:10.1016/j.epsl.2013.07.020. 3.1, 5.3, 6.2.1

Jolivet, R., T. Candela, C. Lasserre, F. Renard, Y. Klinger, and M. P. Doin (2015), The burst-like behavior of aseismic slip on a rough fault: The creeping section of the Haiyuan fault, China, *Bulletin of the Seismological Society of America*, *105*(1), 480–488, doi:10.1785/0120140237. 3.1, 5.3, 6.2.1

Kanamori, H. (1977), The energy release in great earthquakes, *Journal of Geophysical Research*, *82*(20), 2981–2987, doi:10.1029/JB082i020p02981. 2.1, 2.1.3, 2.3.6, 2.4.2, 2.5, A.1

Kanamori, H., L. Rivera, and W. H. K. Lee (2010), Historical seismograms for unravelling a mysterious earthquake: The 1907 Sumatra Earthquake, *Geophysical Journal International*, *183*(1), 358–374, doi:10.1111/j.1365-246X.2010.04731.x. 2.1

Kennett, B. L. N., E. R. Engdahl, and R. Buland (1995), Constraints on seismic velocities in the Earth from travel-times, *Geophysical Journal International*, *122*(1), 108–124, doi:10.1111/j.1365-246X.1995.tb03540.x. 2.2.2

King, G., and J. Nábělek (1985), Role of fault bends in the initiation and termination of earthquake rupture, *Science*, *228*(4702), 984–987, doi:10.1126/science.228.4702.984. 2.4.5, 5.2.2, 5.2.5

King, G., Y. Klinger, D. Bowman, and P. Tapponnier (2005), Slip-partitioned surface breaks for the Mw 7.8 2001 Kokoxili earthquake, China, *Bulletin of the Seismological Society of America*, *95*(2), 731–738, doi:10.1785/0120040101. 2.3.5

Kirby, E., N. Harkins, E. Wang, X. Shi, C. Fan, and D. Burbank (2007), Slip rate gradients along the eastern Kunlun fault, *Tectonics*, *26*(2), 1–16, doi:10.1029/2006TC002033. 1.3

Klinger, Y., X. Xu, P. Tapponnier, J. Van der Woerd, C. Lasserre, and G. King (2005), High-resolution satellite imagery mapping for the surface rupture and slip distribution of the Mw 7.8, 14 November 2001 Kokoxili earthquake, Kunlun fault, northern Tibet, China, *Bulletin of the Seismological Society of America*, *95*(5), 1970–1987, doi:10.1785/0120040233. 2.4.1, 2.4.5, 3.1

Klinger, Y., M. Etchebes, P. Tapponnier, and C. Narteau (2011), Characteristic slip for five great earthquakes along the Fuyun Fault in China, *Nature Geoscience*, *4*, 389–392, doi:10.1038/ngeo1158. 2.3.6

Kostrov, V., and V. Riznichenko (1974), Seismic moment and energy of earthquakes, and seismic flow of rock, *International Journal of Rock Mechanics and Mining Sciences & Geomechanics Abstracts*, *1*, 23–40, doi:10.1016/0148-9062(76)90256-4. 6.4.2

Kreemer, C., G. Blewitt, and E. C. Klein (2014), A geodetic plate motion and Global Strain Rate Model, *Geochemistry, Geophysics, Geosystems*, *15*, 3849–3889, doi:10.1002/2014GC005407. (document), 1.4, 1.10

Kulikova, G., and F. Krüger (2015), Source process of the 1911 M8.0 Chon-Kemin earthquake: investigation results by analogue seismic records, *Geophysical Journal International*, *201*(3), 1891–1911, doi:10.1093/gji/ggv091. 2.1, 2.2.1, 2.2.4, 2.2.4

Kulikova, G., and F. Krüger (2017), Historical seismogram reproductions for the source parameters determination of the 1902, Atushi (Kashgar) earthquake, *Journal of Seismology*, *21*(6), 1577–1597, doi:10.1007/s10950-017-9683-z. 2.1, 2.2.4, 2.2.4

Kulikova, G., B. Schurr, F. Krüger, E. Brzoska, and S. Heimann (2016), Source parameters of the Sarez-Pamir earthquake of 1911 February 18, *Geophysical Journal International Geophys. J. Int*, *205*, 1086–1098, doi:10.1093/gji/ggw069. 2.1, 2.2.4, 2.2.4

Kurtz, R., Y. Klinger, M. Ferry, and J.-F. F. Ritz (2018), Horizontal surface-slip distribution through several seismic cycles: The Eastern Bogd fault, Gobi-Altai, Mongolia, *Tectonophysics*, *734-735*(July 2017), 167–182, doi:10.1016/j.tecto.2018.03.011. 2.1, 2.3.6

Laske, G., G. Masters, Z. Ma, and M. Pasyanos (2013), Update on CRUST1.0 - A 1-degree global model of Earth's crust, *Abstract EGU2013-2658 presented at 2013 Geophys. Res. Abstracts 15*, *15*. 2.2.2

Lasserre, C., P.-H. Morel, Y. Gaudemer, P. Tapponnier, F. J. Ryerson, G. C. P. King, F. Métivier, M. Kasser, M. Kashgarian, B. Liu, T. Lu, and D. Yuan (1999), Postglacial left slip rate and past occurrence of M > 8 earthquakes on the western Haiyuan fault, Gansu, China, *Journal of Geophysical Research*, *104*, 17,633–17,651, doi:10.1029/1998JB900082. 1.3, 2.1, 6.2.2

Lasserre, C., B. Bukchin, P. Bernard, P. Tapponnier, Y. Gaudemer, A. Mostinsky, and R. Dailu (2001), Source parametrs and tectonic origin of the 1996 June 1 Tianzhu (Mw=5.2) and 1995 July 21 Yongden (Mw=5.6) earthquakes near the Haiyuan Fault (Gansu, China), *Geophysical Journal International*, *144*(1), 206–220, doi:10.1046/j.1365-246x.2001.00313.x. 2.4.5, 6.2.2

Lasserre, C., Y. Gaudemer, P. Tapponnier, A. S. Mériaux, J. van der Woerd, Y. Daoyang, F. Ryerson, R. Finkel, and M. W. Caffee (2002), Fast late Pleistocene slip rate on the Leng Long Ling segment of the Haiyuan fault, Qinghai, China, *Journal of Geophysical Research*, *107*(B11), 1–15, doi:10.1029/2000JB000060. 1.3, 2.1

Lasserre, C., G. Peltzer, F. Crampé, Y. Klinger, J. Van der Woerd, and P. Tapponnier (2005), Coseismic deformation of the 2001 Mw = 7.8 Kokoxili earthquake in Tibet, measured by synthetic aperture radar interferometry, *Journal of Geophysical Research: Solid Earth*, *110*(12), 1–17, doi:10.1029/2004JB003500. 2.4.1

Lasserre, C., O. Cavalié, G. Peltzer, A. Socquet, M.-P. Doin, J. Sun, X. Xu, Z.-K. Shen, Q. Wang, and Y. Gaudemer (2007), Interseismic strain across the Altyn Tagh and Haiyuan faults at the northern edge of the Tibetan plateau, measured by space geodesy, *Geophysical Research Abstracts*, *9*. 2.1

Lawrence, M., R. Bullock, and Z. Liu (2019), *China's High-Speed Rail Development*, 16 pp., World Bank Group. 1.1

Lazecký, M., K. Spaans, P. J. González, Y. Maghsoudi, Y. Morishita, F. Albino, J. Elliott, N. Greenall, E. Hatton, A. Hooper, D. Juncu, A. McDougall, R. J. Walters, C. S. Watson, J. R. Weiss, and T. J. Wright (2020), LiCSAR: An Automatic InSAR Tool for Measuring and Monitoring Tectonic and Volcanic Activity, *Remote Sensing*, *12*(15), 2430, doi:10.3390/rs12152430. 3.1, 3.3, 3.4, 3.4.1, 3.4.4, 6.3.2

Lee, W. H. K., F. T. Wu, and C. Jacobsen (1976), A CATALOG OF HISTORICAL EARTHQUAKES IN CHINA COMPILED FROM RECENT CHINESE PUBLICATIONS, *Bulletin of the Seismological Society of America*, *66*(6), 2003–2016. 1.4

Li, C., P.-z. Zhang, J. Yin, and W. Min (2009), Late Quaternary left-lateral slip rate of the Haiyuan fault, northeastern margin of the Tibetan Plateau, *Tectonics*, *28*(5), doi:10.1029/2008TC002302. 1.2, 1.3, 2.1.1

Li, C., W. Xu, J. Wu, and M. Gao (2016a), Using new models to assess probabilistic seismic hazard of the North–South Seismic Zone in China, *Natural Hazards*, *82*(1), 659–681, doi:10.1007/s11069-016-2212-5. 1.4

Li, H., Y. Zhang, S. Dong, J. Zhang, Y. Sun, and Q. Wang (2020a), Neotectonics of the Bailongjiang and Hanan faults: New insights into late Cenozoic deformation along the eastern margin of the Tibetan Plateau, *GSA Bulletin*, pp. 1–18, doi:10.1130/b35374.1. (document), 1.3, 1.5, 3.5, 4.5.2, 4.5.2

Li, J., Y. Zhang, H. Li, J. Xiong, J. Li, and T. Wu (2016b), Revisiting Late Quaternary Slip-rate along the Maqu Segment of the Eastern Kunlun Fault, Northeast Tibet, *Acta Seismologica Sinica (English Edition)*, *90*(2), 486–502. 1.3

Li, J., M. Böse, M. Wyss, D. J. Wald, A. Hutchison, J. F. Clinton, Z. Wu, C. Jiang, and S. Zhou (2020b), Estimating rupture dimensions of three major earthquakes in Sichuan, China, for early warning and rapid loss estimates, *Bulletin of the Seismological Society of America*, *110*(2), 920–936, doi:10.1785/0120190117. 1.1

Li, S. (1960), *China Earthquake Catalogue*, Science Press, Beijing. 2.4.4, 2.5

Li, X., C. Li, S. G. Wesnousky, P. Zhang, W. Zheng, I. K. Pierce, and X. Wang (2017a), Paleoseismology and slip rate of the western Tianjingshan fault of NE Tibet, China, *Journal of Asian Earth Sciences*, *146*(1), 304–316, doi:10.1016/j.jseaes.2017.04.031. 2.1.1

Li, X., H. Ran, S. Duan, S. Li, Y. Zhou, and X. Zhang (2017b), Study on Surface Wave Magnitude Gauge Function and Station Correction Value of Teleseismic Events in Korla Station, *Journal of Geodesy and Geodynamics*, *37*(S3), 87–90, doi:10.14075/j.jgg.2017.S3.019. (document), 5.14

Li, Y. (2016), China High Speed Railways and Stations (2016), doi:10.7910/DVN/JIISNB. (document), 1.3

Li, Y., W. Jiang, J. Zhang, and Y. Luo (2016c), Space geodetic observations and modeling of 2016 Mw 5.9 Menyuan earthquake: Implications on seismogenic tectonic motion, *Remote Sensing*, *8*(6), 1–11, doi:10.3390/rs8060519. 2.1.1

Li, Y., X. Shan, C. Qu, and Z. Wang (2016d), Fault locking and slip rate deficit of the Haiyuan-Liupanshan fault zone in the northeastern margin of the Tibetan Plateau, *Journal of Geodynamics*, *102*, 47–57, doi:10.1016/j.jog.2016.07.005. 2.1, 2.1.1, 3.1

Li, Y., Y. Wang, W. Chen, S. Liang, K. Zhang, Y. Zhang, W. Gan, Y. Wang, W. Chen, S. Liang, K. Zhang, and Y. Zhang (2016e), Seismogenic structure of the 2016 Ms6.4 Menyuan earthquake and its effect on the Tianzhu seismic gap, *Geodesy and Geodynamics*, *7*(4), 230–236, doi:10.1016/j.geog.2016.07.002. 2.1.1

Li, Y., X. Shan, C. Qu, Y. Zhang, X. Song, Y. Jiang, G. Zhang, J.-M. Nocquet, W. Gong, W. Gan, and C. Wang (2017c), Elastic block and strain modeling of GPS data around the Haiyuan-Liupanshan fault, northeastern Tibetan Plateau, *Journal of Asian Earth Sciences*, *150*, 87–97, doi:10.1016/J.JSEAES.2017.10.010. 1.4, 6.2.2

Li, Y., M. Liu, Q. Wang, and D. Cui (2018), Present-day crustal deformation and strain transfer in northeastern Tibetan Plateau, *Earth and Planetary Science Letters*, *487*, 179–189, doi:10.1016/j.epsl.2018.01.024. (document), 1.4, 1.10

Liang, S., W. Gan, C. Shen, G. Xiao, J. Liu, W. Chen, X. Ding, D. Zhou, S. Liang, W. Gan, C. Shen, G. Xiao, J. Liu, W. Chen, X. Ding, and D. Zhou (2013), Three-dimensional velocity field of present-day crustal motion of the Tibetan Plateau derived from GPS measurements, *J. Geophys. Res. Solid Earth*, *118*, 5722–5732, doi:10.1002/2013JB010503. (document), 3.1, 4.3.1, 4.5, 4.3.1

Lin, A., Z. Ren, D. Jia, and X. Wu (2009), Co-seismic thrusting rupture and slip distribution produced by the 2008 Mw 7.9 Wenchuan earthquake, China, *Tectonophysics*, *471*(3-4), 203–215, doi:10.1016/j.tecto.2009.02.014. 2.4.1

Liu, Y., G. Zhang, Y. Zhang, and X. Shan (2018), Source parameters of the 2016 Menyuan earthquake in the northeastern Tibetan Plateau determined from regional seismic waveforms and InSAR measurements, *Journal of Asian Earth Sciences*, *158*(February), 103–111, doi:10.1016/j.jseaes.2018.02.009. 3.1

Liu-Zeng, J., Z. Zhang, L. Wen, P. Tapponnier, J. Sun, X. Xing, G. Hu, Q. Xu, L. Zeng, L. Ding, C. Ji, K. W. Hudnut, and J. van der Woerd (2009), Co-seismic ruptures of the 12 May 2008, Ms 8.0 Wenchuan earthquake, Sichuan: East-west crustal shortening on oblique, parallel thrusts along the eastern edge of Tibet, *Earth and Planetary Science Letters*, *286*(3-4), 355–370, doi:10.1016/j.epsl.2009.07.017. 2.4.1

Liu-zeng, J., Y. Shao, Y. Klinger, K. Xie, D. Yuan, and Z. Lei (2015), Variability in magnitude of paleoearthquakes revealed by trenching and historical records, along the Haiyuan Fault, China, *Journal of Geophysical Research: Solid Earth*, *120*, 8304–8333, doi:DOI: 10.1002/2015JB012163. 1.5, 2.1, A.1

López-Quiroz, P., M. P. Doin, F. Tupin, P. Briole, and J. M. Nicolas (2009), Time series analysis of Mexico City subsidence constrained by radar interferometry, *Journal of Applied Geophysics*, *69*(1), 1–15, doi:10.1016/j.jappgeo.2009.02.006. 3.4.5

Ma, J., X. J. Feng, G. Y. Li, and X. N. Li (2020), New insights from analysis of historical texts on the 1568 Northeast Xi'an earthquake, Shaanxi, China, *International Journal of Disaster Risk Reduction*, *44*(November 2019), doi:10.1016/j.ijdrr.2019.101417. 1.4

Mackenzie, D., and A. Elliott (2017), Untangling tectonic slip from the potentially misleading effects of landform geometry, *Geosphere*, *13*(4), 1310–1328, doi:10.1130/GES01386.1. 2.3.6

Massonnet, D., and J.-C. Souyris (2008), *Imaging with synthetic aperture radar*, 1-298 pp. (document), 3.2

Matrau, R., Y. Klinger, J. V. D. Woerd, Z. Li, and X. Xu (2019), Late Pleistocene - Holocene slip rate along the Hasi Shan restraining bend of the Haiyuan fault : implication for faulting dynamics of a complex fault system, *Tectonics*, pp. 0–3, doi:10.1029/2019TC005488. 2.1.1

Maubant, L., E. Pathier, S. Daout, M. Radiguet, M.-P. Doin, E. Kazachkina, V. Kostoglodov, N. Cotte, and A. Walpersdorf (2020), Independent Component Analysis and Parametric Approach for Source Separation in InSAR Time Series at Regional Scale: Application to the 2017–2018 Slow Slip Event in Guerrero (Mexico), *Journal of Geophysical Research: Solid Earth*, *125*(3), e2019JB018,187, doi:10.1029/2019JB018187. 3.2, 3.4.3

McComb, H., and C. J. West (1931), List of Seismological Stations of the World, 2nd ed., *Tech. rep.*, The National Research Council of the National Academy of Sciences, Washington, D. C. 2.2.1, 2.2.1, 2.2.4, 6.3.1, A.2

Mériaux, A. S., P. Tapponnier, F. J. Ryerson, X. Xu, G. King, J. Van der Woerd, R. C. Finkel, L. Haibing, M. W. Caffee, Z. Xu, and W. Chen (2005), The Aksay segment of the northern Altyn Tagh fault: Tectonic geomorphology, landscape evolution, and Holocene slip rate, *Journal of Geophysical Research: Solid Earth*, *110*(4), 1–32, doi:10.1029/2004JB003210. 1.3

Mériaux, A. S., J. Van Der Woerd, P. Tapponnier, F. J. Ryerson, R. C. Finkel, C. Lasserre, and X. Xu (2012), The Pingding segment of the Altyn Tagh Fault (91E): Holocene slip-rate determination from cosmogenic radionuclide dating of offset fluvial terraces, *Journal of Geophysical Research: Solid Earth*, *117*(9), 1–26, doi:10.1029/2012JB009289. 1.3

Meyer, B., P. Tapponnier, L. Bourjot, F. Métivier, Y. Gaudemer, G. Peltzer, G. Shunmin, and C. Zhitai (1998), Crustal thickening in Gansu-Qinghai, lithospheric mantle subduction, and oblique, strike-slip controlled growth of the Tibet Plateau, *Geophysical Journal International*, *135*(1), 1–47, doi:10.1046/j.1365-246X.1998.00567.x. 2.1.1

Middleton, T. A., R. T. Walker, B. Parsons, Q. Lei, Y. Zhou, and Z. Ren (2015), A major , intraplate , normal-faulting earthquake : The 1739 Yinchuan event in northern China, *Journal of Geophysical Research : Solid Earth*, *4*, 293–320, doi:10.1002/2015JB012355. 1.4, 2.1, 2.3.1

Milliner, C. W. D., J. F. Dolan, J. Hollingsworth, S. Leprince, F. Ayoub, and C. G. Sammis (2015), Quantifying near-field and off-fault deformation patterns of the 1992 Mw 7.3 Landers earthquake Christopher, *Geochemistry, Geophysics, Geosystems*, *16*, 1577–1598, doi:10.1002/2014GC005693. 2.3.6

Mo, X., Z. Zhao, J. Deng, M. Flower, X. Yu, Z. Luo, Y. Li, S. Zhou, G. Dong, D. Zhu, and L. Wang (2006), Petrology and geochemistry of postcollisional volcanic rocks from the Tibetan plateau: Implications for lithosphere heterogeneity and collision-induced asthenospheric mantle flow, *Special Paper of the Geological Society of America*, *409*(June), 507–530, doi:10.1130/2006.2409(24). 1.2

Molnar, P. (1979), Earthquake recurrence intervals and plate tectonics, *Bulletin of the Seismological Society of America*, *69*(1), 115–133. 1.4, 5.3, 6.4.2

Morishita, Y., M. Lazecky, T. J. Wright, J. R. Weiss, J. R. Elliott, and A. Hooper (2020), LiCSBAS: An open-source insar time series analysis package integrated with the LiCSAR automated sentinel-1 InSAR processor, *Remote Sensing*, *12*(3), 5–8, doi:10.3390/rs12030424. 3.1, 3.2, 3.3, 3.4.2

Murray, K. D., D. P. Bekaert, and R. B. Lohman (2019), Tropospheric corrections for InSAR: Statistical assessments and applications to the Central United States and Mexico, *Remote Sensing of Environment*, *232*, 111,326, doi:https://doi.org/10.1016/j.rse.2019.111326. 3.2, 4.5.1

National Geophysical Data Center / World Data Service (NGDC/WDS) (2020), NCEI/WDS Global Significant Earthquake Database. NOAA National Centers for Environmental Information, doi:10.7289/V5TD9V7K. (document), 1.1, 1.2

NBSC, N. B. o. S. o. C. (2019), *China Statistical Yearbook*. 1.1

Niu, Z., M. Wang, H. Sun, J. Sun, X. You, W. Gan, G. Xue, J. Hao, S. Xin, Y. Wang, Y. Wang, and B. Li (2005), Contemporary velocity field of crustal movement of Chinese mainland from Global Positioning System measurements, *Chinese Science Bulletin*, *50*(9), 939–941, doi:10.1007/BF02897392. 3.1

OECD (2018), The Belt and Road Initiative in the global trade, investment and finance landscape, *Tech. rep.*, doi:10.1787/bus$_f in_o ut - 2018 - 6 - en$. 1.1

Okal, E. A. (1977), The July 9 and 23, 1905, Mongolian earthquakes: A surface wave investigation, *Earth and Planetary Science Letters*, *34*(2), 326–331. 5.3

Okal, E. A. (2015), Historical seismograms: Preserving an endangered species, *GeoResJ*, *6*(April 1889), 53–64, doi:10.1016/j.grj.2015.01.007. 2.1, 2.2.1, 6.3.1, 6.4.1

Onn, F., and H. A. Zebker (2006), Correction for interferometric synthetic aperture radar atmospheric phase artifacts using time series of zenith wet delay observations from a GPS network, *Journal of Geophysical Research: Solid Earth*, *111*(9), 1–16, doi:10.1029/2005JB004012. 3.2

OpenStreetMap contributors (2020), Planet dump retrieved from https://planet.osm.org , `https://www.openstreetmap.org`. (document), 1.3

Pacheco, J. F., and L. R. Sykes (1992), Seismic Moment Catalog of Large Shallow Earthquakes, 1900 to 1989, *Bulletin of the Geological Society of America*, *82*(3), 1306–1349. 2.1.3, A.1

Pan, Z., Z. Yun, and Z. Shao (2020), Contemporary crustal deformation of Northeast Tibet from geodetic investigations and a comparison between the seismic and geodetic moment release rates, *Physics of the Earth and Planetary Interiors*, *304*(March 2019), 106,489, doi:10.1016/j.pepi.2020.106489. 1.4

Peng, C., Q. Ma, P. Jiang, W. Huang, D. Yang, H. Peng, L. Chen, and J. Yang (2020), Performance of a hybrid demonstration earthquake early warning system in the sichuan-yunnan border region, *Seismological Research Letters*, *91*(2A), 835–846, doi:10.1785/0220190101. 1.1

RACAB (2019), Observatory Fabra - Reial Academia de Ciències i Arts de Barcelona. (document)

Reid, H. F. (1910), Mechanics of the earthquake, the California Earthquake of April 18, 1906. Report of the State Investigation Commission, Carnegie Institution of Washington, Washington DC., *Tech. rep.* 5.3

Ren, Z., Z. Zhang, T. Chen, S. Yan, J. Yin, P. Zhang, and W. Zheng (2016), Clustering of offsets on the haiyuan fault and their relationship to paleoearthquakes, *Bulletin of the Geological Society of America*, *128*(1-2), 3–18, doi:10.1130/B31155.1. (document), 2.1, 2.1, 2.2, 2.1.2, 2.3, 2.3, 2.8, 2.9, 2.3.2, 2.15, 2.3.4, 2.3.6

Ren, Z., Z. Zhang, and P. Zhang (2018), Different earthquake patterns for two neighboring fault segments within the Haiyuan Fault zone, *Earth and Planetary Physics Earth Planet. Phys*, *2*(2), 67–73, doi:10.26464/epp2018006. 2.1

Richter, C. F. (1958), *Elementary seismology*, W. H. Freeman and Company, New York. 2.4.2, 2.4.4

Rizza, M., J. F. Ritz, C. Prentice, R. Vassallo, R. Braucher, C. Larroque, A. Arzhannikova, S. Arzhannikov, S. Mahan, M. Massault, J. L. Michelot, M. Todbileg, M. Arnold, G. Aumaître, D. Bourlès, and K. Keddadouche (2015), Earthquake geology of the Bulnay fault (Mongolia), *Bulletin of the Seismological Society of America*, *105*(1), 72–93, doi:10.1785/0120140119. 5.3

Rodgers, J., G. Su, W. Qi, D. Milledge, A. Densmore, C. Davis, P. England, J. Young, Y. Cao, A. Chakos, X. Li, T. Sim, E. So, B. Parsons, L. Sun, J. Yu, and C. Guo (2020), Creating an earthquake scenario in China: A case study in Weinan City, Shaanxi province, *International Journal of Disaster Risk Reduction*, *42*(August 2019), 101,305, doi:10.1016/j.ijdrr.2019.101305. 1.1

Rollins, C., and J.-P. P. Avouac (2019), A geodesy- and seismicity-based local earthquake likelihood model for central Los Angeles, *Geophysical Research Letters*, *46*, 3153–3162, doi:10.1029/2018GL080868. 1.4, 5.3

Rong, Y., X. Xu, J. Cheng, G. Chen, H. Magistrale, and Z. K. Shen (2020), A probabilistic seismic hazard model for Mainland China, *Earthquake Spectra*, doi:10.1177/8755293020910754. 1.4, 1.4, 5.3

Sagiya, T., T. Nishimura, and Y. Iio (2004), Heterogeneous crustal deformation along the central-northern Itoigawa-Shizuoka Tectonic Line Fault system, Central Japan, *Earth, Planets and Space*, *56*(12), 1247–1252, doi:10.1186/BF03353347. 5.2.2

Sandwell, D. T., and P. Wessel (2016), Interpolation of 2-D vector data using constraints from elasticity, *Geophysical Research Letters*, *43*(10), 10,703–10,709, doi:10.1002/2016GL070340. 5.2.1

Savage, J. C., W. Gan, and J. L. Svarc (2001), Strain accumulation and rotation in the Eastern California Shear Zone, *Journal of Geophysical Research: Solid Earth*, *106*(B10), 21,995–22,007, doi:10.1029/2000jb000127. 5.2.4, 5.2.5

Scharer, K. M., J. B. Salisbury, J. R. Arrowsmith, and T. K. Rockwell (2014), Southern san andreas fault evaluation field activity: Approaches to measuring small geomorphic offsets-challenges and recommendations for active fault studies, *Seismological Research Letters*, *85*(1), 68–76, doi:10.1785/0220130108. 2.3.2

Scherbaum, F. (2001), *Of poles and zeros : fundamentals of digital seismology*, 268 pp., Kluwer Academic Publishers, Dordrecht, doi:10.1007/978-1-4020-6861-4. 2.2.1, 2.2.1

Schweitzer, J. (2001), HYPOSAT - An Enhanced Routine to Locate Seismic Events, *Pure appl. geophys.*, *158*, 277–289, doi:https://doi.org/10.1007/PL00001160. 2.2.2

Shao, Y., J. Liu-zeng, J. V. D. Woerd, Y. Klinger, M. E. Oskin, J. Zhang, P. Wang, P. Wang, W. Wang, and W. Yao (2020), Late Pleistocene slip rate of the central Haiyuan fault constrained from optically stimulated luminescence , 14 C , and cosmogenic isotope dating and high-resolution topography, pp. 1–23, doi:10.1130/B35571.1/5173570/b35571.pdf. (document), 1.3, 1.5

Shen, L., A. Hooper, and J. Elliott (2019), A Spatially Varying Scaling Method for InSAR Tropospheric Corrections Using a High-Resolution Weather Model, *Journal of Geophysical Research: Solid Earth*, pp. 1–18, doi:10.1029/2018JB016189. 1.3, 3.2

SNSN (1904), Swedish National Seismic Network. Uppsala University, Uppsala, Sweden. Other/Seismic network, doi:10.18159/SNSN. (document)

Song, X., Y. Jiang, X. Shan, W. Gong, and C. Qu (2019), A fine velocity and strain rate field of present-day crustal motion of the northeastern Tibetan Plateau inverted jointly by InSAR and GPS, *Remote Sensing*, *11*(4), doi:10.3390/rs11040435. (document), 1.4, 1.10, 2.1.1, 3.1

SSN (2019), Servicio Sismológico Nacional, Instituto de Geofísica, Universidad Nacional Autónoma de México, México, doi:https://doi.org/10.21766/SSNMX/SN/MX. (document)

Stammler, K. (1993), Seismichandler—Programmable multichannel data handler for interactive and automatic processing of seismological analyses, *Computers & Geosciences*, *19*(2), 135–140, doi:10.1016/0098-3004(93)90110-Q. 2.2.5

Stewart, N., Y. Gaudemer, I. Manighetti, L. Serreau, A. Vincendeau, S. Dominguez, L. Mattéo, and J. Malavieille (2018), "3D_Fault_Offsets," a Matlab Code to Automatically Measure Lateral and Vertical Fault Offsets in Topographic Data: Application to San Andreas, Owens Valley, and Hope Faults, *Journal of Geophysical Research: Solid Earth*, *123*(1), doi:10.1002/2017JB014863. 2.3.6

Storchak, D., D. Di Giacomo, I. Bondár, J. Harris, E. Engdahl, W. Lee, A. Villaseñor, P. Bormann, and G. Ferrari (2012), ISC-GEM Global Instrumental Earthquake Catalogue (1900-2009), *GEM Technical Report 2012-01*, *V1.0.0*, 128pp, doi:10.13117/GEM.GEGD.TR2012.01. (document), 2.4.1, 2.2, 2.4.3

Storchak, D., D. Di Giacomo, E. Engdahl, J. Harris, I. Bondár, W. Lee, P. Bormann, and A. Villaseñor (2015), The ISC-GEM Global Instrumental Earthquake Catalogue (1900–2009): Introduction, *Physics of the Earth and Planetary Interiors*, *239*, 48 – 63, doi:https://doi.org/10.1016/j.pepi.2014.06.009. A.1

Storchak, D. A., D. Di Giacomo, I. Bondár, E. R. Engdahl, J. Harris, W. H. K. Lee, A. Villaseñor, and P. Bormann (2013), Public Release of the ISC–GEM Global Instrumental Earthquake Catalogue (1900–2009), *Seismological Research Letters*, *84*(5), 810–815, doi:10.1785/0220130034. A.1

Su, X., L. Yao, W. Wu, G. Meng, L. Su, R. Xiong, and S. Hong (2019), Crustal deformation on the northeastern margin of the Tibetan Plateau from continuous GPS observations, *Remote Sensing*, *11*(1), 1–21, doi:10.3390/rs11010034. 1.4

Sudhaus, H., and S. Jónsson (2009), Improved source modelling through combined use of InSAR and GPS under consideration of correlated data errors: Application to the June 2000 Kleifarvatn earthquake, Iceland, *Geophysical Journal International*, *176*(2), 389–404, doi:10.1111/j.1365-246X.2008.03989.x. 4.5.1

Tape, C., P. Musé, M. Simons, D. Dong, and F. Webb (2009), Multiscale estimation of GPS velocity fields, *Geophysical Journal International*, *179*(2), 945–971, doi:10.1111/j.1365-246X.2009.04337.x. 6.4.2

Tapponnier, P., G. Peltzer, and R. Armijo (1986), On the mechanics of the collision between India and Asia, *Geological Society, London, Special Publications*, *19*, 113–157, doi:10.1144/GSL.SP.1986.019.01.07. 2.1.1

Tapponnier, P., F. J. Ryerson, J. Van der Woerd, A.-S. Mériaux, and C. Lasserre (2001a), Long-term slip rates and characteristic slip: keys to active fault behaviour and earthquake hazard, *Comptes Rendus de l'Académie des Sciences - Series IIA - Earth and Planetary Science*, *333*(9), 483–494, doi:10.1016/S1251-8050(01)01668-8. 1.2, 2.1.1

Tapponnier, P., X. Zhiqin, F. Roger, B. Meyer, N. Arnaud, G. Wittlinger, and Y. Jingsui (2001b), Oblique stepwise rise and growth of the tibet plateau, *Science*, *294*(5547), 1671–1677, doi:10.1126/science.105978. 1.2

Thatcher, W. (2009), How the continents deform: The evidence from tectonic geodesy, *Annual Review of Earth and Planetary Sciences*, *37*, 237–262, doi:10.1146/annurev.earth.031208.100035. 1.2

UNESCO (2002), Integral Study of the Silk Roads: Roads of Dialogue, 1988-1997, *Tech. Rep. 1*. (document), 1.3

Vauchez, A., A. Tommasi, and G. Barruol (1998), Rheological heterogeneity, mechanical anisotropy and deformation of the continental lithosphere, *Tectonophysics*, *296*(1-2), 61–86, doi:10.1016/S0040-1951(98)00137-1. 1.2

Villasenor, A., and E. R. Engdahl (2005), A Digital Hypocenter Catalog for the International Seismological Summary, *Seismological Research Letters*, *76*(5), 554–559, doi:10.1785/gssrl.76.5.554. (document), 2.2

Villaseñor, A., E. A. Bergman, T. M. Boyd, E. R. Engdahl, D. W. Frazier, M. M. Harden, J. L. Orth, R. L. Parkes, and K. M. Shedlock (1997), Toward a comprehensive catalog of global historical seismicity, *Eos*, *78*(50), 581–582, doi:10.1029/97EO00346. (document), 2.2

Walters, R. J., J. R. Elliott, Z. Li, and B. Parsons (2013), Rapid strain accumulation on the Ashkabad fault (Turkmenistan) from atmosphere-corrected InSAR, *Journal of Geophysical Research: Solid Earth*, *118*(7), 3674–3690, doi:10.1002/jgrb.50236. 3.2

Walters, R. J., B. Parsons, and T. J. Wright (2014), Constraining crustal velocity fields with InSAR for Eastern Turkey: Limits to the block-like behavior of Eastern Anatolia, *Journal of Geophysical Research: Solid Earth*, *119*(6), 5215–5234, doi:10.1002/2013JB010909. 6.4.2

Wang, H., and T. J. Wright (2012), Satellite geodetic imaging reveals internal deformation of western Tibet, *Geophysical Research Letters*, *39*(7), 1–5, doi:10.1029/2012GL051222. 3.1, 4.4, 5.2.1, 5.2.4, 6.4.2

Wang, H., R. Gao, A. Yin, X. Xiong, C. Kuang, W. Li, and W. Huang (2012), Deep structure geometry features of Haiyuan Fault and deformation of the crust revealed by deep seismic reflection profiling (), *Chinese J. Geophys.*, *55*(12), 3902–3909, doi:10.6038/j.issn.0001-5733.2012.12.003. 2.1.1, 2.2.3

Wang, H., R. Gao, L. Zeng, Z. Kuang, A. Xue, W. Li, X. Xiong, and W. Huang (2014), Crustal structure and Moho geometry of the northeastern Tibetan plateau as revealed by SinoProbe-02 deep seismic-reflection profiling, *Tectonophysics*, *636*, 32–39, doi:10.1016/j.tecto.2014.08.010. 2.1.1, 2.1.1, 2.2.3

Wang, H., T. J. Wright, J. Liu-Zeng, and L. Peng (2019), Strain Rate Distribution in South-Central Tibet From Two Decades of InSAR and GPS, *Geophysical Research Letters*, *46*(10), 5170–5179, doi:10.1029/2019GL081916. 5.2.4

Wang, M., and Z.-K. Shen (2020), Present-Day Crustal Deformation of Continental China Derived From GPS and Its Tectonic Implications, *Journal of Geophysical Research: Solid Earth*, *125*(2), doi:10.1029/2019JB018774. (document), 1.2, 1.5, 1.4, 1.10, 2.1, 3.1, 4.3.1, 4.5, 4.4.2, 4.17, 5.2.1, 5.2.5

Wang, Q., P.-Z. Zhang, J. T. Freymueller, R. Bilham, K. Larson, X. Lai, X. You, Z. Niu, J. Wu, Y. Li, J. Liu, Z. Yang, and Q. Chen (2001), Present-Day Crustal Deformation in China Constrained by Global Positioning System Measurements, *Science*, *294*(5542), 574–577, doi:10.1126/science.1063647. 2.1.1

Wang, R. (1999), A simple orthonormalization method for stable and efficient computation of Green's functions, *Bulletin of the Seismological Society of America*, *89*(3), 733–741. 2.2.3

Wegnüller, U., C. Werner, T. Strozzi, A. Wiesmann, O. Frey, and M. Santoro (2016), Sentinel-1 Support in the GAMMA Software, *Procedia Computer Science*, *100*, 1305 – 1312, doi:https://doi.org/10.1016/j.procs.2016.09.246. 3.4

Weiss, J. R., R. J. Walters, Y. Morishita, T. J. Wright, M. Lazecky, H. Wang, E. Hussain, A. J. Hooper, J. R. Elliott, C. Rollins, C. Yu, P. J. González, K. Spaans, Z. Li, and B. Parsons (2020), High-resolution surface velocities and strain for Anatolia from Sentinel-1 InSAR and GNSS data, *Geophysical Research Letters*, pp. 0–2, doi:10.1029/2020GL087376. 1.2, 1.4, 3.1, 3.2, 3.4.2, 4.3, 4.4, 6.4.2

Wells, D. L., and K. J. Coppersmith (1994), New Empirical Relationships among Magnitude, Rupture Length, Rupture Width, Rupture Area, and Surface Displacement, *Tech. Rep. 4*. 2.4.1

Westoby, M. J., J. Brasington, N. F. Glasser, M. J. Hambrey, and J. M. Reynolds (2012), 'Structure-from-Motion' photogrammetry: A low-cost, effective tool for geoscience applications, *Geomorphology*, *179*, 300–314, doi:10.1016/j.geomorph.2012.08.021. 2.3.1

Wicks, C., C. Weaver, P. Bodin, and B. Sherrod (2013), InSAR Evidence for an active shallow thrust fault beneath the city of Spokane Washington, USA, *Journal of Geophysical Research: Solid Earth*, *118*(3), 1268–1276, doi:10.1002/jgrb.50118. 1.4, 3.1

Wicks, C. W., D. Dzurisin, S. Ingebritsen, W. Thatcher, Z. Lu, and J. Iverson (2002), Magmatic activity beneath the quiescent Three Sisters volcanic center, central Oregon Cascade Range, USA, *Geophysical Research Letters*, *29*(7), 26–1–26–4, doi:10.1029/2001GL014205. 3.2

Wood, H. O. (1921), A List of Seismologic Stations of the World, *Tech. rep.*, The National Research Council of the National Academy of Sciences, Washington, D. C. 2.2.1, 2.2.1, 2.2.4, 2.2.5, 6.3.1, A.2

Wright, T., B. Parsons, and E. Fielding (2001), the North Anatolian interferometry Fault by satellite radar, *Anatolia*, *28*(10), 2117–2120. 3.2

Wright, T. J., B. Parsons, P. C. England, and E. J. Fielding (2004), InSAR Observations of Low Slip Rates on the Major Faults of Western Tibet, *Science*, *305*(5681), 236–239, doi:10.1126/science.1096388. 3.1

Xie, Y. (1986), *China Earthquake Historical Data Compilation.*, Science Press, Beijing. A.1

Xu, X., and D. T. Sandwell (2020), Toward Absolute Phase Change Recovery With InSAR: Correcting for Earth Tides and Phase Unwrapping Ambiguities, *IEEE Transactions on Geoscience and Remote Sensing*, *58*(1), 726–733. 3.4.3

Xu, X., X. Wen, G. Yu, G. Chen, Y. Klinger, J. Hubbard, and J. Shaw (2009), Coseismic reverse- and oblique-slip surface faulting generated by the 2008 Mw 7.9 Wenchuan earthquake, China, *Geology*, *37*(6), 515–518, doi:10.1130/G25462A.1. 2.4.1

Xu, X., Z. Zhang, F. Hu, and X. Chen (2019), Dynamic Rupture Simulations of the 1920 M s 8 . 5 Haiyuan Earthquake in China, *109*(5), 2009–2020, doi:10.1785/0120190061. (document), 2.2, 2.1.1, 2.1.2, 2.9, A.1

Yao, W., J. Liu-Zeng, M. E. Oskin, W. Wang, Z. Li, V. Prush, J. Zhang, Y. Shao, Z. Yuan, and Y. Klinger (2019), Reevaluation of the Late Pleistocene Slip Rate of the Haiyuan Fault Near Songshan, Gansu Province, China, *Journal of Geophysical Research: Solid Earth*, *124*(5), 5217–5240, doi:10.1029/2018JB016907. (document), 1.3, 1.5

Yu, C., N. T. Penna, and Z. Li (2017), Generation of real-time mode high-resolution water vapor fields from GPS observations, *Journal of Geophysical Research: Atmospheres*, *122*(3), 2008–2025, doi:10.1002/2016JD025753. 3.2

Yu, C., Z. Li, and N. T. Penna (2018a), Interferometric synthetic aperture radar atmospheric correction using a GPS-based iterative tropospheric decomposition model, *Remote Sensing of Environment*, *204*, 109 – 121, doi:https://doi.org/10.1016/j.rse.2017.10.038. 3.2

Yu, C., Z. Li, N. T. Penna, and P. Crippa (2018b), Generic Atmospheric Correction Model for Interferometric Synthetic Aperture Radar Observations, *Journal of Geophysical Research: Solid Earth*, *123*(10), 9202–9222, doi:10.1029/2017JB015305. 3.2, 3.4.2

Yuan, D.-Y., Z.-S. Lei, W.-G. He, Z. Xiong, W.-P. Ge, X.-W. Liu, and B.-C. Liu (2007), Textual research of Wudu earthquake in 186 B.C. in Gansu Province, China and discussion on its causative structure _ Enhanced Reader.pdf, *Acta Seismologica Sinica*, *20*(6), 696–707. 6.2.3

Yuan, D. Y., J. D. Champagnac, W. P. Ge, P. Molnar, P. Z. Zhang, W. J. Zheng, H. P. Zhang, and X. W. Liu (2011), Late Quaternary right-lateral slip rates of faults adjacent to the lake Qinghai, northeastern margin of the Tibetan Plateau, *Bulletin* *of the Geological Society of America*, *123*(9-10), 2016–2030, doi:10.1130/B30315.1. 1.2, 1.3

Yuan, D. Y., W. P. Ge, Z. W. Chen, C. Y. Li, Z. C. Wang, H. P. Zhang, P. Z. Zhang, D. W. Zheng, W. J. Zheng, W. H. Craddock, K. E. Dayem, A. R. Duvall, B. G. Hough, R. O. Lease, J. D. Champagnac, D. W. Burbank, M. K. Clark, K. A. Farley, C. N. Garzione, E. Kirby, P. Molnar, and G. H. Roe (2013), The growth of northeastern Tibet and its relevance to large-scale continental geodynamics: A review of recent studies, *Tectonics*, *32*(5), 1358–1370, doi:10.1002/tect.20081. (document), 1.2, 1.3, 1.6, 4.5.2

Zebker, H. A., P. A. Rosen, and S. Hensley (1997), Atmospheric effects in interferometric synthetic aperture radar surface deformation and topographic maps, *Journal of Geophysical Research*, *102*(B4), 7547–7563. 3.2

Zhang, J., Y. Bock, H. Johnson, P. Fang, S. Williams, J. Genrich, S. Wdowinski, and J. Behr (1997), Southern California Permanent GPS Geodetic Array: Error analysis of daily position estimates and site velocities, *Journal of Geophysical Research*, *102*(B8), 18,035–18,005, doi:10.1029/97JB01380. 3.3

Zhang, P. (1993), Seismic hazard assessment in Continental Asia, *ANNALI DI GEOFISICA*, *XXXVI*(3-4), 41–59. 1.4

Zhang, P., P. Molnar, B. C. C. Burchfiel, L. Royden, Y. Wang, Q. Deng, F. Song, W. Zhang, D. Jiao, Zhang Peizhen, P. Molnar, B. C. C. Burchfiel, L. Royden, Wang Yipeng, Deng Qidong, Song Fangmin, Zhang Weiqi, and Jiao Decheng (1988a), Bounds on the Holocene slip rate of the Haiyuan fault, North-Central China, *Quaternary Research*, *30*(2), 151–164, doi:10.1016/0033-5894(88)90020-8. 1.3

Zhang, P., P. Molnar, W. W. Zhang, Q. Deng, Y. Wang, B. Burchfiel, F. Song, L. Royden, and D. Jiao (1988b), Bounds on the average recurrence interval of major earthquakes along the Haiyuan Fault in north-central China, *Seismological Research Letters*, *59*(3), 81–89, doi:10.1785/gssrl.59.3.81. 2.1

Zhang, P., Z.-x. Yang, H. K. Gupta, S. C. Bhatia, and K. M. Shedlock (1999), Global Seismic Hazard Assessment Program (GSHAP) in continental Asia, *Annali di Geofisica*, *42*(6), 1167–1190. 1.4, 6.4.1

Zhang, P., Q. Deng, G. Zhang, J. Ma, W. Gan, W. Min, F. Mao, and Q. Wang (2003), Active tectonic blocks and strong earthquakes in the continent of China, *Science in China (Series D)*, *46*(October), 13–24, doi:10.1360/03dz0002. 1.1

Zhang, P., W. Min, Q. Deng, and F. Mao (2005), Paleoearthquake rupture behavior and recurrence of great earthquakes along the Haiyuan fault, northwestern China, *Science in China Ser. D Earth Sciences*, *48*(3), 364–375, doi:10.1360/02YD0464. 2.1.2

Zhang, P. Z. (2013), A review on active tectonics and deep crustal processes of the Western Sichuan region, eastern margin of the Tibetan Plateau, *Tectonophysics*, *584*, 7–22, doi:10.1016/j.tecto.2012.02.021. 1.1

Zhang, P. Z., P. Molnar, and X. Xu (2007), Late Quaternary and present-day rates of slip along the Altyn Tagh Fault, northern margin of the Tibetan Plateau, *Tectonics*, *26*(5), 1–24, doi:10.1029/2006TC002014. (document), 1.3, 1.5

Zhang, W., D. Jiao, P. Zhang, P. Molnar, B. Burchfiel, Q. Deng, Y. Wang, and F. Song (1987), Displacement along the Haiyuan fault associated with the great 1920 Haiyuan, China, earthquake, *Bull. Seismol. Soc. Am.*, *77*, 117–131. 1.1, 1.5, 2.1, 2.1, 2.3, 2.3

Zheng, D., P. Z. Zhang, J. Wan, D. Yuan, C. Li, G. Yin, G. Zhang, Z. Wang, W. Min, and J. Chen (2006), Rapid exhumation at ˜ 8 Ma on the Liupan Shan thrust fault from apatite fission-track thermochronology: Implications for growth of the northeastern Tibetan Plateau margin, *Earth and Planetary Science Letters*, *248*(1-2), 183–193, doi:10.1016/j.epsl.2006.05.023. 2.1.1

Zheng, G., H. Wang, T. J. Wright, Y. Lou, R. Zhang, W. Zhang, C. Shi, J. Huang, and N. Wei (2017), Crustal Deformation in the India-Eurasia Collision Zone From 25 Years of GPS Measurements, *Journal of Geophysical Research: Solid Earth*, *122*(11), 9290–9312, doi:10.1002/2017JB014465. 1.4

Zheng, W., P. Zhang, W. He, D. Yuan, Y. Shao, D. Zheng, W. Ge, and W. Min (2013a), Transformation of displacement between strike-slip and crustal shortening in the northern margin of the Tibetan Plateau: Evidence from decadal GPS measurements and late Quaternary slip rates on faults, *Tectonophysics*, *584*, 267–280, doi:10.1016/j.tecto.2012.01.006. 1.2, 1.3

Zheng, W., D. Yuan, P. Zhang, J. Yu, Q. Lei, W. Wang, D. Zheng, H. Zhang, X. Li, C. Li, and X. Liu (2016), Tectonic geometry and kinematic dissipation of the active faults in the northeastern Tibetan Plateau and their implications for understanding northeastern growth of the plateau ( ), *Quaternary Sciences*, *36*(4), 775–788, doi:10.11928/j.issn.1001-7410.2016.04.01. (document), 1.5, 1.3, 1.7, 2.1.1

Zheng, W. J., P. Z. Zhang, W. P. Ge, P. Molnar, H. P. Zhang, D. Y. Yuan, and J. H. Liu (2013b), Late Quaternary slip rate of the South Heli Shan Fault (northern Hexi Corridor, NW China) and its implications for northeastward growth of the Tibetan Plateau, *Tectonics*, *32*(2), 271–293, doi:10.1002/tect.20022. 4.5.2

Zhou, B.-j., and Q.-l. Jia (2011), Application of virtual reality simulation technology to earthquake emergency drill, *Journal of Natural Disasters*, *5*. 1.1

Zhou, Y. (1990), Optimization of groundwater pumping strategies of the Wuwei basin by integrated use of systems analysis and groundwater management model, *SPRINGER-VERLAG BERLIN, BERLIN 33,(GER).*, pp. 545–550. 4.5.2

Zhou, Y., J. R. Elliott, B. Parsons, and R. T. Walker (2015a), The 2013 Balochistan earthquake: An extraordinary or completely ordinary event?, *Geophysical Research Letters*, *42*(15), 6236–6243, doi:10.1002/2015GL065096. 2.1, 2.3, 2.3.1

Zhou, Y., B. Parsons, J. R. Elliott, I. Barisin, and R. T. Walker (2015b), Assessing the ability of Pleiades stereo imagery to determine height changes in earthquakes: A case study for the El Mayor-Cucapah epicentral area, *Journal of Geophysical Research: Solid Earth*, *120*(12), 8793–8808, doi:10.1002/2015JB012358. (document), 2.13

Zhuang, J., J. Peng, C. Xu, Z. Li, A. Densmore, D. Milledge, J. Iqbal, and Y. Cui (2018), Distribution and characteristics of loess landslides triggered by the 1920 Haiyuan Earthquake, Northwest of China, *Geomorphology*, *314*, 1–12, doi:10.1016/j.geomorph.2018.04.012. (document), 2.2, 2.2.2

Ziegler, P. A., J. D. Van Wees, and S. Cloetingh (1998), Mechanical controls on collision-related compressional intraplate deformation, *Tectonophysics*, *300*(1-4), 103–129, doi:10.1016/S0040-1951(98)00236-4. 1.2

Zielke, O., J. R. Arrowsmith, L. Grant Ludwig, and S. O. Akçiz (2010), Slip in the 1857 and earlier large earthquakes along the Carrizo Plain, San Andreas Fault, *Science*, *327*(5969), 1119–22, doi:10.1126/science.1182781. 2.1, 2.3.6

Zielke, O., Y. Klinger, and J. R. Arrowsmith (2015), Fault slip and earthquake recurrence along strike-slip faults - Contributions of high-resolution geomorphic data, *Tectonophysics*, *638*, 43–62, doi:10.1016/j.tecto.2014.11.004. 2.3.6

Appendix A

1920 Haiyuan Earthquake

Table A.1: Primary Literature and Catalogue Readings with Associated Methods.

Magnitude	Reference	Method
M 8.5	*Gutenberg and Richter* (1941)	Surface-wave amplitudes with period ~20 s
m 7.9	*Gutenberg* (1956)	m_B formula (Eq (2.5))
M_W 8.3	*Chen and Molnar* (1977)	Spectral densities of Rayleigh waves
M_W 7.8	*Kanamori* (1977)	Based on Mo from *Chen and Molnar* (1977)
M_S 8.6	*Abe* (1981)	Reworked from Gutenberg's notes
m_B 7.9	*Abe* (1981)	Reworked from Gutenberg's notes
M 8.5	*Gu* (1983)	Intensity of shaking, $M = 0.58\ I_o + 1.5$
M_W 8	*Deng et al.* (1984)	Revised from *Chen and Molnar* (1977)
M 8.6	*Xie* (1986)	Compiled using method of *Gutenberg* (1945a)
M_S 8.4	*Pacheco and Sykes* (1992)	Magnitude corrected from 8.6
M_W 8.3	ISC-GEM (2013)*	*Chen and Molnar* (1977)
MS 8.7	ISC (2014)**	Computed from bulletin records
M_W 7.8	*Liu-zeng et al.* (2015)	Rupture length and maximum slip
M_W 8.2	*Xu et al.* (2019)	Physics-based rupture model

* See *Storchak et al.* (2013), *Storchak et al.* (2015) and *Di Giacomo et al.* (2018).

** MS 8.7 is the first MS result ISC published in 2014, with err=0.2 and Nsta =3 (`www.isc.ac.uk/cgi-bin/web-db-v4?event_id=912687&out_format=IMS1.0&request=COMPREHENSIVE`). The three stations included were RIV with 7.85, LPZ with 8.68 and FBR with 8.81. MS 8.7 was rounded from the median value of 8.68 from LPZ, which itself was later reprocessed by ISC to become $M_S(BB)$ 8.57. The latest result from ISC is $M_S(BB) = 8.06 \pm 0.11$, based on amplitude and period measurements recorded in 9 station bulletins (*Di Giacomo et al.*, 2015b,a; *Di Giacomo*, 2020). Unfortunately, this finding does not resolve the mystery around the M 8.7 quoted in literature since 1986 (Section 2.1).

Table A.2: Stations, Instruments and Instrument Response Parameters.

Station[a]	**Comp**[b]	**Location**	**Instrument**	V_o	T_o	h
GIFH	E	Gifu, Japan	Omori formula simple micrometer	50	3.4	0.06[c]
GIFH	N	Gifu, Japan	Omori formula simple micrometer	50	4	0.07[c]
MTMH	E	Matsumoto, Japan	Simple micrometer	20	5	0.2
MTMH	N	Matsumoto, Japan	Simple micrometer	20	6	0.3
AKIH	E	Akita, Japan	Omori formula simple micrometer	50	4	0.06[d]
AKIH	N	Akita, Japan	Omori formula simple micrometer	50	4	0.06[d]
HNGB[e]	E	Hongo, Japan	Bosch-Omori	19	16.1	0.4
HNGB[e]	N	Hongo, Japan	Bosch-Omori	20	16.1	0.4
HNGE[e]	Z	Hongo, Japan	Ewing	2	5	0.06
DJAH	E	Jakarta, Indonesia	Wiechert	210	6.5	0.36
DJAH	N	Jakarta, Indonesia	Wiechert	193	6.7	0.36
UPPH	E	Uppsala, Sweden	Wiechert inverted pendulum	187	9.6	0.39
UPPH	N	Uppsala, Sweden	Wiechert inverted pendulum	196	10.1	0.38
POTH	N	Potsdam, Germany	Wiechert inverted pendulum	220	5	0.4
HAMH	Z	Hamburg, Germany	Wiechert vertical motion seismograph	200	5	0.46
HAMH	E	Hamburg, Germany	Wiechert inverted pendulum	200	10	0.46
HAMH	N	Hamburg, Germany	Wiechert inverted pendulum	200	10	0.46
JENH	E	Jena, Germany	Wiechert inverted pendulum	200	8	0.33
JENH	N	Jena, Germany	Wiechert inverted pendulum	210	8.1	0.37
GTTH	Z	Gottingen, Germany	Wiechert	179	5.24	0.42
GTTH	N	Gottingen, Germany	Wiechert	142	11.7	0.36
GTTH	E	Gottingen, Germany	Wiechert	164	12.1	0.41
MNHH	N	Munich, Germany	Wiechert	190	9	0.46
MNHH	E	Munich, Germany	Wiechert	190	9	0.46
DBNB	N	De Bilt, Netherlands	Bosch-Omori	20.3	18.3	0.4
DBNB	E	De Bilt, Netherlands	Bosch-Omori	20.3	18.5	0.4
DBNG	N	De Bilt, Netherlands	Gallitzin	307	24.43	0.7
DBNG	E	De Bilt, Netherlands	Gallitzin	315	24.96	0.7
RCRH	NE	Collegio Romano, Italy	Agamennone horizontal pendula	50	8	0.03[c]

Continued on next page

Table A.2 – continued from previous page

Station[a]	**Comp**[b]	**Location**	**Instrument**	V_o	T_o	h
RCRH	NW	Collegio Romano, Italy	Agamennone horizontal pendula	50	8	0.03[c]
CHVH	N35E	Chiavari, Italy	Stiattesi horizontal pendulum	35	11	0.05[c]
CHVH	S55E	Chiavari, Italy	Stiattesi horizontal pendulum	46	12.8	0.05[c]
FBRH	E	Fabra, Spain	Mainka bifilar pendulum	65	8.6	0.43
FBRH	N	Fabra, Spain	Mainka bifilar pendulum	78	9.1	0.37
EBRH	E	Ebro, Spain	Mainka	110	7.8	0.3
EBRH	N	Ebro, Spain	Mainka	200	14.8	0.4
TOLH	E	Toledo, Spain	Bosch-Omori	15	12	0.05[c]
TOLH	N	Toledo, Spain	Bosch-Omori	20	17	0.05[c]
RIVW	N	Riverview, Australia	Wiechert	151	8.7	0.48
RIVW	E	Riverview, Australia	Wiechert	164	8.7	0.41
APIH	E	Apia, Samoa	Wiechert inverted pendulum	130	9	0.43
APIH	N	Apia, Samoa	Wiechert inverted pendulum	130	9	0.43
DENH	N	Denver, the US	Wiechert inverted pendulum	130	4.3	0.33
DENH	E	Denver, the US	Wiechert inverted pendulum	120	4.4	0.22
CLEH	N	Cleveland, the US	Wiechert inverted pendulum	80	7	0.46
TACB	N	Tacubaya, Mexico	Bosch-Omori	59	30.5	0.4[d]
TACW	E	Tacubaya, Mexico	Wiechert Horizontal	200	8	0.5
TACW	N	Tacubaya, Mexico	Wiechert Horizontal	200	8	0.5
LPZH[f]	E	La Paz, Bolivia	Bifilar horizontal pendulum	25/80	20/18	0.22[d]

[a] The last digit of the four-letter station code is used to differentiate seismograms recorded by multiple types of instruments at the same station. 'B' = Bosch-Omori, 'W' = Wiechert, 'G' = Gallitzin, 'E' = Ewing, and 'H' = historical when only one type of instrument was in operation.

[b] 'E' = east-west, 'N' = north-south, 'Z' = vertical, 'NE' = northeast-southwest, 'NW' = northwest-southeast, 'N35E' = 35°-215°, 'S55E' = 125°-305°, following *Wood* (1921) and *McComb and West* (1931).

[c] Damping constant measured from calibration pulse on the seismograms.

[d] Damping constant unknown and calibration pulse not found; taking the typical value of the instrument type instead.

[e] Records scanned from microfilms without accurate length scales.

[f] Waveforms with unknown components.

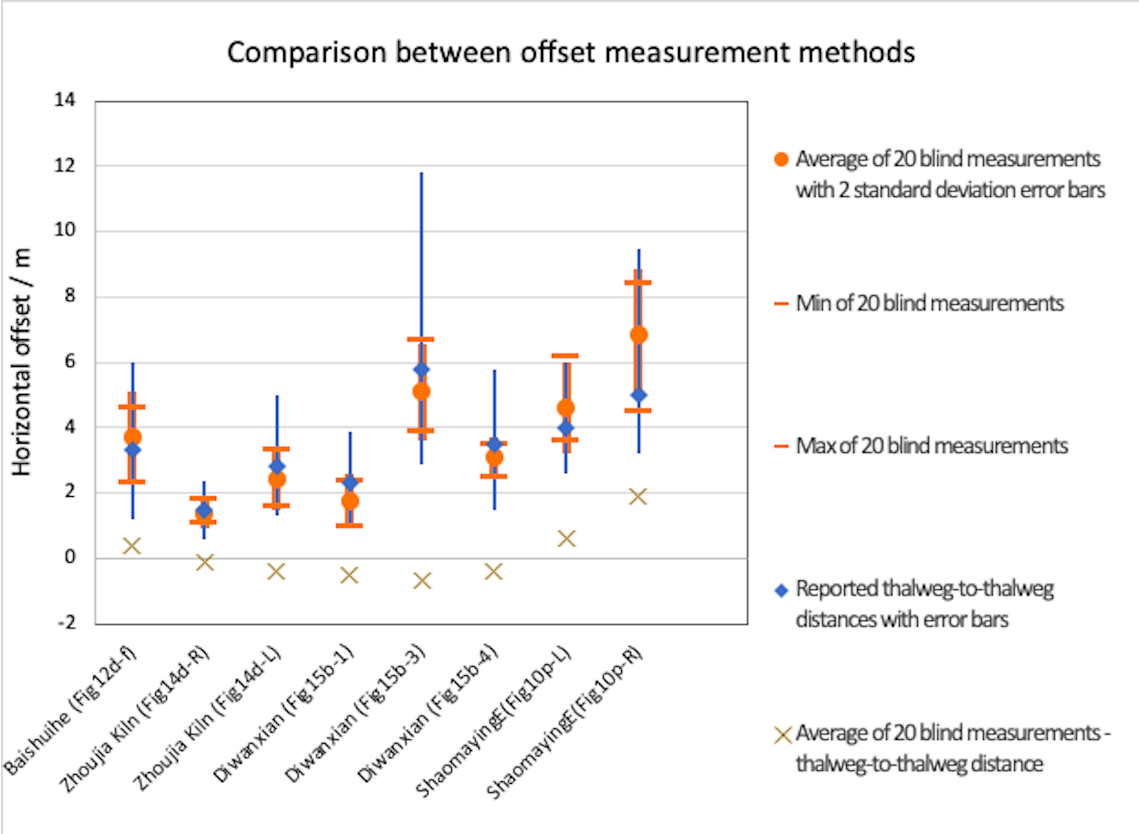

Figure A.1: Comparison between 20 blind measurements and method described in Fig 11 across 8 example sites. The differences between measurement methods among this subset of sites have an average of 0.1 m, well within our reported uncertainties, but do not show a systematic bias higher or lower, confirming the reliability of our derived seismic moment.

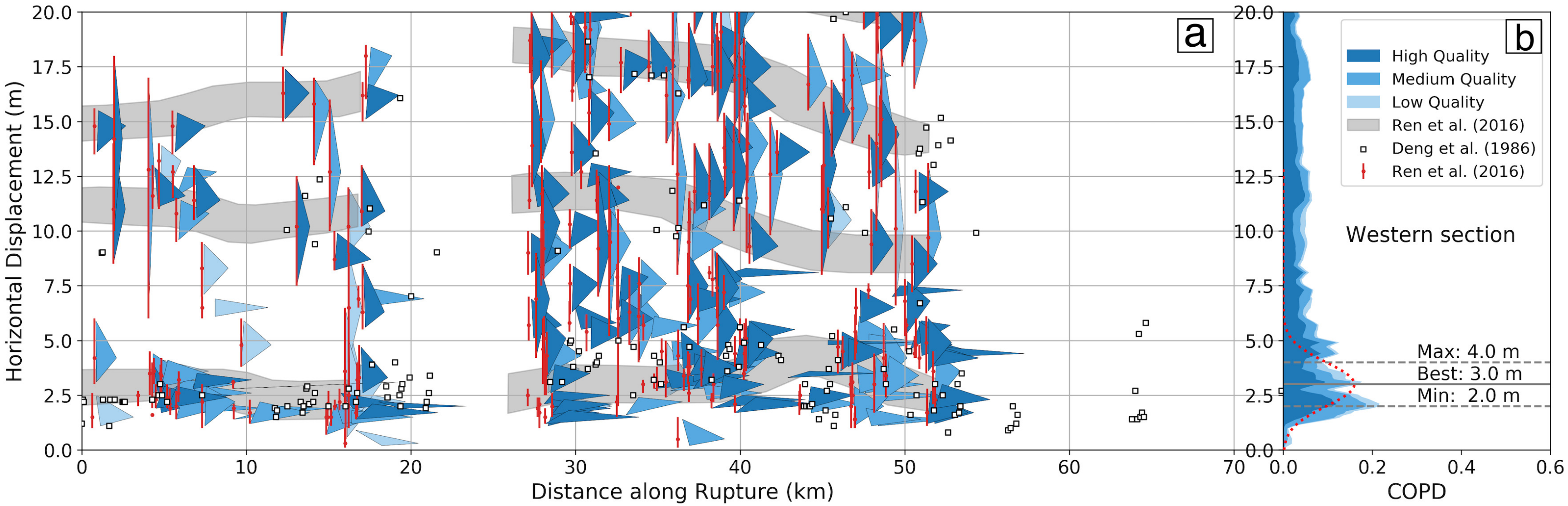

Figure A.2: (a) Measurements by Ren et al. (2016) plotted as equal area triangular probability density functions on the western section. High Quality = “High” and “High-medium” qualities in Ren et al. (2016); Medium Quality = “Medium” quality in Ren et al. (2016); Low Quality = “Medium-low” and “low” qualities in Ren et al. (2016). (b) COPD (blue) of measurements from Ren et al. (2016) in comparison with the Gaussian fitting (red) of the lowest COPD peak in this study.

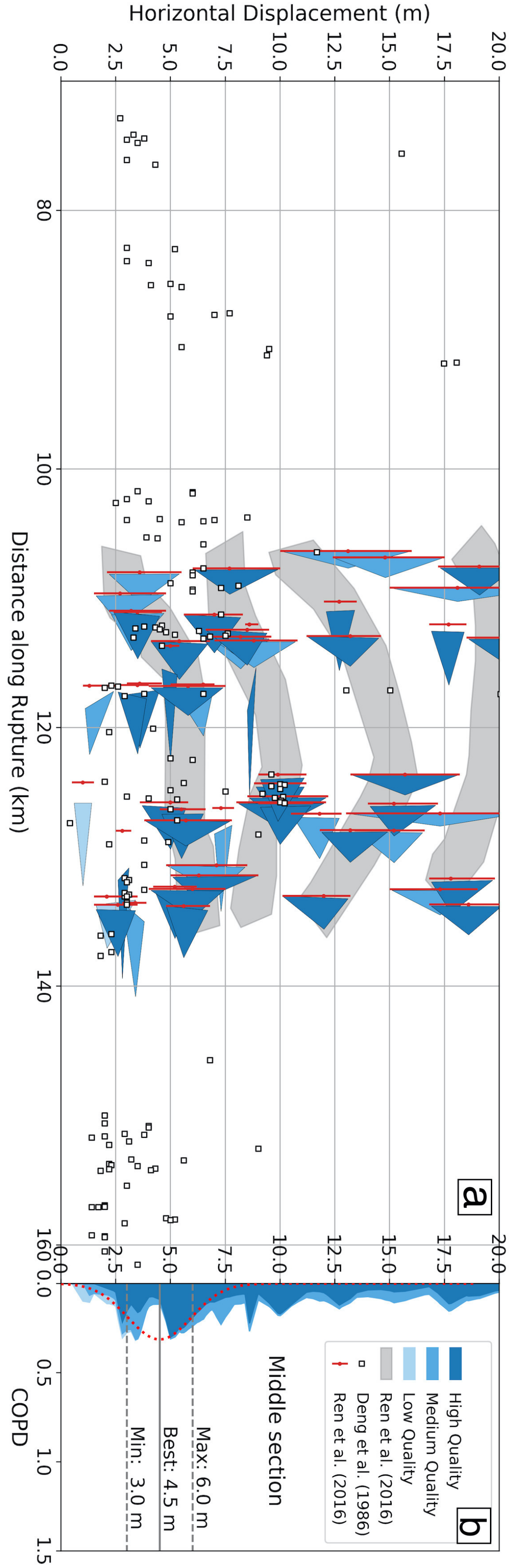

Figure A.3: Same as Fig A.2 but for the middle section.

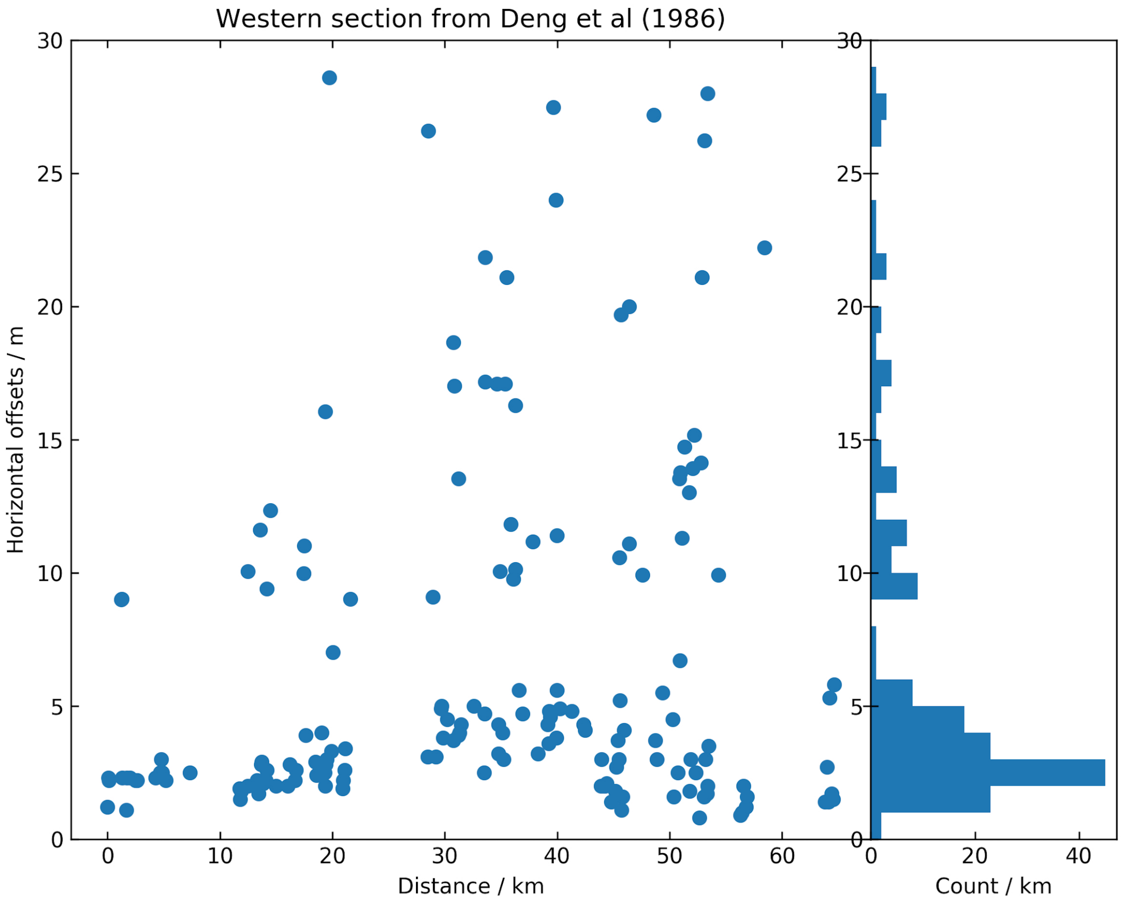

Figure A.4: Histogram of offset measurements from the western section reported by Deng et al. (1986).

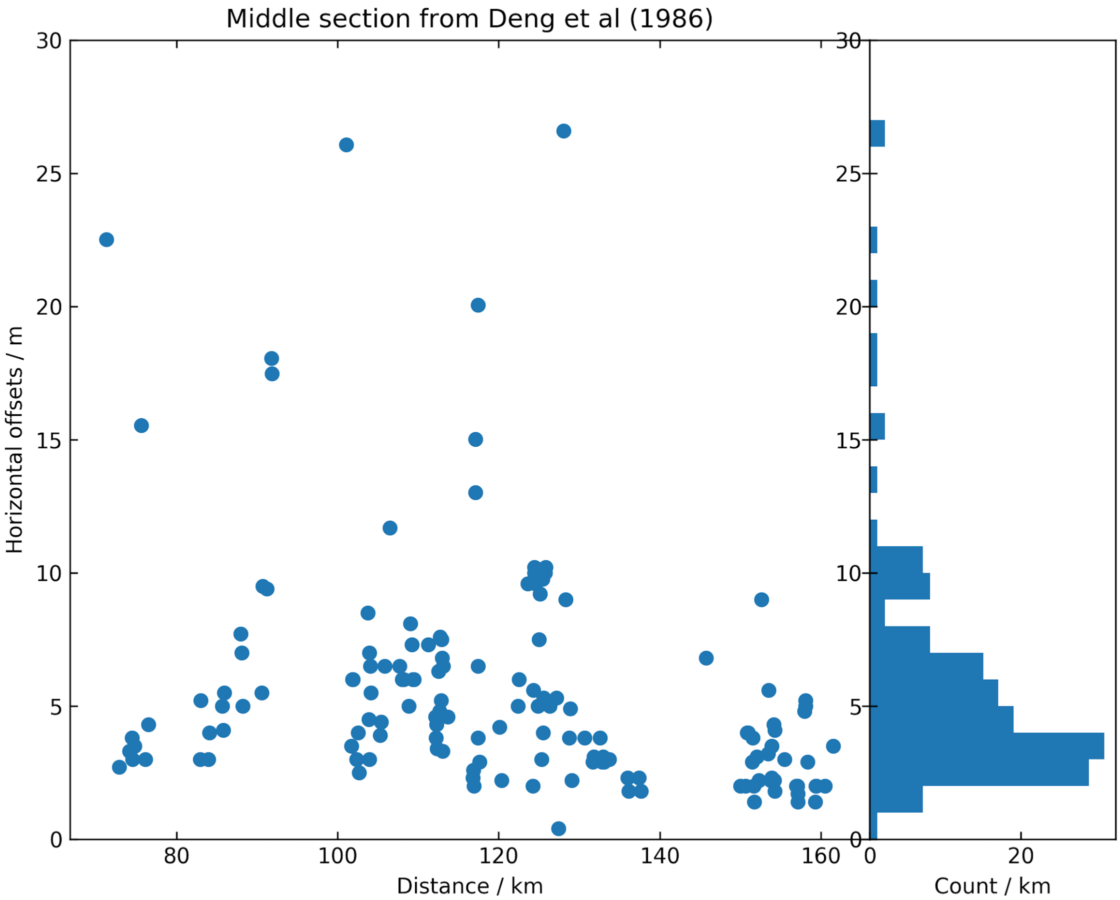

Figure A.5: Histogram of offset measurements from the middle section reported by Deng et al. (1986).

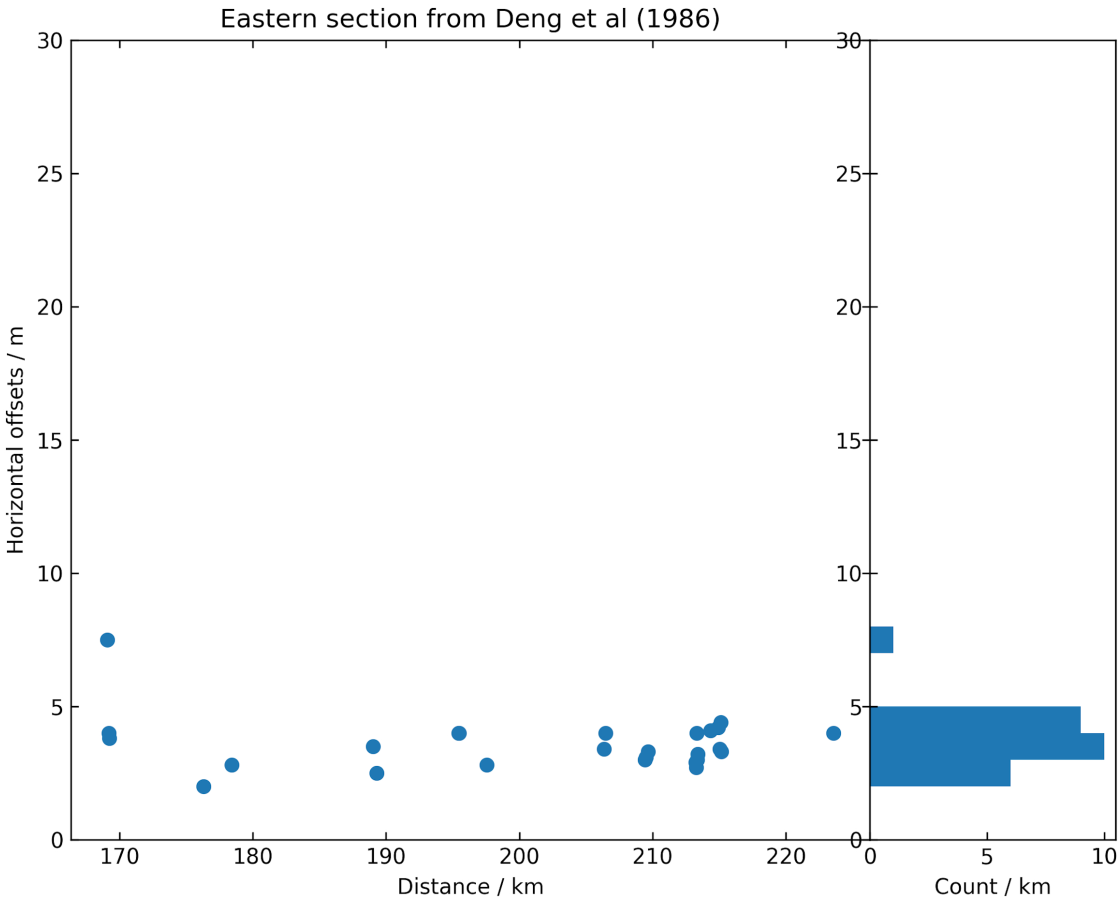

Figure A.6: Histogram of offset measurements from the eastern section reported by Deng et al. (1986).

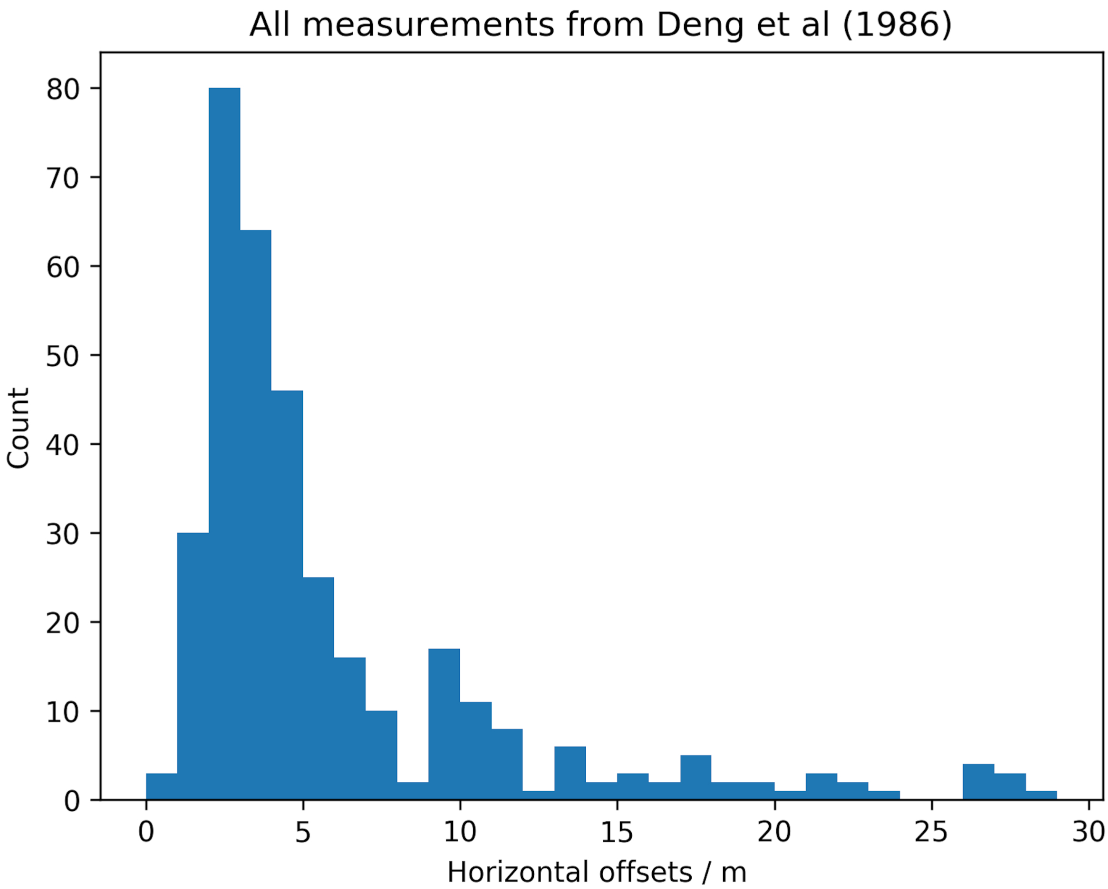

Figure A.7: Histogram of offset measurements from the entire 1920 rupture reported by Deng et al. (1986).

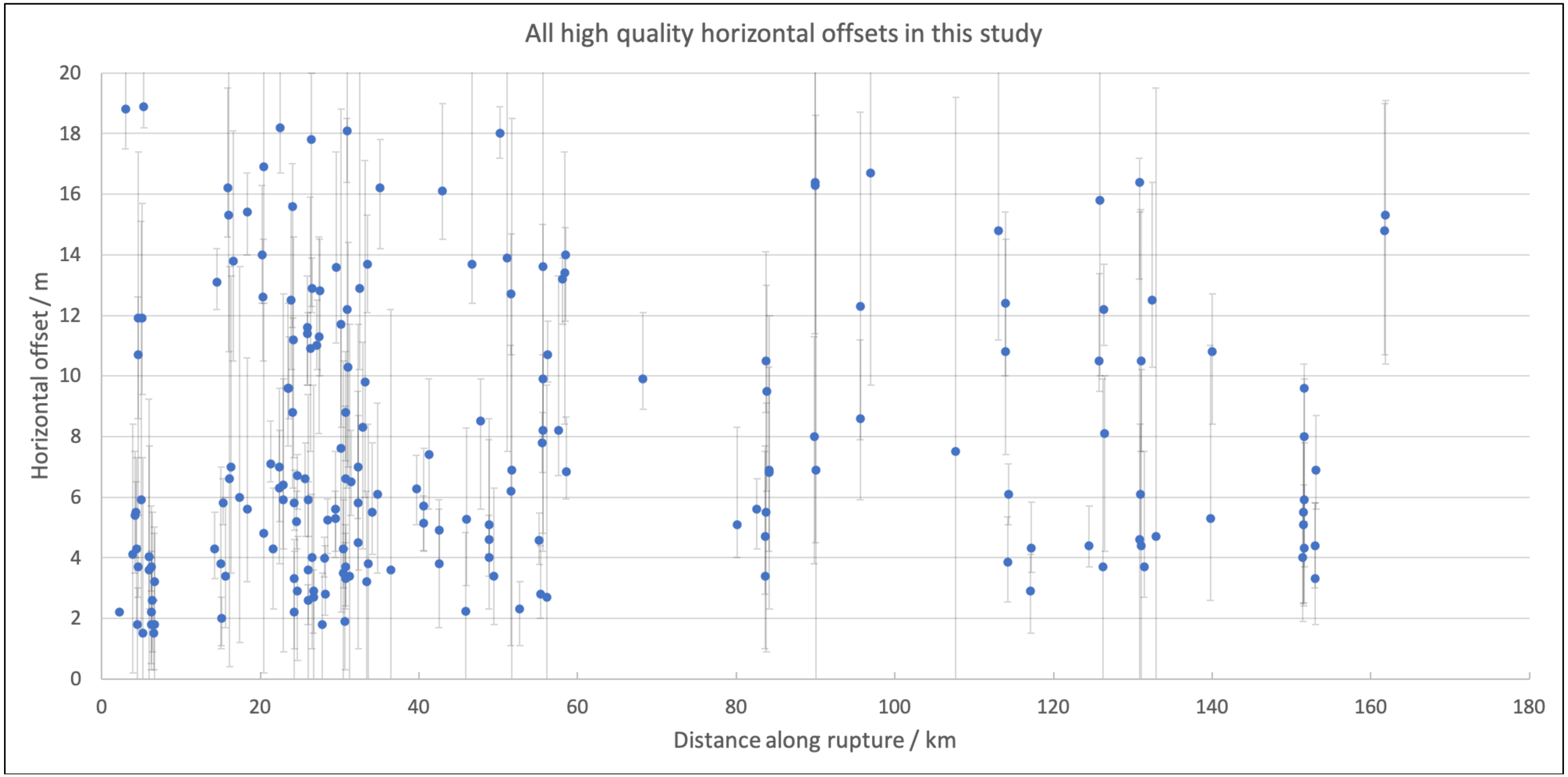

Figure A.8: High quality horizontal offsets measured in this study along the western and middle sections combined.

Appendix B

Frame Stitching and Velocity Decomposition

B.1 Overlap between tracks

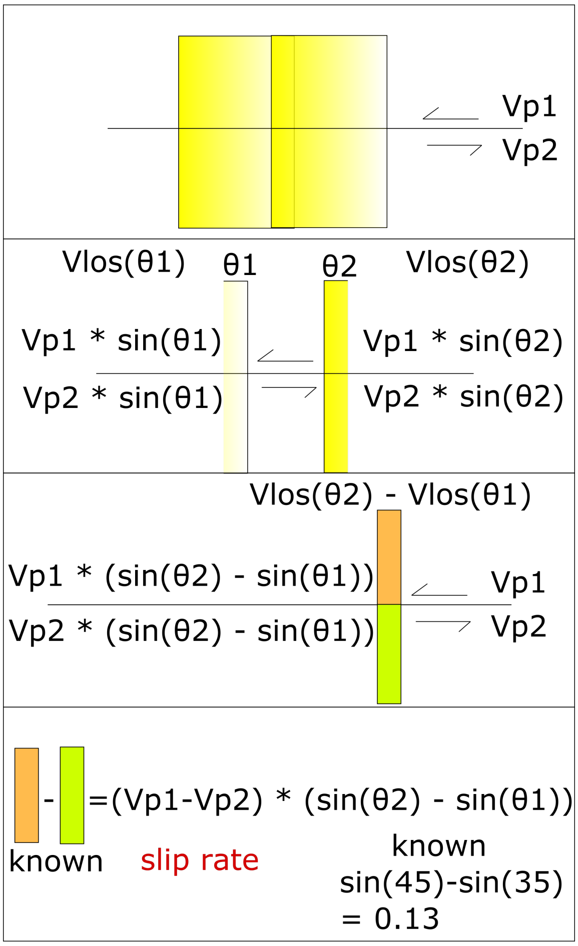

Figure B.1: Cartoon explaining expected steps in overlap between tracks across strike slip faults, where $\theta 1$ and $\theta 2$ are the incidence angles at positions $p1$ and $p2$.

B.2 Test for the necessity of azimuthal ramp

I choose the 128A track for the test, which is the best covered by GNSS stations. I first fix the northern frame and merge frames systematically to the south with ramps in the range direction removed based on their frame overlap. I fit a planar ramp to only the GNSS LOS velocities in the middle frame, and extend the best-fitting ramp in the azimuth direction and apply it to the whole merged track (Fig B.2). The residuals in the northern frame (2.8 ± 1.8 mm/yr) systematically deviate from zero and display an increasing trend northwards up to 5.8 mm/yr. The fact that the northern 128A_05172_131313 frame contains the Haiyuan Fault, again, testifies the idea that such tilt could be introduced by the ramp removal across faults during the time series processing.

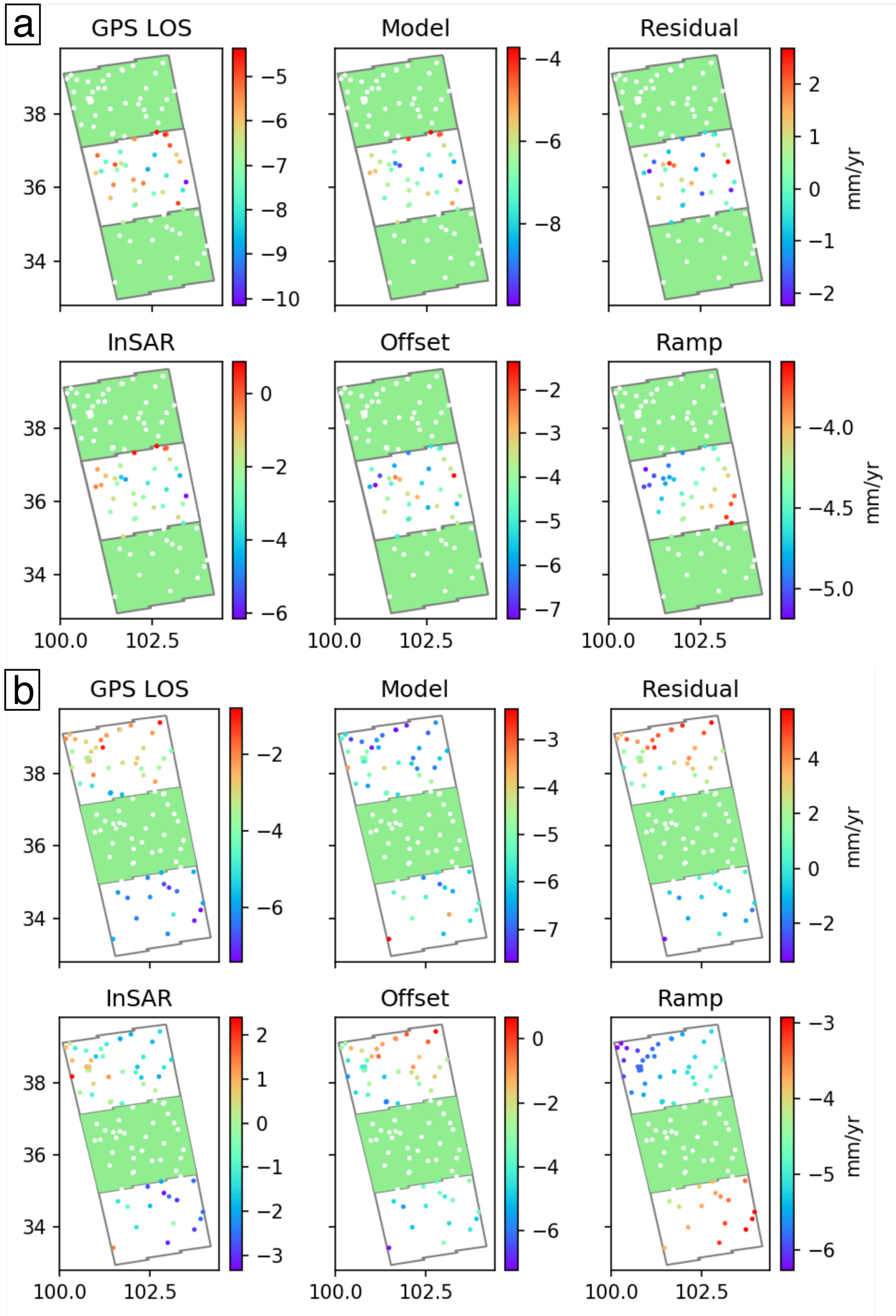

Figure B.2: (a) Fitting a ramp to the offsets between GNSS(LOS) and the averages of 9x9 InSAR pixels around the GNSS locations inside the middle frame of the 128A track. Offset = GNSS(LOS) - InSAR; Model = InSAR + Ramp; Residual = Offset - Ramp. (b) Apply the ramp extended from the middle frame to the whole track to compare the residuals in the northern and southern frames with that in the middle frame.

.

B.3 Three-step approach - reference for joint inversion

Assuming projecting each frame to the GNSS LOS has taken care of the ramp along the azimuth direction (step 1), I can make the final adjustments along the range direction only. First, I merged the projected frames along track successively to the south, removing any small remaining ramps in the overlapping region between frames by applying ramps along the range direction (step 2). This results in a smaller average standard deviation of 0.84 mm/yr and an average mode of -0.01 mm/yr for the overlap offsets (Fig B.3), but leaving the merged track only referenced to the GNSS data in the northernmost frame. To minimise the deviation from the overall GNSS reference frame, I reprojected the merged track to all the GNSS data within the track by inverting for a ramp along the range direction (Fig B.4) (step 3). The resultant histograms of the residuals between the InSAR LOS and GNSS LOS in the tracks have an average standard deviation of 1.36 mm/yr (Fig B.5).

The resultant ascending and descending LOS velocity maps are shown in Fig B.6. In comparison to the initial LOS maps where each frame was referenced to a chosen point within it and flattened on its own (Fig 4.1), Fig B.6 highlights the tectonic signal much more clearly, especially in the ascending map across the Qilianshan and Haiyuan Fault (Fig 4.5), and exhibits much smoother transition between the frames along track. The offsets between tracks are also reduced from before (compare Fig B.7 and Fig 4.4).

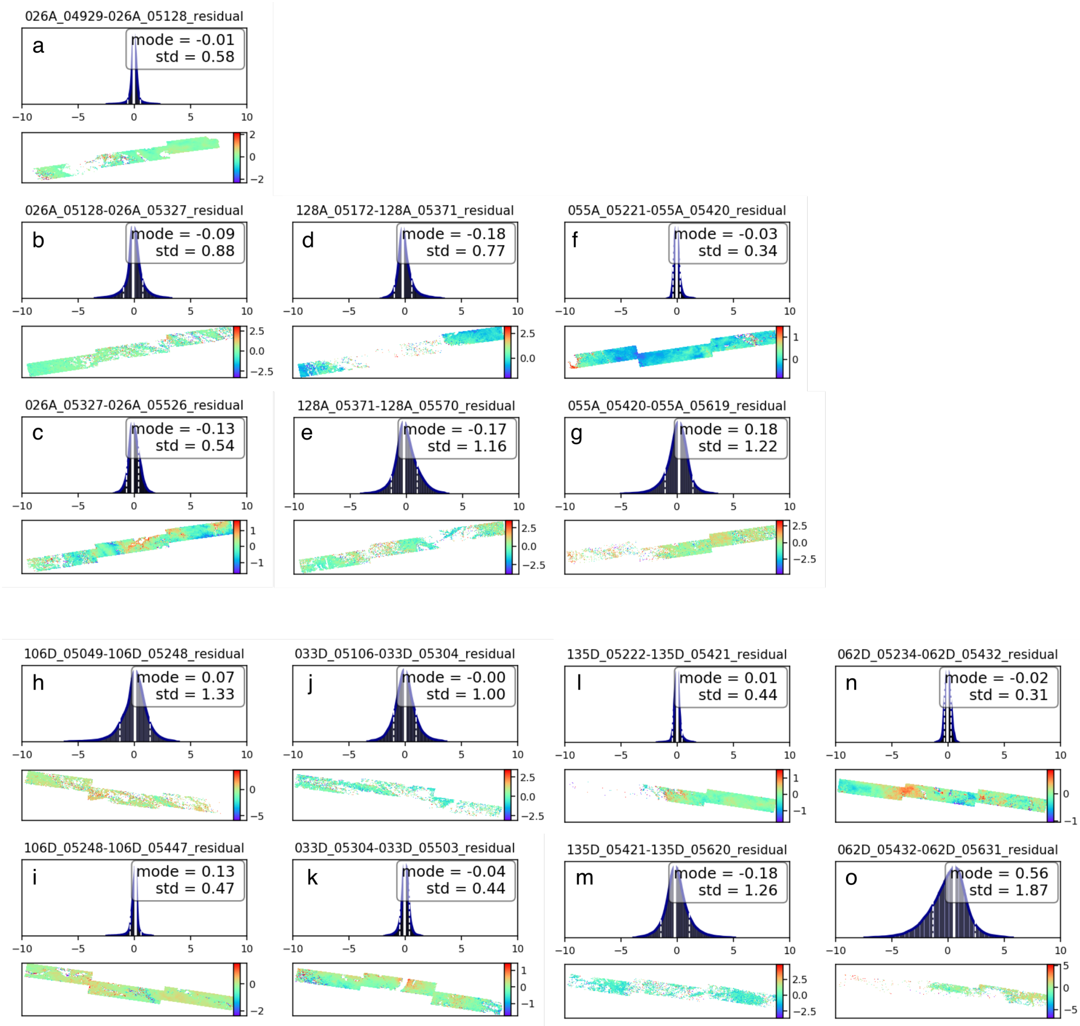

Figure B.3: Histograms of pixel differences between overlap areas of frames along track after projecting each frame to the GNSS LOS velocities, and applying a ramp along range to remove the ramp in the overlap offsets. Solid white lines mark the mode of the histogram. Dotted white lines mark one standard deviation from the mode.

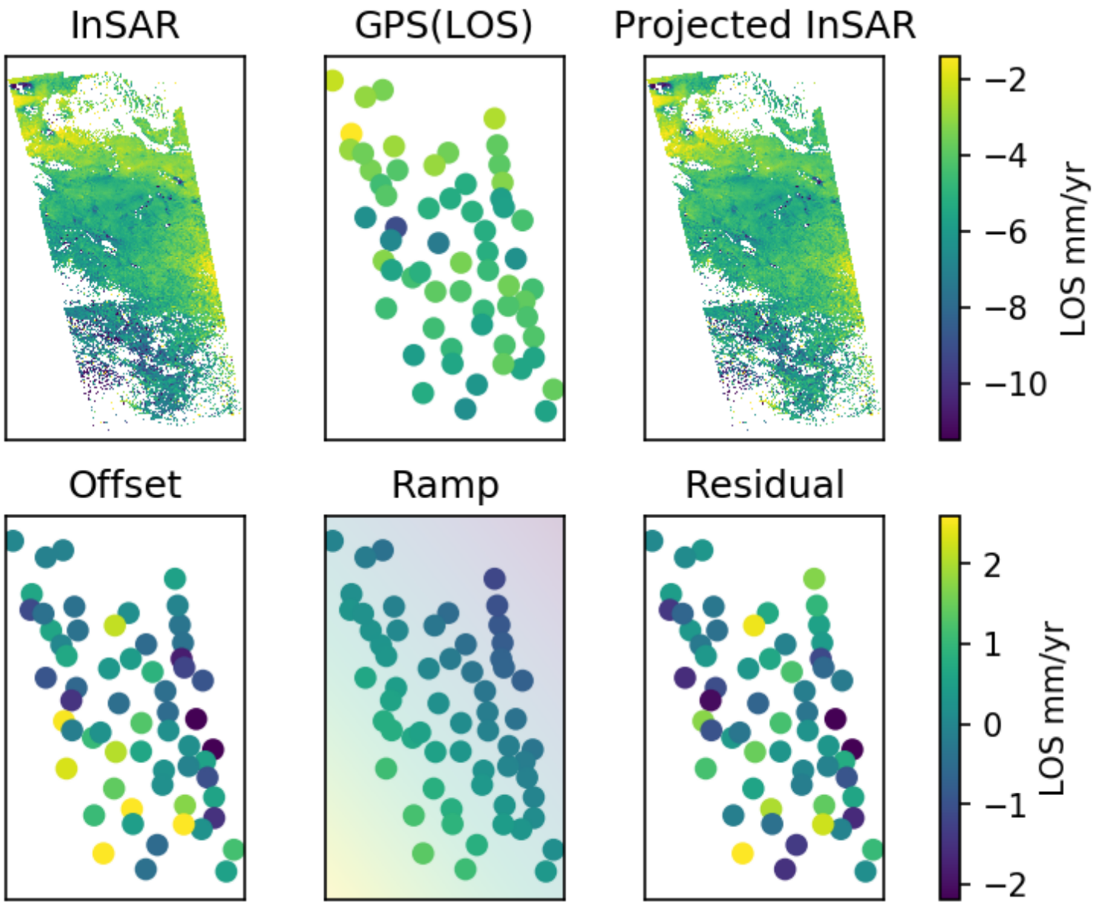

Figure B.4: An example of reprojecting the InSAR LOS velocities to all 3D GNSS LOS velocities within the track 055A (Fig 4.6b). Offset = GNSS(LOS) - InSAR, Projected InSAR = InSAR + Ramp, Residual = Offset - Ramp. The semi-transparent background colour of the Ramp panel represents the ramp applied to the InSAR LOS map with the dots in full colour representing the ramp values at the GNSS locations. The colour scales apply to all three panels in a row.

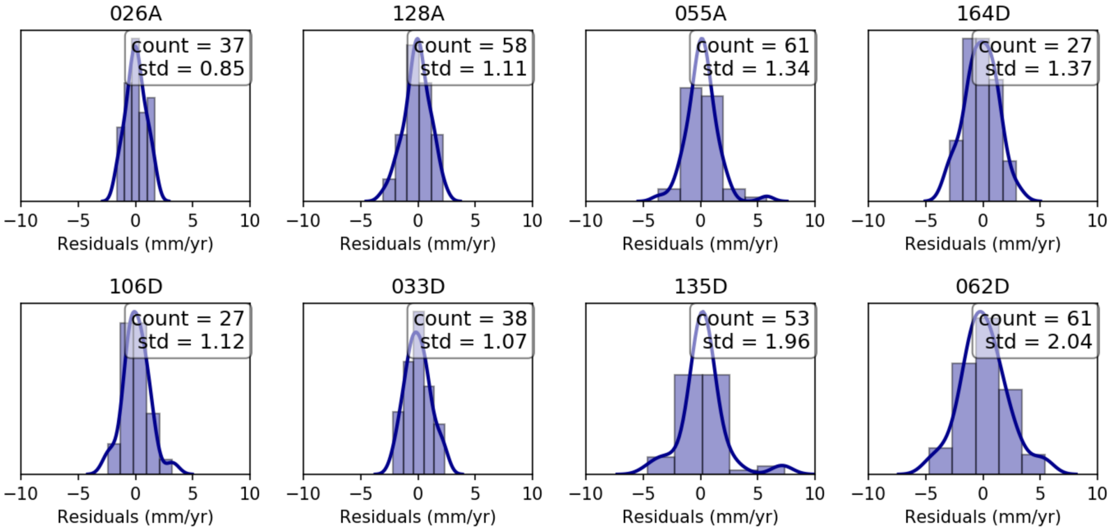

Figure B.5: Histograms of residuals between the GNSS and InSAR LOS velocities for each track.

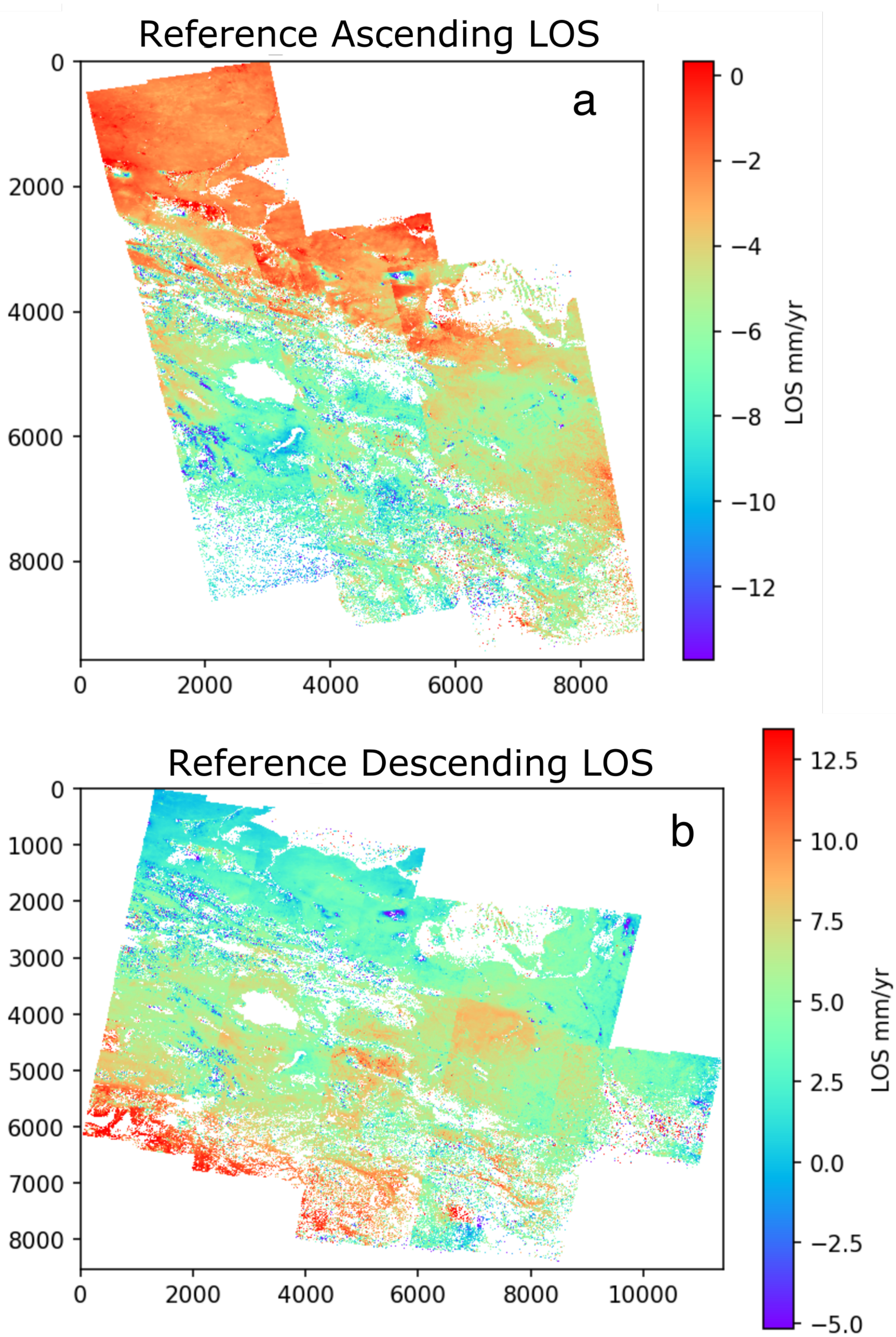

Figure B.6: (a) Ascending and (b) descending InSAR LOS velocity maps after projecting each frame to the GNSS LOS in the frame, then applying a ramp along range between frames within the same track, and finally projecting each merged track to the GNSS LOS in the track.

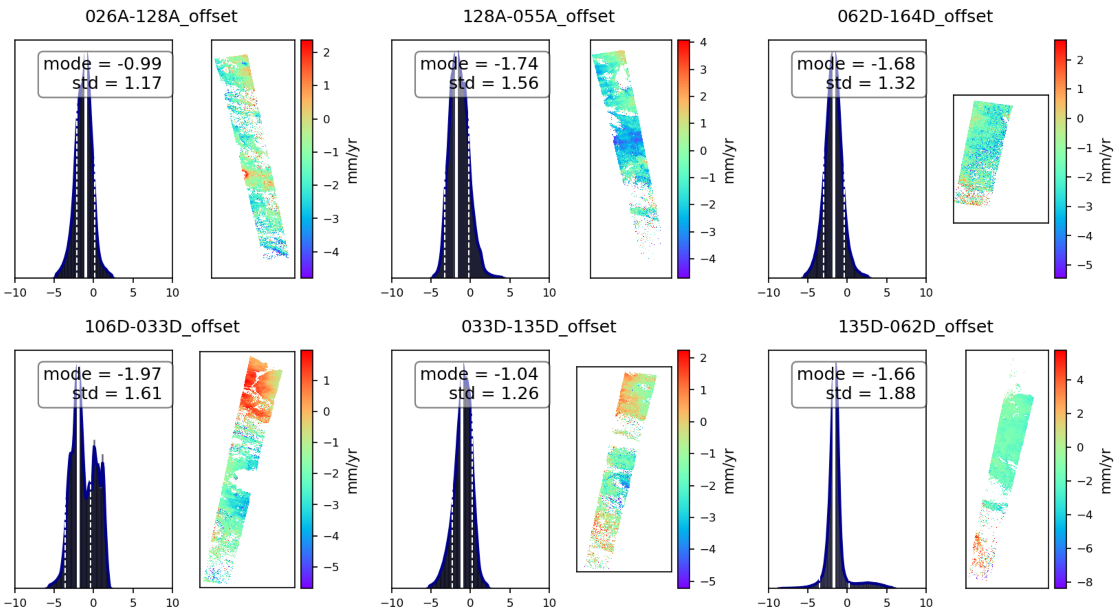

Figure B.7: Histograms of pixel differences between overlap areas of merged tracks after projecting each frame to GNSS LOS, applying a ramp in the range direction to close the gaps between the frames, and reprojecting the track to GNSS LOS in the track. Solid white lines mark the mode of the histogram. Dotted white lines mark one standard deviation from the mode.

B.4 Joint inversion weighting test

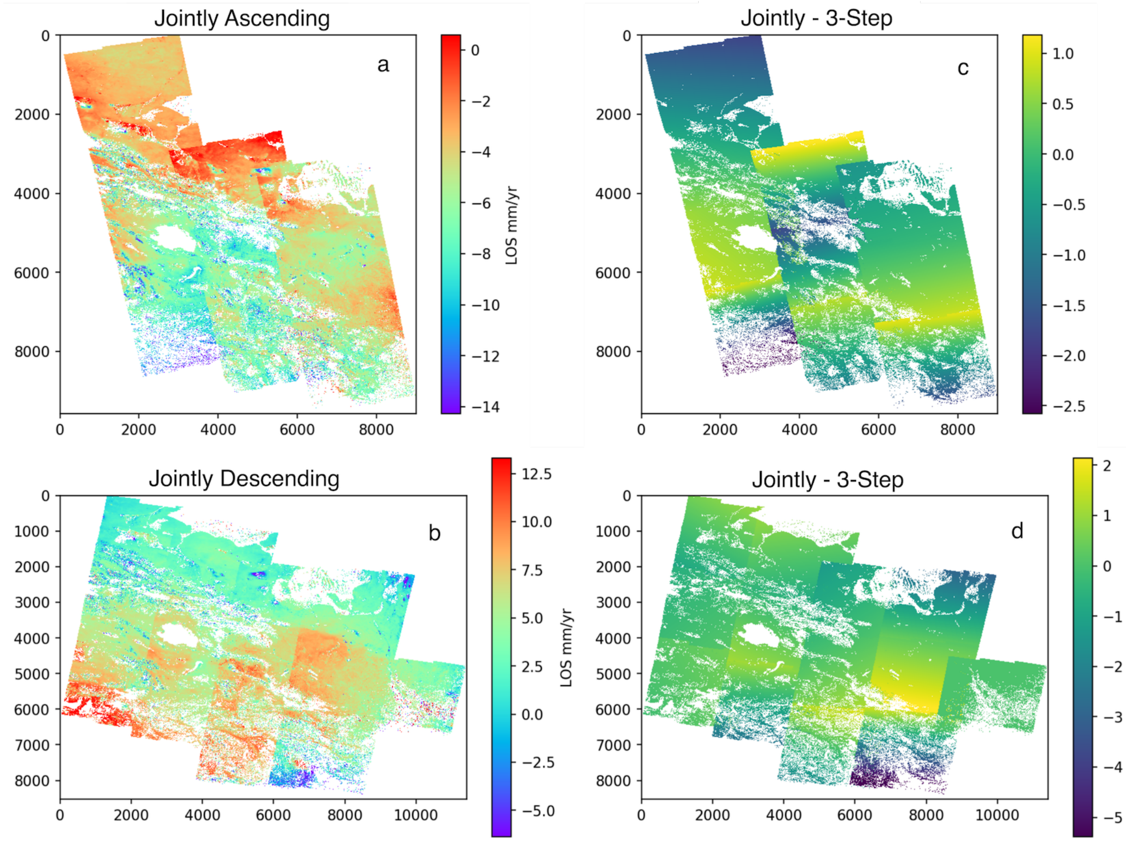

Figure B.8: LOS maps of joint inversion with weighting factor $w = 1$ and their differences with the LOS maps produced from the 3-step approach.

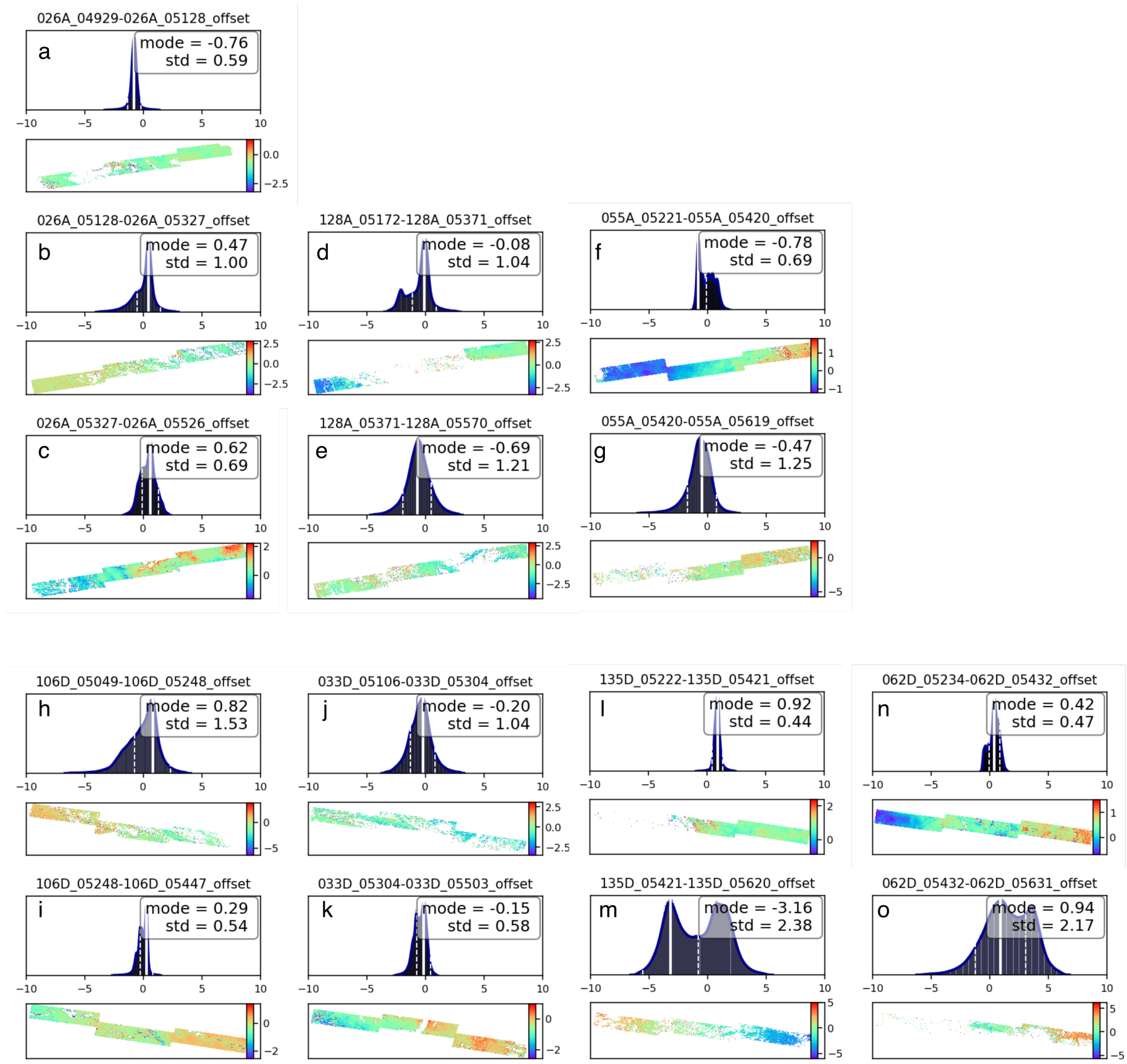

Figure B.9: Histograms of pixel differences between frame overlaps after joint inversion with weight $w = m/n$. The ramps reappeared because too much emphasis was put on the GNSS points.

B.5 Proof of V_E V_{UN} decomposition

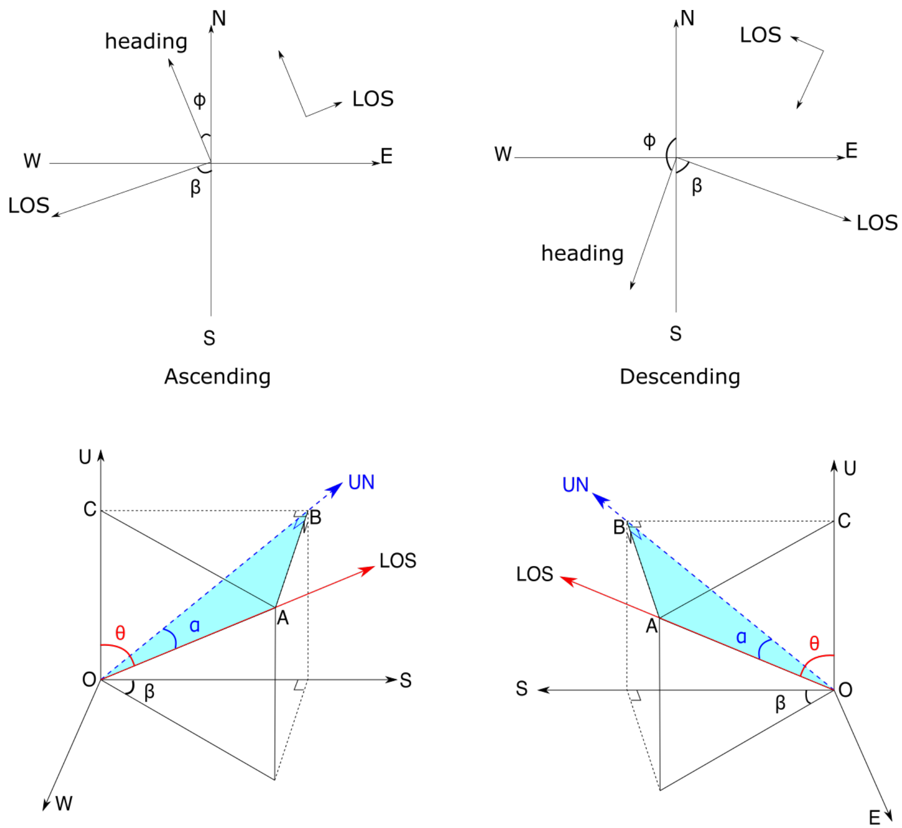

Ascending:
$\phi \sim -10$
$\beta = 180 - 90 + \phi = \phi + 90$
$\sin(\beta) = \sin(\phi+90) = \cos(\phi)$
$V_{LOS} = -V_E \cos(-\phi) \sin(\theta) + (-V_N)\sin(-\phi)\sin(\theta) + V_U \cos(\theta)$
$= -V_E \cos(\phi) \sin(\theta) + V_N \sin(\phi)\sin(\theta) + V_U \cos(\theta)$

Descending:
$\phi \sim -170$
$\beta = 90 - (\phi + 180) = -(\phi + 90)$
$\sin(\beta) = -\sin(\phi+90) = -\cos(\phi)$
$V_{LOS} = V_E \cos(180+\phi) \sin(\theta) + (-V_N)\sin(180+\phi)\sin(\theta) + V_U \cos(\theta)$
$= -V_E \cos(\phi) \sin(\theta) + V_N \sin(\phi)\sin(\theta) + V_U \cos(\theta)$

Geometry:
$AB = OA \sin(\alpha) = OA \sin(\theta) \sin(\beta)$
so, $\sin(\alpha) = \sin(\theta) \sin(\beta)$
$\cos(\alpha) = \mathrm{sqrt}(1 - \sin^2(\alpha))$
$= \mathrm{sqrt}(1 - \sin^2(\theta) \sin^2(\beta))$
$= \mathrm{sqrt}(1 - \sin^2(\theta) \cos^2(\phi))$

Decomposition:
$V_{LOS} = -V_E \cos(\phi) \sin(\theta) + V_N \sin(\phi)\sin(\theta) + V_U \cos(\theta)$
$= -V_E \cos(\phi) \sin(\theta) + V_{UN} \cos(\alpha)$
$= -V_E \cos(\phi) \sin(\theta) + V_{UN}\, \mathrm{sqrt}(1-\sin^2(\theta)\cos^2(\phi))$

so, $V_{UN} = (V_N \sin(\phi)\sin(\theta) + V_U \cos(\theta)) / \mathrm{sqrt}(1- \sin^2(\theta) \cos^2(\phi))$

Figure B.10: Geometry for calculating LOS from E-W, N-S and U-D velocity components. O=Ground pixel, N=North, E=East, S=South, W=West, LOS=Line of sight direction from the point of observation to the satellite, UN=Projection of LOS to the north-up plane. ϕ=Heading angle, θ=Incidence angle, α=Angle between LOS and UN.

B.6 Decomposition per overlap area

Equation 4.6 is solved for overlapping regions between all possible combinations of an ascending and a descending track. The decomposed V_E and V_{UN} for each track combination is shown in Fig B.11. Fig B.12 shows the merged V_E and V_{UN} velocity maps from the individual track overlaps.

As an additional test for the quality of the velocity fields, I calculate the pixel differences between overlapping areas of the V_E and V_{UN} patches obtained this way (Fig B.13 and Fig B.14). These little overlapping areas between the V_E and V_{UN} patches will together make up the shapes of the thin strips of track overlaps, with one (2 choose 2) layer of offsets for areas covered by three tracks as there are 2 possible track combinations (e.g., $a_0\_d_0$ and $a_0\_d_1$) and six (4 choose 2) layers of offsets for areas covered by four tracks as there are four track combinations (i.e., $a_0\_d_0$, $a_0\_d_1$, $a_1\_d_0$ and $a_1\_d_1$). The important information from the plots are the modes, which indicate the systematic biases from choosing a particular track combination to assume equal V_{UN}. The standard deviations indicate the scatter of such offsets which reflect the level of noise in the measurements. The facts that the average of the modes are close to zero and the largest absolute value of the modes is 1.2 mm/yr mean the uncertainties from the approximation of equal V_{UN} is at a similar level as that from the measurements.

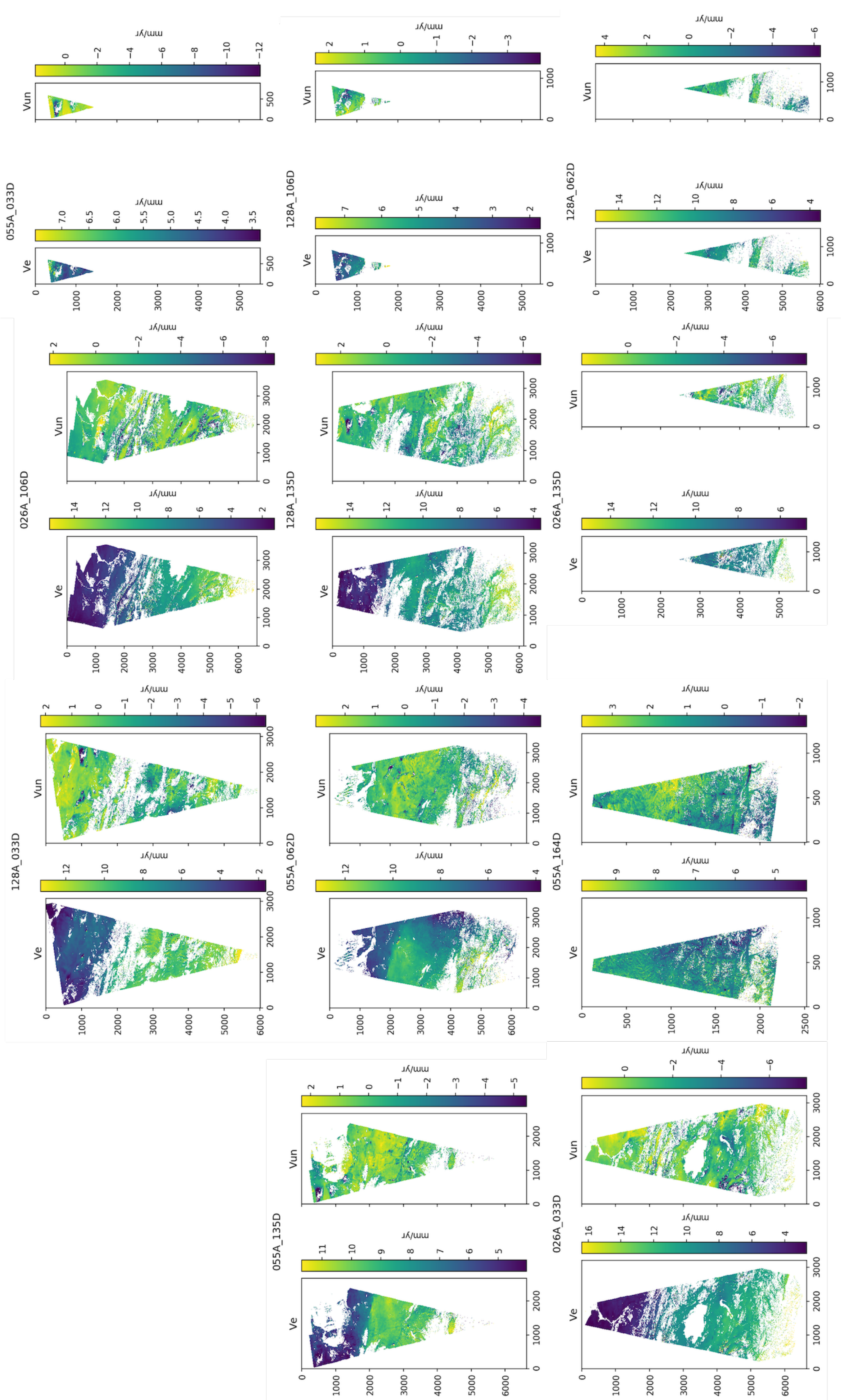

Figure B.11: Results of V_E and V_{UN} decomposition per overlapping area labeled by track numbers.

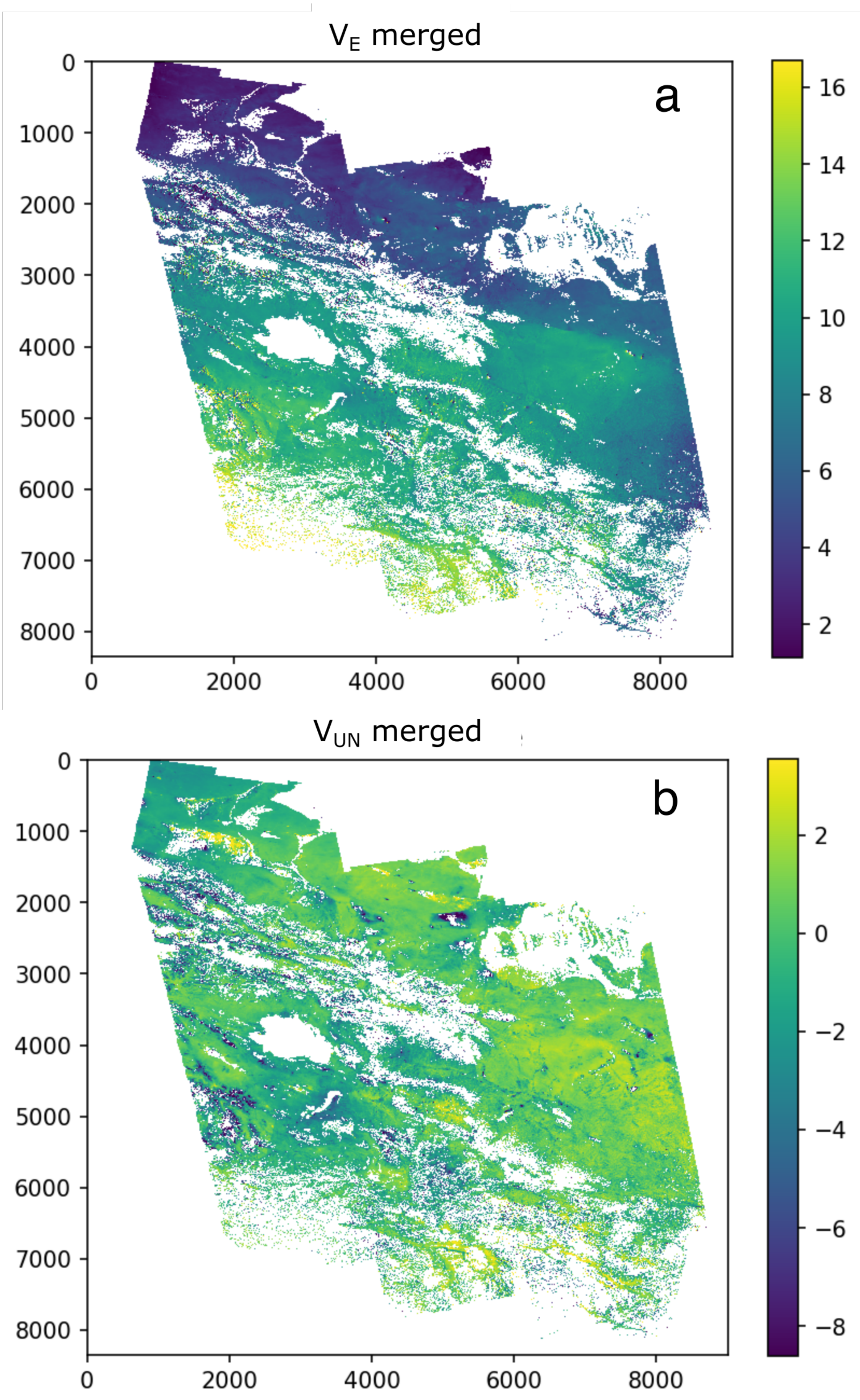

Figure B.12: Merged maps of (a) V_E and (b) V_{UN} fields.

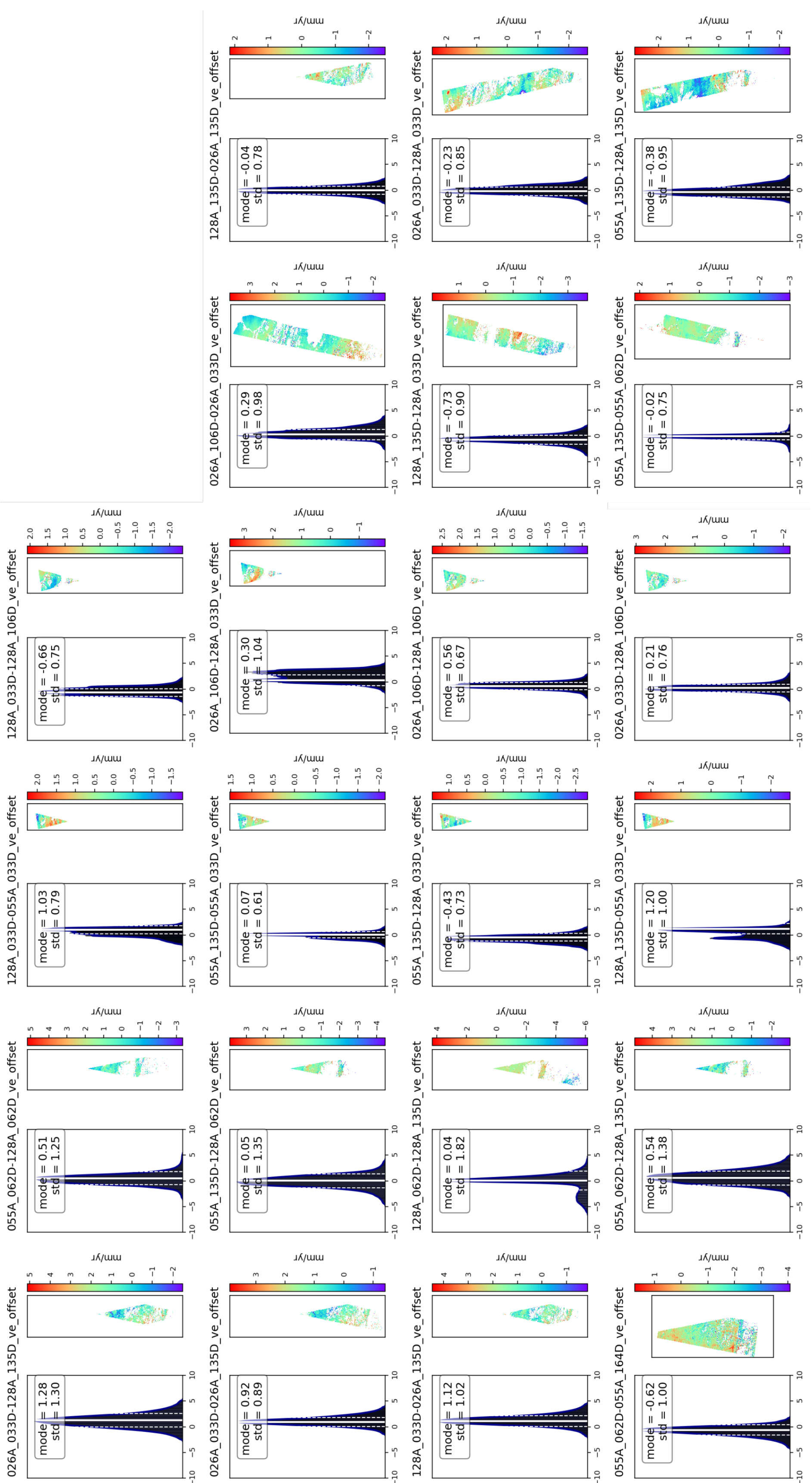

Figure B.13: Pixel differences between all possible combinations of overlapping V_E patches. Panels are labeled by Asc1_Dsc1-Asc2_Dsc2 where the difference histogram and map are between V_E resolved from Asc1 and Dsc1 LOS velocities and V_E resolved from Asc2 and Dsc2 LOS velocities.

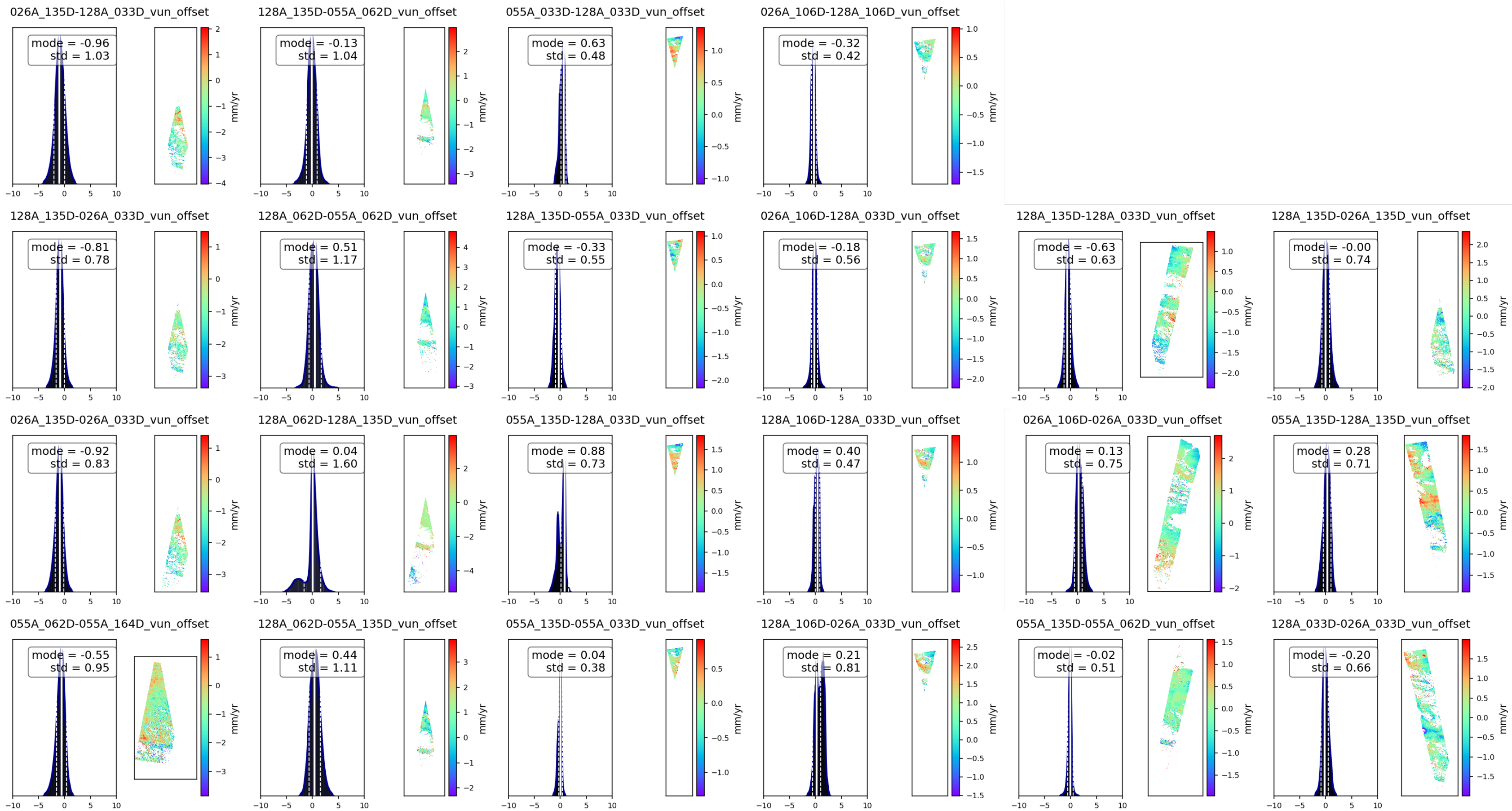

Figure B.14: Differences between all possible combinations of overlapping V_{UN} patches. Panels are labeled with 'Asc1_Dsc1-Asc2_Dsc2' where the difference histrogram and map are between V_{UN} resolved from Asc1 and Dsc1 LOS velocities and V_{UN} resolved from Asc2 and Dsc2 LOS velocities.

B.7 Enlarged V_U Maps

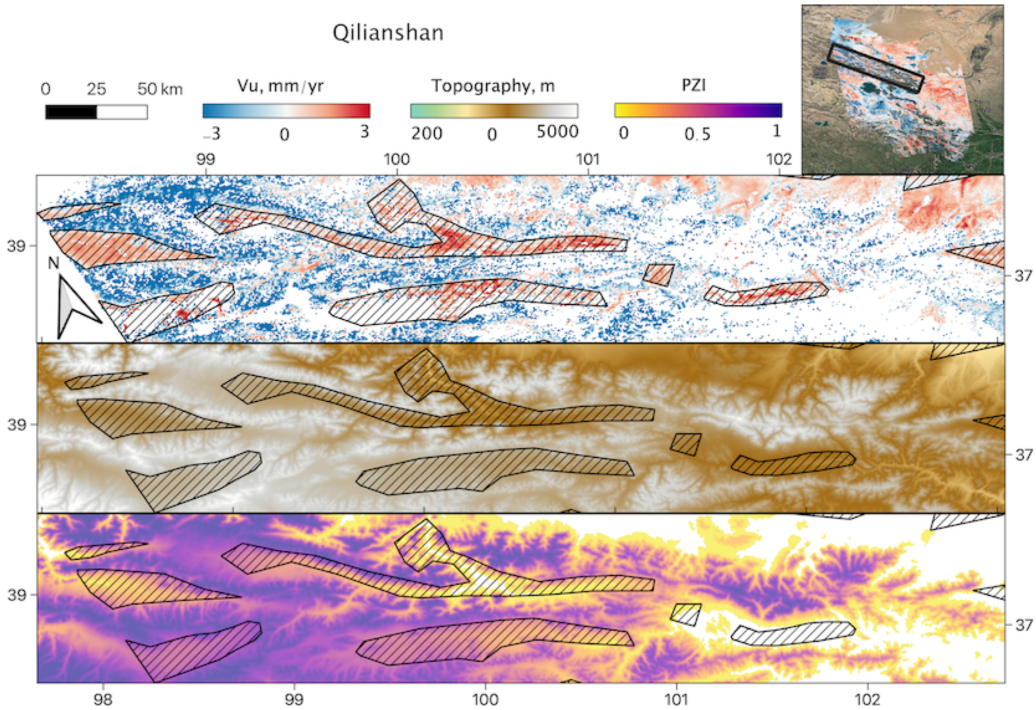

Figure B.15: Comparison between V_U, Shuttle Radar Topography Mission (SRTM) Digital Elevation Model (DEM), and Permafrost Zonation Index (PZI) (*Gruber*, 2012) across the Qilianshan thrusts. High PZI represents permafrost in nearly all conditions; low PZI represents permafrost only in very favourable conditions.

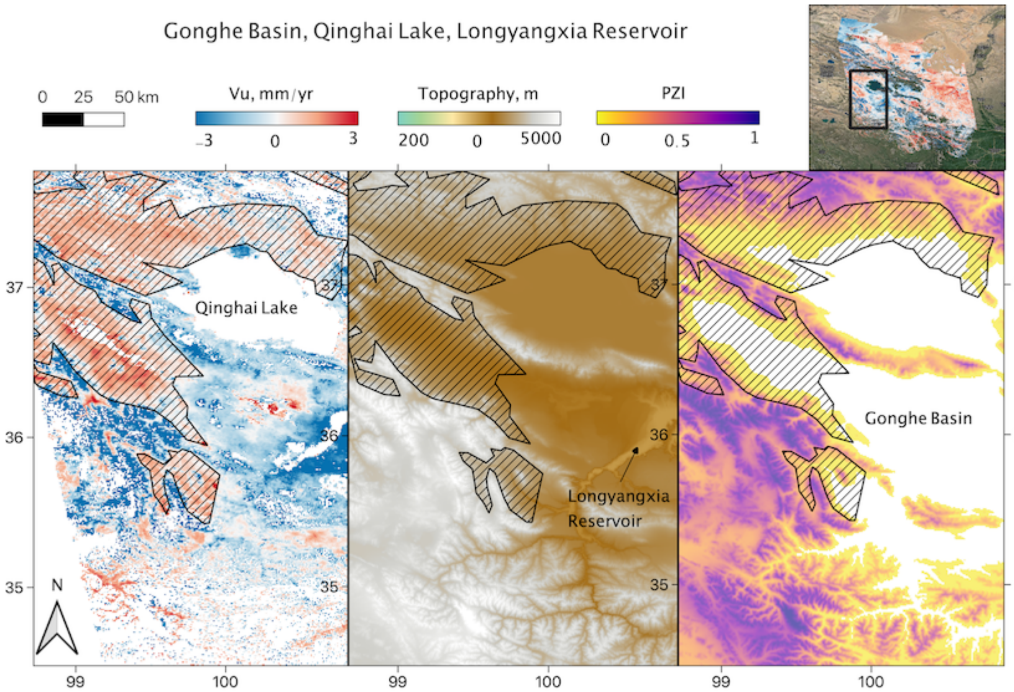

Figure B.16: Same as in Fig B.15 for the Gonghe Basin, the Qinghai Lake and the Longyangxia Reservoir.

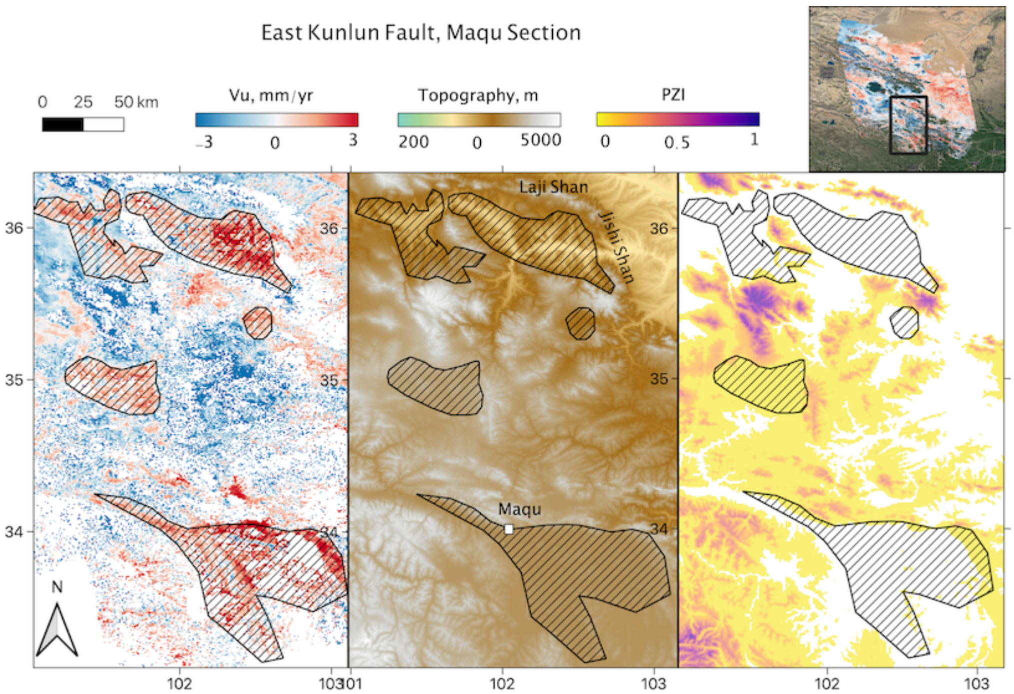

Figure B.17: Same as in Fig B.15 for the Laji Shan and Jishi Shan, as well as the Maqu section of the East Kunlun Fault.

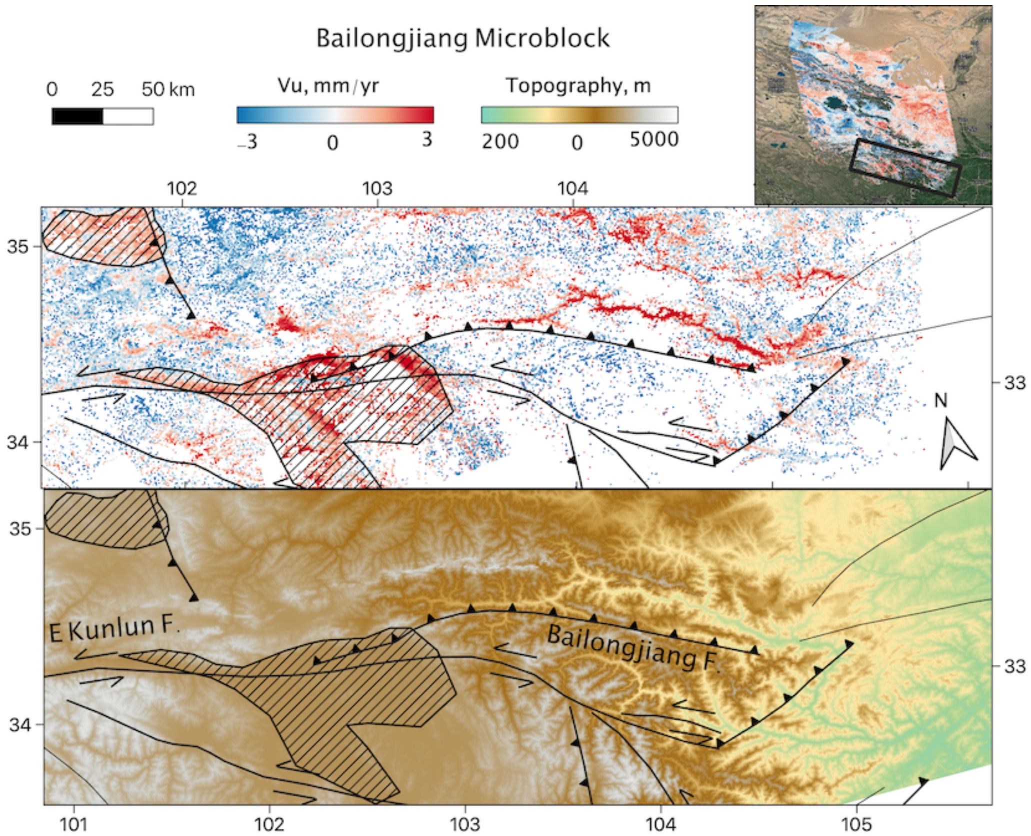

Figure B.18: Same as in Fig B.15 for Bailongjiang thrust.

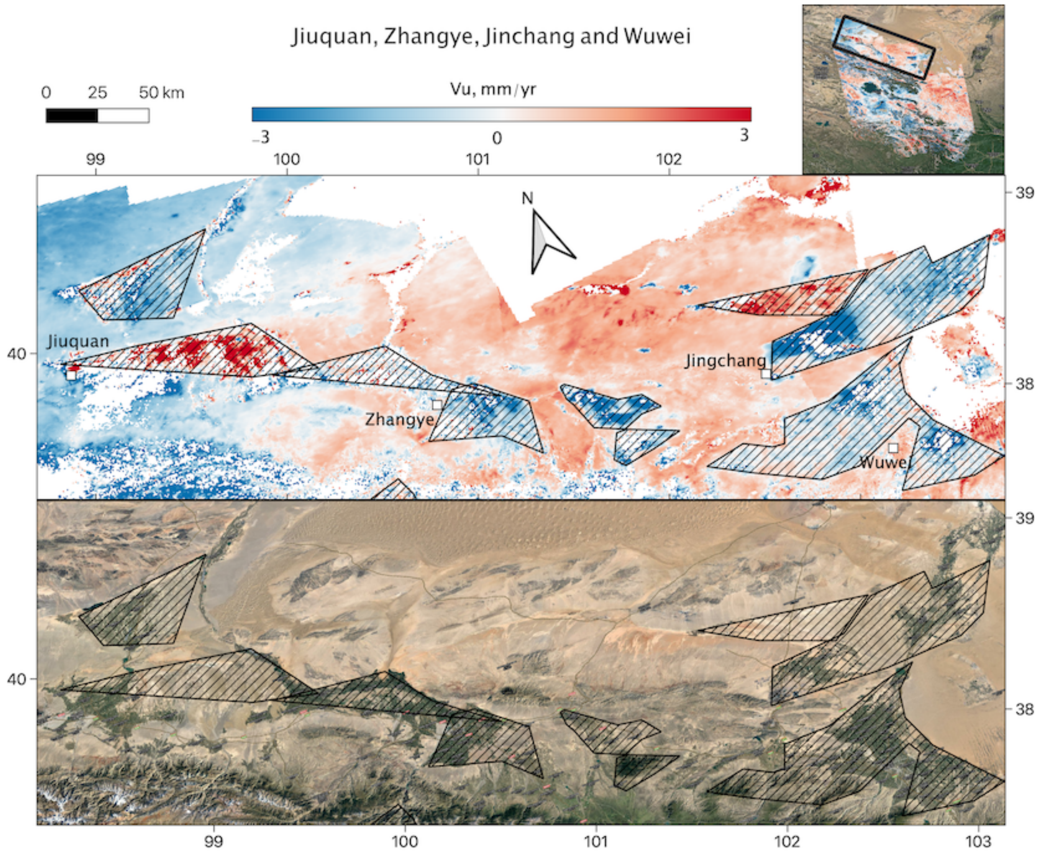

Figure B.19: Same as in Fig B.15 for the major cities to the north of the Qilianshan.

Appendix C

Strain Rates and Seismic Hazard Assessment

C.1 Velocity Gradient Components

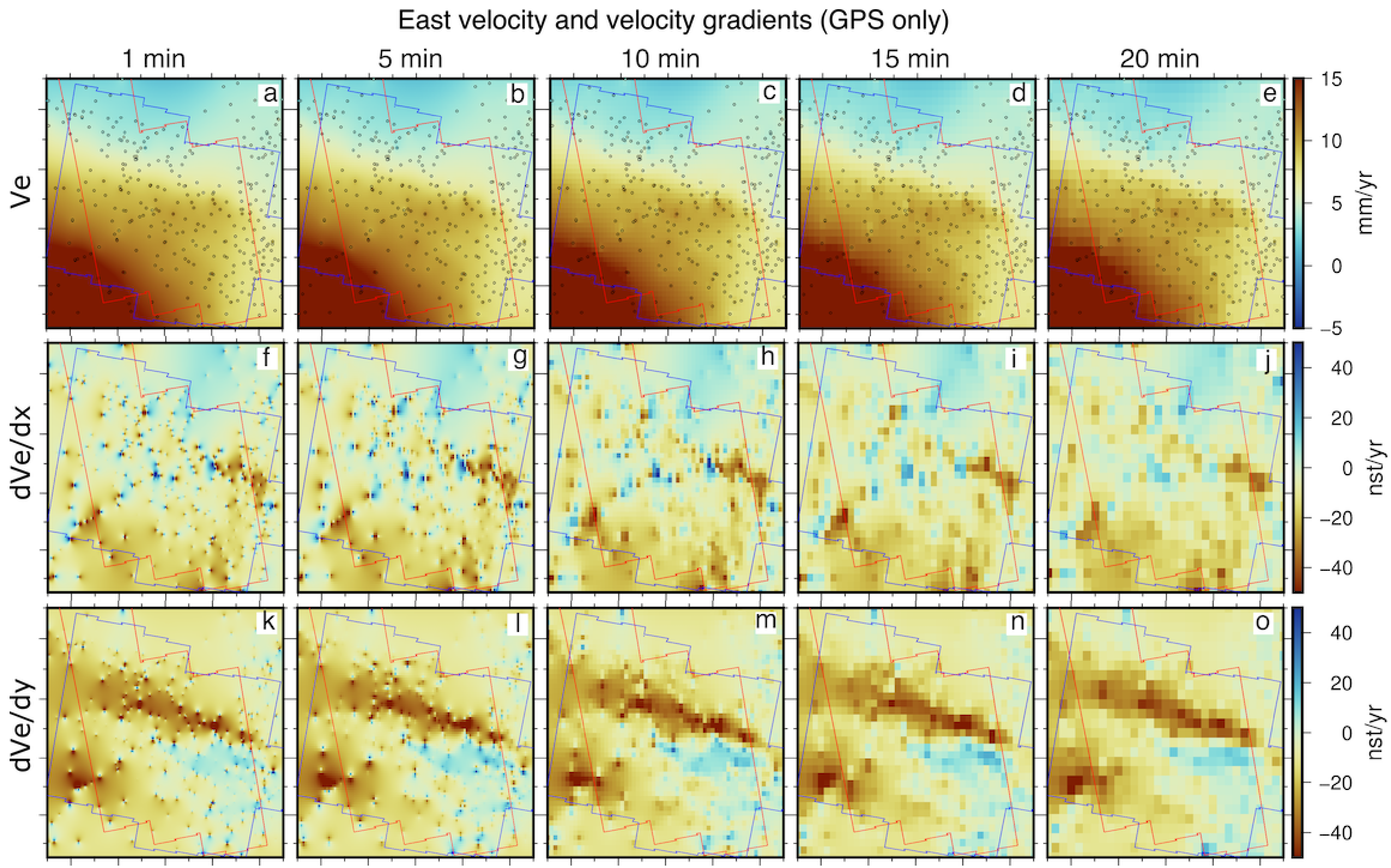

Figure C.1: E-W velocity maps based on *surface* fitted to the GNSS velocities and filtered down to resolutions of (a) 1 arcminute, (b) 5 arcminutes, (c) 10 arcminutes, (d) 15 arcminutes and (e) 10 arcminutes. (f-i) are the derivatives of (a-e) in the E-W direction. (k-o) are the derivatives of (a-e) in the N-S direction.

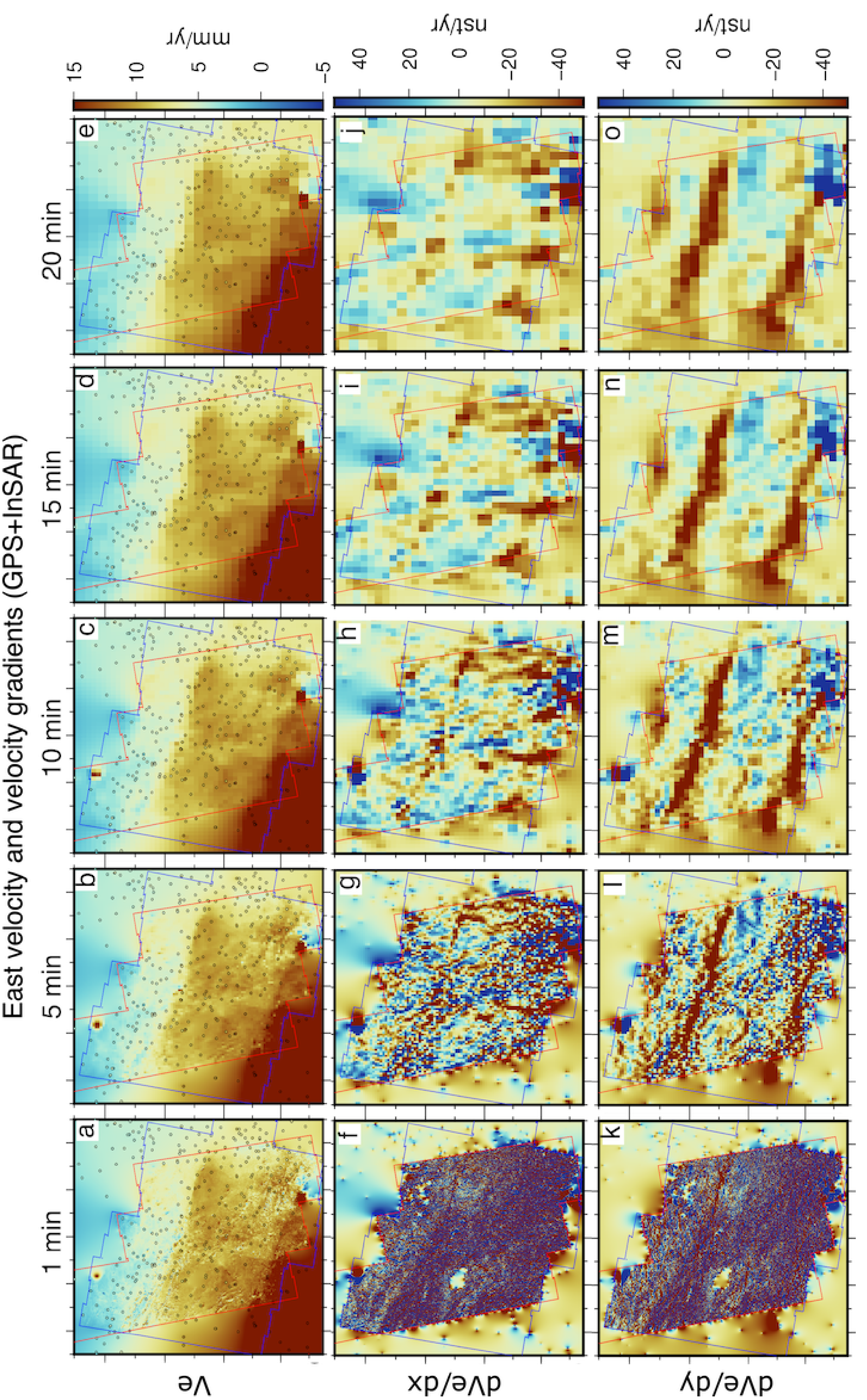

Figure C.2: E-W velocity maps based on *surface* fitted to the combined data set of InSAR and GNSS velocities and filtered down to resolutions of (a) 1 arcminute, (b) 5 arcminutes, (c) 10 arcminutes, (d) 15 arcminutes and (e) 10 arcminutes. (f-i) are the derivatives of (a-e) in the E-W direction. (k-o) are the derivatives of (a-e) in the N-S direction.

C.2 VELMAP Strain Rate Products

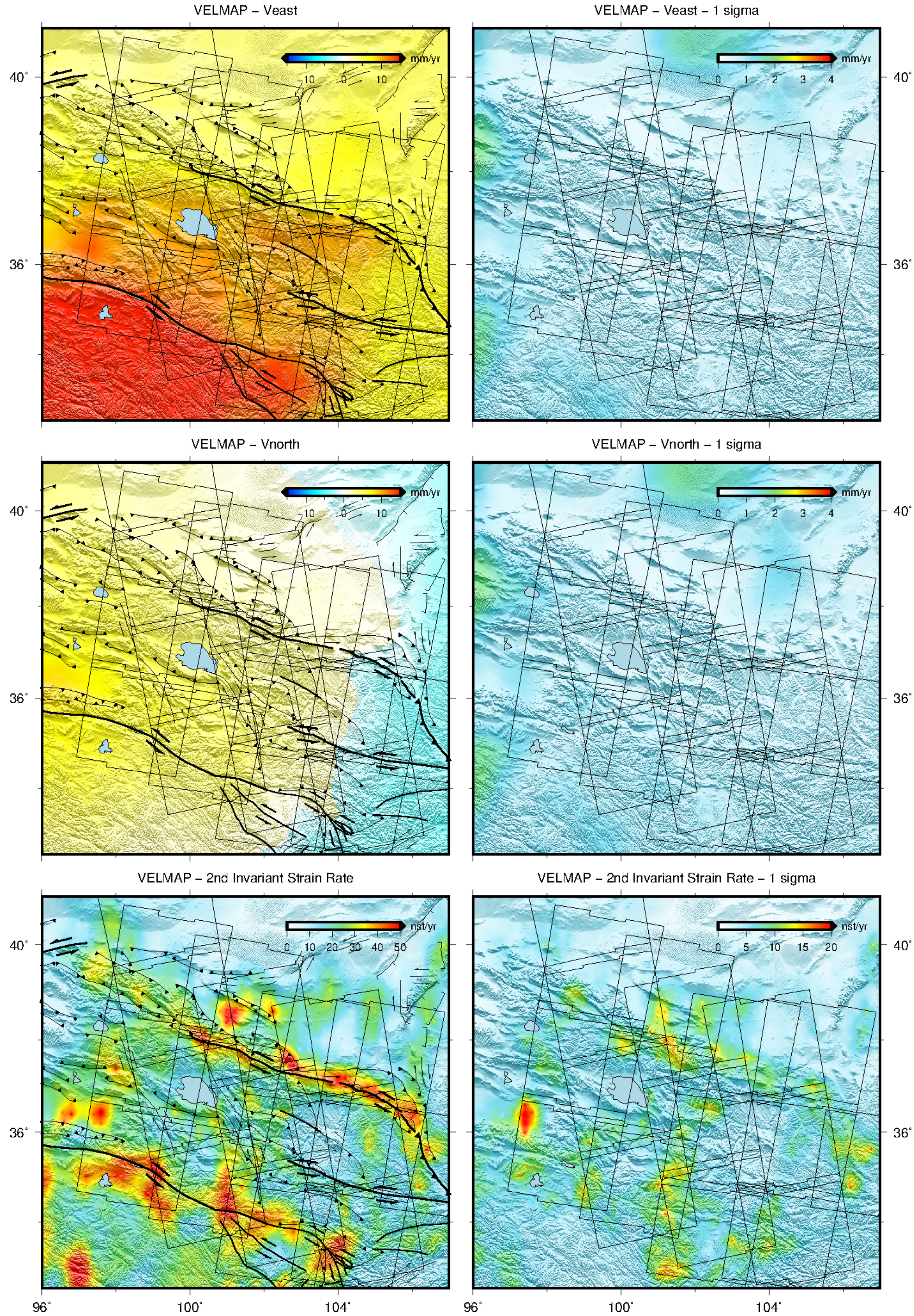

Figure C.3: VELMAP outputs of E-W, N-S and 2nd invariant strain rate and associated uncertainties, calculated with smoothing factor of 1.2, multilook factor of 10, distance between mesh nodes of 20 km, E-fold distance of variance-covariance matrix of 10 km and with 3D GNSS and ascending and descending LOS tracks.

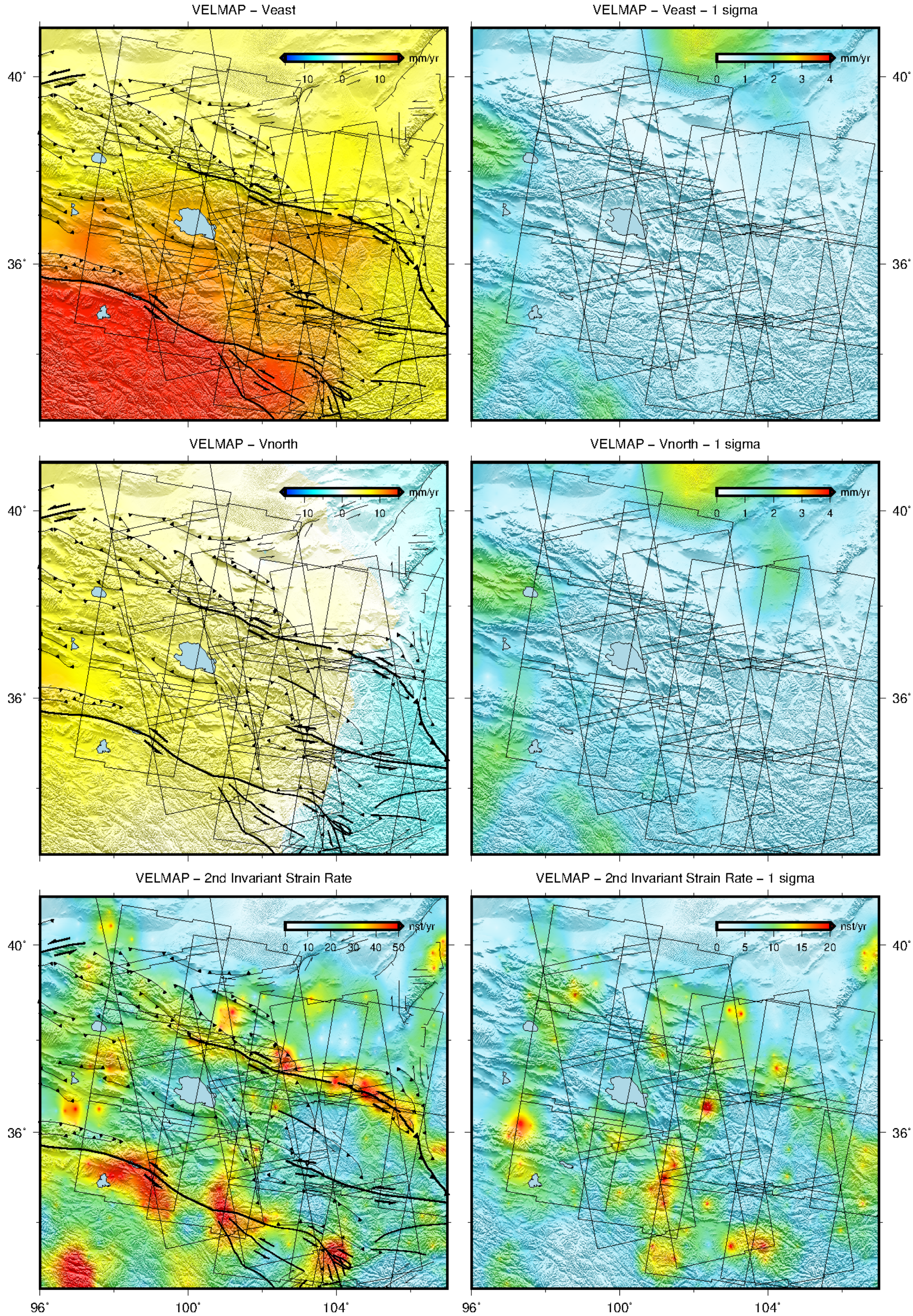

Figure C.4: Same as in Fig C.3 but with distance between mesh nodes of 30 km.

C.3 Seismic Hazard Assessment

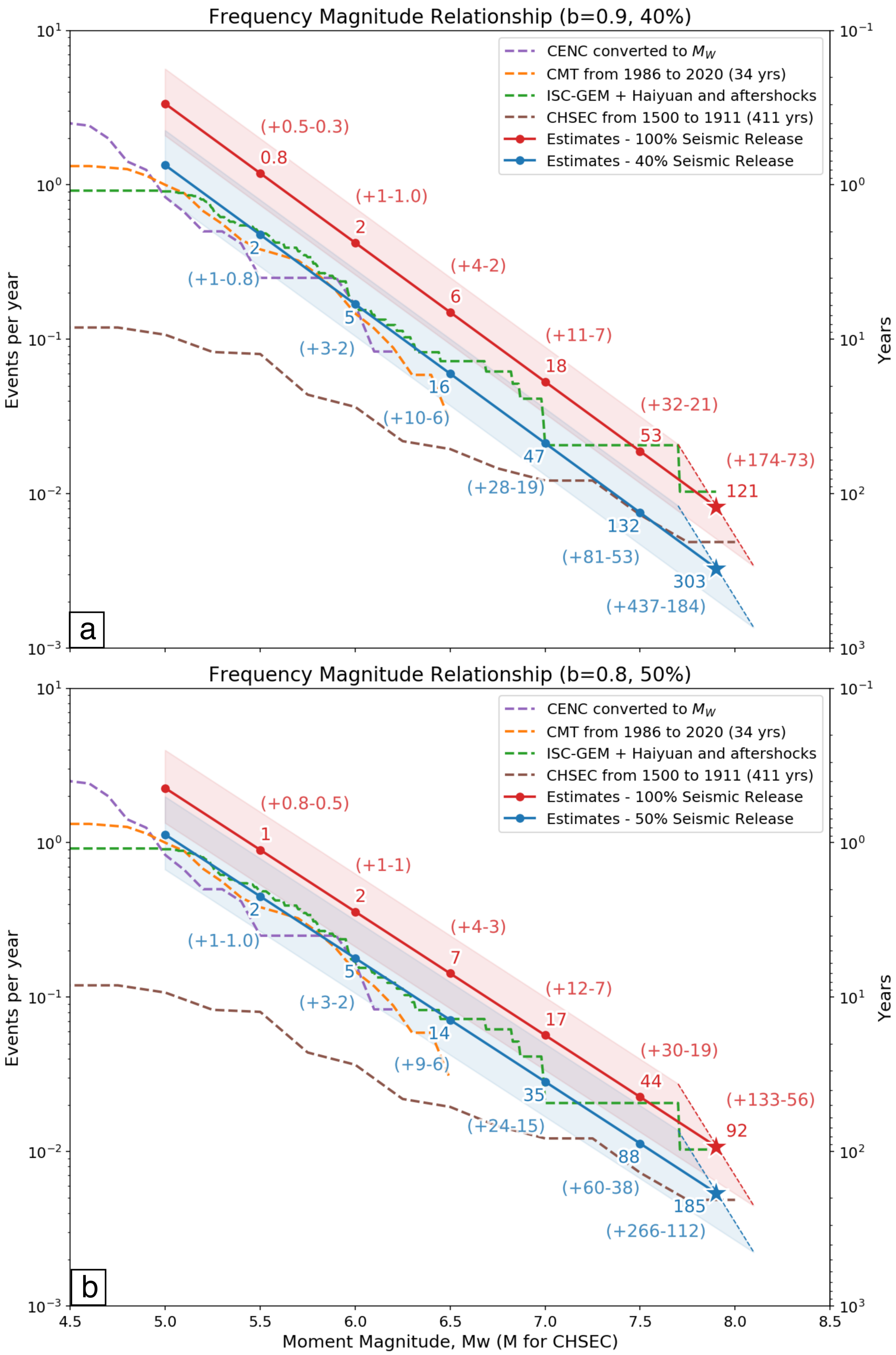

Figure C.5: Same as in Fig 5.16 but with (a) b value of 0.9 and 40% seismic release of strain and (b) b value of 0.8 and 50% seismic release of strain.